FACULTES UNIVERSITAIRES
NOTRE-DAME DE LA PAIX
NAMUR

FACULTE DES SCIENCES

Département de Mathématique

Global dynamics of geosynchronous space debris with high area-to-mass ratios

Dissertation présentée par

Stéphane Valk

en vue de l'obtention du grade
de Docteur en Sciences

Composition du Jury :

Kaare AKSNES
Luciano ANSELMO
Timoteo CARLETTI
Anne LEMAÎTRE (Ph.D. Advisor/Promoteur)
Philippe TOINT

2008

Rempart de la Vierge, 13
B–5000 Namur (Belgique)

Imprimé en Belgique

ISBN : 978-2-87037-603-4
Dépôt légal : D / 2008 / 1881 / 32

Dynamique globale des débris spatiaux géosynchrones caractérisés par de grands rapports aire-sur-masse

par Stéphane Valk

Résumé : Le travail effectué dans cette thèse s'appuie sur le développement d'une méthode semi-analytique (basée sur le concept de mouvement moyen) particulièrement bien adaptée à l'étude à long terme des débris spatiaux situés au voisinage de l'orbite géostationnaire. Deux approches sont développées en parallèle : la première consiste à donner une solution alternative aux problèmes induits par les singularités rencontrées pour les orbites circulaires et équatoriales et à proposer une approche hamiltonienne de la modélisation de la résonance géostationnaire. La seconde, suite à la découverte de la nouvelle population de débris spatiaux avec grands rapports aire-sur-masse, étend la méthode de base, en tenant compte d'une modélisation adaptée de la pression de radiation solaire, dont les effets principaux sont mis en évidence par l'étude du mouvement à long terme des vecteurs excentricité et inclinaison. De plus, toujours à long terme, les effets induits par l'ombre de la Terre sont intégrés dans le modèle au moyen d'un algorithme spécialement développé à cet effet. Finalement, une étude systématique de la stabilité des débris spatiaux proches de l'orbite géostationnaire avec grands rapports aire-sur-masse est effectuée, au moyen d'un indicateur de chaos, le MEGNO, basé sur le concept de système d'équations aux variations et met en évidence certaines zones spécifiques de la dynamique.

Global dynamics of geosynchronous space debris with high area-to-mass ratios

by Stéphane Valk

Abstract: This Ph.D. thesis is devoted to the development of a specific semi-analytical algorithm especially well-suited to derive the long-term evolution of near geosynchronous space debris and based on the concept of mean orbital motion. In a first approach, the semi-analytical theory is concerned with the singularity issues arising for circular and equatorial orbits as well as with the geostationary resonance modeling. In a second part, motivated by the discovery of high area-to-mass ratios space debris in high altitude Earth's orbit (mostly near the geosynchronous region), the direct radiation pressure models are revisited and completed. Within this context, the main effects of the direct solar radiation pressure for the mid- and long-term evolution of both the eccentricity and the inclination vectors are analyzed through a well-suited model. Moreover, by means of a smart extension, the passage in the Earth's shadow is taken into account in the computations of the orbits. Finally, a further insight into the intrinsic stability of such space debris is performed, by means of a recent numerical technique (MEGNO) which is based on the concept of "variational chaos indicator".

Dissertation doctorale en Sciences mathématiques (Ph.D. thesis in Mathematics)
Date : 19-06-2008
Département de Mathématique
Unité de Systèmes Dynamiques
Promoteur (Ph.D. Advisor) : Prof. A. LEMAÎTRE

First there was the "Big Ocean Theory", which basically meant that the ocean was so big that humans could dump any amount of waste into it without environmental consequence. Of course, that theory has proven to be false as ocean ecosystems today suffer from dying coral reefs and fish populations poisoned with mercury and other pollutants. Next came the "Big Atmosphere Theory", which assumed that we could belch out billions of tons of air pollution and carbon dioxide from our smoke stacks and tail pipes without environmental repercussions. We all know how that idea has impacted the planet : air pollution, acid rain, ozone depletion and global warming. Now we have a "Big Space Theory", namely, that space is so big that the waste we create in it will cause no harm. That's right folks, fifty years after Sputnik launched the space age, humans have turned space into yet another junk yard, with millions of pieces of man-made debris orbiting the Earth. The space debris problem is becoming so critical that space may become too trashed to use at all. What the world needs now, before it becomes too late, is an environmental movement in heaven : Space Ecology.

By Lynda Williams, 2007

Remerciements

Arrivé au terme de mon aventure au pays merveilleux des débris spatiaux, je tiens à exprimer ma reconnaissance à tout ceux qui, de près ou de loin, ont contribué au bon déroulement de ce travail de thèse.

Je tiens tout d'abord à exprimer ma plus sincère et profonde gratitude à Anne Lemaître, mon directeur de thèse, pour m'avoir donné l'opportunité de réaliser ce projet ambitieux. Je la remercie pour la confiance et la liberté qu'elle m'a accordées, pour son encadrement quotidien ainsi que pour ses encouragements dans les moments les plus difficiles. Je tiens également à la remercier pour son enthousiasme et ses qualités humaines qui ont fait de ces six années une première expérience professionnelle dont je garderai des souvenirs exceptionnels.

Je souhaite également remercier tous les membres du jury pour avoir accepté d'évaluer mon travail de thèse ainsi que pour leurs remarques constructives et leurs conseils judicieux. Plus particulièrement, je souhaite adresser ma gratitude à Luciano Anselmo et Timoteo Carletti pour nos collaborations qui se sont avérées être des expériences scientifiques enrichissantes.

Je suis aussi particulièrement reconnaissant envers Nicolas Delsate, sans qui mon dernier projet de recherche n'aurait certainement pas vu le jour aussi rapidement. Merci pour ta disponibilité, pour ton enthousiasme et ton efficacité face à la recherche scientifique, mais aussi pour ces traditionnelles et néanmoins indispensables pauses café. Nico, je te souhaite une très belle route à venir !

Merci également à Julien Dufey pour avoir toujours veillé à entretenir cette inoubliable ambiance "de travail" dans notre bureau. Je garderai un souvenir impérissable de nos multiples fous rires dont il est préférable de taire les raisons dans ces quelques lignes. Ju, merci pour ta bonne humeur et ton amitié !

Je tiens encore à remercier Ravi Ramdoyal pour sa disponibilité et son aide multilingue dans la rédaction de mon manuscrit. Merci Ravi pour ton ouverture d'esprit ainsi que pour l'écoute dont tu as fait preuve envers moi au cours de ces dix dernières années. Tonton, merci pour l'amitié inconditionnelle et si précieuse que nous partageons et qui, je l'espère, sera encore longue !

Tous mes remerciements également aux membres du département de mathématique et en particulier à l'équipe de systèmes dynamiques. Toutes ces années passées parmi vous resteront gravées dans ma mémoire.

Un tout grand merci également à l'équipe de géodésie et mécanique céleste (GEMINI) de l'observatoire de la Côte d'Azur (Grasse) pour m'avoir accueilli quelques mois dans le cadre d'un séjour de recherche. Plus particulièrement, je suis reconnaissant envers Florent Deleflie pour avoir joué incontestablement un rôle initiateur et moteur dans le développement de mon sujet de thèse. Florent, merci pour tous ces échanges que nous avons partagés et qui ont été aussi riches scientifiquement qu'humainement !

C'est avec beaucoup d'émotion que je tiens à remercier ma famille et plus particulièrement mes parents pour leur affection et leur soutien permanent durant mes longues années d'études, sans lesquels je n'aurais pas pu réaliser ce travail. Maman, Papa, si j'ai réussi à relever ce défi, si je suis devenu celui que je suis aujourd'hui, c'est en grande partie grâce à vous. Pour tout cela, et pour bien plus encore, mille fois merci !
Je ne voudrais pas non plus oublier ma grand-mère qui a toujours suivi mon parcours avec beaucoup d'attention. Merci Mammy lunettes !

Enfin, merci à toi, Anne-Sophie, mon rayon de soleil, pour le soutien moral sans faille que tu m'as réservé. Merci pour ton amour, tes encouragements, ton dynamisme débordant et inégalable qui ont grandement contribué à la réussite de ce projet. Ensemble, l'aventure continue !

Je dédie cette thèse à mes parents. J'espère pouvoir leur rendre un jour tout ce qu'ils m'ont apporté.

Contents

Introduction

The present near-Earth space environment is the result of a few more than 50 years of space activities. The well-known first artificial satellite, *Sputnik 1*, has been launched in October 1957 by the Soviet Union (USSR). Since that time, space exploration constantly kept on producing significant amounts of man-made objects in space. Actually, the near-Earth region was probably the only close environment which remained unspoiled by human activities. One can feel the uneasiness brought by such a statement.

The space debris issue is unquestionably a growing concern. Indeed, orbital debris generally move at very high speeds relative to current operational satellites. At this velocity, even a small particle contains significant kinetic energy and momentum to damage or even destroy functional satellites during an impact[1]. Collisions between satellites and debris have already been observed. One of the first unintentional collision in space history occurred on July 1996 when a fragment of about 10 cm^2 (coming from the explosion of an Ariane rocket upper stage launched ten years before) hit the French satellite *Cerise* at the relative velocity of 14 km/s (Alby et al., 1997; Rossi, 2005).

Even more recently, the space debris concern has been put forward after the successful deployment of an anti-satellite (*ASAT*) missile by the People's Republic of China. Indeed, in January 2007, the 880 kg weather spacecraft *Fengyun-1C*, launched in 1999 into a sun-synchronous orbit with a mean altitude of about 850 km, has been deliberately destroyed over central China without any legal consequence (Pardini and Anselmo, 2007). This break-up produced around 2 600 debris, mostly larger than 10 cm (Orbital Debris Quarterly News, January 2008), thereby increasing the total amount of cataloged space junk by about 20%. The generated debris cloud currently crosses the orbits of many satellites in low-Earth orbit, increasing the hazard of debris collision by over 15%. For the sake of completeness, we ought also to mention that this event is not unprecedented. Indeed, the space exploration history reveals that anti-satellite weapons date back to the 1960s with the US and USSR separately engaging in the development and deployment of such space weapons. In particular, a successful *ASAT* test was performed by the United States in September 1985. During this event, the spacecraft *Solwind P78-1* was destroyed by an anti-satellite missile which was launched from a fighter aircraft along the Californian coastline, producing about 285 space debris of significant size

[1]To gain insight on this point, let us note that a 1-g mass travelling at 10 km/s has approximately the same kinetic energy as a 100 kg mass travelling at 100 km/h.

(Klinkrad, 2006).

For all theses reasons, the space debris problematic has rapidly become a major matter of concern which in turn has been extensively investigated by the scientific community over the past few years. Currently, the space debris investigations are essentially performed by using models which provide a mathematical description of the distribution of objects in space, the motion and flux of objects and their physical characteristics. These models are said to be statistical if they are devoted to the characterization of a large set of debris by a sample of objects. The models are deterministic if each object is described individually by its orbital elements and physical characteristics. Anyhow, most of these models are actually conceived within the context of a complete numerical integration of the equations of motion, regardless the computational performances. Moreover, while numerical integrations are especially straightforward and efficient when deriving a particular solution of a differential system of equations, they fail in providing a complete or general solution in order to give a clear understanding of the physical nature of the dynamics.

On the contrary, this Ph.D. thesis largely focuses on the development of a specific deterministic theory which extensively takes advantages of several concepts derived from Celestial Mechanics. Among others, we can mention, an adapted Hamiltonian formalism coupled with the well-known symplectic Lie algorithm, the resonance concerns as well as the mean orbital motion theories. This theory can therefore be applied to derive the evolution of specific space debris over time scales as high as several decades, while giving a detailed interpretation of the observed dynamics.

We now give a brief description of the contents of this thesis project and the contributions included therein.

Contributions and structure of the manuscript

Chapter 1 gives an introduction to the space debris problematic. In particular, we shortly define the concept of space debris which is followed by a description of the current space debris population. Subsequently, this chapter is also devoted to give further insights into the all-important geostationary region which will actually be the background and the major concern of our research work. In addition, we will give a general survey of the new unexpected population of space debris that has been discovered recently near the geostationary region on behalf of European Space Agency. As a matter of fact, these objects turn out to be fairly exceptional. Indeed, these space debris are presumably characterized by both a large outermost area and a very small weight. These space debris are said to be marked by high area-to-mass ratios.

Chapter 2 is mostly devoted to the development of a specific theory which is intended to give the long-term description of an arbitrary space debris located near the geostationary

ring[2]. This chapter is effectively far from being exhaustive and is essentially devoted to give the outline of the so-called semi-analytical theory that will be discussed, extensively used and improved in the following chapters. In particular this semi-analytical theory is based on the concept of mean orbital motion. In this field, what is of special relevance is not the complete description of the motion but the prediction of an approximate position at a given time while improving considerably the computational performance of the algorithm. On the other hand, this chapter is also concerned with the singularity issues arising for circular and equatorial orbits as well as with the challenging resonance modeling for which we propose a well-adapted solution. The results of Chapter 2 have been previously submitted in Valk et al. (2007a).

As a result of the unexpected discovery of high-area-to-mass ratio space debris, we seized the opportunity to extend our semi-analytical theory by including the solar radiation pressure acceleration which is assumed to be the major perturbation experienced by those space debris. This extension is developed in Chapter 3 and is especially intended to derive the main effects of the direct solar radiation pressure by analyzing the mid- and long-term evolution of both the eccentricity and the inclination vectors. In addition, we also emphasize the importance of adopting a well-suited solar radiation pressure modeling when deriving the motion of these unfamiliar space debris. The results of Chapter 3 have been previously published in Valk et al. (2007b).

The main objective of Chapter 4 is dedicated to an extension of the solar radiation pressure modeling. This extension gives an improvement of the theory developed in Chapter 3 by taking into account the long-term effects induced by the Earth's shadow. In this approach, the perturbations accounting for the direct solar radiation pressure with the Earth's shadow are computed on a revolution-by-revolution basis, retaining the original unexpanded form of the so-called shadow function. This latter approach is also generalized into a convenient non-singular formalism, particularly appropriate for both near-circular and near-equatorial orbits as well as for orbits which transit periodically around null eccentricities and null inclinations. As an application, we propose to apply this algorithm in order to give further insight into the dynamics of high area-to-mass ratio space debris that are subject to the Earth's shadowing effects. The results of Chapter 4 have been previously published in Valk and Lemaître (2008).

Besides the above-mentioned semi-analytical investigations, we also propose to study the stability of the high area-to-mass ratio space debris. These investigations are performed by using a recent numerical technique that is based on the concept of "variational chaos indicator". This method is especially devoted to the investigation of both the regular and chaotic components of the phase space. The results, which are given in Chapter 5, provide an accurate understanding of the location of both the stable and unstable orbits as well as the time scale of their exponential divergence in case of chaotic motion. In addition, we also perform some additional frequency analysis investigations in order to give a insightful understanding of the

[2]Let us remark that "space debris" is commonly considered as a plural. However, in this manuscript, the expression "a space debris" will be regularly used as "a piece of space debris".

structures appearing in the phase space. The results of Chapter 5 have been previously submitted in Valk et al. (2008).

Finally, we conclude this manuscript by giving a summary of the work accomplished so far and by suggesting some possible outlooks for future research.

Let us also mention the work introduced in Appendix H, and which was initially devoted to the orbital determination of near-Earth asteroids. This work is mainly intended to the so-called *Admissible region* which can be computed as part of an orbital determination process, even if the complete set of six orbital elements can not be derived. In particular, we dedicate this work to the investigation of some important aspects related to the admissible region and to its refinement for the short distances with respect to the Earth. This work is all the more important as it has been recently extended to the main problem of orbit determination of the space debris population. The results of Appendix H have been previously published in Valk and Lemaître (2007a).

Part I

PRELIMINARY

Chapter 1

A brief overview of space debris

> *"Space debris are all man-made objects, including their fragments and parts, whether their owners can be identified or not, in Earth orbit or re-entering the dense layers of the atmosphere that are non-functional with no reasonable expectation of their being able to assume or resume their intended functions or any other functions for which they are or can be authorized."*
>
> United Nations, New York, 1999 (UN, 1999)

1.1 What are space debris ?

Orbital space debris generally refer to man-made objects which are in Earth's orbit as the result of space missions, but are no longer serving any useful purpose. The sources and the characteristics of such "space junks" are highly diversified. For instance, regarding the largest, these objects come in the form of rocket upper stages, defunct satellites and various mission related debris such as discarded equipments released during extra-vehicular activities, sensors caps, momentum flywheels used to stabilize the spacecrafts attitude, etc., to name only a few of them. In addition, the space debris population also includes smaller objects (centimeter- up to meter-sized) such as fragments created by the break-up of satellites and rocket upper stages but also millimeter-sized particles coming from material degradation as a result of solar heating and solar radiation, as well as solid rocket motor slag.

For the sake of completeness, it is worth noting that the official definition of space debris also includes re-entry objects, which are captured by the Earth's atmosphere. Actually, more than 60% of the objects which have been launched since the beginning of the space age have decayed by burning into the atmosphere, even though some of them are known to have survived reentry and crashed down on Earth. Typically, one "larger" man-made cataloged space debris is known to fall back on Earth every day (Schildknecht, 2007).

1.2 The current space debris population and its sources

Nowadays, as a consequence of a systematic and regular space activity, the space debris population has significantly increased. Indeed, during each launch, only a part of the total mass brought into space consists of active payloads[1]. The other remaining part are actually made of released objects which quickly become space debris. This is the reason why the current active artificial satellites only account for about 7% of the present known artificial objects larger that 10 cm whose number reached 12 456 in January 2008 (The Orbital Debris Quarterly News, January 2008). These objects are by the so-called US Space Surveillance Network (part of the USSTRATCOM, i.e. US Strategic Command) which is a major survey system consisting mostly of radars and optical telescopes. Figure 1.1 reports the time evolution of the trackable on-orbit population according to their sources. This latter classification clearly shows that the fragments resulting from break-ups contribute to about 40% of the total population. Approximately 30% of the cataloged objects are payloads (wherein only 7% are active satellites), about 17% are upper stages of the rockets used to place the satellite in orbit whereas the remaining part are mission related debris, i.e all objects dispensed, separated, or released as parts of the planned missions. Furthermore, let us also remark that the *Fengyun-1C* event, which occurred in January 2007, is clearly identifiable at the end of the time window. This event is by far surpassing the 713 objects created in the break-up of the Pegasus rocket body on June 1996 or similarly surpassing the *Solwind ASAT* test of September 1985. For an exhaustive enumeration of the most severe on-orbit fragmentation events, we refer to Klinkrad (2006).

The orbital space debris are not uniformly distributed in space but are concentrated in those regions that are heavily used by satellites. Practically, the near-Earth environment can be approximately split into three distinct regions, namely the low-Earth, the medium-Earth and the geostationary orbit regions.

The Low Earth Orbit region (LEO) can be defined as the region from the Earth's surface up to 2 000 km in altitude. In this region, the sensitivity threshold of the sensors limits the observations to the 5–10 centimeters in size objects. At the present time, we can almost pretend to know all the objects larger than about 20 cm. Radars have proved their efficiency in detecting small objects in LEO. This is why the observations in LEO are mainly performed by radars whereas the observations at higher altitudes are achieved by means of outperforming optical systems. The high-altitude orbits are located into the region spanning the area between 2 000 km and about 36 000 km. This widespread region is actually constituted by a large set of orbits having various characteristics. One of the most familiar high-altitude region is unquestionably the so-called geostationary region (GEO) located at 36 000 km altitude. An object placed in the GEO region will orbit around the Earth with an orbital period close to the rotational period of the Earth, remaining almost fixed with respect to the Earth's surface. As a consequence, this region is extensively used for the purpose of telecommunications as well as for weather forecasting satellites. Typically, the usual optical survey strategies allow to

[1] Let us remark that, in the special case of the Space Shuttle, the most part of the total mass is actually an active payload.

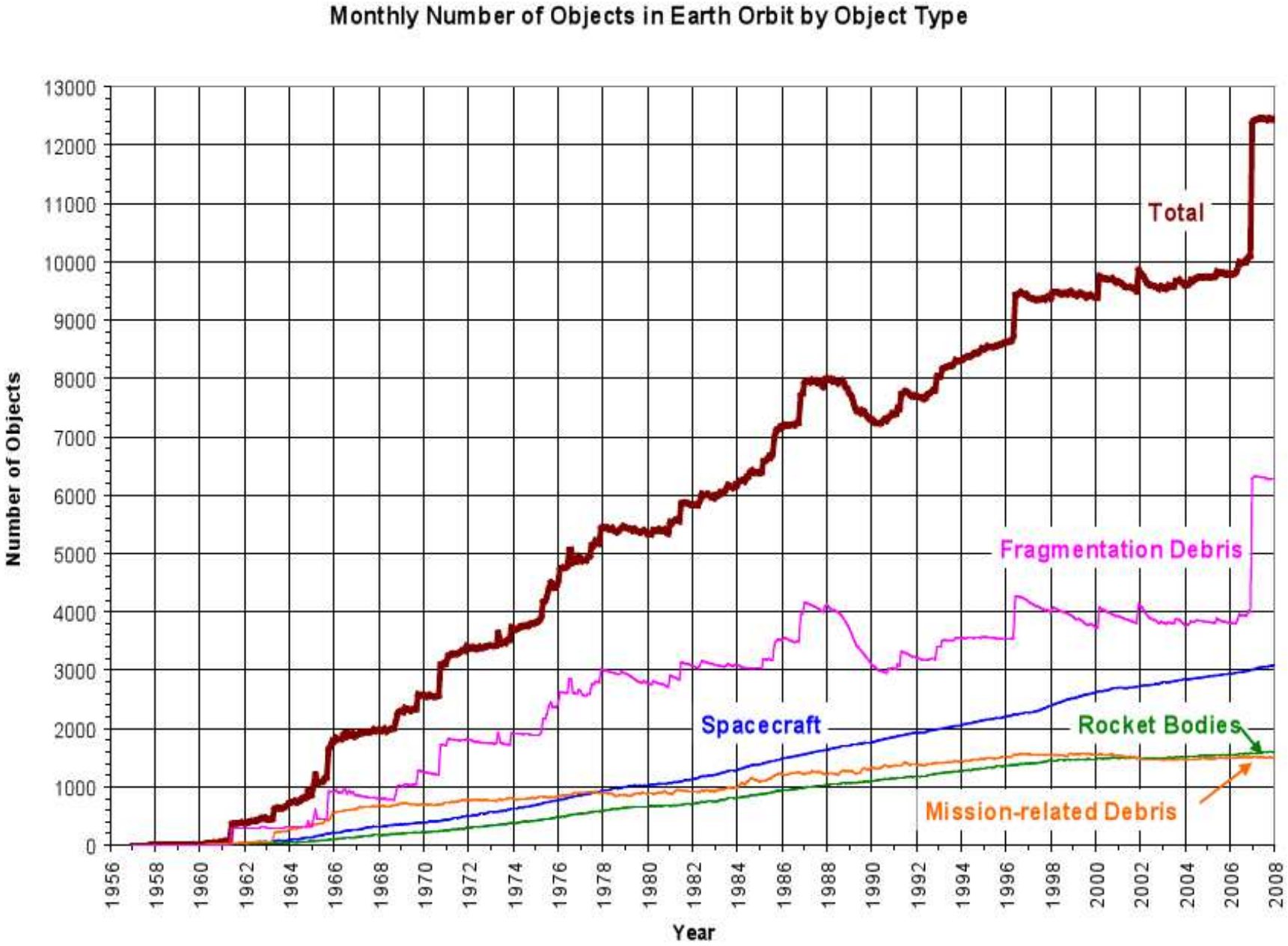

Figure 1.1: Number of cataloged objects in Earth orbit by object type: This chart displays a summary of all objects in Earth orbit officially cataloged by the U.S. Space Surveillance. "Fragmentation" includes satellite break-up debris and anomalous event debris, "mission-related" includes all objects dispensed, separated, or released as part of the planned mission. [*Orbital Debris Quarterly News, January 2008*]

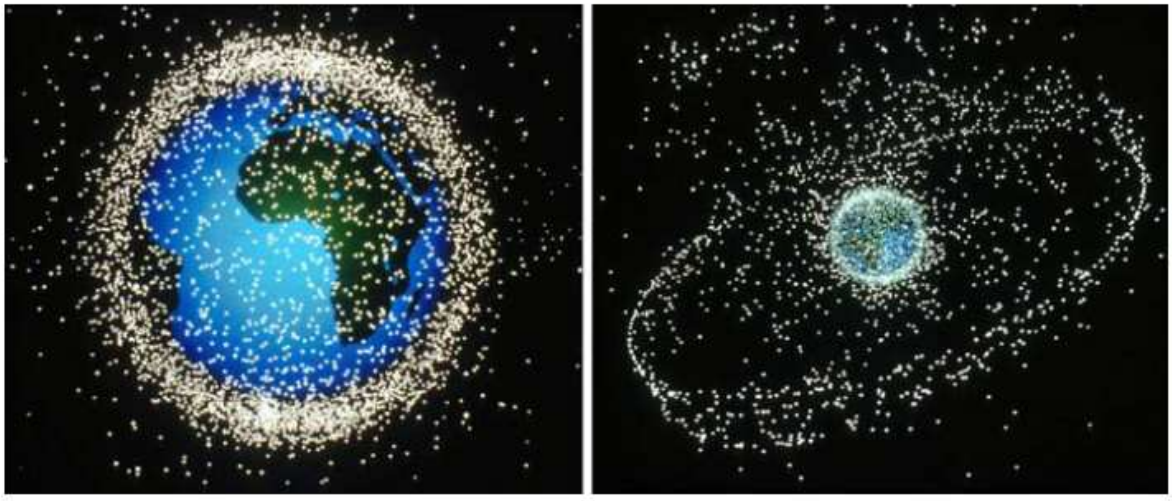

Figure 1.2: These graphics show the space debris population (cataloged objects). For the LEO region [left] and for high altitude orbits [right]. Approximately 95% of the objects in these illustrations are orbital debris, i.e. non-functional satellites. [Computer generated snapshot, source: ESA]

detect such objects whose size is on the order of 1 meter. One has also to mentioned that GEO satellites are set into the geostationary orbit by means of the Geostationary Transfer Orbits (GTO), which are characterized by highly eccentric orbits in such a way that the perigee is located at low altitudes and apogee precisely located at the GEO altitude. These Geostationary Transfer Orbits extend through the so-called Medium Earth Orbit (MEO) region which is the area where Global Navigation Satellites are placed. These constellations of satellites, such as *GPS*, *GLONASS* and more recently *GALILEO*, span the region between 20 000 and 22 000 km.

To clarify these points, Figure 1.2 shows the distribution of the cataloged objects from two vantage points. On the left, the figure reports the space debris population in LEO. On the right, the figure illustrates the spatial distribution as a global view as seen from a distance of 15 Earth's radii. In the latter figure, the geostationary orbit region is clearly identifiable. In addition, Figure 1.3 reports the spatial density of space debris as a function of their orbital regime. The results are given for three different categories of objects, namely the objects whose size is larger than 1 mm, 1 cm, and 10 cm. Actually, except for the objects larger than 10 cm, we only have limited statistical information, like the number and the size of pieces in particular orbit regions. This is the reason why the latter figure has been realized by means of a specific model which reconstructs the near-Earth environment by reproducing all the known sources and sink mechanisms. These elaborated mathematical and physical models, called MASTER models, are developed at the European Space Agency (ESA), or under ESA contracts. Even if this kind of models is surely all-important as part of space debris modeling, they exceed by far the objective of this overview. For further details, we refer to Klinkrad (2006) which gives an general overview of the most important space debris environment models. Figure 1.3 clearly brings to the fore the three main regions mentioned before. In particular, for the objects larger that 10 cm in size, this chart shows that almost 70% of the cataloged objects are actually in

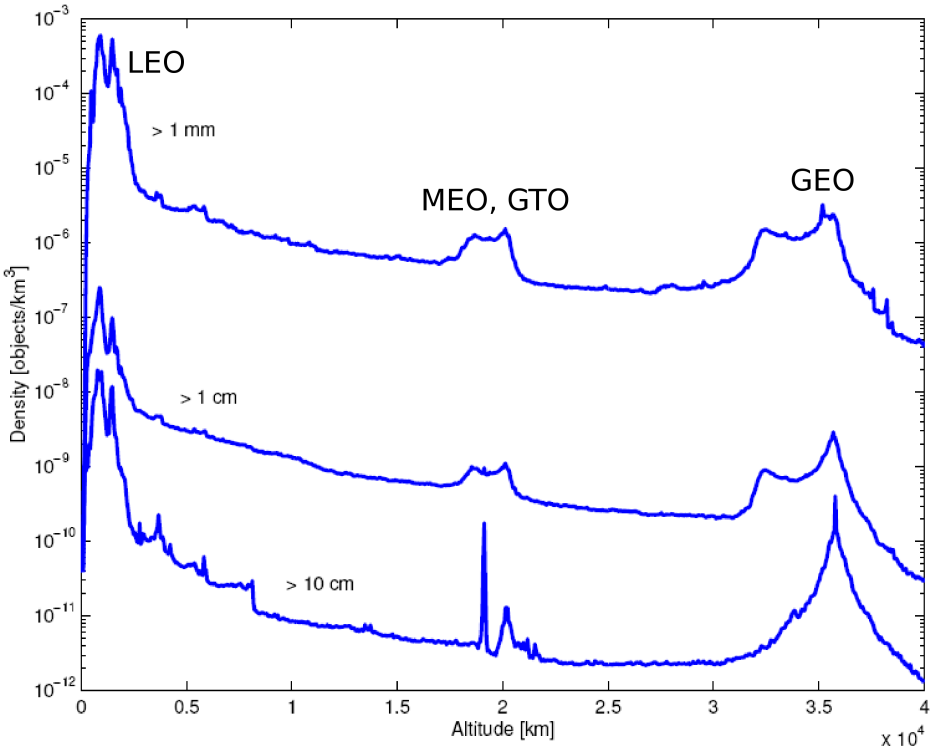

Figure 1.3: Density of the space debris population as a function of the altitude. The density is shown for three different characteristic values, i.e the objects whose size is larger than 1 mm, 1 cm, and 10 cm. This chart has been produced by using the MASTER 2001 population of objects. [Source: *Rossi (2005)*]

LEO, i.e at altitudes lower that 2000 km, 9% are in the vicinity of the GEO region, 8% are beyond the GEO region, 10% are on high elliptical orbits such as the Geostationary Transfer Orbits (GTO), and the small remaining part are in MEO.

It is worth noting that the space debris problematic is basically the same in these three regions. However, due the large discrepancies regarding the information available in these regions as well as the various dynamical properties of the objects with respect to their orbital regime, the space debris issue requires different as well as specific approaches and solutions. This is the reason why, from now on and within the context of this manuscript, we will restrict our investigations to the near-geostationary region.

1.3 The geostationary orbit region

Except to the fact that an object located on the GEO region remains almost fixed with respect to the Earth's surface, one of the most specific feature of geostationary orbits, is that in contrast to the LEO region, there are no natural energy-dissipating mechanisms, such as air-drag caused by the resistance of the Earth's atmosphere, to remove objects from that altitude (Klinkrad, 2006). As a matter of fact, for LEO orbits and in particular at small altitudes of 600–800 km,

most of the objects reenter into the atmosphere if no active propulsion system is operational. On the contrary, regarding the near-GEO region, the air-drag is so insignificant that the orbital lifetime of such orbits is usually considered as immeasurable. As a consequence, since the deployment of the first geostationary satellite Syncom-3 in August 1964, the GEO population is increasing slowly but surely at a regular rate of about 25–30 objects per year.

Actually, an ideal geostationary orbit would be defined as a perfectly circular orbit (null eccentricity) located in the equatorial plane (null inclination). The radius of such orbit would also have to be 42 164 km to ensure that the orbital period is exactly the same as the rotational period of the Earth (one sidereal day, 23 h 56 m 4 s). However, due to some external perturbations, a GEO satellite must regularly performs some additional corrections in order to change its orbital elements, or in other words, in order to stay within an assigned and confined region above the Earth's surface. For these reasons, the near-geostationary region is actually operationally limited. Indeed, when a satellite reaches its end of life, its assigned region is not anymore usable by other spacecrafts (Rossi, 2005). We ought also to mention that in recent years, since geostationary satellites are at some risk of colliding with uncontrolled objects, the space community has developed a new technique consisting of transferring spacecraft at the end of their operational life into a so-called "disposal orbit", also called "graveyard orbit", which is located at least 300 km above the nominal geostationary orbit, in order to protect this region from the natural evolution of objects without any operational control.

The latter natural evolution of non-functional objects is evidently governed by the main perturbing forces acting on these objects. For this purpose, let us first consider a large set of perturbing effects which are usually taken into account in the general context of artificial satellite theories.

Let us recall that the Earth is not a perfect sphere. Actually, in first approximation, the Earth has to be considered as an ellipsoid, that is an oblate spheroid with an equatorial diameter that exceeds the polar diameter by about 20 km. More generally, the geopotential perturbations are due to asymmetries in the Earth's gravitational field which can be expressed in terms of the so-called spherical harmonics expansion (for technical details, we refer to Subsection 2.2.1). The second degree harmonic (denoted by J_2), also called the oblateness coefficient, actually dominates all the other geopotential perturbations (excepted for the central term, GM) and exerts a force that tries to align the orbital plane with the equatorial plane. Aside for the geopotential perturbations, every artificial satellite is also subject to the third-body perturbations that arise from the gravitational attraction of both the Moon and the Sun. Similar forces as for the Moon and the Sun arise from the gravitational attraction of the planets of the Solar System. However, their amplitude is several orders of magnitude smaller than the luni-solar perturbations. In addition to the perturbations arising from gravitational influence, we have also to recall that artificial satellites are subject to further perturbing accelerations which depend on both the mass and the area of the objects. For low-Earth orbit objects, we have already mentioned the air-drag which tends to reduce the orbital kinetic energy or equivalently the altitude and, as

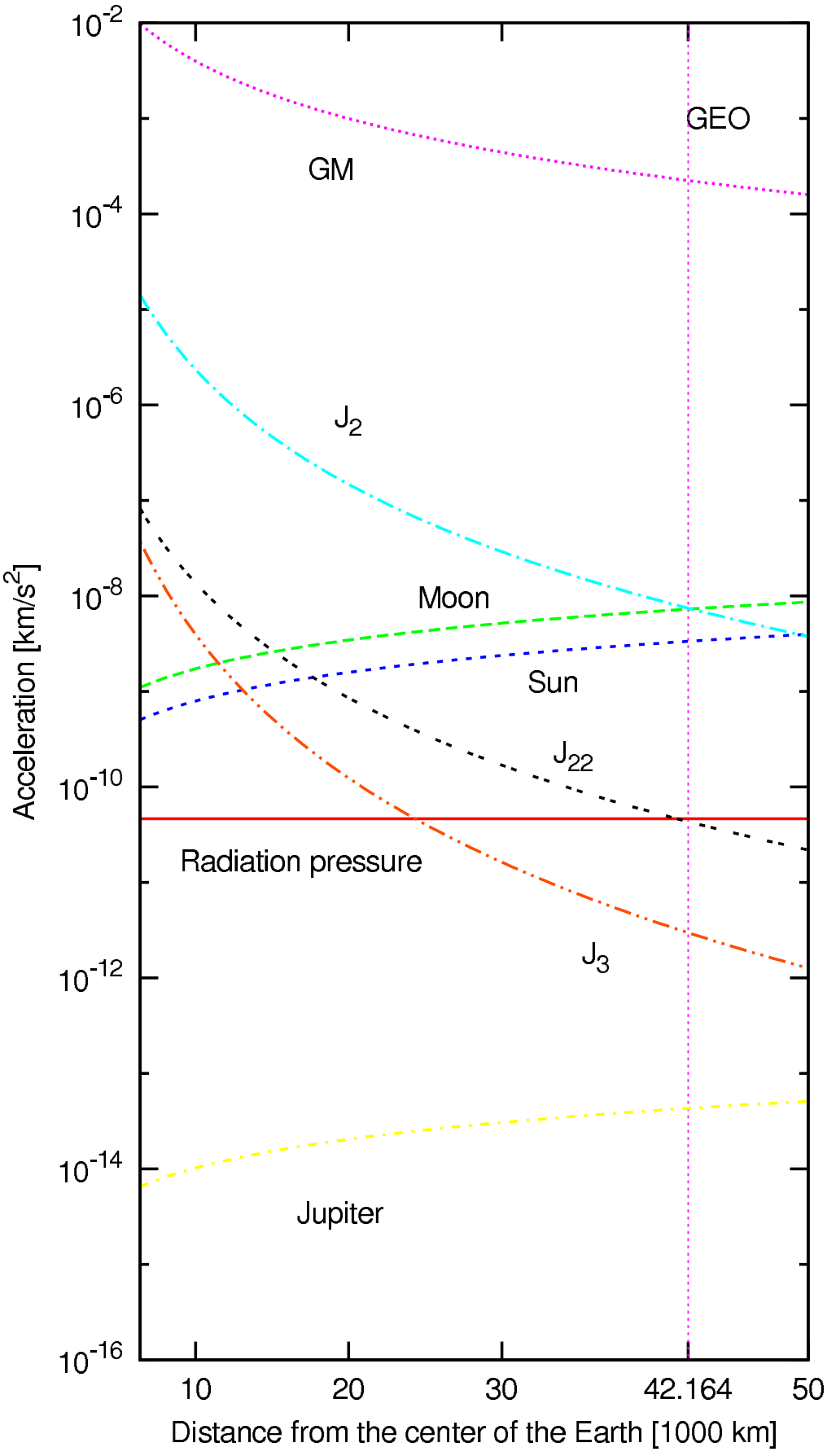

Figure 1.4: Order of magnitude of the main perturbations (gravitational influence and direct radiation pressure with typical area-to-mass ratio ($A/m = 0.01\ \mathrm{m}^2/\mathrm{kg}$) acting on Earth's orbiting objects as a function of the distance from the Earth's center.

a consequence, the orbital life time. Another well-known perturbing effect is the solar radiation pressure acceleration resulting from the interaction of the sunlight with the surface of the object. In contrast with the dissipative force arising from the air-drag, the radiation pressure mainly depends on the so-called area-to-mass ratio, denoted by A/m. We could also cite minor perturbations which produce extremely small variations of the orbital elements. These perturbing effects are for instance, the acceleration resulting from the solar radiation reflected by the Earth (albedo), both the terrestrial and ocean tides and the relativistic effects, to name only a few of them. Those effects will be disregarded in the context of this work.

Among the above-mentioned perturbations, the major effects experienced by an object located near the GEO region can be easily derived. This can be accomplished by using simplified expressions which give the relations between the order of magnitude of the perturbations as a function of the distance with respect to the Earth center. The results are given in Figure 1.4. This chart clearly indicates that the order of magnitude of the luni-solar perturbations actually increases almost linearly with the distance between the Earth and the space debris. Consequently, in the neighborhood of the geostationary region (enhanced by the vertical dashed line), the order of magnitude of these perturbations are comparable in size to that of the dominant Earth's oblateness. Figure 1.4 also reports that the remaining perturbing accelerations are at least two orders of magnitude lower.

The influence of the Earth's flattening combined with the gravitational attraction of both the Moon and the Sun actually force the orbital plane to precess with a typical period of roughly 54 years (where the precession angle is the longitude of the ascending node denoted

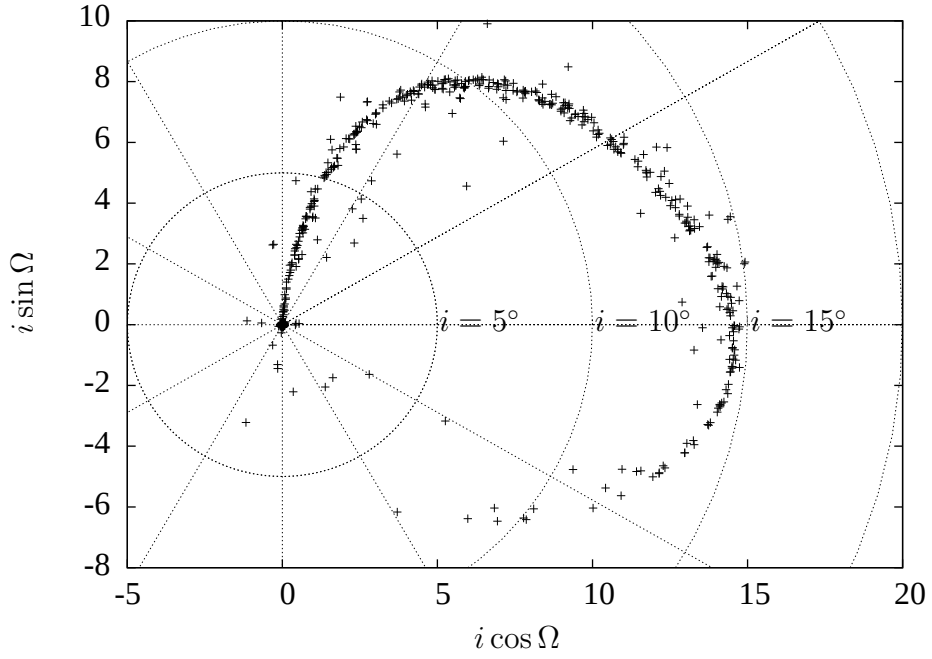

Figure 1.5: Projection of the orbital poles of all known geostationary space debris and artificial satellites moving in the gravitational field of the Earth (status: April 2008).

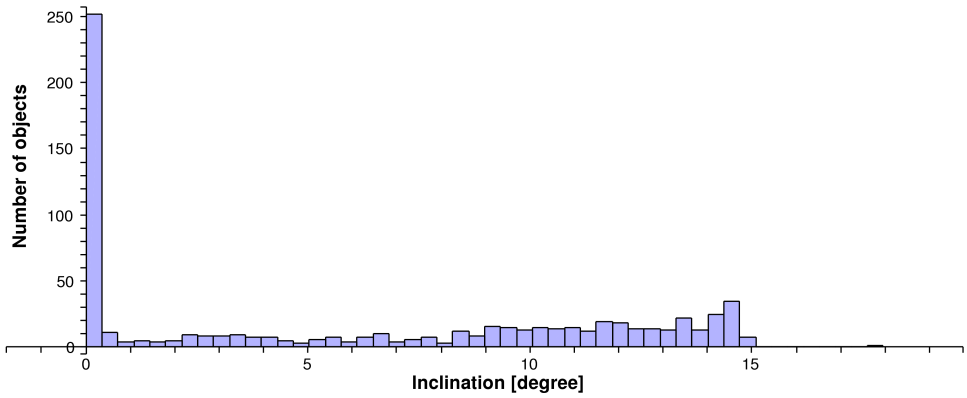

Figure 1.6: Histogram of the distribution of GEO Catalog's objects with the inclination of their orbit (class width: $\Delta\, i = 0.3°$, status: April 2008).

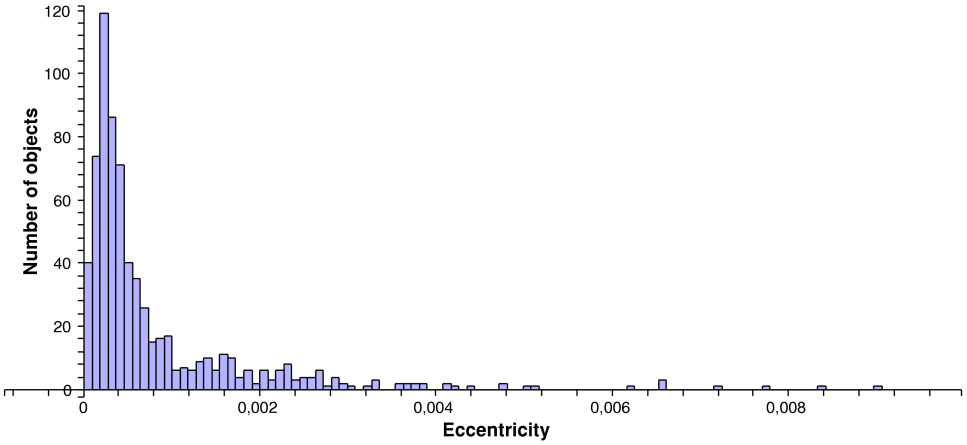

Figure 1.7: Histogram of the distribution of GEO Catalog's objects with the eccentricity of their orbit (class width: $\Delta\, e = 1 \times 10^{-4}$, status: April 2008)

by Ω). This precessional motion can actually be seen as the motion of a gyroscope around a fixed plane (Allen and Cook, 1964). This theoretical plane, called the Laplace plane, is inclined of about 7.5 degrees with respect to the equatorial plane leading to an orbital inclination which in turn oscillates with approximately 15 degrees of magnitude. In order to make this point clear, Figure 1.5 shows the so-called inclination vector, i.e, $(\sin i\, \cos\Omega, \sin i\, \sin\,\Omega) \simeq (i\, \cos\Omega, i\, \sin\Omega)$ of all GEO objects in the catalog. In order to give additional information, the GEO trackable objects can also be classified according to their orbital elements. In particular, it could be interesting to focus our attention to both the eccentricity and the inclination distribution. First, regarding the inclination distribution, Figure 1.6 reports a wide range of values ranging from 0 to approximately 15 degrees with a evident peak clearly identifiable close to the null inclination. This peak actually corresponds to the current active satellites which are repetitively kept inside their assigned slot in order to counteracting the perturbations that would tend to change the orbital elements such as the orbital inclination. On the contrary, the

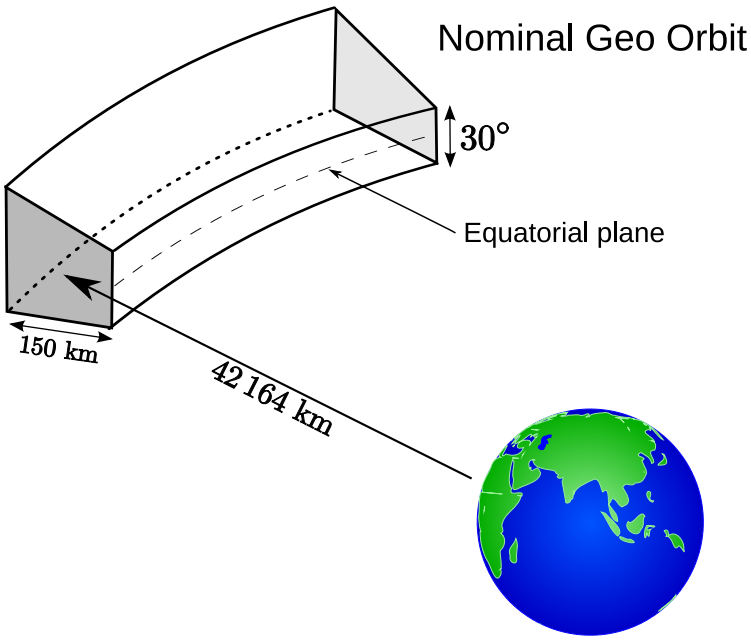

Figure 1.8: The geostationary ring (section) where are located the present cataloged space debris. The thickness in latitude is $\pm 15^{\circ}$ whereas the radial thickness is ± 75 km.

remaining objects consist of space debris. Second, in contrast to the inclination distribution, the eccentricity distribution shown in Figure 1.7, reports that the great majority of the objects of the catalog are clearly related to eccentricity values which correspond nearly to circular orbits. The small variations of the eccentricity can readily be explained by the combined interactions of both the third-body acceleration and the solar radiation pressure. Finally, it is worth stressing that although these eccentricity values are small, the corresponding variation of the geocentric distance, i.e. the maximum radial variation $2ae$, can be significant (typically on the order of 75 km on both sides of the nominal geostationary orbit for $e = 0.0017$). For all these reasons, the geostationary ring is thus theoretically defined as the segment of a spherical shell with a radial thickness of 150 km and delimited by ± 15 degrees in latitude (see Figure 1.8).

We can not conclude this section without also mentioning that a near-geostationary object is also significantly subject to the longitude-dependent spherical harmonics associated with the Earth's gravity field. The main longitude-dependent term of the geopotential expansion is actually related to the J_{22} acceleration appearing in Figure 1.4. Indeed, if a space debris revolution period is commensurate with the sidereal revolution period of the Earth, the higher-order terms of the Earth's potential may produce the so-called resonant perturbations, the amplitudes of which may become orders of magnitude larger than ordinary high-order perturbations. Resonant perturbations are also typically of very long periods. Therefore, the resonant perturbations will turn out to be inescapable in the specific case of near-geostationary orbits. However, a complete description of these resonant effects are beyond the scope of this overview. This is the reason why it will be discussed in more detail in Chapter 2.

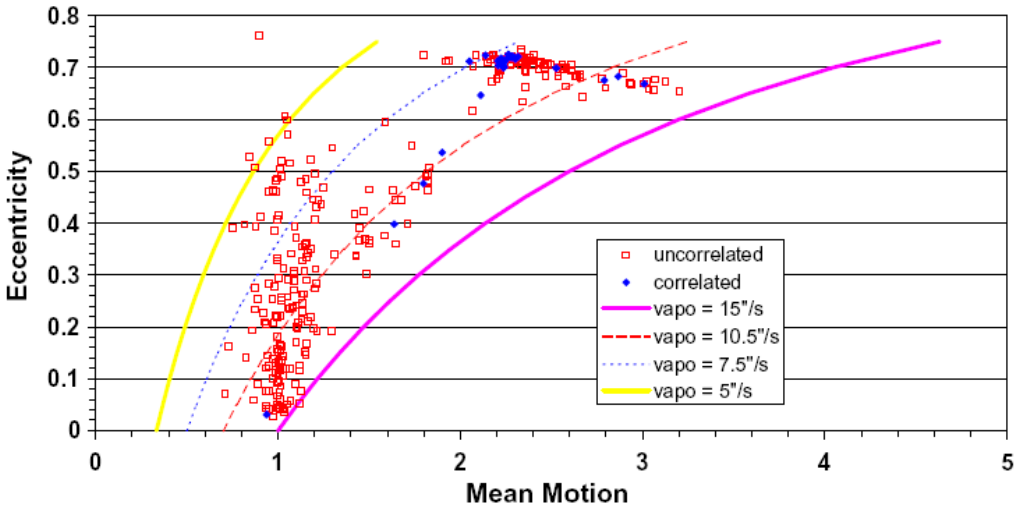

Figure 1.9: Eccentricity as a function of the mean motion for 332 objects with elliptical orbits. [*Graphics by Schildknecht et al. (2007)*].

1.4 Discovery of the high area-to-mass ratio population

The near-Earth environment and in particular the LEO region has already been intensively studied during the last dozens of years. On the contrary, and as already mentioned in the previous section, the lower size threshold of objects which can be observed in the geostationary regime is on the order of 1 meter. As a consequence, the available information in GEO is still very sparse in comparison with the LEO regime. However, since the significance of this region is indisputably all-important for both commercial and scientific missions, ESA has recently initiated an optical search for fragments in the geostationary ring in order to improve the knowledge about the debris population in GEO and to understand the future evolution of its population (Schildknecht et al., 2005). These observations have actually been performed, on behalf of ESA, by the Astronomical Institute of the University of Bern (AIUB) by using the European 1 meter telescope located in Tenerife (Canary Islands).

Even more recently, some new optical surveys have been coordinated in order to detect space debris orbiting on highly elliptical orbits. In particular, for a subset of the detections, the space debris have been followed in real-time in order to deduce a complete set of six orbital elements whereas only circular orbits were determined for the remaining objects. Although these latter survey campaigns were first optimized to find space debris in the Geostationary Transfer Orbits (GTO), in particular to search out the small-sized debris population which originates from well-know break-ups of Ariane upper stages, the results of these surveys revealed not only a substantial amount of space debris at high-altitudes in the size range from 0.1 to 1 meter, but also a new unexpected population for which no potential parent object could be identified. The mean motion of this new space debris population actually turns out to be on the order of one revolution per day whereas the eccentricities scattered between 0 and 0.6.

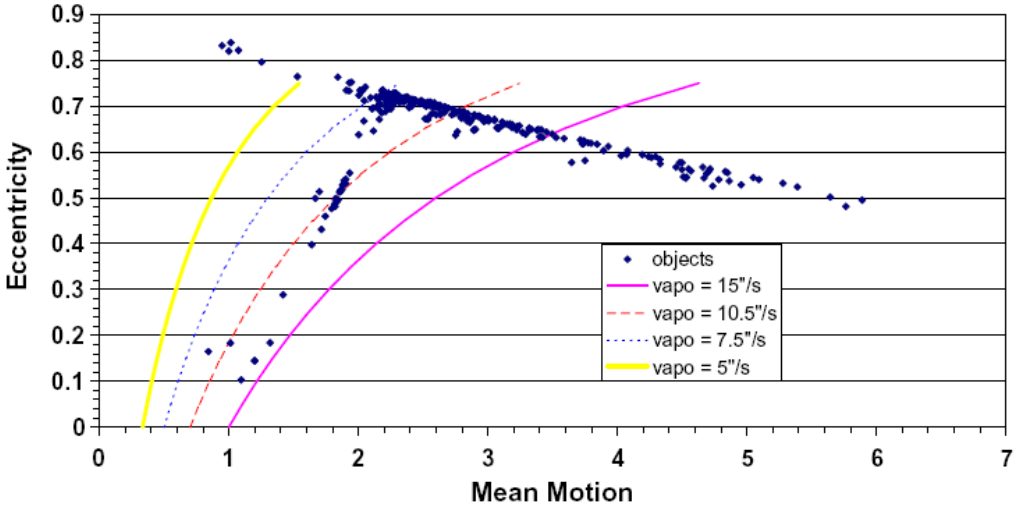

Figure 1.10: Eccentricity as a function of the mean motion for the objects in the catalog. [*Graphics by Schildknecht et al. (2007)*].

To clarify this point, Figure 1.9 shows the eccentricity e as a function of the mean motion n, in revolution per day, for a data set of 332 objects from the ESA surveys for which elliptical orbits were determined. In Figure 1.10, we show the corresponding cataloged objects in which the data were filtered with respect to the eccentricity ($0.1 < e < 0.9$), to the inclination ($0 < i < 20°$) and to the mean motion ($0.3 < n < 6$). In this figure, the curved lines correspond to the locations of constant apparent motion in right ascension when the objects are at the apogee. In particular, the solid curved lines indicate the boundaries of region where the survey was able to detect objects. Consequently, the objects moving slower than $5''$/s or equivalently faster that $15''$/s have not been detected. The before-mentioned new population of objects is clearly visible in Figure 1.9. These objects are actually shown as uncorrelated objects which are particularly concentrated about the mean motion of near-geosynchronous objects. In comparison with Figure 1.10, these discovered objects do not correspond to any data in the catalog.

These objects are probably the result of undetermined surface degradation or low intensity phenomena that occurred near the geostationary ring. Initially, Liou and Weaver (2004) suggested that some of the resulting fragments are actually characterized by high area-to-mass ratios compared to those of typical spacecrafts and upper stages which range from about 0.01 to 0.02 m^2/kg. As a consequence, they proposed a simple explanation to the astonishing discovery of high eccentricity objects: the solar radiation might induce such a particular dynamics on space debris with such high area-to-mass ratio. Indeed, a satellite or a space debris exposed to solar radiation pressure undergoes a force that arises from the absorption or reflection of photons. In contrast to gravitational perturbations, the acceleration due to solar radiation pressure depends linearly on the area-to-mass ratio. Under such assumptions, space debris may reached significant large eccentricities.

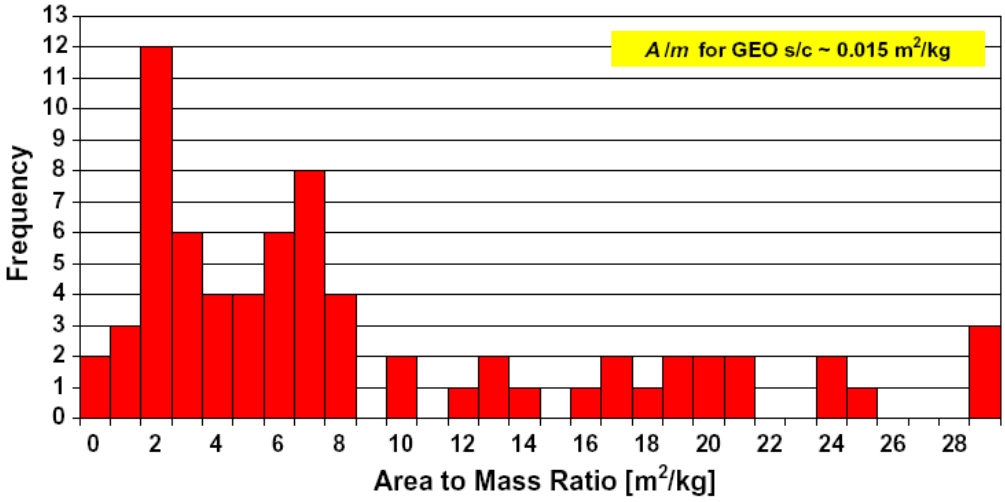

Object	A/m [m^2/kg]
Lageos 1 and 2	0.0007
Starlette	0.001
GPS (Block II)	0.02
Moon	1.3×10^{-10}
Space debris	$0 < A/m < \sim 30$

Figure 1.11: Distribution of the area-to-mass ratios of 73 objects from the recent ESA optical survey in near GEO [*Graphics and caption by Schildknecht et al. (2007)*] [top]. Order of magnitude of the area-to-mass ratios A/m for various Earth-orbiting objects [bottom].

Indeed, by following in real-time some of these uncommon space debris and in order to give additional measurements and mostly improve the restitution process, it was possible to derive the area-to-mass ratios by estimating this parameter in the orbit determination process. For instance, for a subset of the survey data, the corresponding distribution for 73 objects is given in Figure 1.11 (top). The results clearly report that the area-to-mass ratios related to the uncorrelated objects always reach significant values which are several orders of magnitude greater than typical Earth-orbiting objects. For the sake of comparison, we show in Figure 1.11 (bottom) the area-to-mass ratios of several well-known satellites. Indeed, the first three satellites (*Lageos 1 & 2*, *Starlette*) were intentionally designed as geodetic satellites, i.e small spherical satellites which explains the small area-to-mass ratios. On the contrary, the *GPS* satellites, such as most of the Navigation satellites and GEO satellites have a rather "large" area-to-mass ratio since they are typically equipped with wide solar panels of a few square meters. Consequently, these new unexpected objects must be effectively lightweight since a standard sheet of paper has an area-to-mass ratio of about 13 m^2/kg.

Chapter 2

Semi-analytical theory of mean orbital motion for geosynchronous space debris under gravitational influence

> *"For two hundred years, satellites of all shapes and sizes, from loose nuts and bolts to entire space villages, had been accumulating in Earth orbit. All that came below the extreme elevation of the Tower, at any time, now had to be accounted for, since they created a possible hazard..."*
>
> Arthur C. Clarke, *The Fountains of Paradise*, 1978

– The results of this chapter have been previously submitted in Valk et al. (2007a) –

Within the context of space debris modeling, it is convenient to distinguish two approaches, namely the study of the evolution of space debris over short and long timescales. The short-time analyses consist in propagating orbits over a period of days up to several weeks. Within this context, the numerical integration of the osculating equations of motion is especially suited as long as some valuable initial conditions are available. However, as soon as we are interested in the study of the motion over longer timescales, typically one year up to several dozens of years, the numerical integration remains technically conceivable but becomes practically inappropriate regarding the CPU time consumption.

In this chapter, we develop a semi-analytical theory of the mean orbital motion based on the concept of mean orbital elements. The characteristic of the method is based on an analytical averaging of the initial differential system followed by a numerical integration of the transformed equations. The main motivation of this investigation is the development of an accurate and extensive theory well-suited for the study of near-geosynchronous space debris over very long periods of time. The method allows the inclusion of both zonal and tesseral harmonics as well as the third-body attractions induced by the Sun and the Moon and provides

long-term solutions that are valid for a wide range of eccentricities and inclinations.

The main objective of this chapter is basically twofold. On the one hand, we first derive the major disturbing function acting on near-geosynchronous space debris. These perturbations are then transformed by using modified orbital elements which in turn are suited for the two singularities appearing in the problem of near-geosynchronous space debris. On the other hand, we apply the theory by means of the above-mentioned analytical averaging process. Therefore, the numerical integrations of the averaged systems of equations show that this theory is especially well-suited for the long-term investigation and combine the ideal properties of numerical integrations and analytical theories to obtain the best compromises between accuracy and efficiency.

Section 2.2 is intended to derive the disturbing functions related to the major perturbations, that is the gravitational perturbations induced both by the Earth's gravity field and by the combined attraction of the Sun and the Moon. Subsequently, we introduce the first analytical development of these disturbing functions expressed in Keplerian elements by means of a series expansion in powers of the eccentricity and of the inclination.

Section 2.3 is devoted to the singularities appearing in the numerical integrations of the dynamical equations expressed in such classical Keplerian elements. As an alternative, we propose a general solution based on a set of "near-canonical" and entirely non-singular variables (universal elements). This set of variables leads to the choice of a Hamiltonian formalism and extends the period of validity of the solution while preserving a high stability of the numerical integrations over very long time spans.

In Section 2.4 we explicitly present the analytical averaging process over the short periods and we take the opportunity to present our home-made symbolic manipulator software used for the analytical processing of the various series expansions.

In order to give a first validation of our semi-analytical theory, we give in Section 2.5 some comparisons between numerical integrations and semi-analytical propagations. The method is applied considering both the second degree zonal harmonic J_2 and the combined third-body attraction of the Sun and the Moon. We also take advantage of these various propagations to underline the main characteristics of high-altitude objects (not being subject to resonance).

Finally, we devote the end of this chapter to the investigation of the resonant effects induced by the 1:1 resonance occurring for near-geosynchronous space debris. First, we briefly depict the concept of resonance by stressing the main terms appearing in the geopotential expansion. Second, we describe how to adapt the Hamiltonian formalism to ensure that the resonant long-periodic effects are preserved throughout the averaging process. Moreover, we give a simplified analytical model to underline the main effects of the above-mentioned resonance (equilibrium points, stability, fundamental frequencies, width of the resonance area). At

last, we give some semi-analytical propagations to show how the method is in good agreement with both our simplified analytical model and the theory of geostationary satellite.

2.1 The perturbed equations of motion

The general form of equations of motion with perturbations can be expressed in Cartesian coordinates as follows

$$\ddot{\boldsymbol{r}} = \boldsymbol{a}_{pot} + \boldsymbol{a}_{☾} + \boldsymbol{a}_{\odot} + \boldsymbol{a}_{rp} + \boldsymbol{a}_{neglected}\,, \tag{2.1}$$

where $\boldsymbol{a}_{pot}$ is the acceleration resulting from Earth gravity harmonics that includes the central attraction (two-body acceleration). The perturbing accelerations, $\boldsymbol{a}_{☾}$ and $\boldsymbol{a}_{\odot}$ are the results of the third-body attraction induced by the Moon and the Sun, respectively. The component $\boldsymbol{a}_{rp}$ is related to the acceleration induced by the solar radiation pressure. Concerning the last term in Eq. (2.1), it is related to the forces which are neglected in the context of this work. This component contains the accelerations caused by small forces (essentially non-gravitational) such those related to thermal or relativistic effects (Yarkovsky-O'Keefe-Radzievskii-Paddack, Schwarzschild correction, ...); the atmospheric drag, highly insignificant in the case of high-altitude orbits; the solid and ocean tides of the Earth as well as the third-body accelerations related to the other planets of the Solar System, such as Jupiter.

Let us remark that in order to benefit of the large set of first-order integration methods, the second-order differential equation (2.1) is usually reformulated as a set of two first order differential equations. This new system is then written as

$$\begin{aligned} \dot{\boldsymbol{r}} &= \boldsymbol{v} \\ \dot{\boldsymbol{v}} &= \boldsymbol{a}_{pot} + \boldsymbol{a}_{☾} + \boldsymbol{a}_{\odot} + \boldsymbol{a}_{rp} + \boldsymbol{a}_{neglected}\,, \end{aligned} \tag{2.2}$$

where $\boldsymbol{v}(t)$ is the velocity vector of the propagated object at time t. However, it is also worth noting that all the forces taken into account are actually conservative (even though a special attention has to be given for the solar radiation pressure, see Chapter 3). As a consequence, the total energy of the system will be constant, whereas dissipative systems may lose or gain energy. This remark is relevant insofar as the accelerations will be further related to the gradient of a potential disturbing function.

As shown in Eq. (2.2), the orbital state vector is implicitly expressed in terms of six Cartesian coordinates (x, y, z) of the position $\boldsymbol{r}$ and $(\dot{x}, \dot{y}, \dot{z})$ of the velocity $\dot{\boldsymbol{r}}$. However, it is well known that this natural set of coordinates is not well-suited for the development of both analytical and semi-analytical theories due to their fast variations with high amplitudes.

There are several alternative sets of orbital parameters into which the Cartesian state can be converted. One such set are the six Kepler's orbital elements (hereafter ***Keplerian elements***): a

(*semi-major axis*), e (*eccentricity*), i (*inclination*), Ω (*right ascension of the ascending node*), ω (*argument of perigee*) and M (*mean anomaly*), which are well-suited to describe a conical section. Actually, expressing the orbit elements in terms of Keplerian elements has a great asset. Indeed, while position and velocity vectors undergo larger changes with time, most of the Keplerian elements undergo small variations in perturbed motion. In particular, in the case of an unperturbed motion, only the mean anomaly M changes with time at a constant rate called the mean motion.

The Keplerian elements will be systematically used in order to depict the dynamics, since they are particularly well adapted to interpret the motion. Furthermore, the Keplerian elements are also the founding grounds of the so-called expansions in powers of the eccentricity and of the inclination developed in Section 2.2. Indeed, the main objective of the following sections is to derive the expressions of the disturbing functions related to the major perturbations, i.e. the gravitational perturbations induced by both the Earth's gravity field and the combined attraction of the Sun and the Moon.

2.2 Disturbing functions – expansion in powers of the eccentricity and of the inclination

2.2.1 Potential of the Earth

According to the Newton universal law of gravitation, the force of attraction between two particles of masses m_1 and m_2 at a distance r from each other will be

$$\boldsymbol{F} = -\,G\,\frac{m_1\,m_2}{r^2}\,\boldsymbol{r}\,,$$

where G is the universal constant of gravitation. Assuming the Earth to be spherical and homogeneous and considering its mass is concentrated at its center, the force $\boldsymbol{F}$ can be obtained by expressing the acceleration as the gradient of a scalar function, called potential U. This potential per unit of mass is written as

$$U = -\frac{\mu}{r}\,,$$

where $\mu = G\,m_\oplus$ is the so-called gravitational constant of the Earth.

However, the Earth is neither spherical nor homogeneous. Therefore, the previous assumptions are no longer verified. However, the expression of the potential function may easily be generalized to an arbitrary mass distribution by summing up the contributions created by individual mass elements. In particular, we have

$$U(\boldsymbol{r}) = \mu \int_V \frac{\rho(\boldsymbol{r_p})}{\|\boldsymbol{r} - \boldsymbol{r_p}\|}\,dV\,, \tag{2.3}$$

where $\rho(\boldsymbol{r_p})$ stands for the density at some point $\boldsymbol{r_p}$ inside the Earth, and $\|\boldsymbol{r} - \boldsymbol{r_p}\|$ is the distance between the object and a particular volume element located at the geocentric position $\boldsymbol{r_p}$.

First, let us note that the typical denominator appearing in Eq. (2.3) may be developed into a rapidly convergent series

$$\frac{1}{\|\boldsymbol{r} - \boldsymbol{r_p}\|} = \frac{1}{r}\sum_{n=0}^{\infty}\left(\frac{r_p}{r}\right)^n \mathcal{P}_n\left(\frac{\langle \boldsymbol{r} \cdot \boldsymbol{r_p}\rangle}{r\, r_p}\right) = \frac{1}{r}\sum_{n=0}^{\infty}\left(\frac{r_p}{r}\right)^n \mathcal{P}_n\left(\cos\,\psi\right)\,, \tag{2.4}$$

where r_p/r is the argument of the series expansion, ψ the geocentric angle between $\boldsymbol{r}$ and $\boldsymbol{r_p}$, and $\mathcal{P}_n$ are the so-called *Legendre polynomials* of degree n.

Second, by introducing the spherical coordinates in the Earth-fixed reference frame, i.e. the geocentric longitude λ (counted positively towards the Earth) and the geocentric latitude ϕ of the geocentric position $\boldsymbol{r}$

$$\begin{aligned} x &= r\,\cos\phi\,\cos\lambda \\ y &= r\,\cos\phi\,\sin\lambda \\ z &= r\,\sin\phi\,, \end{aligned}$$

as well as the corresponding quantities λ_p and ϕ_p for the volume element at $\boldsymbol{r_p}$, and by using the decomposition formula, the Legendre polynomials can be expanded into spherical harmonics

$$\mathcal{P}_n(\cos\,\psi) = \sum_{m=0}^{n}(2-\delta_{0m})\,\frac{(n-m)!}{(n+m)!}\,\mathcal{P}_n^m(\sin\phi_p)\,\cos(m(\lambda-\lambda_p))\,,$$

where δ_{ij} is the Kronecker function, $\delta_{ij} = 1$ for $i = j$ and zero otherwise. $\mathcal{P}_n^m$ are the so-called *associated Legendre functions*, which may be defined as

$$\begin{aligned} \mathcal{P}_n(x) &= \mathcal{P}_n(x) = \frac{1}{2^n\,n!}\,\frac{\mathrm{d}^n}{\mathrm{d}x^n}\Big\{(x^2-1)^n\Big\} \\ \mathcal{P}_n^m(x) &= (1-x^2)^{m/2}\,\frac{\mathrm{d}^m}{\mathrm{d}x^m}\Big\{\mathcal{P}_n(x)\Big\}\,. \end{aligned}$$

We finally write the Earth's gravity potential in the form

$$U(r,\lambda,\phi) = -\frac{\mu}{r}\sum_{n=0}^{\infty}\sum_{m=0}^{n}\left(\frac{R_e}{r}\right)^n \mathcal{P}_n^m(\sin\phi)(C_{nm}\cos\,m\lambda + S_{nm}\sin\,m\lambda)\,, \tag{2.5}$$

where R_e is the equatorial Earth's radius and where the quantities C_{nm} and S_{nm} are the spherical harmonics coefficients which are given by

$$\begin{aligned} C_{nm} &= \frac{2-\delta_{0m}}{M_\oplus}\,\frac{(n-m)!}{(n+m)!}\int_V\left(\frac{r_p}{R_e}\right)^n \mathcal{P}_n^m(\sin\phi_p)\cos\left(m\lambda_p\right)\rho(\boldsymbol{r_p})\,dV \\ S_{nm} &= \frac{2-\delta_{0m}}{M_\oplus}\,\frac{(n-m)!}{(n+m)!}\int_V\left(\frac{r_p}{R_e}\right)^n \mathcal{P}_n^m(\sin\phi_p)\sin\left(m\lambda_p\right)\rho(\boldsymbol{r_p})\,dV\,. \end{aligned} \tag{2.6}$$

Let us remark that even though the expressions (2.6) of the geopotential coefficients seem to be fairly complicated, some first degree and order coefficients may be computed readily. First, it is shown that the coefficient C_{00} is equal to 1. As a consequence, the first term in the expansion is nothing else than the two-body potential $-\mu/r$. Moreover, it is worth noting that all terms S_{n0} are zero, since $\sin(m\lambda_p)$ in the integrand (2.6) is equal to zero for $m = 0$. It can also be shown easily that the coefficients C_{10}, C_{11} and S_{11} correspond to the center of mass coordinates divided by the equatorial Earth's radius. Therefore, these coefficients are zero if the coordinate system refers to the Earth's center of mass. Similarly, the coefficients C_{21} and S_{21}, are zero as long as the z-axis is aligned with the Earth's main axis of inertia. Finally, it can be shown that

$$J_2 = -C_{20} = \frac{2C - B - A}{2\, M_\oplus\, R_e^2} \qquad \text{and} \quad C_{22} = \frac{B - A}{4\, M_\oplus\, R_e^2}\,,$$

where A, B and C (with $A < B < C$) are the principal moments of inertia of the Earth and $M_\oplus$ is the Earth's mass.

Similarly, the potential may be expressed using an alternative way, with a single cosine term, a phase difference λ_{nm} as well as a new J_{nm} coefficient

$$U(r,\lambda,\phi) = -\frac{\mu}{r} + \frac{\mu}{r}\sum_{n=2}^{\infty}\sum_{m=0}^{n}\left(\frac{R_e}{r}\right)^n \mathcal{P}_n^m(\sin\phi)\, J_{nm}\, \cos m(\lambda - \lambda_{nm})\,, \tag{2.7}$$

using the definitions for $n \geq m \geq 0$

$$\begin{aligned} C_{nm} &= -J_{nm}\, \cos(m\lambda_{nm}) \\ S_{nm} &= -J_{nm}\, \sin(m\lambda_{nm}) \\ J_{nm} &= \sqrt{C_{nm}^2 + S_{nm}^2} \\ m\,\lambda_{nm} &= \arctan\left(\frac{-S_{nm}}{-C_{nm}}\right)\,. \end{aligned}$$

The use of the Earth's equatorial radius R_e and the isolation of the factor μ/r in Eqs. (2.5) and (2.7) have the advantage that the coefficients C_{nm} and S_{nm} (similarly J_{nm}) are non-dimensional. The index n is called the *degree* and m the *order* of the spherical harmonics expansion. Coefficients with $m = 0$, which are only latitude-dependent, are denoted as *zonal harmonics*. If $n \neq m$, the C_{nm} and S_{nm} coefficients are referred to as *tesseral harmonics* and if $n = m$, they are referred to as *sectorial harmonics*. They describe the purely longitude-dependent part of the geopotential. Figure 2.1 illustrates the first order and degree harmonics of the geopotential (2.7).

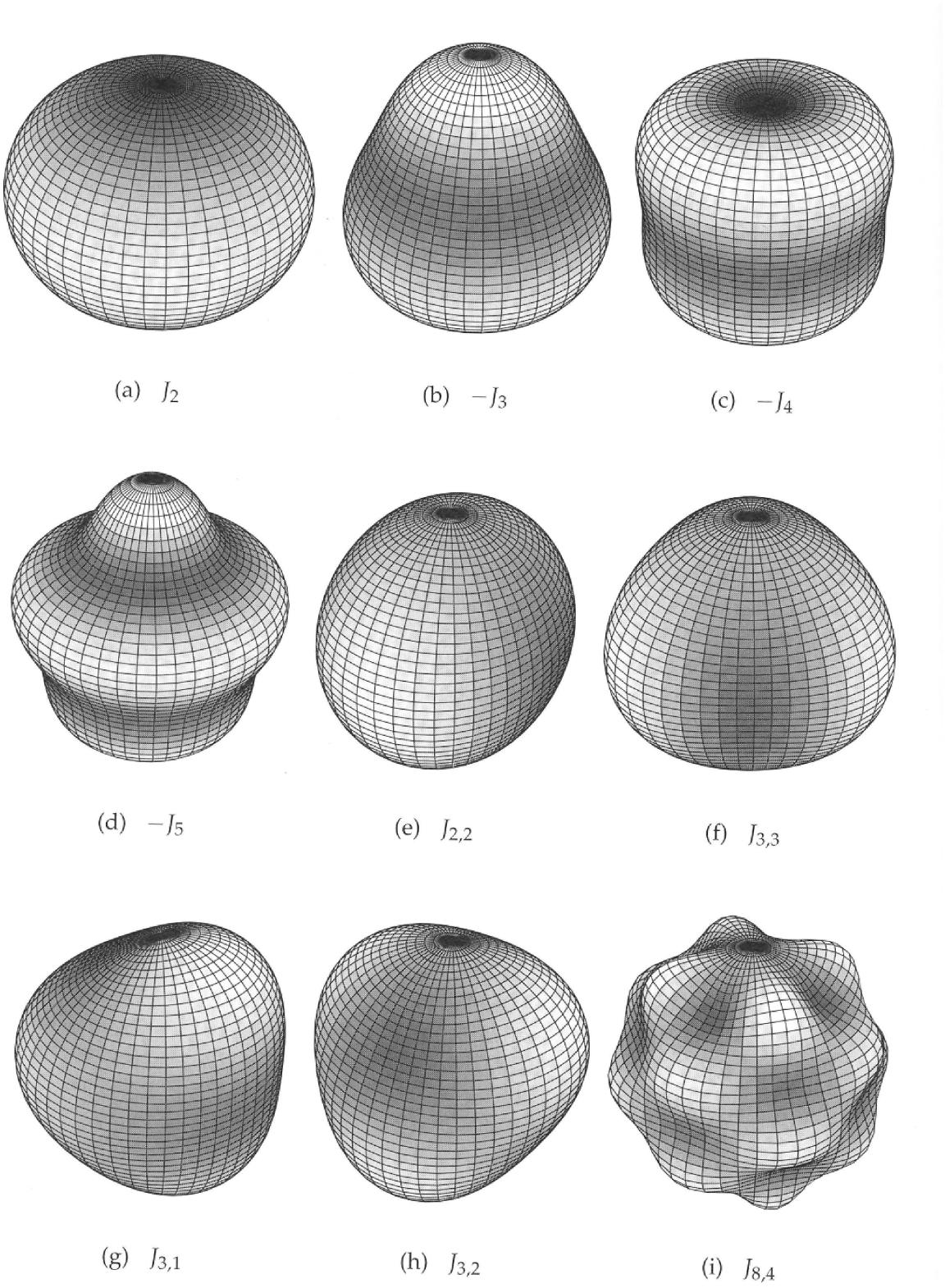

Figure 2.1: Illustration of the spherical harmonics J_{nm} of the geopotential for low degrees n and order $m \leq n$. Bright regions indicate mass accumulations, while dark regions indicate mass deficiencies. [*Graphic and caption by Klinkrad (2006)*].

2.2.2 Gravity field in terms of the satellite orbital elements

In Section 2.2.1, the potential has been developed into spherical coordinates (r, λ, ϕ). Even though these formulations are rather important, it is also sometimes useful to represent the potential in terms of the classical Keplerian elements $(a, e, i, \Omega, \omega, M)$. This last formulation may be more convenient when using the Lagrangian as well as the Gaussian equations developed in Appendix E (page 173). Moreover, the expansion into Keplerian elements is also relevant when developing a simplified analytical model. Besides, the partial derivatives of this form can be used to evaluate numerical, analytical, and semi-analytical methods.

Several authors discussed such an expansion, in particular, Kaula (1966) which is usually associated to this technique. As a final result, Kaula (1966) represents the Earth's gravitational field as

$$U = -\frac{\mu}{r} - \sum_{n=2}^{\infty} \sum_{m=0}^{n} \sum_{p=0}^{n} \sum_{q=-\infty}^{+\infty} \frac{\mu}{a} \left(\frac{R_e}{a}\right)^n F_{nmp}(i)\, G_{npq}(e)\, S_{nmpq}(\Omega, \omega, M, \theta)\,, \tag{2.8}$$

where the functions S_{nmpq} depend on the geopotential coefficients C_{nm} and S_{nm}

$$\begin{aligned} S_{nmpq}(\Omega, \omega, M, \theta) &= \left[\begin{array}{c} +C_{nm} \\ -S_{nm} \end{array}\right]_{n-m\,\text{odd}}^{n-m\,\text{even}} \cos\,\Theta_{nmpq}(\Omega, \omega, M, \theta) \\ &+ \left[\begin{array}{c} +S_{nm} \\ +C_{nm} \end{array}\right]_{n-m\,\text{odd}}^{n-m\,\text{even}} \sin\,\Theta_{nmpq}(\Omega, \omega, M, \theta)\,, \end{aligned}$$

defined with respect to the ***Kaula gravitational argument***

$$\Theta_{nmpq}(\Omega, \omega, M, \theta) = (n - 2p)\,\omega + (n - 2p + q)\,M + m(\Omega - \theta)\,.$$

where θ is the sidereal time. The subscript indexes represented by n, m, p, q are integers that identify the terms in the so-called *inclination functions* $F_{nmp}(i)$ and *eccentricity functions* $G_{npq}(e)$ for a particular harmonic (n, m).

For the sake of clarity, both the eccentricity functions and the inclination functions are presented in Eqs. (C.1) and (C.2) of Appendix C, page 165.

2.2.3 Luni-solar perturbations

As mentioned before (Figure 1.4), third bodies, such as the Sun and the Moon, have greater influence on space debris in higher altitude orbits. According to the Newton's law of gravity, the acceleration of an object by a point mass m_i is given by

$$\ddot{\boldsymbol{r}} = -\mu_i \frac{\boldsymbol{r} - \boldsymbol{r_i}}{\|\boldsymbol{r} - \boldsymbol{r_i}\|^3}\,, \tag{2.9}$$

where $\boldsymbol{r}$ and $\boldsymbol{r_i}$ are the geocentric coordinates of the space debris and of the mass m_i, respectively. The quantity $\mu_i = G\,m_i$ is the gravitational constant of the third body. However, Eq. (2.9) can not be used directly for describing the motion of space debris with respect to the center of the Earth. Actually, the acceleration defined in Eq. (2.9) refers to an inertial coordinate system in which the Earth is not at rest, but is itself subject to an acceleration (Montenbruck and Gill, 2000)

$$\ddot{\boldsymbol{r}} = \mu_i \frac{\boldsymbol{r_i}}{\|\boldsymbol{r_i}\|^3} \,.$$

As a consequence, the acceleration of the space debris, expressed with respect to the Earth's center of mass is given as

$$\ddot{\boldsymbol{r}} = -\mu_i \left(\frac{\boldsymbol{r} - \boldsymbol{r_i}}{\|\boldsymbol{r} - \boldsymbol{r_i}\|^3} + \frac{\boldsymbol{r_i}}{\|\boldsymbol{r_i}\|^3} \right) .$$

The first term of the third-body perturbation is known as the *direct effect* and the second term is the *indirect effect* accounting for the inertial acceleration of the geocenter.

Because the reason of perturbations from a third body is the gravitational attraction, it is also reasonable to use a disturbing function. The potential disturbing function can be written as

$$\mathcal{R}_i = \mu_i \left(\frac{1}{\|\boldsymbol{r} - \boldsymbol{r_i}\|} - \frac{\langle \boldsymbol{r} \,.\, \boldsymbol{r_i} \rangle}{\|\boldsymbol{r_i}\|^3} \right) . \tag{2.10}$$

Expansion using Legendre Polynomials

In keeping with Eq. (2.4), we find the final formulation by expressing the potential (2.10) in terms of the Legendre polynomials

$$\mathcal{R}_i = \frac{\mu_i}{r_i} \sum_{n \geq 2} \left(\frac{r}{r_i} \right)^n \mathcal{P}_n(\cos\psi) \,, \tag{2.11}$$

where r_i is the geocentric distance and ψ is the geocentric angle between the third body and the satellite. $\mathcal{P}_n$ is the Legendre polynomial of degree n.

Let us now derive the expansion of the disturbing function in power series of the eccentricity and of the inclination. To reach this goal, let us first consider the three components (x, y, z) of the position vector $\boldsymbol{r}$ expressed with respect to the Keplerian elements $(a, e, i, \Omega, \omega, f)$ where

f is the true anomaly. We have

$$\begin{pmatrix} x \\ y \\ z \end{pmatrix} = \begin{pmatrix} \cos\Omega & -\sin\Omega & 0 \\ \sin\Omega & \cos\Omega & 0 \\ 0 & 0 & 1 \end{pmatrix} \begin{pmatrix} 1 & 0 & 0 \\ 0 & \cos i & -\sin i \\ 0 & \sin i & \cos i \end{pmatrix} \times \begin{pmatrix} \cos\omega & -\sin\omega & 0 \\ \sin\omega & \cos\omega & 0 \\ 0 & 0 & 1 \end{pmatrix} \begin{pmatrix} r\cos f \\ r\sin f \\ 0 \end{pmatrix} .$$

Second, let us also consider the Cartesian coordinates X_i, Y_i and Z_i of the unit vector pointing towards the third body. Consequently, the cosine of the geocentric angle can be expressed as

$$\begin{aligned} \cos\psi &= X_i\,\bar{x} + Y_i\,\bar{y} + Z_i\,\bar{z} \\ &= X_i\,\left[\cos(f+\omega+\Omega) + 2\,\sin(f+\omega)\,\sin\Omega\,\sin^2 i/2\right] \\ &+ Y_i\,\left[\sin(f+\omega+\Omega) - 2\,\sin(f+\omega)\,\cos\Omega\,\sin^2 i/2\right] \\ &+ Z_i\,2\,\sin(f+\omega)\,\sin i/2\,\cos i/2\,, \end{aligned}$$

where we used $i/2$ instead of the inclination and where $(\bar{x}, \bar{y}, \bar{z})$ are the components of the unit vector pointing toward the space debris. To derive a series expansion for $\cos\psi$ we also need to make use of the expansions for $\sin f$ and $\cos f$ in terms of the mean anomaly which correspond to d'Alembert series, i.e. Fourier series in the mean anomaly with coefficients containing higher powers of the eccentricity for the higher harmonics. These expansions are given by (Brouwer and Clemence, 1961)

$$\begin{aligned} \sin f &= 2\sqrt{1-e^2}\sum_{s=1}^{+\infty}\frac{1}{s}\frac{\mathrm{d}}{\mathrm{d}e}J_s(se)\sin sM \\ &= \sin M + e\sin 2M + e^2\left(\frac{9}{8}\sin 3M - \frac{7}{8}\sin M\right) \\ &\quad + e^3\left(\frac{4}{3}\sin 4M - \frac{7}{6}\sin 2M\right) \\ &\quad + e^4\left(\frac{5}{192}\cos M - \frac{45}{128}\cos 3M + \frac{125}{384}\cos 5M\right) + \mathcal{O}(e^5) \end{aligned}$$

and similarly

$$\begin{aligned} \cos f &= -e + \frac{2(1-e^2)}{e}\sum_{s=1}^{+\infty}\cos sM, \\ &= \cos M + e\,(\cos 2M - 1) + \frac{9e^2}{8}\,(\cos 3M - \cos M) \\ &\quad + \frac{4e^3}{3}\,(\cos 4M - \cos 2M) \\ &\quad + \left(\frac{25}{192}\cos M - \frac{225}{128}\cos 3M + \frac{625}{384}\cos 5M\right) + \mathcal{O}(e^5)\,. \end{aligned}$$

We also need the expansion of r/a, indirectly present in Eq. (2.11) because of

$$(r/r_i)^n = (r/a)^n \, r_i^{-n} \, a^n.$$

We have

$$\begin{aligned}
\frac{r}{a} &= 1 + \frac{1}{2}e^2 - 2e \sum_{s=1}^{+\infty} \frac{1}{s^2} \frac{\mathrm{d}}{\mathrm{d}e} J_s(se) \cos sM \\
&= 1 - e\cos M + \frac{e^2}{2}\left(1 - \cos 2M\right) + \frac{3e^3}{8}\left(\cos M - \cos 3M\right) \\
&\quad + \frac{e^4}{3}\left(\cos 2M - \cos 4M\right) + \mathcal{O}(e^5)\,.
\end{aligned}$$

We show that the expansion of (2.11) has the form

$$\mathcal{R}_i = \frac{\mu_i}{r_i} \sum_{n=2}^{+\infty} \sum_{k,l,j_1,j_2,j_3} \left(\frac{a}{r_i}\right)^n A^{(n)}_{k,l,j_1,j_2,j_3}(X_i, Y_i, Z_i)\, e^{|k|+2j_2} \left(\sin\frac{i}{2}\right)^{|l|+2j_3} \cos\,\Phi\,, \quad (2.12)$$

where $A^{(n)}_{k,l,j_1,j_2,j_3}(X_i, Y_i, Z_i)$ are polynomial functions which depend on the Cartesian coordinates of the third-body. Here, Φ is a linear combination with general form

$$\Phi = j_1\,\lambda + j_2\,\varpi + j_3\,\Omega\,.$$

where λ is the mean longitude, which is the sum of the mean anomaly, the argument of perigee and the longitude of the ascending node, that is $\lambda = M + \omega + \Omega$; and ϖ is longitude of the perigee, i.e. $\varpi = \omega + M$.

This potential is obviously time dependent through the position of the perturbing body. This particular formulation has two benefits: first, the expansion is rather compact which is relevant since these series will be evaluated at each step of the numerical integration process; second, the chosen parameters are easily derived from other sets of variables such as equatorial or ecliptic spherical coordinates. Therefore, we can use any available numerical or analytical ephemeris. In our implementation, we choose the highly accurate and well-known `DE405` solar system ephemeris. The Jet Propulsion Laboratory (`JPL`) provides these solar system ephemeris in the form of Chebyshev approximations. The Development Ephemeris (`DE`) are publicly available and have emerged as a standard for high-precision planetary coordinates (Montenbruck and Gill, 2000). For further details, we refer to Standish (1998).

2.3 Expansion of the disturbing functions in universal elements

2.3.1 Singularities and numerical integrations

The Keplerian elements ($a,\ e,\ i,\ \Omega,\ \omega,\ M$) present three cases of singularity in the problem of an Earth-orbiting object. For circular orbits ($e = 0$), the mean anomaly M and the argument of perigee ω are undetermined but the sum $M + \omega$ is well defined. Meanwhile, for equatorial orbits ($i = 0$), the argument of perigee and the longitude of the ascending node Ω are undetermined but the sum $\omega + \Omega$ is well defined. Finally, when the eccentricity $e = 0$ and the inclination $i = 0$, only the sum $M + \omega + \Omega$ is well defined (Henrard, 1974). However, it is worth stressing that there is no physical instability corresponding to this mathematical singularity. In other words, for a very small value of the eccentricity, a large change in the argument of perigee ω corresponds to a small change in both the position and the velocity vectors $\boldsymbol{r},\ \dot{\boldsymbol{r}}$, respectively. For the sake of the illustration, we refer to both the Lagrangian and Gaussian equations developed in Appendix E (page 173), where the mathematical singularities are clearly apparent through the presence of the so-called *small divisors* terms of the form $1/e$ and $1/\sin i$.

As an illustration of the effects of singularities in numerical propagations, we analyze the stability of an osculating numerical integration process with and without small divisors. In order to perform these tests, we have taken advantage of a suite of complete numerical osculating propagators called `LAGRAN-MICROZ` developed at "L'Observatoire de la Côte d'Azur" in Grasse (France). This extensive numerical software allows to propagate various sets of Earth-orbiting objects while taking into account a large set of perturbations. Moreover, the latter allows to consider two different integration algorithms. Hereafter, we consider the Adams-Moulton-Cowell multistep algorithm of order 12. To sum up, in brief, one can say that the `LAGRAN` software is based on the numerical integrations of both the osculating Lagrangian and Gaussian equations of motions expressed in Keplerian elements (even though some extensions have been given to partly avoid the singularities (Deleflie, 2002)). On the other hand, the `MICROZ` software is based on the numerical integrations of the osculating equations of motion expressed in Cartesian coordinates.

In our investigations, we performed numerical propagations over a period of 60 days with an integration step size of 90 s. The dynamical model includes the Earth's gravity field developed up to degree and order 20 and the luni-solar perturbations. The initial conditions used in the simulations are those of nearly geosynchronous space debris, that is $a_0 = 42\,164\,\mathrm{km},\ e_0 = 10^{-4},\ i_0 = 10^{-4}$ rad. The validation is performed by considering the differences between a forward and a backward numerical integration. That is the final state vector of the first numerical integration is used as initial condition of the second numerical integration which is performed with a negative step size. As a consequence, the zero point of the difference is then located at the end of the time window. Figure 2.2 shows the differences using Keplerian

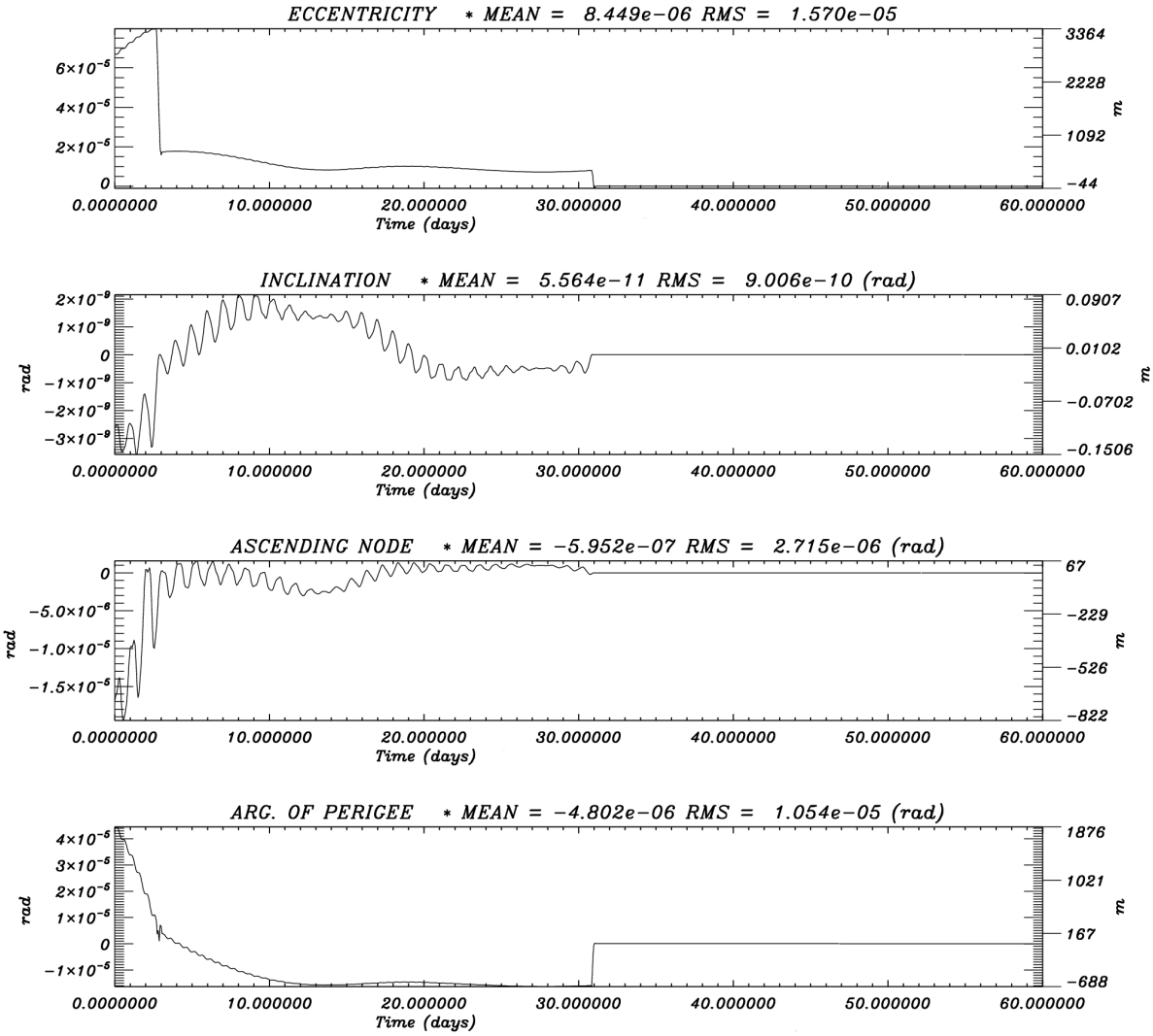

Figure 2.2: Stability of numerical integration in case of small divisors (singularities): Keplerian elements of two numerical integrations performed in singular coordinates $(e,\ i,\ \Omega,\ \omega)$ using the LAGRAN software. Differences between a forward integration and a backward integration ($a_0 = 42\,164$ km, $e_0 = 10^{-4}$, $i_0 = 10^{-4}$ rad). Dynamical model: Earth's gravity field up to degree and order 20, luni-solar attractions. On each graph, on the left are shown $(\Delta e,\ \Delta i,\ \Delta\Omega,\ \Delta\omega)$ and on the right $(a_0\Delta e,\ a_0\Delta i,\ a_0\Delta\Omega,\ a_0\Delta\omega)$.

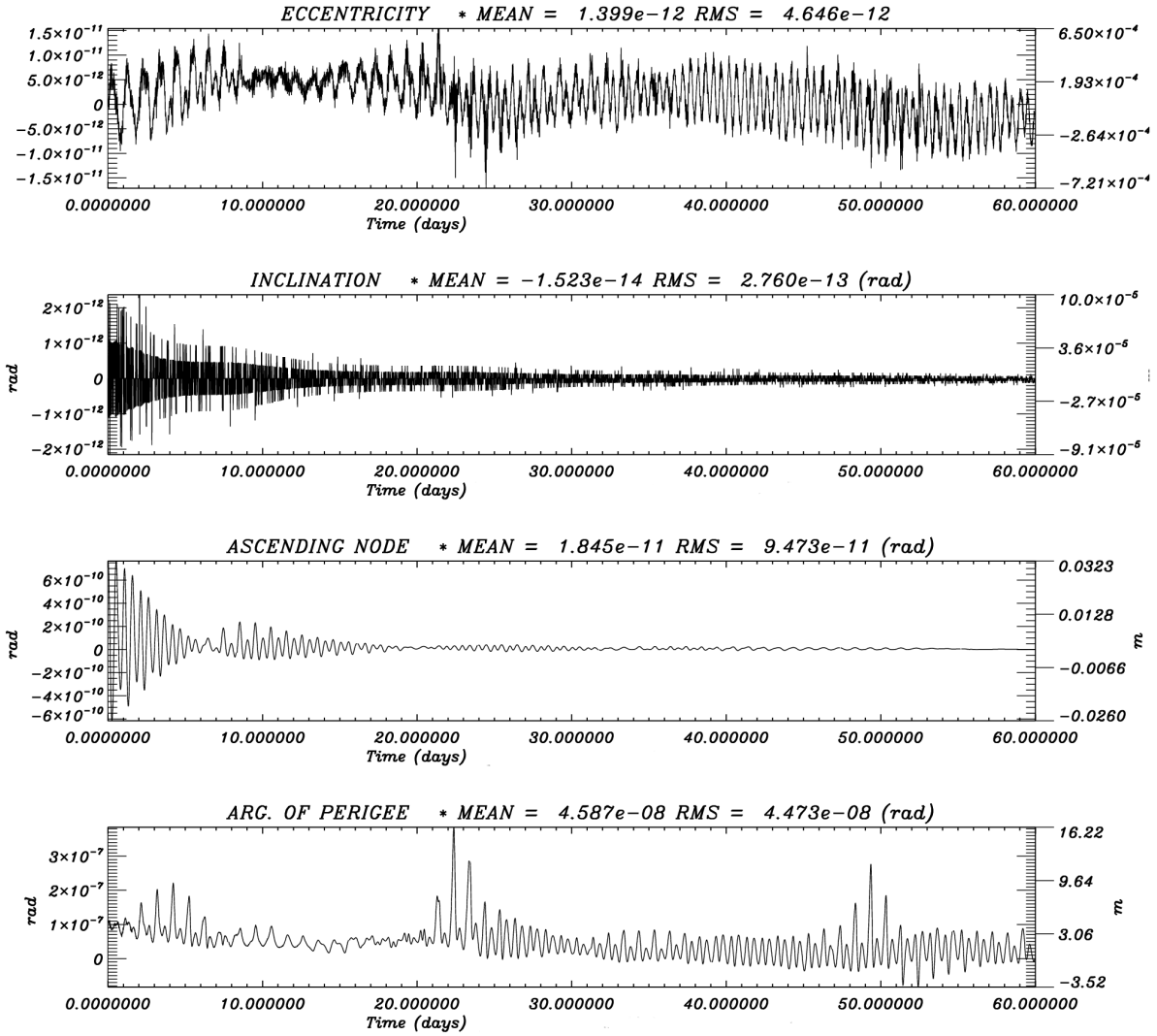

Figure 2.3: Stability of numerical integration without small divisors (without singularity): Keplerian elements of two numerical integrations performed in non-singular Cartesian coordinates (e, i, Ω, ω) using the `MICROZ` software. Differences between a forward integration and a backward integration ($a_0 = 42\,164$ km, $e_0 = 10^{-4}$, $i_0 = 10^{-4}$ rad). Dynamical model: Earth's gravity field up to degree and order 20, luni-solar attractions. On each graph, on the left are shown $(\Delta e,\ \Delta i,\ \Delta\Omega,\ \Delta\omega)$ and on the right $(a_0\Delta e,\ a_0\Delta i,\ a_0\Delta\Omega,\ a_0\Delta\omega)$.

Table 2.1: Statistical analysis of numerical integration errors. Dynamical model: Earth's gravity field up to degree and order 20, luni-solar perturbations. Comparison between the forward numerical integration and the associated backward numerical integration with and without small divisors. In each orbit, there is one point every 15 min (with a total of $n = 5761$ points).

$a_0 = 42\,164$ km, $e_0 = 10^{-4}$, $i_0 = 10^{-4}$ rad, $\Omega_0 = \omega_0 = M_0 = 0$ rad

		Keplerian elements			Non-singular elements		
		Mean	RMS	χ^2	Mean	RMS	χ^2
a	[m]	$0.664\,10^{-03}$	$0.472\,10^{-01}$	$0.305\,10^{-06}$	$0.464\,10^{-03}$	$0.560\,10^{-03}$	$0.724\,10^{-10}$
e		$0.842\,10^{-05}$	$0.156\,10^{-04}$	0.878	$-0.139\,10^{-11}$	$0.464\,10^{-11}$	$0.129\,10^{-14}$
i	[rad]	$0.568\,10^{-10}$	$0.898\,10^{-09}$	$0.269\,10^{-10}$	$0.152\,10^{-13}$	$0.275\,10^{-12}$	$0.240\,10^{-17}$
Ω	[rad]	$-0.588\,10^{-06}$	$0.269\,10^{-05}$	$0.112\,10^{-05}$	$-0.184\,10^{-10}$	$0.947\,10^{-10}$	$0.982\,10^{-14}$
ω	[rad]	$-0.483\,10^{-05}$	$0.104\,10^{-04}$	0.189	$-0.458\,10^{-07}$	$0.447\,10^{-07}$	$0.157\,10^{-10}$
M	[rad]	$-0.109\,10^{-02}$	$0.827\,10^{-01}$	$0.363\,10^{-07}$	$-0.109\,10^{-02}$	$0.827\,10^{-01}$	$0.237\,10^{-10}$

elements during the integration process (using the LAGRAN software). As a consequence, the eccentricity and the inclination are small enough to induce small divisors in the equations of motion. The propagation of the numerical errors is quite fast and involves a deviance of several thousands meters between the two orbits only after 60 days.

On the contrary, Figure 2.3 shows the differences between the same orbits integrated in non-singular Cartesian elements (using the MICROZ software), namely the projection of the Cartesian coordinates into classical Keplerian elements. In this case, the differences remain quite small and underline mainly the characteristics of the chosen numerical integrator.

In order to quantify the significance of singularities in the latter numerical integrations, we have computed a couple of statistic quantities shown in Table 2.1. The statistic quantities characterize the similarity between the n points x_i of the orbit obtained by the forward numerical integration, and the n points x'_i of the orbit obtained with the backward numerical integration. The first two columns correspond to the mean values and the standard deviation (Root Mean Square) of the differences. The third column shows the quantity χ^2 where

$$\chi^2 = \sum_{i=1}^{n} \frac{(x'_i - x_i)^2}{|x_i|}.$$

The smaller χ^2, the higher the similarity between the two numerical integrations. By means of this quantity, it is even clearer that the numerical integration performed with MICROZ, i.e. by using a set of variables avoiding the small divisors in the equations of motion, is significantly more stable than numerical integrations performed in classical Keplerian elements.

2.3.2 Universal set of variables: the Poincaré variables

As shown in the previous section, it is relevant to consider a specific set of variables avoiding both singularities and still ensuring an easy geometrical interpretation of the motion.

Non-singular sets of variables already exist in the literature. As an example, the following equinoctial elements: a, $\lambda = M+\omega+\Omega$, $e\,\sin(\omega+\Omega)$, $e\,\cos(\omega+\Omega)$, $\tan\frac{i}{2}\,\sin\Omega$, $\tan\frac{i}{2}\,\cos\Omega$ are used extensively in several domains of celestial mechanics. The associated Lagrangian equations have been computed (Giacaglia, 1977; Nacozy and Dallas, 1977; Wytrzyszczak, 1986). However, these equations are rather complicated.

As an alternative, in our approach, we prefer to adopt a non-singular set of variables which is also canonical. The following Poincaré variables $(x_1,\ \ldots,\ x_6)$ hold these specific characteristics and are defined by

$$\begin{aligned} x_1 &= \sqrt{2P}\,\sin p\,, & x_4 &= \sqrt{2P}\,\cos p\,,\\ x_2 &= \sqrt{2Q}\,\sin q\,, & x_5 &= \sqrt{2Q}\,\cos q\,,\\ x_3 &= \lambda = M+\Omega+\omega\,, & x_6 &= L\,, \end{aligned} \tag{2.13}$$

where

$$\begin{aligned} P &= L-G\,, & p &= -\omega-\Omega\,,\\ Q &= G-H\,, & q &= -\Omega\,, \end{aligned}$$

and (L, G, H) are the Delaunay's elements defined by

$$L=\sqrt{\mu\,a},\qquad G=\sqrt{\mu\,a(1-e^2)}\,,\qquad H=\sqrt{\mu\,a(1-e^2)}\,\cos i$$

as well as λ, the mean longitude. As a consequence, canonical properties will greatly simplify the dynamical equations leading to the following Hamiltonian system of equations

$$\begin{aligned} \frac{\mathrm{d}x_j}{\mathrm{d}t} &= \frac{\partial\mathcal{H}(x_1,\ldots,x_6)}{\partial x_{j+3}} & 1\le j\le 3\,,\\ \frac{\mathrm{d}x_j}{\mathrm{d}t} &= -\frac{\partial\mathcal{H}(x_1,\ldots,x_6)}{\partial x_{j-3}} & 4\le j\le 6\,, \end{aligned} \tag{2.14}$$

where $\mathcal{H}$ is the Hamiltonian function taken into account. The system (2.14) is said to be a Hamiltonian system of order 6, or, equivalently, of 3 degrees of freedom. The quantities $x_j\ (j=1,\ldots,3)$ are called the variables (similarly the coordinates) while the quantities $x_j\ (j=4,\ldots,6)$ are called the momenta, which are conjugated to the $x_j\ (j=1,\ldots,3)$.

The Hamiltonian equations of motion differs from the Lagrangian equations because the canonical elements rates depend not only on the disturbing function but also on the total energy of the system. In particular, when the Hamiltonian function $\mathcal{H}$ is autonomous, i.e. it does not depend explicitly on the time t, one can show that $\mathcal{H}$ is the sum of the kinetic $\mathcal{T}$ and potential

energy $\mathcal{V}$ of the system and so equals the total energy, an integral of the system. Generally, we have a Hamiltonian

$$\begin{aligned}\mathcal{H} &= \mathcal{T} + \mathcal{V} + \dot{\theta}\,\Lambda \\ &= \mathcal{H}_{2b} + \sum_n \mathcal{R}_n + \dot{\theta}\,\Lambda \\ &= -\frac{\mu^2}{2\,L^2} + \sum_n \mathcal{R}_n + \dot{\theta}\,\Lambda\end{aligned}$$

where $-\mu^2/2L^2$ is the Hamiltonian for the two-body problem and $\mathcal{R}_n$ are the various disturbing functions which are possibly taken into account. In order to preserve an autonomous Hamiltonian, we also consider a correcting term $\dot{\theta}\,\Lambda$ which is due to the Earth's rotation. The quantity Λ is the momentum conjugated to the sidereal time θ.

One major benefit of Hamiltonian systems is that it makes specific coordinate transformations easier to carry out, which will be particularly relevant when we will investigate resonant dynamics. More generally, the canonical form of the differential equations can be easily preserved while considering the so-called canonical transformations which define a subset of transformations from one set of canonical variables to another set. Furthermore, we ought to mention that the canonical properties will also greatly simplify the further analytical filtering in order to eliminate the short-period variations.

However, expressed in this form, the canonical set of elements (2.13) is not well suited for the implementation of a perturbation theory because the potentials, expressed as a function of them, are not simple Poisson series. This is due in part to the fact that P and Q are not dimension-free (Henrard, 1974). A more convenient (but not canonical) set of elements would be

$$U = \sqrt{\frac{2P}{L}}\,, \qquad V = \sqrt{\frac{2Q}{L}}\,.$$

Because of their design, these elements are dimension-free and thus well suited for series expansions.

Let us note that for small to moderate eccentricity and inclination, these elements are directly related to both the eccentricity and the inclination. Actually, we have

$$U \approx e\,, \qquad V \approx 2\,\sin\frac{i}{2}$$

since

$$\begin{aligned}e &= U\left(1 - \frac{U^2}{4}\right)^{\frac{1}{2}} \\ &= U - \frac{1}{8}U^3 - \frac{1}{128}U^5 + \mathcal{O}(U^7)\end{aligned}$$

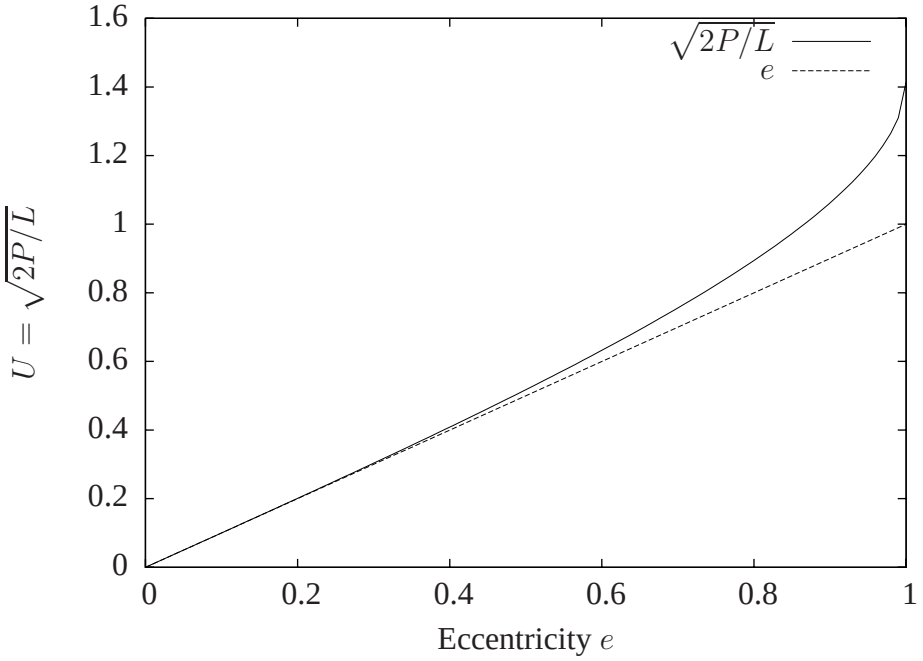

Figure 2.4: Graphic of $U = \sqrt{2P/L}$ with respect to the eccentricity e. For eccentricity values such as $e < 0.5$, the two quantities are very close.

as well as

$$\begin{aligned} 2\,\sin\frac{i}{2} &= V\left[1-\frac{U^2}{2}\right]^{-\frac{1}{2}} \\ &= V+\frac{1}{4}\,VU^2+\frac{3}{32}\,VU^4+\mathcal{O}(U^6)\,. \end{aligned}$$

For the sake of comparison, in Figures 2.4 and 2.5, we plot the values of both $U = \sqrt{2P/L}$ and $V = \sqrt{2Q/L}$ with respect to the eccentricity and the inclination, respectively. It is clear that for eccentricity values such as $e < 0.5$, U and e are very close. Similarly, for small to moderate values of the inclination and of the eccentricity, the quantities V and $2\sin i/2$ are also very similar.

If the series expansions are performed and truncated, the Hamiltonian functions taken into account in the problem of space debris, such as the geopotential (2.8) and the third-body (2.12) disturbing functions can be easily expressed as a combination between polynomials in U and V and trigonometric functions with respect to the angular quantities. Regarding the geopotential expansion and for an arbitrary harmonic of degree n, we formally have

$$\mathcal{R}_{pot}^{(n)} = \frac{1}{L^{2n+2}}\sum_{j=1}^{N_n}\mathcal{A}_j^{(n)}(U,V)\,\mathcal{B}_j^{(n)}(\lambda,p,q,\theta)\,,$$

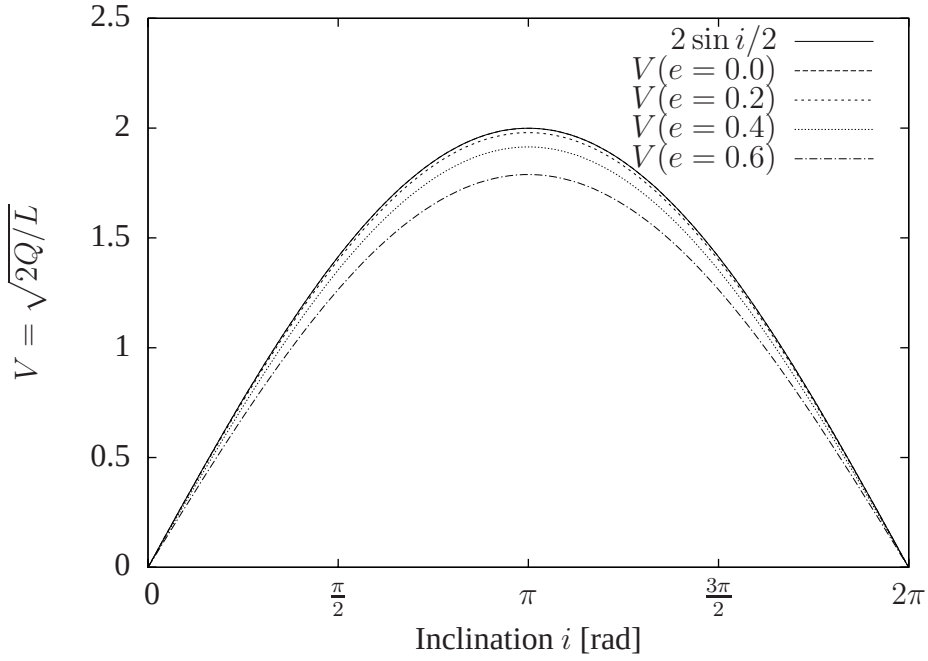

Figure 2.5: Graphic of $V = \sqrt{2Q/L}$ with respect to the inclination i for various values of the eccentricity e.

whereas the n-degree third-body expansion is related to

$$\mathcal{R}_i^{(n)} = \frac{L^{2n}}{r_i^{n+1}} \sum_{j=1}^{N_n} \mathcal{A}_j^{(n)}(U, V, X_i, Y_i, Z_i)\, \mathcal{B}_j^{(n)}(\lambda, p, q)\,.$$

The quantity $\mathcal{B}_j^{(n)}$ is a trigonometric function which depends on the angular variables λ, p, q and possibly θ. $\mathcal{A}_j^{(n)}$ is a polynomial in the U and V variables and possibly depending on the Cartesian coordinates of the third-body when considering the third-body expansion. n_{max} is the maximum degree of the expansion and N_n is the number of terms in the n-degree expansion. Let us note that the sidereal time θ is only present in the case of tesseral and sectorial harmonics due to the asymmetry in longitude.

Therefore, it is straightforward to deduce the final expansion in a set of non-dimensional Cartesian variables X_1, Y_1, X_2, Y_2, that is

$$\begin{aligned} \mathcal{H}_{pot} &= \mathcal{H}_{2b} + \dot{\theta}\,\Lambda + \sum_{n=2}^{n_{max}} \mathcal{R}_{pot}^{(n)} \\ &= -\frac{\mu^2}{2\,L^2} + \dot{\theta}\,\Lambda + \sum_{n=2}^{n_{max}} \frac{1}{L^{2n+2}} \sum_{j=1}^{N_n} \mathcal{A}_j^{(n)}(X_1, Y_1, X_2, Y_2)\, \mathcal{B}_j^{(n)}(\lambda, \theta)\,, \end{aligned} \tag{2.15}$$

where Λ is the momentum conjugated to the sidereal time θ. Similarly, from Eq. (2.12), we obtain the third-body expansion

$$\begin{aligned}\mathcal{H}_i &= \sum_{n=2}^{n_{max}} \mathcal{R}_i^{(n)} \\ &= \sum_{n=2}^{n_{max}} \frac{L^{2n}}{r_i^{n+1}} \sum_{j=1}^{N_n} \mathcal{A}_j^{(n)}(X_1, Y_1, X_2, Y_2, X_i, Y_i, Z_i)\, \mathcal{B}_j^{(n)}(\lambda)\,,\end{aligned} \tag{2.16}$$

where

$$\begin{aligned} X_1 &= U\,\sin p = \sqrt{\frac{2P}{L}}\,\sin p\,, & Y_1 &= U\,\cos p = \sqrt{\frac{2P}{L}}\,\cos p\,, \\ X_2 &= V\,\sin q = \sqrt{\frac{2Q}{L}}\,\sin q\,, & Y_2 &= V\,\cos q = \sqrt{\frac{2Q}{L}}\,\cos q\,. \end{aligned} \tag{2.17}$$

These variables are similar to the elements that we have introduced in Eq. (2.13). It is worth noting that despite the fact that this set of variables is at present non-dimensional, the new differential system of the equations of motion remains simple and is said to be *quasi-Hamiltonian*, i.e. Hamiltonian when excluding the non-dimensional variables substitutions. We mean that we keep the Hamiltonian formulation of the differential equations, after having divided the momenta P and Q by L, making them non-dimensional. Of course, this division generates some corrective terms. The new differential system of equations reads

$$\begin{aligned} \dot{X}_i &= \frac{1}{L}\frac{\partial \mathcal{H}}{\partial Y_i}\,, \qquad \dot{Y}_i = -\frac{1}{L}\frac{\partial \mathcal{H}}{\partial X_i}\,, \qquad i = 1, 2 \\ \dot{\lambda} &= \frac{\partial \mathcal{H}}{\partial L} - \frac{1}{2L}\left[\sum_{i=1}^{2} \frac{\partial \mathcal{H}}{\partial X_i} X_i + \sum_{i=1}^{2} \frac{\partial \mathcal{H}}{\partial Y_i} Y_i\right], \qquad \dot{L} = -\frac{\partial \mathcal{H}}{\partial \lambda}\,, \end{aligned} \tag{2.18}$$

where $\mathcal{H}$ is the Hamiltonian function (2.15) and/or (2.16) taken into account and expressed in the before-mentioned non-dimensional and Cartesian set of variables (2.17).

2.4 Manipulating series and first order averaging process

2.4.1 The Poisson series manipulator – `MSNAM`

It is clear that the expansion of the disturbing functions performed so far is a non-trivial task: it is best undertaken with the assistance of computer algebra systems (Murray et Dermott, 1999). Actually, the various Hamiltonian series involve an extremely large number of analytical computations, particularly in the case of a high order development. Hand computations are then avoided.

To tackle this technical difficulty, we use a symbolic software developed in our University. This tool is called the `MSNAM`, standing for **Nam**ur **S**eries **M**anipulator. It is based on the idea described by Henrard (1986). This software was first written in `Fortran77` by Michèle

Moons (Moons, 1993) and was further extended and improved by Jacques Henrard in 2004. This software is at present written in `Fortran90` and is used for manipulating *Poisson series* of the form

$$\alpha \prod_{i=1}^{p} \chi_i^{exp(i)} \left(\begin{array}{c} \cos \\ \sin \end{array} \right) \left(\sum_{j=1}^{q} arg(j)\, \phi_j \right) ,$$

that is Fourier series in the q angles $\phi_1, \cdots, \phi_q$ the coefficients of which are polynomials in p variables $\chi_1, \cdots, \chi_p$. The arguments $arg(j)_{j=1\cdots q}$ and exponents $exp(i)_{i=1\cdots p}$ are integers and the α coefficient is a real number.

The software package is provided with various mathematical operation functionalities such as the addition, the multiplication of series as well as the partial differentiation and integration with respect to both polynomial and trigonometric variables.

When multiplying such series, more and more terms are produced and they are always reduced to linear form by the following well-known relationships

$$\begin{aligned}
\sin A \, \cos B &= \tfrac{1}{2} \, (\, \sin(A+B) + \sin(A-B) \,) \\
\cos A \, \sin B &= \tfrac{1}{2} \, (\, \sin(A+B) - \sin(A-B) \,) \\
\cos A \, \cos B &= \tfrac{1}{2} \, (\, \cos(A+B) + \cos(A-B) \,) \\
\sin A \, \sin B &= \tfrac{1}{2} \, (\, \cos(A+B) + \cos(A-B) \,) \, .
\end{aligned}$$

The concern to keep a linear expression in both the sine and cosine functions is actually mandatory for the manipulation of the series. In particular, it is essential when differentiating the Hamiltonian function in order to derive the differential equations, but also in order to perform the averaging process which will be discussed further.

2.4.2 Averaging over the short periods

Before presenting the averaging algorithm, let us first recall that the perturbations acting on an Earth-orbit object can be categorized with respect to their periodicity. First, the ***short-periodic*** perturbations are said to be harmonic changes in the orbital elements with a periodicity which is on the order of the orbital period. Second, the ***long-periodic*** perturbations are characterized by harmonic changes in the orbital elements with periods on the order of the periodicity of both the perigee and the longitude of the ascending node. These perturbation oscillations are typically on the order of several dozens of years. Finally, the ***secular*** perturbations are characterized by time-proportional changes of the orbital elements. Moreover, we should also define the resonant changes related to resonance effects linked to some synchronism between the orbital motion and a perturbing environment. This peculiar case will be discussed further.

Figure 2.6 shows schematically the characteristics of the perturbation classes according to their periodicity as defined above. In this figure, we show the time evolution of an arbitrary

osculating element $E(t)$ as well as the related mean element $E'(t)$ which includes both the long-periodic and secular variations (filtered over the short periods). $E'(t)$ is usually called a *single-averaged* element as the result of removing the short-periodic motion from the osculating element $E(t)$. Removing the long-periodic effects would lead to the so-called *doubly-averaged* element which is only associated with the secular changes represented by the straight line.

Let us recall that in completely numerical integrations, such as those obtained in Figures 2.2 and 2.3, the state vector or more generally the chosen set of orbital elements is propagated along the osculating trajectory. The integration step in such integrations is typically on the order of a few minutes to ensure a sufficiently high stability when following orbits which are subject to high-frequency perturbations. In this framework, the right-hand sides of the differential system of equations are evaluated a huge number of times.

The main idea of our approach consists in using first an analytical filtering procedure of the initial osculating equations of motion, and second a numerical integration of these transformed equations. This approach is well-known and is said to be a ***semi-analytical theory***. The main interest of semi-analytical theories is the determination of long-term ephemerides. In this field, what is of special relevance is not the complete description of the solution requiring a lot of

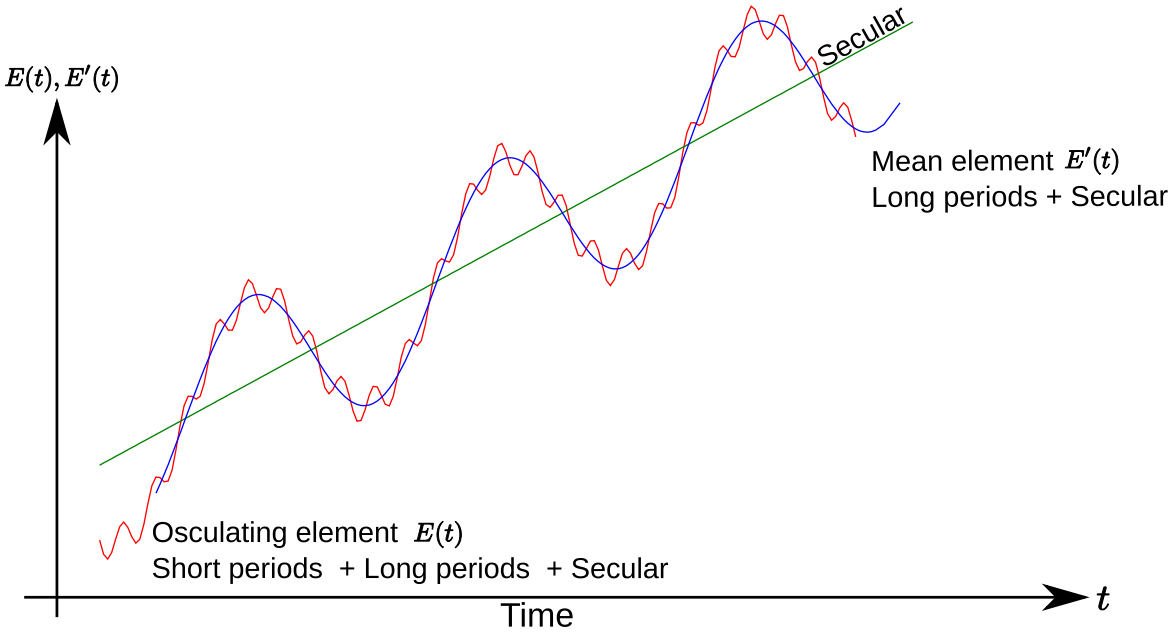

Figure 2.6: Schematic illustration of short-period, long-period as well as secular effects with respect to a generic perturbation. $E(t)$ and $E'(t)$ stand for an arbitrary osculating and mean element, respectively. The straight line shows secular effects. The large oscillation line shows the secular plus long-periodic effects, and the small oscillation line, which combine all the effects, shows the short-periodic effects.

CPU time consumption, but the prediction of an approximate position at a given time.

Before proceeding with the averaging process, it is obviously necessary to specify the cut-off period. In our theory, the cut-off period has been set to the orbital period of the space debris, that is 1 day in the specific case of a geosynchronous space debris. As a consequence, in our approach, the so-called approximate position will simply corresponds to the propagation of the long-periodic curve (Figure 2.6). When propagating along this long-periodic curve, the integration step can be significantly increased. Typically the entry-level time step is chosen to be on the order of 1 day. Consequently, the numerical integration of the transformed system of equation guarantees a great precision for the future solution and is very fast thanks to the absence of short-periodic oscillations in the equations (At least ten times faster than traditional numerical extrapolation, depending on the order of the expansion).

The averaging process can be easily explained by first separating the fast periodic terms from the long periodic ones. For geopotential and luni-solar perturbations, this has been accomplished by means of expansions with respect to our non-singular and Cartesian set of variables (dimension-free Poincaré variables defined in Eq. (2.17)). Therefore, from Eqs. (2.15) and (2.16), we can formally consider the following generic Hamiltonian function $\mathcal{H}$

$$\begin{aligned}\mathcal{H} \;=\; \sum_{n=2}^{n_{max}} \mathcal{F}^{(n)}(L) \sum_{j=1}^{N_n} \Big(& \mathcal{C}_j^{(n)}(X_1, Y_1, X_2, Y_2, X_i, Y_i, Z_i)\, \mathcal{B}_j^{(n)}(\lambda, \theta) \\ & + \mathcal{A}_j^{(n)}(X_1, Y_1, X_2, Y_2, X_i, Y_i, Z_i) \Big) ,\end{aligned}$$

where $\mathcal{F}$ is a positive or negative power function of L. As we are interested in the long-term dynamics and as we assume at this stage that we are not close to a resonance with respect to the mean longitude λ, we average the disturbing functions over the fast variable, i.e. the mean longitude λ. As shown before, all the forces taken into account induce accelerations of the same order of magnitude. As a consequence and as a first approach, we average the disturbing functions to the first order by dropping the fast periodic terms in the trigonometric functions leading to the general averaged Hamiltonian formulation

$$\overline{\mathcal{H}} = \sum_{n=2}^{n_{max}} \mathcal{F}^{(n)}(L') \sum_{j=1}^{N_n} \mathcal{A}_j^{(n)}(X_1', Y_1', X_2', Y_2', X_i, Y_i, Z_i) ,$$

where X_1', Y_1', X_2', Y_2' as well as L' denote the averaged quantities (mean elements). For the sake of simplicity, the primes will be omitted further on. Let us note that, at present, the fast variable λ is now disregarded which means that the mean semi-major axis will remain constant, which is compatible with a first order theory. Therefore, we find easily the transformed system

Table 2.2: First terms (4-order expansion) of the averaged Hamiltonian series $\overline{\mathcal{H}}_{J_2}$ associated with the second degree harmonic. Let us notice that for some convenient reasons, we use the geostationary semi-major axis (42 164 km) as the distance unit. Moreover, the gravitational constant μ is set to unity.

λ	θ	X_1	Y_1	X_2	Y_2	L	$X_{\leftmoon}$	$Y_{\leftmoon}$	$Z_{\leftmoon}$	$r_{\leftmoon}$	$X_{\odot}$	$Y_{\odot}$	$Z_{\odot}$	$r_{\odot}$	Coefficient
cos (0	0)	(0	0	0	0	-6	0	0	0	0	0	0	0	0)	0.123866193131270D-04
cos (0	0)	(0	0	0	2	-6	0	0	0	0	0	0	0	0)	-0.185799289696905D-04
cos (0	0)	(0	0	0	4	-6	0	0	0	0	0	0	0	0)	0.464498224242264D-05
cos (0	0)	(0	0	2	0	-6	0	0	0	0	0	0	0	0)	-0.185799289696905D-04
cos (0	0)	(0	0	2	2	-6	0	0	0	0	0	0	0	0)	0.928996448484529D-05
cos (0	0)	(0	0	4	0	-6	0	0	0	0	0	0	0	0)	0.464498224242264D-05
cos (0	0)	(0	2	0	0	-6	0	0	0	0	0	0	0	0)	0.185799289696905D-04
cos (0	0)	(0	2	0	2	-6	0	0	0	0	0	0	0	0)	-0.371598579393811D-04
cos (0	0)	(0	2	2	0	-6	0	0	0	0	0	0	0	0)	-0.371598579393811D-04
cos (0	0)	(0	4	0	0	-6	0	0	0	0	0	0	0	0)	0.185799289696905D-04
cos (0	0)	(2	0	0	0	-6	0	0	0	0	0	0	0	0)	0.185799289696905D-04
cos (0	0)	(2	0	0	2	-6	0	0	0	0	0	0	0	0)	-0.371598579393811D-04
cos (0	0)	(2	0	2	0	-6	0	0	0	0	0	0	0	0)	-0.371598579393811D-04
cos (0	0)	(2	2	0	0	-6	0	0	0	0	0	0	0	0)	0.371598579393811D-04
cos (0	0)	(4	0	0	0	-6	0	0	0	0	0	0	0	0)	0.185799289696905D-04

of equations (quasi-Hamiltonian)

$$\begin{aligned} \dot{X}_i &= \frac{1}{L}\frac{\partial \overline{\mathcal{H}}}{\partial Y_i}\,, \qquad \dot{Y}_i = -\frac{1}{L}\frac{\partial \overline{\mathcal{H}}}{\partial X_i}\,, \qquad i = 1,2 \\ \dot{\lambda} &= \frac{\partial \overline{\mathcal{H}}}{\partial L} - \frac{1}{2L}\left[\sum_{i=1}^{2}\frac{\partial \overline{\mathcal{H}}}{\partial X_i}X_i + \sum_{i=1}^{2}\frac{\partial \overline{\mathcal{H}}}{\partial Y_i}Y_i\right]\,, \qquad \dot{L} = -\frac{\partial \overline{\mathcal{H}}}{\partial \lambda} = 0\,. \end{aligned} \tag{2.19}$$

2.4.3 Characteristic series expansion and coding illustration

As an illustration, Table 2.2 shows the first terms of the non-singular averaged series $\mathcal{H}_{J_2}$ associated with the second degree harmonic. The related Hamiltonian disturbing function is given by

$$\begin{aligned} \mathcal{H}_{J_2} &= \frac{1}{2}\,\frac{\mu^4\,R_e^2}{L^6}\,\left(\frac{a}{r}\right)^3\,\left(1 - 3\sin^2\phi\right) \\ &= \frac{1}{2}\,\frac{\mu^4\,R_e^2}{L^6}\,\left(\frac{a}{r}\right)^3\,\left(1 - 3\,\bar{z}^2\right)\,. \end{aligned}$$

In the present case, the Hamiltonian series is obviously independent of the positions of the Sun and the Moon leading to the null values of the exponents. Furthermore, to give an idea of the complexity of the various perturbations expanded in power series, we also compute the Hamiltonian series for several order expansions. Table 2.3 gives the numbers of terms for each perturbation which is taken into account.

Table 2.3: Number of terms in the various averaged and osculating Hamiltonian series expressed in non-singular Poincaré variables. The number of osculating terms are inside parentheses.

Perturbation	Number of terms			
n-order expansion $X_1^{i_1}Y_1^{i_2}X_2^{i_3}Y_2^{i_4}$ with $i_1+i_2+i_3+i_4 \leq n$	$n=2$	$n=4$	$n=6$	$n=8$
Geopotential				
$\mathcal{H}_{J_2}$	5 (33)	15 (145)	31 (410)	53 (895)
External Body - Sun & Moon				
up to degree 2	27 (205)	86 (836)	197 (2374)	390 (5480)
up to degree 3	73 (645)	250 (2642)	611 (7854)	1227 (18380)

Finally, we refer to Appendix G (page 181) where the terms are also given for the third-body series expansion.

2.5 Checking the method

As mentioned before, the semi-analytical theory has been developed to avoid the use of numerical integration of the complete differential system over very long periods of time, which are typically on the order of several years up to hundred years. However, the numerical integration scheme is always considered to be the reference if it is properly applied. As a consequence, and in order to give a first validation of the theory, we applied our semi-analytical theory to the typical case of a high-altitude abandoned space debris and we compared our results with respect to the osculating orbits derived from complete numerical integrations.

It is worth noting that the usual way of testing semi-analytical theories that consists in comparing directly the semi-analytical solution with the result of the osculating numerical integration is not entirely consistent. As a matter of fact, the osculating elements and the mean elements are not directly comparable. Therefore, a highly accurate testing procedure should have regard for this difference. For instance, Exertier and Métris (1995) describe such an accurate method based on the concept of *theoretical filtered elements*. Within this context, the osculating orbit is first numerically and analytically filtered over the short periods leading to the so-called *observed filtered elements*. Subsequently, the evolution of the mean elements computed using the transformed dynamical model (semi-analytical method) is finely tuned on the observed filtered elements, with adjusted initial conditions by a differential correction procedure. For further details concerning this testing procedure, we refer to Métris (1991), Exertier and Métris (1995) and Deleflie (2002). However, even though this testing procedure

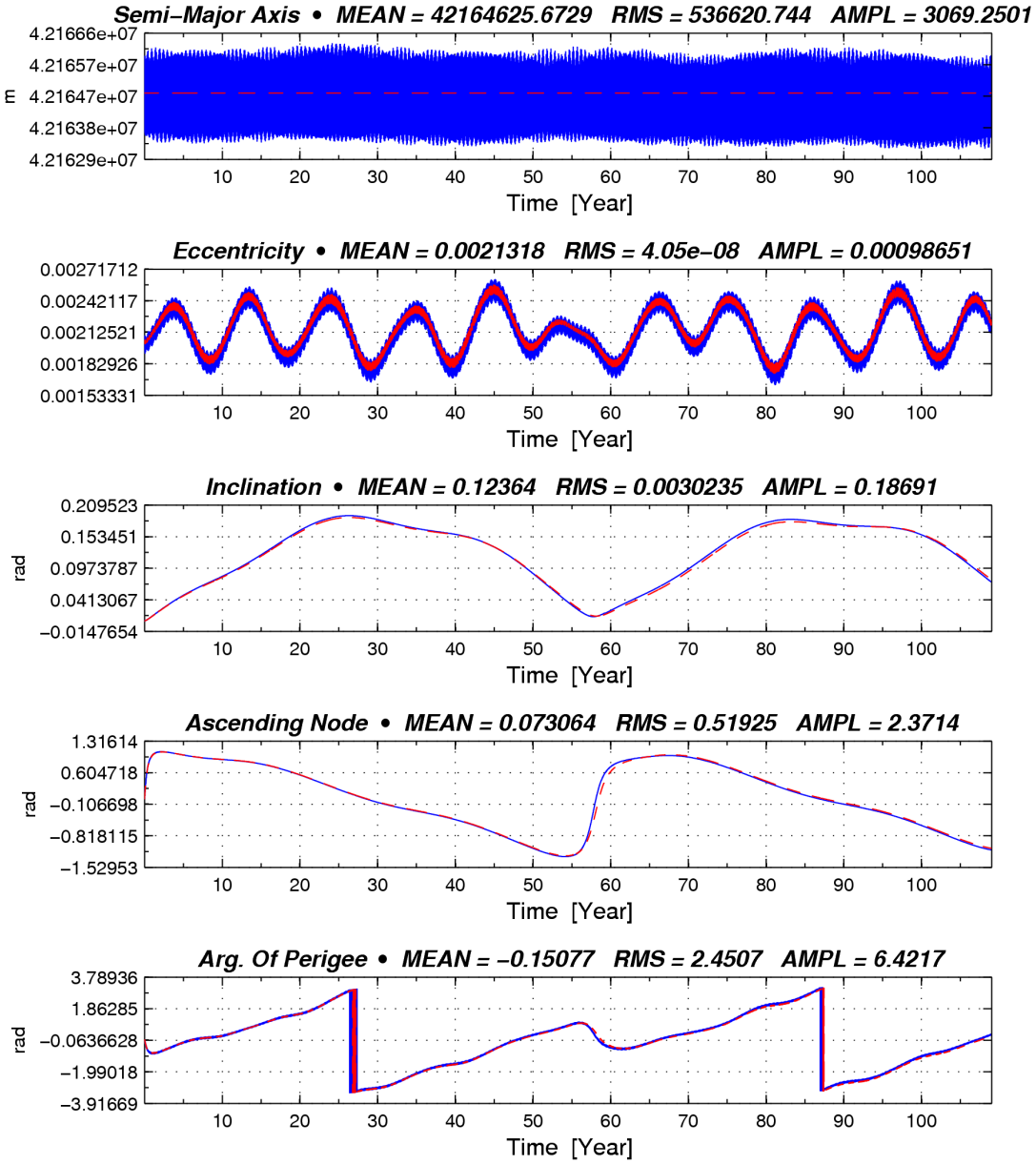

Figure 2.7: Comparison between the osculating orbit (blue solid line) and the mean orbit (red dashed line) for the long-term time evolution of a fictitious space debris subject to the second order harmonic J_2 and to the third-body perturbation (Moon). Initial conditions are $a_0 = 42\,164$ km, $e_0 = 0$, $i_0 = 0$ rad, $\Omega_0 = \omega_0 = \lambda_0 = 0$ rad. Initial time at epoch is 25 January 1991.

is much more rigorous, we consider that the time taken to implement such a procedure is too much regarding the fact that our main purpose is to give a “first order” comparison.

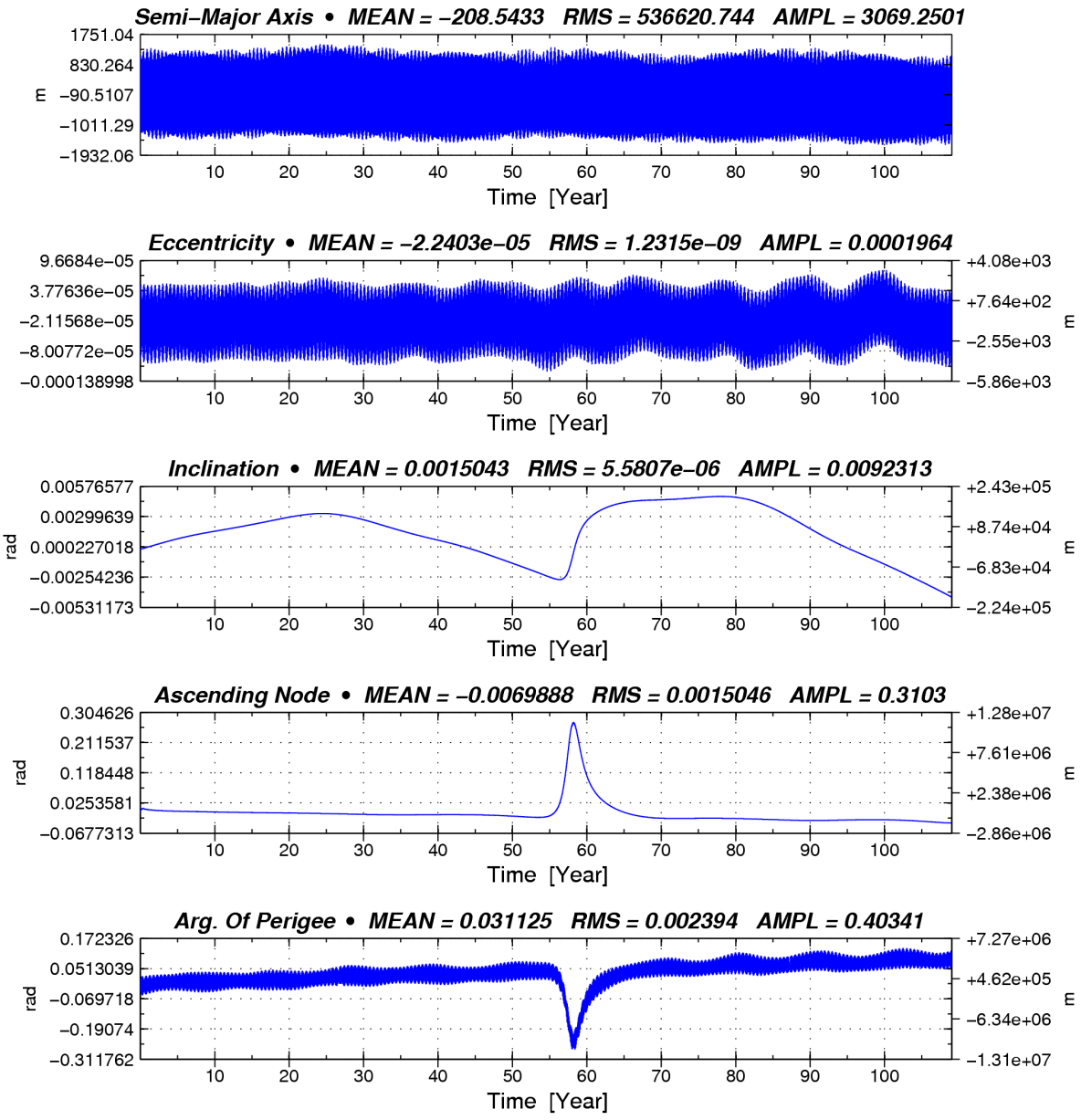

Figure 2.8: Differences between the osculating orbit and the mean orbit for the long-term time evolution of a typical abandoned space debris. The model of forces is equivalent to the one chosen in Figure 2.7.

Here, in order to make these comparisons achievable, we take advantage of a home-made numerical software. This software has been first developed by N. Delsate and has been recently extended for the special needs of the investigations developed in this manuscript. This extensive tool allows to derive the osculating motion of an arbitrary object orbiting any of the terrestrial planets of our Solar System. Similarly to the `MICROZ` software mentioned earlier, the osculating equations of motion are expressed using Cartesian coordinates which ensures

a high stability of the numerical solution by avoiding both the eccentricity and inclination singularities. The packages include the combined third-body attractions of the Sun and the Moon, the direct radiation pressure (possibly including the Earth's shadow), the Earth gravitational field expanded up to an arbitrary degree and order harmonic (`EGM96` model, Lemoine et al., 1987) using the Cunningham algorithm (see Appendix B, page 161) and air drag when applicable. The latter software allows to consider two different integration algorithms. Hereafter, we adopt the variable step size Bulirsh-Stoer algorithm (see e.g. Bulirsh and Stoer, 1966; Stoer and Bulirsh, 1980). For further details concerning a context where this software is used extensively, we refer to Chapters 4 and 5. Concerning the numerical algorithm used in the semi-analytical propagations, we also adopted the Bulirsh-Stoer algorithm as well as a fourth-order Runge-Kutta algorithm when a fixed step size is required.

From this point, let us consider the dynamical evolution of a theoretical high-altitude space debris. As a first approach, the perturbations taken into account are the oblateness of the Earth and the third-body perturbation induced by the Moon. Figure 2.7 shows the variation of both the inclination and the eccentricity as well as the associated longitude of the ascending node and the argument of perigee over a period of more than 100 years (40 000 days). In this figure, the mean orbit (red dashed line) obtained by our semi-analytical theory is superimposed with the related osculating orbit resulting from the integration of the full differential system. It is worth stressing at this point that the entry-level step size used in the osculating numerical integration is fixed at 200 seconds, whereas we defined a 1 day step size when integrating the averaged system of equations.

It is also worth noting that the short-periodic effects are especially significant on the semi-major axis and to a lesser extent on the eccentricity. Actually, the angular quantities, that is the inclination, the argument of perigee and the longitude of the ascending node are also subject to short-period oscillations but with small amplitudes. In order to give a quantitative estimation of the accuracy of the method, Figure 2.8 shows the difference between both orbits. First, when regarding the semi-major axis, it is clear that the difference is mostly induced by the short-period amplitudes. Second, on the remaining orbital elements, the differences remain small although the chosen time of integration is very sizable. Actually, the computed RMS can really be considered as being very small insofar as the comparison has been made without any preliminary fitting of the mean initial conditions. Moreover, the RMS on both the argument of perigee and longitude of the ascending node are mostly influenced by the singular transformation when projecting the integrated non-singular state vector into Keplerian orbital elements.

We seize the opportunity here to regain the main dynamical properties of high-altitude space debris which will be relevant in our further investigations. These properties will be enhanced by drawing the time evolution of the main orbital elements. For this purpose, Figure 2.9 shows the variation of both the inclination and the eccentricity as well as the associated longitude of the ascending node and the argument of perigee over a period of more than 100 years.

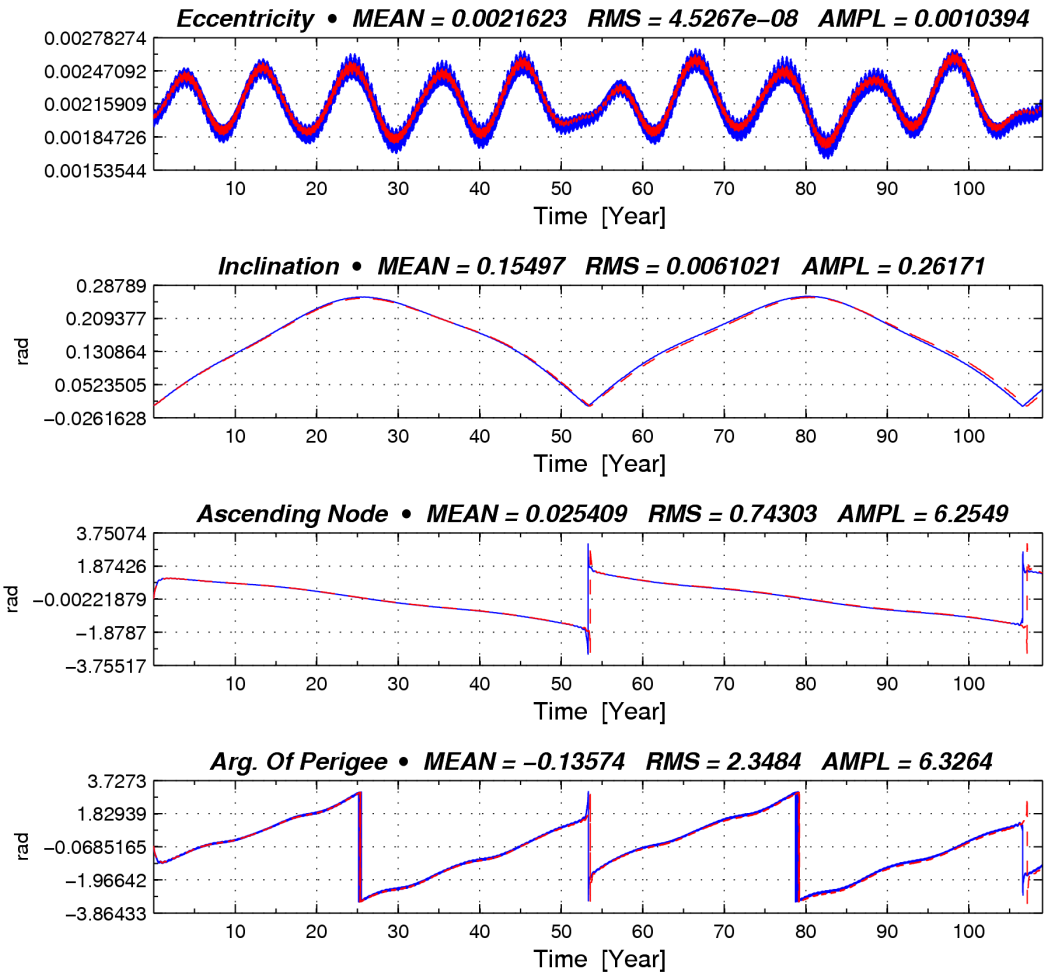

Figure 2.9: Comparison between the osculating orbit (blue solid line) and the mean orbit (red dashed line) for the long-term time evolution of a typical abandoned space debris. The model of forces is the second order harmonic J_2 of the geopotential and the combined Moon and Sun third body attraction. Initial conditions are $a_0 = 42\,164$ km, $e_0 = 0$, $i_0 = 0$ rad, $\Omega_0 = \omega_0 = \lambda_0 = 0$ rad. Initial time at epoch is 25 January 1991.

The perturbations which are considered are the oblateness of the Earth as well as the combined attraction of the Sun and the Moon. As highlighted in the previous chapter, the Earth's oblateness causes the orbital plane of the space debris to regress about the Earth's polar axis. Actually, for low-altitude orbits, the dynamics is mainly affected by the oblateness perturbation, leading essentially to a precession about this axis whereas for high-altitude orbits, such as those of geosynchronous objects, the order of magnitude of the third-body attraction becomes similar to the one related to the Earth's oblateness. Regarding the Sun, the perturbation causes a regression of the orbital plane about the ecliptic pole. Similarly, the Moon's perturbation leads to a regression of the latter plane about an axis normal to the Moon's orbital plane. In practice, we obviously observe a superposition of the three above-mentioned precessional motions. The plane normal to the pole of the resulting motion was called the *Laplace plane*.

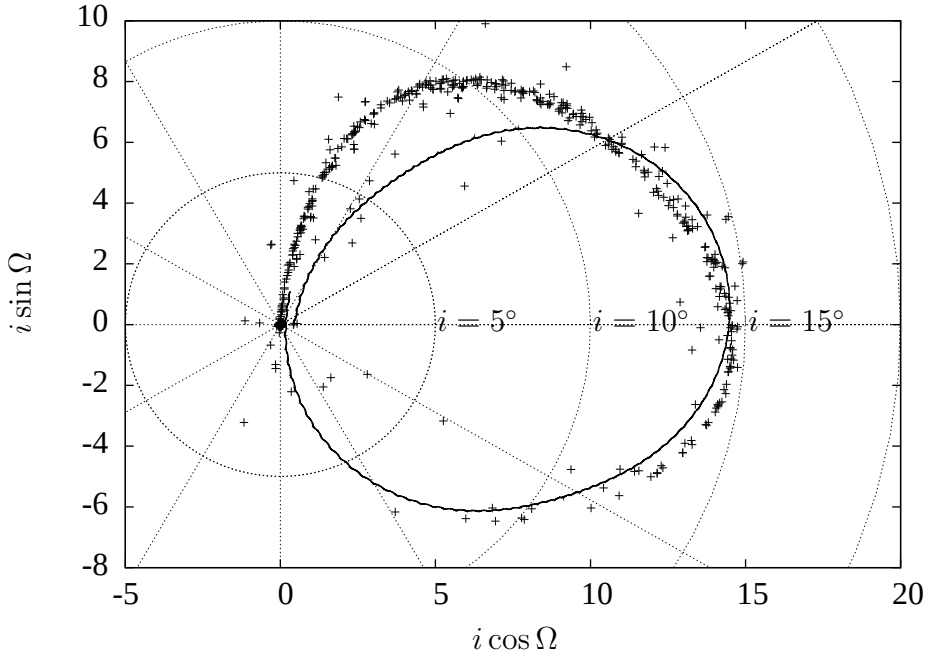

Figure 2.10: Projection of the orbital poles of theoretical geostationary space debris moving in the gravitational field of the Earth. The initial conditions are $a_0 = 42\,164$ km, $e_0 = 4.10^{-2}$, $i_0 = 8.10^{-2}$ rad for the semi-analytical propagation. The model of forces is: oblateness of Earth and the combined attraction of the Sun and the Moon. Time of integration is 54 years. The orbital evolution is superimposed with the current cataloged objects.

The perturbations involve an important long-periodic variation of the inclination with values as high as 15° and a periodicity of about 54 years, which is in agreement with the discussion presented in Section 1.3. Moreover, the argument of perigee also shows a significant precession rate. Let us note that another long period of about 10.5 years, induced by the Sun and the Moon attraction, is also especially apparent on the eccentricity evolution.

In addition, Figure 2.10 shows the projection of the orbital pole of a theoretical space debris placed on a particular geostationary Earth's orbit and propagated by using our semi-analytical theory. The orbital evolution is also superimposed with the current cataloged GEO space debris shown in Figure 1.5 (page 14). The clear differences between the two plots may be explained by the two following statements: firstly, the theoretical object was propagated over a 54 years period whereas the objects cataloged are mostly artificial satellites and space debris which were deployed at most 35 years ago. Secondly, the objects could leave their initial geostationary orbit only after the end of the operational maintenance period, which explains the present distribution of the orbital poles.

2.6 Resonance with the Earth's rotation

The rotation period of an object in Earth's orbit is said to be *in resonance* with the Earth's rotation if it is commensurate with the sidereal rotation period of the Earth. In other words, the object is in resonance if a small integer number q_1 of sidereal days is equal to a small integer number q_2 of revolution periods of the object, that is

$$\frac{P_\oplus}{P_{obj}} = \frac{q_1}{q_2}\,,$$

where $P_\oplus$ is the Earth's rotational period, that is $2\pi/n_\oplus = 1$ day ($n_\oplus = \dot{\theta}$) and P_{obj} is the orbital period of the object taken into account. In those special cases, that is when the orbital period is commensurate with respect to the rotation period of the Earth, the object ground-trace will be a closed or repeating path. The repeating ground-track means the object will periodically encounter the same configuration of gravitational forces. The result is a variation of the motion with very long periods, typically the order of several months, or even years, for deep resonance (Vallado, 2001).

The geopotential resonances exist if at least one of the orbital elements shows a net non-zero accumulated perturbation due to the term considered over one revolution period (Beutler, 2005). These resonances occur for instance when the rate of the Kaula gravitational argument is close to zero, that is

$$\dot{\Theta}_{nmpq}(\dot{\Omega}, \dot{\omega}, \dot{M}, \dot{\theta}) = (n-2p)\,\dot{\omega} + (n-2p+q)\,\dot{M} + m(\dot{\Omega} - \dot{\theta}) \simeq 0\,.$$

Typically, when the condition $q = 0$ is satisfied, that is when considering a zero-order expansion with respect to the eccentricity, we have

$$(n-2p)\,(\dot{\omega} + \dot{M}) \simeq m\,(\dot{\theta} - \dot{\Omega})\,,$$

or similarly

$$\frac{\dot{\omega} + \dot{M}}{\dot{\theta} - \dot{\Omega}} \simeq \frac{q_1}{q_2}\,, \tag{2.20}$$

Such resonances are said to be ***Repeat Ground-Track Resonances***. Typically, the rates of both ω and Ω are small and the condition (2.20) reads

$$\frac{\dot{M}}{\dot{\theta}} \simeq \frac{\dot{\lambda}}{\dot{\theta}} \simeq \frac{q_1}{q_2}\,.$$

When the ratio q_1/q_2 is close to 1, the resonance is clearly associated with the geostationary orbit whereas it is close to 2 for *GPS* satellites.

2.6.1 Resonant Hamiltonian formalism – the resonance angle

In order to describe the motion of a near-geostationary space debris, we take into account the fact that the Earth's sidereal rotation period and the revolution period of the space debris are nearly commensurate. In the case of a purely geostationary space debris, the two frequencies are exactly the same. Therefore, this repeat ground-track resonance will drastically increase the amplitude of the harmonics by producing small divisors in the coefficient of the trigonometric terms.

Let us rewrite the Hamiltonian function of the second order and degree harmonic, denoted by $\mathcal{H}_{J_{22}}$, which can also be expanded in series of non-dimensional Poincaré variables

$$\begin{aligned} \mathcal{H}_{J_{22}} &= 3\,\frac{\mu^4\,R_e^2}{L^6}\left[C_{22}\,(\bar{x}^2-\bar{y}^2)+S_{22}\,(2\bar{x}\bar{y})\right] \\ &= \mathcal{H}_{J_{22}}(X_1,X_2,Y_1,Y_2,\Lambda,\lambda,L,\theta)+\dot{\theta}\,\Lambda\,. \end{aligned}$$

Let us define the so-called ***resonant angle*** σ

$$\sigma = \lambda - \theta\,, \tag{2.21}$$

where λ is the mean longitude defined in Eq. (2.13). In order to keep a canonical set of variables, we use the following symplectic transformation

$$d\sigma\,L' + d\theta'\,\Lambda' = d\lambda\,L + d\theta\,\Lambda\,, \tag{2.22}$$

leading to the new set of canonical variables

$$L' = L, \qquad \theta' = \theta, \qquad \Lambda' = \Lambda + L$$

and the new Hamiltonian formulation including the resonant angle

$$\mathcal{H}_{J_{22}}\,(X_1,Y_1,X_2,Y_2,\sigma,L',\theta)+\dot{\theta}\;(\Lambda'-L')\;. \tag{2.23}$$

Averaging process

Thanks to the introduction of the resonant angle σ, it is now conceivable to average the Hamiltonian after making sure that only the short-periodic terms disappear, that is guaranteeing that long periods associated with commensurate or near-commensurate orbits are preserved. To proceed with this particular averaging process, it is only necessary to average the Hamiltonian disturbing function $\mathcal{H}_{J_{22}}$ over the fast angular variable, namely the sidereal time, since the mean longitude has been replaced by the combination between the resonant angle and the

sidereal time. The averaging process can be formally illustrated by the following relations

$$\begin{array}{c} \mathcal{H}_{J_{22}}\left(X_1, Y_1, X_2, Y_2, L, \Lambda, \theta, \lambda\right) \\ \Big\downarrow \\ \mathcal{H}_{J_{22}}\left(X_1, Y_1, X_2, Y_2, L, \Lambda, \theta, \sigma\right) \\ \Big\downarrow \\ \overline{\mathcal{H}}_{J_{22}}\left(X_1, Y_1, X_2, Y_2, L, \Lambda, -, \sigma\right) , \end{array}$$

Consequently, the differential system of equations related to this new averaged Hamiltonian is given by

$$\begin{aligned} \dot{X}_i &= \frac{1}{L}\frac{\partial \overline{\mathcal{H}}_{J_{22}}}{\partial Y_i}, \qquad \dot{Y}_i = -\frac{1}{L}\frac{\partial \overline{\mathcal{H}}_{J_{22}}}{\partial X_i}, \qquad i = 1, 2 \\ \dot{\sigma} &= \frac{\partial \overline{\mathcal{H}}_{J_{22}}}{\partial L} - \frac{1}{2L}\left[\sum_{i=1}^{2}\frac{\partial \overline{\mathcal{H}}_{J_{22}}}{\partial X_i}X_i + \sum_{i=1}^{2}\frac{\partial \overline{\mathcal{H}}_{J_{22}}}{\partial Y_i}Y_i\right], \qquad \dot{L} = -\frac{\partial \overline{\mathcal{H}}_{J_{22}}}{\partial \sigma}, \end{aligned}$$

which is very similar to Eq. (2.18) except that L is at present conjugated to the resonant angle σ. For the sake of completeness, Table 2.4 gives the number of terms appearing in the disturbing function and Table 2.5 gives the first terms of the expansion. The 4th-order series expansion is given in Appendix G (page 181).

Table 2.4: Number of terms appearing in both the averaged and osculating Hamiltonian series expressed in dimension-free Poincaré variables. The number of osculating terms are inside round brackets.

Perturbation	Number of terms			
n-order expansion $X_1^{i_1}Y_1^{i_2}X_2^{i_3}Y_2^{i_4}$ with $i_1+i_2+i_3+i_4 \leq n$	$n=2$	$n=4$	$n=6$	$n=8$
Resonant disturbing function				
$\mathcal{H}_{J_{22}} = \mathcal{H}_{C_{22}} + \mathcal{H}_{S_{22}}$	10 (94)	40 (468)	104 (1392)	206 (3178)

2.6.2 Long-term effects induced by the Earth's rotation – simplified analytical model

Subsequently, we will confine ourselves to the discussion of circular orbits in the equatorial plane. Within these assumptions and in order to outline the main features of the 1:1 resonance, we consider the following "minimum" resonant Hamiltonian $\mathcal{H}$ including the two body problem as well as the second degree and order harmonic of the geopotential. From Eq. (2.23), we have

$$\mathcal{H}(L, \sigma, \Lambda) = -\frac{\mu^2}{2L^2} + \dot{\theta}(\Lambda - L) + \frac{1}{L^6}\left[\alpha_1 \cos 2\sigma + \alpha_2 \sin 2\sigma\right],$$

Table 2.5: First terms (2-order expansion) of the averaged Hamiltonian series $\overline{\mathcal{H}}_{J_{22}}$ associated with the second degree and order harmonic. Let us notice that for some convenient reasons, we use the geostationary semi-major axis (42 164 km) as the distance unit. Moreover, the gravitational constant μ is set to unity.

σ	θ	X_1	Y_1	X_2	Y_2	L	$X_{\leftmoon}$	$Y_{\leftmoon}$	$Z_{\leftmoon}$	$r_{\leftmoon}$	$X_{\odot}$	$Y_{\odot}$	$Z_{\odot}$	$r_{\odot}$	Coefficient
cos	(2	0)	(0	0	0	0	-6	0	0	0	0	0	0	0	0) 0.1077767255434384D-06
cos	(2	0)	(0	0	0	0	-6	0	0	0	0	0	0	0	0) 0.1080907167254767D-06
cos	(2	0)	(0	0	0	2	-6	0	0	0	0	0	0	0	0) -0.5404535836273835D-07
cos	(2	0)	(0	0	2	0	-6	0	0	0	0	0	0	0	0) -0.5404535836273835D-07
cos	(2	0)	(0	2	0	0	-6	0	0	0	0	0	0	0	0) -0.2702267918136917D-06
cos	(2	0)	(2	0	0	0	-6	0	0	0	0	0	0	0	0) -0.2702267918136917D-06
sin	(2	0)	(0	0	0	0	-6	0	0	0	0	0	0	0	0) -0.6204881922826443D-07
sin	(2	0)	(0	0	0	2	-6	0	0	0	0	0	0	0	0) 0.3102440961413221D-07
sin	(2	0)	(0	0	2	0	-6	0	0	0	0	0	0	0	0) 0.3102440961413221D-07
sin	(2	0)	(0	2	0	0	-6	0	0	0	0	0	0	0	0) 0.1551220480706611D-06
sin	(2	0)	(2	0	0	0	-6	0	0	0	0	0	0	0	0) 0.1551220480706611D-06

where α_1 and α_2 are the numerical values of the first terms appearing in the Hamiltonian series as shown in Table 2.5, that is

$$\alpha_1 \simeq 0.1077 \times 10^{-6}, \qquad \alpha_2 \simeq -0.6204 \times 10^{-7}\,.$$

Two stable equilibria $(\sigma_{11}^*, L_{11}^*)$, $(\sigma_{12}^*, L_{12}^*)$ as well as two unstable equilibria $(\sigma_{21}^*, L_{21}^*)$, $(\sigma_{22}^*, L_{22}^*)$ are found to be solutions of

$$\frac{\partial \mathcal{H}}{\partial L} = \frac{\partial \mathcal{H}}{\partial \sigma} = 0\,,$$

where

$$\begin{aligned} \sigma_{11}^* &= \lambda^* & \sigma_{12}^* &= \lambda^* + \pi \\ \sigma_{21}^* &= \lambda^* + \frac{\pi}{2} & \sigma_{22}^* &= \lambda^* + \frac{3\pi}{2}\,, \end{aligned}$$

as well as

$$L_{11}^* = L_{12}^* = 0.99999971, \qquad L_{21}^* = L_{22}^* = 1.00000029,$$

where the distance unit has been set to 42 164 km. The angular value λ^* is the first quadrant solution of

$$\tan 2\lambda^* = \frac{S_{22}}{C_{22}} = \frac{\alpha_2}{\alpha_1}\,,$$

that is $\lambda^* \simeq 75.07°$.

We can understand the existence of these four equilibrium points through physical arguments. First, let us consider the peculiar case of a perfect geostationary object which means that its orbital period is exactly one sidereal day. Second, let us recognize that within these assumptions, the Earth's gravity field is only longitude-dependent when considering only the second degree and order harmonics which correspond physically to the ellipticity of the equa-

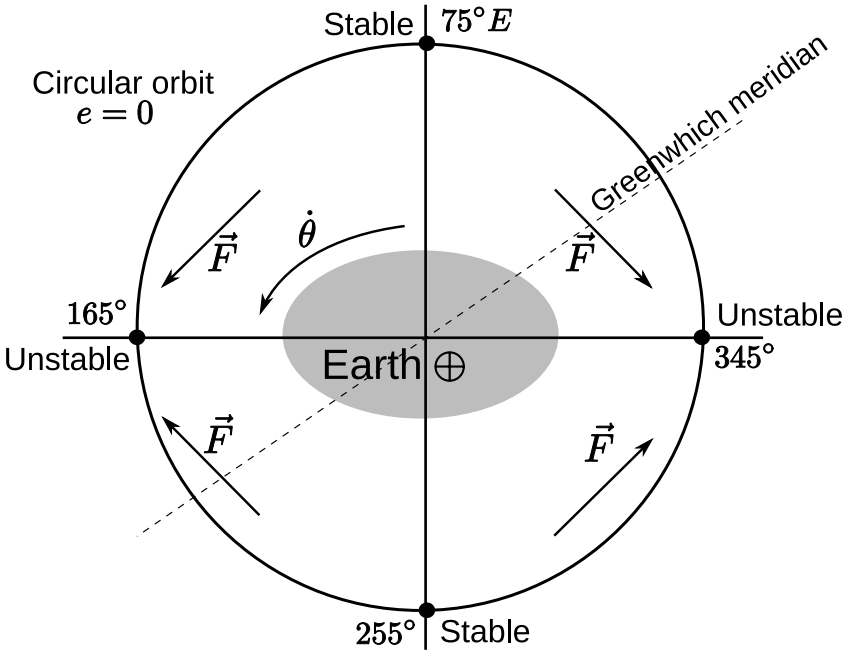

Figure 2.11: Polar view of an equatorial section of the Earth. Schematic illustration of both the stable and unstable equilibrium points.

torial radius of the Earth (Figure 2.11). As quoted by Vallado (2001): "*In a reference frame rotating with the Earth, it is clear that when the object is on the extension of either axis of the equatorial ellipse, the gravitational force is purely radial. These must then be equilibrium positions or stationary points in the rotating reference frame. On the other hand, when the object is off-axis, there will be a net tangential force,* $\boldsymbol{F}$*, toward the nearest major axis. On first examination, we might expect the satellite to accelerate in the direction of the* $\boldsymbol{F}$*. However, the drag paradox dictates just the opposite, and the satellite will accelerate toward the nearest equilibrium position on the minor axis. Because it acquires momentum, the satellite will actually drift past* S*, and the direction of* $\boldsymbol{F}$ *will then be reversed. The drift will gradually be reversed. Hence, points* S *on the minor axis are positions of stable equilibrium, whereas* U *are unstable positions*."

To investigate analytically this two degree of freedom problem, the Hamiltonian is first reduced to a quadratic form in a neighborhood of a stable equilibrium point. After diagonalizing the Hessian matrix, we will be able to verify that the problem remains decoupled and that the proper frequency is also computed from the local analysis.

Let us introduce the resonant Cartesian coordinates $(x = \sqrt{2L}\cos\sigma, y = \sqrt{2L}\sin\sigma)$ and at any equilibrium $(x^* = \sqrt{2L^*}\cos\sigma^*, y^* = \sqrt{2L^*}\sin\sigma^*)$. Developing the Hamiltonian function in Taylor series around one of the stable equilibria (x^*, y^*), up to the second order,

we find (having dropped the constant additive terms)

$$\mathcal{H}^*(X, Y, \Lambda) = \dot{\theta}\,\Lambda + \frac{1}{2}(aX^2 + 2bXY + cY^2) + \cdots ,$$

where X and Y are defined as

$$X = (x - x^*), \qquad Y = (y - y^*)\,.$$

The values a, b and c stand for the second order derivatives

$$a = \left.\frac{\partial^2 \mathcal{H}}{\partial x^2}\right|_{(L^*,\sigma^*)}, \qquad b = \left.\frac{\partial^2 \mathcal{H}}{\partial x \partial y}\right|_{(L^*,\sigma^*)}, \qquad c = \left.\frac{\partial^2 \mathcal{H}}{\partial y^2}\right|_{(L^*,\sigma^*)},$$

where (L^*, σ^*) are the values of (L, σ) evaluated at the first stable equilibrium. It is thus possible to introduce *action-angle* variables. This can best be performed using the so-called *reducing transformation* in order to eliminate the mixed terms in such a quadratic Hamiltonian (for further details concerning contexts where similar transformations are useful, we refer to Henrard 1988). Here, the transformation is given by

$$X = \; p\,\cos\Psi + q\,\sin\Psi \quad \text{ and } \quad Y = -p\,\sin\Psi + q\,\cos\Psi\,,$$

that is a Ψ angle rotation, solution of

$$(a - c)\sin 2\Psi + 2b\cos 2\Psi = 0\,.$$

As a consequence, we find the new Hamiltonian formulation

$$\mathcal{H}^*(p, q, \Lambda) = \dot{\theta}\,\Lambda + \frac{1}{2}\left[A\,p^2 + C\,q^2\right] ,$$

with

$$A = a\cos 2\Psi - 2b\sin\Psi\cos\Psi + c\sin 2\Psi$$

and

$$C = a\sin 2\Psi + 2b\sin\Psi\cos\Psi + c\cos 2\Psi.$$

A last scaling canonical transformation of the form $p = \alpha\,p'$ and $q = \frac{1}{\alpha}\,q'$ obtained by solving the following equation $A\,\alpha^2 = \dfrac{C}{\alpha^2}$, allows us to write the new Hamiltonian as

$$\mathcal{H}(J, \phi, \Lambda) = \dot{\theta}\,\Lambda + \sqrt{AC}\,J\,,$$

where (J, ϕ) are the corresponding *action-angle* variables

$$p' = \sqrt{2J}\cos\phi\,, \quad q' = \sqrt{2J}\cos\phi\,.$$

Subsequently, we find two frequencies, namely the frequency of the sidereal time and the so-called ***resonant fundamental frequency*** ν_f at equilibrium.

$$\dot{\theta} = \frac{\partial \mathcal{H}}{\partial \Lambda}\,, \qquad \nu_f = \frac{\partial \mathcal{H}}{\partial J} = \sqrt{AC}\,.$$

Numerical computations lead to the following value of the fundamental frequency

$$\nu_f = 7.674 \times 10^{-3}/[\text{days}]\,,$$

that is a period of 818.7 days.

By a similar approach, we can easily estimate the width of the resonant zone; we take the Hamiltonian level curve corresponding to one of the unstable equilibria L_u and σ_u

$$\mathcal{H}(L_u, \sigma_u, \Lambda) = -\frac{\mu^2}{2L^2} + \dot{\theta}(\Lambda - L) + \frac{1}{L^6}\left[\alpha_1 \cos 2\sigma + \alpha_2 \sin 2\sigma\right]\,,$$

and we find the maxima and minima of this "banana curve", corresponding to the stable equilibria; by a quadratic approximation about L_u, we obtain the width of the banana at the stable points, i.e. the width Δ of the resonant zone. It can be approached by

$$\Delta = \sqrt{\frac{\gamma^2 + 8\delta\beta}{\beta^2}}\,, \quad \delta = \frac{\alpha_1}{L_u^6 \cos 2\sigma_u}\,, \quad \beta = -\frac{3}{2}\frac{\mu^2}{L_u^4}\,, \quad \gamma = \frac{\mu^2}{L_u^3} - \dot{\theta}\,. \tag{2.24}$$

The numerical value of the width of the resonance zone is of the order of 69 km.

2.6.3 Resonant effects – numerical investigations

Let us show how the semi-analytical method can highlight the main features of the debris population in the geostationary region. In this section, we present the resonant motion and its main characteristics: equilibria, stability, fundamental frequencies and width of the resonant area, by comparison with our basic simplified model defined in Subsection 2.6.2.

Figure 2.12 shows the mean semi-major axis and the resonant angle (that is the mean longitude in a frame rotating with the Earth) for a set of three geosynchronous space debris propagated over a period of more than 8 years where the only perturbation taken into account is the second degree and order tesseral (sectorial) harmonic. The mean semi-major axis as well as the resonant angle are subject to very-long period oscillations. Near the first stable equilibrium, namely $\lambda = \lambda^*$, we observe that the period of oscillation is about 800 days, value very close to our formal calculation of 818.7 days.

Further, the periods increase as the deviance $\Delta\lambda = |\lambda_0 - \lambda^*|$ increases with respect to the stable equilibrium point. As a consequence, an arbitrary space debris orbiting the geosyn-

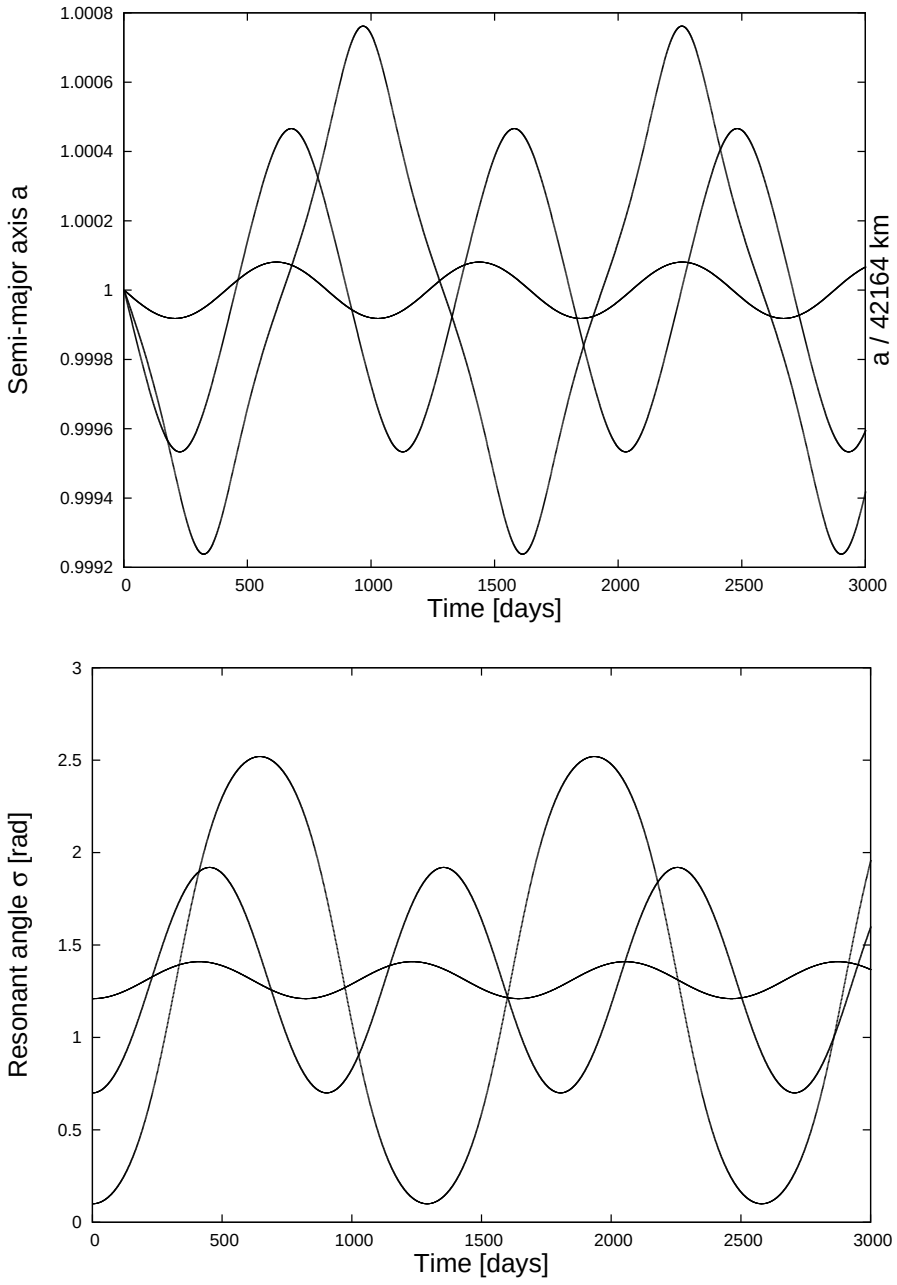

Figure 2.12: Semi-major axis a [top] and resonant angle $\sigma = \lambda - \theta$ [bottom] of several geosynchronous space debris with initial conditions $a_0 = 42\,164$ km, $e_0 = 0$, $i_0 = 0$ rad, $\Omega_0 = \omega_0 = 0$ rad, the initial longitude of which are $\lambda_0 = 5°, 35°, 75°$.

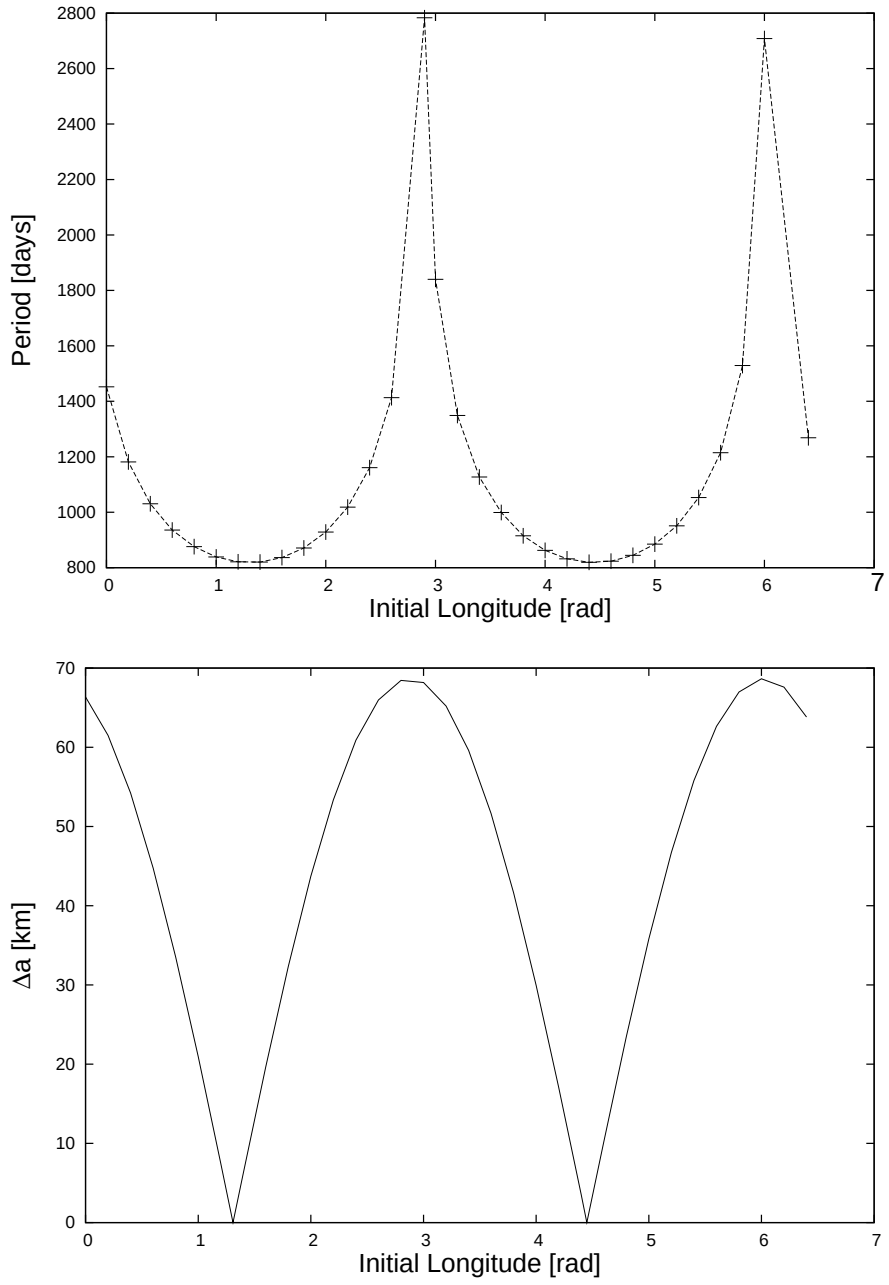

Figure 2.13: Libration periods [top] and width of resonance [bottom] related to 32 virtual space debris the initial longitude λ_0 of which varied from 0 to 2π. The solid curves are obtained by interpolation.

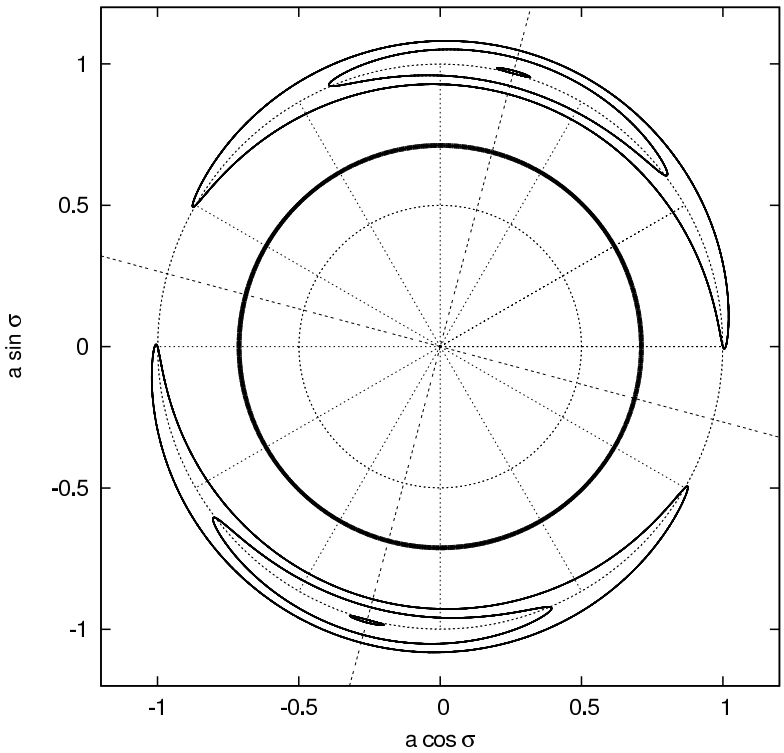

Figure 2.14: Motion of a geostationary space debris near stable equilibria in a rotating reference frame as seen from the pole. The variations on the mean semi-major axis have been amplified for the illustration by a factor 100.

chronous Earth's orbit may considerably librate except if it is exactly located at the theoretical stable equilibrium point. As in the case of the first model of resonance (see for instance Breiter, 2003; Henrard and Lemaître, 1983), the amplitudes of the perturbations affecting the mean longitudes are observed to be $2\,\Delta\lambda$. Moreover, the perturbations seem to induce relevant variations on the mean semi-major axis. Figure 2.13 shows the variations of the periods as well as the mean variations observed on the semi-major axis as a function of the initial mean longitude. The two stable equilibrium points as well as the two unstable ones appear clearly. Near the first stable equilibrium, the period converges to the so-called fundamental period. As a consequence, the variation on the mean semi-major axis converges to zero. On the contrary, the periods diverge to infinity near the unstable equilibria and the variations on the mean semi-major axis reach their maximum that is almost 70 km in the worst case, value in agreement with our 69 km obtained analytically in Equation (2.24). These results seem to be in agreements with Beutler (2005) where the libration period is found to be

$$P = \frac{2\pi}{\nu_f}\widetilde{K}(k),$$

with $k = \sin 2\,\Delta\lambda$, $\Delta\lambda$ is the mean longitude deviance with respect to λ^* and $\widetilde{K}(k)$ is the normalized elliptic function of the first kind in k.

We also represent the phase space $(a\cos\sigma,\ a\sin\sigma)$; Figure 2.14 shows clearly the existence of three distinct regions: the internal region corresponds to orbital motion the period of which is less than 24 hours. In this case, the longitude of the space debris is increasing; that is, the space debris seems to orbit eastward around the Earth. The second region is characterized by mean motions synchronized with the Earth's rotation, we deal with the so-called geosynchronous orbits. When the object is near one of the two stable equilibria, the space debris oscillates. As shown previously, this oscillation consists of a long periodic libration around the equilibrium. The last region is external, and the motion does not show anymore significant long-periodic variations.

Part II

High area-to-mass ratios GEO space debris

Semi-analytical investigations

Chapter 3

Analytical and semi-analytical investigations of geosynchronous space debris with high area-to-mass ratios

"Houston, we have a trash problem !"

By Sean Cooper, Wired Magazine, Issue 15.05

– The results of this chapter have been previously published in Valk et al. (2007b) –

The recent observational discoveries in high altitude Earth's orbit (for the most part in geosynchronous orbits), stimulated the revisit of direct solar radiation pressure models. In particular, recent numerical investigations were performed in order to assess the time evolution of objects subject to such extreme situations (Anselmo and Pardini, 2005; Liou and Weaver, 2004; McKee, 2004). In this framework, short-term as well as long-term evolutions of geosynchronous space debris were studied in detail. Liou and Weaver (2005) also proposed the source of such high area-to-mass ratios, namely thermal blankets or multi-layer insulation (MLI), which are made from Mylar®, Kapton® or Nomex®.

The topic specifically addressed in this chapter is the development of an accurate semi-analytical theory. This theory provides a Hamiltonian formulation for GEO space debris subjected to direct solar radiation pressure. Similarly to the semi-analytical theory developed in Chapter 2, this theory is still based on the concept of averaged equations of motion over the short periods and is of order 1 regarding the averaging process. The transformed differential system of equations is then numerically integrated over the long periods.

First, for the sake of clarity and completeness, we present both the description and the modeling of direct radiation pressure in Section 3.1.

Sections 3.2 and 3.3 describe the osculating equations of motion associated with the direct solar radiation pressure followed by the non-relativistic assumption leading to our Hamiltonian

formulation. This formulation is based on the analytical expansion of the disturbing function using canonical and non-singular variables with respect to an expansion in powers of the eccentricity and of the inclination truncated at an arbitrary high order.

In addition, in order to underline the main effects induced by the direct solar radiation pressure, Section 3.4 describes simplified analytical models expressed in non-singular elements. The aim of this section elaborates and is an improvement of the analytical model presented by Chao and Baker (1983) and Chao (2006), in order to obtain not only the averaged equations in eccentricity and longitude of perigee, but also the coupling equations between eccentricity and inclination as well.

Finally, Section 3.5 consists of a comparison of various assumptions in the modeling of direct solar radiation pressure and emphasize the importance of adopting an accurate model of radiation pressure when dealing with high area-to-mass ratios. Moreover, this section claims to be the counterpart of previously published results (Anselmo and Pardini, 2005; Schildknecht et al., 2007).

3.1 The direct solar radiation pressure

By direct solar radiation pressure, we mean the net acceleration resulting from the interaction of the sunlight with each elementary surface of the space debris. The Quantum Mechanics says that each photon of frequency ν and wavelength $\lambda = c/\nu$ carries the energy

$$E = h\,\nu\,,$$

where $h = 6.62 \times 10^{-34}$ J s is the Planck's constant and c is the speed of light in vacuum. The photons carry not only energy but also linear momentum which is given by

$$\boldsymbol{p} = -\frac{h\,\nu}{c}\,\boldsymbol{s},$$

where $\boldsymbol{s}$ is the unit vector pointing toward the Sun. The momentum transferred per time unit onto a unit surface in a radiation field is called *radiation pressure*. As a consequence, the radiation pressure is a vectorial quantity (Beutler, 2005).

To model what happens of the linear momentum carried by the radiation impacting the surface, we can use a combination of three standard physical models, namely, the **absorption**, the **reflection** and the **diffusion**. For each elementary surface dS of the space debris, one can define the coefficients α, ρ and δ, that is the fractions of incident sunlight which are absorbed, reflected and diffused, respectively. These coefficients are related to the following equation

$$\alpha + \rho + \delta = 1\,.$$

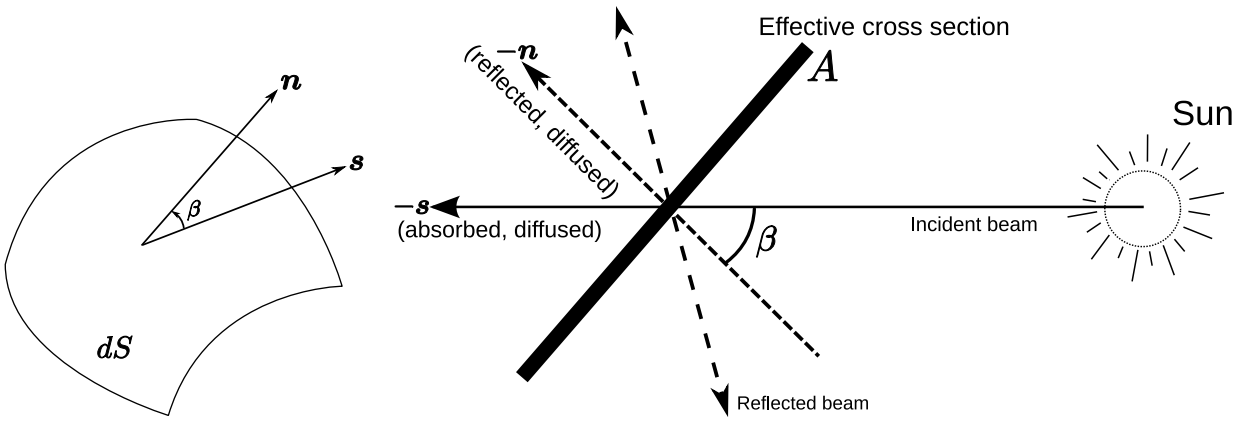

Figure 3.1: Elementary surface dS, and the angle β between the normal vector $\boldsymbol{n}$ and the direction of the Sun $\boldsymbol{s}$ [left]. Geometry of the incident, reflected, diffused and absorbed radiation [right].

To simplify the investigations of radiation pressure, it is convenient to consider the following assumptions

- the absorbed light is not re-emitted (black body);
- for a given direction, the intensity of diffused light is proportional to the cosine of the angle β from the normal to the surface dS (Lambert law) (Figure 3.1, left);
- the reflection is perfectly specular, which means that the photons bounce on a smooth surface following the laws of mirror reflection;
- the elementary surface dS behaves like a linear combination of three physical models: that is a combination of a black body, a perfect mirror and a Lambert diffuser. As a consequence, the three coefficients completely specify the optical properties of the surface taken into consideration (Figure 3.1, right).

Making use of these assumptions, the force induced by the radiation pressure is directed in part along the normal $\boldsymbol{n}$ to the surface and in part along the direction of the Sun $\boldsymbol{s}$. This force can be easily obtained by adding together the elementary forces $d\boldsymbol{F}_\alpha$, $d\boldsymbol{F}_\rho$ and $d\boldsymbol{F}_\delta$ induced by the absorbed, the reflected and the diffused sunlight, respectively.

The elementary force acting on a surface element dS due to the absorption is naturally oriented along the $-\boldsymbol{s}$ direction and is proportional to the cross section $dS|\cos\beta|$, that is

$$d\boldsymbol{F}_\alpha = -\frac{\Phi_\odot}{c}\,\alpha\,\cos\beta\,\boldsymbol{s}\,dS,$$

where $\Phi_\odot$ is the energy flux, that is the flux per unit of area. Let us also remark that the energy flux $\Phi_\odot$ is also called the *solar-radiation constant*, giving the energy flowing through

this surface per time unit at the distance of 1 AU. The value of this constant is

$$\Phi_\odot = 1368 \ \mathrm{Watt/m^2} \, .$$

Concerning the elementary force resulting from the reflection of the sunlight, we know that it will be directed along the $-\boldsymbol{n}$ direction, with a force directly proportional to the cross section. Moreover, the fraction of photons corresponding to the reflection coefficient transfers to the spacecraft, not only the momentum they had upon arrival, but also the recoil momentum (Milani et al., 1987). Therefore, we have

$$d\boldsymbol{F}_\rho = -\frac{\Phi_\odot}{c} \, 2 \, \rho \cos\beta \, dS \, |\cos\beta| \, \boldsymbol{n}.$$

Finally, regarding the fraction of photons corresponding to the diffusion coefficient, we have

$$d\boldsymbol{F}_\delta = -\frac{\Phi_\odot}{c} \, \delta \, \cos\beta \, dS \, \left[\boldsymbol{s} + \frac{2}{3} \boldsymbol{n} \right]$$

where the $\boldsymbol{s}$-component is first related to the absorbed part of the incident light and where the $\boldsymbol{n}$-component is associated with the re-emitted part.

As a final result, the resultant of the elementary forces is given by

$$\boldsymbol{F}_{rp} = -\frac{\Phi_\odot}{c} \int_S \left[(1-\rho) \, \cos\beta \, \boldsymbol{s} + \left(\frac{2}{3}\delta + 2\rho \, \cos\beta \right) \, \cos\beta \, \boldsymbol{n} \right] \, dS \, , \tag{3.1}$$

where S is the portion of the space debris illuminated by the Sun.

In practice, the evaluation of the integral (3.1) is rather complicated. Actually, determining the coefficients properly is extremely difficult. The three coefficients change over time and are virtually impossible to predict. This is especially true for objects with complex shape, eventually made of various materials, that enter and exit eclipse regions, and possibly have a constantly changing orientation (Vallado, 2001). Moreover, it is not guaranteed that the resultant force is applied on the center of mass of the space debris, possibly leading to variations on the attitude. However, as reported by Milani et al. (1987), if the object subjected to direct radiation pressure has some simple shapes, the integral of Eq. (3.1) can be computed analytically. In such a case, the force induced by the radiation pressure can be directly expressed as

$$\boldsymbol{F}_{rp} = -\frac{\Phi_\odot \, A}{c} \, \boldsymbol{s} \, , \tag{3.2}$$

where A is the **effective cross section**. For instance, considering a flat panel oriented orthogonal to the Sun direction vector $\boldsymbol{s}$, the effective cross section is simply related to the area of the panel. Otherwise, in the specific case of a spherical object the radius of which is defined by R,

the effective cross section can be computed as

$$A = \left(\alpha + \rho + \frac{13}{9}\delta\right) \pi R^2 \,, \tag{3.3}$$

where the coefficients defining the optical properties of the objects are assumed to be constant.

Let us also remark that in the literature, the name "reflectivity" coefficient is usually used to represent the single coefficient related to the optical properties of the surface even though it is not only related to the reflectivity properties, as it is shown in Eq. (3.3). Although this misuse is misleading, we will adopt this generic name. This single scalar coefficient will be denoted by C_r further on in this manuscript.

3.2 Osculating equations of motion

In keeping with Eq. (3.2), the acceleration due to the direct radiation pressure can thus be written in the form

$$\mathbf{a_{rp}} = C_r \, P_r \left[\frac{a_\odot}{\|\mathbf{r} - \mathbf{r}_\odot\|}\right]^2 \frac{A}{m} \frac{\mathbf{r} - \mathbf{r}_\odot}{\|\mathbf{r} - \mathbf{r}_\odot\|} \,, \tag{3.4}$$

where C_r is the above-mentioned dimension-free "reflectivity" coefficient (fixed to 1 further on in this manuscript), which depends on the optical properties of the space debris surface; $P_r = \Phi_\odot / c = 4.56 \times 10^{-6}$ N/m^2 is the radiation pressure for an object located at a distance of 1 AU; $a_\odot$ is a constant parameter equal to the mean distance between the Sun and the Earth, that is $a_\odot = 1$ AU; $\mathbf{r}$ is the geocentric position of the space debris and $\mathbf{r}_\odot$ is the geocentric position of the Sun. Finally, m is the mass of the object subject to radiation pressure. Furthermore, the variation of the distance between the Sun and the Earth is implicitly taken into account in Eq. (3.4) since the incoming flux will change because of the eccentricity of the Earth's orbit around the Sun.

Without any assumption, the radiation pressure should be considered as a dissipative force. Therefore, the equations of motion taking into account the effect of the radiation pressure are traditionally written using the Gaussian perturbation equations (see Appendix E.1, page 173). As a consequence, the acceleration is expressed along the radial $\mathbf{S}$, along-track $\mathbf{T}$ (perpendicular to position vector $\mathbf{r}$ in the orbital plane) and out-of-plane $\mathbf{W}$ (normal to the orbital plane) directions. Under the following assumptions

1. The Sun–space debris vector is considered to be equal to the Sun–Earth vector, that is $\mathbf{r} - \mathbf{r}_\odot = -\mathbf{r}_\odot$,
2. The albedo radiation pressure of the Earth is ignored,
3. The Earth's shadowing effects are not taken into account,
4. The light aberration is not taken into account (relativistic effect),

5. The YORP (Yarkovsky-O'Keefe-Radzievskii-Paddack) thermal effect is not taken into account,

6. The radiation pressure acceleration, defined in Eq. (3.4), assumes implicitly a spherical object, with optical properties defined by a single scalar C_r,

the Gaussian equations for the variations of the osculating orbital elements subjected to direct radiation pressure acting along the Sun–Earth direction vector are (Appendix E.1, page 173)

$$\begin{aligned}
\frac{\mathrm{d}a}{\mathrm{d}t} &= \frac{2\,\chi}{n\,\eta}\left[e\,\mathbf{S}(f)\,\sin f + \mathbf{T}(f)\frac{p}{r}\right]\,,\\
\frac{\mathrm{d}e}{\mathrm{d}t} &= \frac{\eta\,\chi}{n\,a}\left\{\mathbf{S}(f)\,\sin f + \mathbf{T}(f)\left[\cos f + \frac{1}{e}\left(1-\frac{r}{a}\right)\right]\right\}\,,\\
\frac{\mathrm{d}i}{\mathrm{d}t} &= \frac{\chi}{n\,a\,\eta}\,\mathbf{W}\frac{r}{a}\,\cos(\omega+f)\,,\\
\frac{\mathrm{d}\omega}{\mathrm{d}t} &= -\cos i\frac{d\Omega}{dt} + \frac{\chi\,\eta}{n\,a\,e}\left[-\mathbf{S}(f)\,\cos f + \mathbf{T}(f)\left(1+\frac{r}{p}\right)\,\sin f\right]\,, \qquad (3.5)\\
\frac{\mathrm{d}\Omega}{\mathrm{d}t} &= \frac{\chi}{n\,a\,\eta\sin i}\,\mathbf{W}\frac{r}{a}\,\sin(\omega+f)\,,\\
\frac{\mathrm{d}M}{\mathrm{d}t} &= n - \frac{2\chi}{n\,a}\,\mathbf{S}(f)\frac{r}{a} - \eta\left(\frac{\mathrm{d}\omega}{\mathrm{d}t} + \cos i\frac{\mathrm{d}\Omega}{\mathrm{d}t}\right)\,.
\end{aligned}$$

In Eqs. (3.5), $\chi = C_r\,P_r\,A/m\,\left(a_\odot/r_\odot\right)^2$; $\eta = \sqrt{1-e^2}$; f is the true anomaly; n the orbital mean motion and $p = a\,(1-e^2)$ is the *semi-latus rectum*. From Kozai (1961) and later Aksnes (1976), we have

$$\begin{aligned}
\left\{\begin{array}{c} S(f) \\ T(f) \end{array}\right\} &= -\cos^2\frac{i}{2}\cos^2\frac{\epsilon}{2}\left\{\begin{array}{c}\cos\\ \sin\end{array}\right\}(\lambda_\odot - \omega - \Omega - f)\\
&\quad -\sin^2\frac{i}{2}\sin^2\frac{\epsilon}{2}\left\{\begin{array}{c}\cos\\ \sin\end{array}\right\}(\lambda_\odot - \omega + \Omega + f)\\
&\quad -\frac{1}{2}\sin i\sin\epsilon\left[\left\{\begin{array}{c}\cos\\ \sin\end{array}\right\}(\lambda_\odot - \omega - f) - \left\{\begin{array}{c}\cos\\ \sin\end{array}\right\}(-\lambda_\odot - \omega - f)\right]\\
&\quad -\sin^2\frac{i}{2}\cos^2\frac{\epsilon}{2}\left\{\begin{array}{c}\cos\\ \sin\end{array}\right\}(-\lambda_\odot - \omega + \Omega - f) \qquad (3.6)\\
&\quad -\cos^2\frac{i}{2}\sin^2\frac{\epsilon}{2}\left\{\begin{array}{c}\cos\\ \sin\end{array}\right\}(-\lambda_\odot - \omega - \Omega - f),\\
W &= \sin i\cos^2\frac{\epsilon}{2}\sin(\lambda_\odot - \Omega)\\
&\quad -\sin i\sin^2\frac{\epsilon}{2}\sin(\lambda_\odot + \Omega) - \cos i\sin\epsilon\sin\lambda_\odot,
\end{aligned}$$

where ϵ is the obliquity of the Earth with respect to the ecliptic and $\lambda_\odot$ is the ecliptic longitude of the Sun.

3.3 Extension of the semi-analytical theory for direct radiation pressure

Let us remark that under the previously defined assumptions, except for the first one which is not a necessary condition, the direct radiation pressure defined in Eq. (3.4) is conservative and therefore does not induce any long-term and secular variations of the semi-major axis (Anselmo et al., 1983; Milani et al., 1987). As a consequence, the direct radiation pressure force may be expressed as the gradient of the following expanded potential (let us note the similarity with Eq. 2.11 on page 29)

$$\mathcal{H}_{rp} = C_r\, P_r\, \frac{A}{m}\, \frac{a_\odot^2}{r_\odot} \sum_{n=0}^{n_{max}} \left(\frac{r}{r_\odot}\right)^n \mathcal{P}_n(\cos\psi)\,, \tag{3.7}$$

where ψ and $\mathcal{P}_n$ are still the geocentric angle between the Sun and the space debris, and the Legendre polynomial of degree n, respectively. In keeping with the expansion of the third-body disturbing function in universal elements (see Section 2.3, page 32), that is using an expansion in powers of the eccentricity and of the inclination, performed typically up to order 10 and followed by convenient substitutions, the potential formulation of Eq. (3.7) may then be expressed in terms of the dimension-free and non-singular variables

$$\mathcal{H}_{rp} = \sum_{n=0}^{n_{max}} \mathcal{R}_n = \sum_{n=0}^{n_{max}} \frac{L^{2n}}{r_\odot^{n+1}} \sum_{j=0}^{N_n} \mathcal{A}_j^n(X_1, Y_1, X_2, Y_2, X_\odot, Y_\odot, Z_\odot)\, \mathcal{B}_j^n(\lambda)\,. \tag{3.8}$$

In Eq. (3.8), the $\mathcal{B}_j^n$ still denote trigonometric functions with respect to the mean longitude λ. The $\mathcal{A}_j^n$ are polynomials in the rectangular coordinates of the Sun as well as the dimension-free *Poincaré variables* which are recalled for the sake of clarity (see Eqs. 2.17, page 40)

$$\begin{aligned} X_1 &= \sqrt{\frac{2P}{L}}\,\sin p, \quad & Y_1 &= \sqrt{\frac{2P}{L}}\,\cos p\,, \\ X_2 &= \sqrt{\frac{2Q}{L}}\,\sin q, \quad & Y_2 &= \sqrt{\frac{2Q}{L}}\,\cos q\,. \end{aligned}$$

For similar developments and further details, we refer to Chapter 2, where the method for the expansion of the geopotential of the Earth and the expansion of the luni-solar perturbations in non-dimensional, non-singular and rectangular variables is presented with its effective implementation in computer algebra. In Eq. (3.8), N_n denotes the number of terms in the n-degree potential functions $\mathcal{R}_n$; n_{max} is the upper limit of the expansion in Legendre polynomials. Let us remark that the potential expansion of Eq. (3.7) restricted to $n_{max} = 1$ corresponds to the case where the Sun–space debris direction is replaced by the direction pointing from the Sun to the Earth, that is $\mathbf{r} - \mathbf{r}_\odot = -\mathbf{r}_\odot$, as it is the case in the Kozai's formulation of Eq. (3.6).

In the framework of a semi-analytical theory and in the same way as described in Chapter 2, the non-singular expanded disturbing function (3.8) can then be subsequently averaged over the

short periods (w.r.t. the mean longitude) in order to derive the so-called averaged differential system of equations. This transformed system of equations is written similarly to the quasi-Hamiltonian system of equations derived in Eq. (2.19, page 44).

3.4 Simplified analytical investigations

As shown in Eq. (3.4), the acceleration induced by the direct solar radiation pressure increases linearly with respect to the area-to-mass ratio of the space debris. As an illustration and for the sake of comparison with Figure 1.4 (page 13), the order of magnitude of the perturbations is again represented in Figure 3.2. Aside from the forces which were represented in Figure 1.4, we also represent the order of magnitude of the direct solar radiation pressure acceleration for various area-to-mass ratios. In a first approximation of Eq. (3.4), we see clearly that the radiation pressure acceleration does not depend on the altitude of the space debris (Milani et al., 1987; Montenbruck and Gill, 2000). Furthermore, for small area-to-mass ratios, namely $0.01\ \mathrm{m}^2/\mathrm{kg}$, the acceleration is several orders of magnitude smaller than the acceleration induced by the second zonal harmonic J_2 of the geopotential. Near the particular value of $A/m \simeq 1.63\ \mathrm{m}^2/\mathrm{kg}$, the solar radiation pressure equals the acceleration from the Earth's dominant zonal gravity term J_2 for an object located at a GEO altitude. Finally, the solar radiation pressure becomes the major perturbation for objects with sufficiently high area-to-mass ratio, such as 10–20 m^2/kg, just behind the central body attraction (denoted by GM). In this last case, the solar radiation pressure becomes more or less two orders of magnitude greater than the second zonal harmonic perturbation.

Referring to Section 3.3, we have developed an accurate semi-analytical method. More precisely, we have written a mean differential system which can be numerically integrated with an integration time step considerably larger than in classical numerical integration. As shown in Chapter 2, this fact reduces hugely the time of integration as well as the round off and truncating errors. The solution of such a mean differential system can be used to define a so-called centered motion, that is a motion which represents the mean characteristics of the osculating orbits. Consequently, as soon as a high quantitative accuracy is needed on a desired mean motion, the orbit extrapolations are obtained using this semi-analytical theory. As specified in Section 3.3, the expansion of the mean differential system of equations is performed typically up to order 10 in eccentricity and in inclination. This high order expansion ensures a theoretical accuracy of a few meters on the position which is largely sufficient. Indeed, the order of magnitude of the neglected effects, such as the Earth's shadow and the assumption of an optically uniform sphere exceeds by far the intrinsic accuracy of our model.

On the other hand, on a qualitative point of view, it would be interesting to underline the main properties of objects with high area-to-mass ratios using simplified equations. Such an approach is adopted in Chao (2006) where the coupling effects between the solar radiation pressure effects and the luni-solar attractions is considered. Within this framework, the latter provides a detailed understanding of the long-term evolution of both eccentricity and inclina-

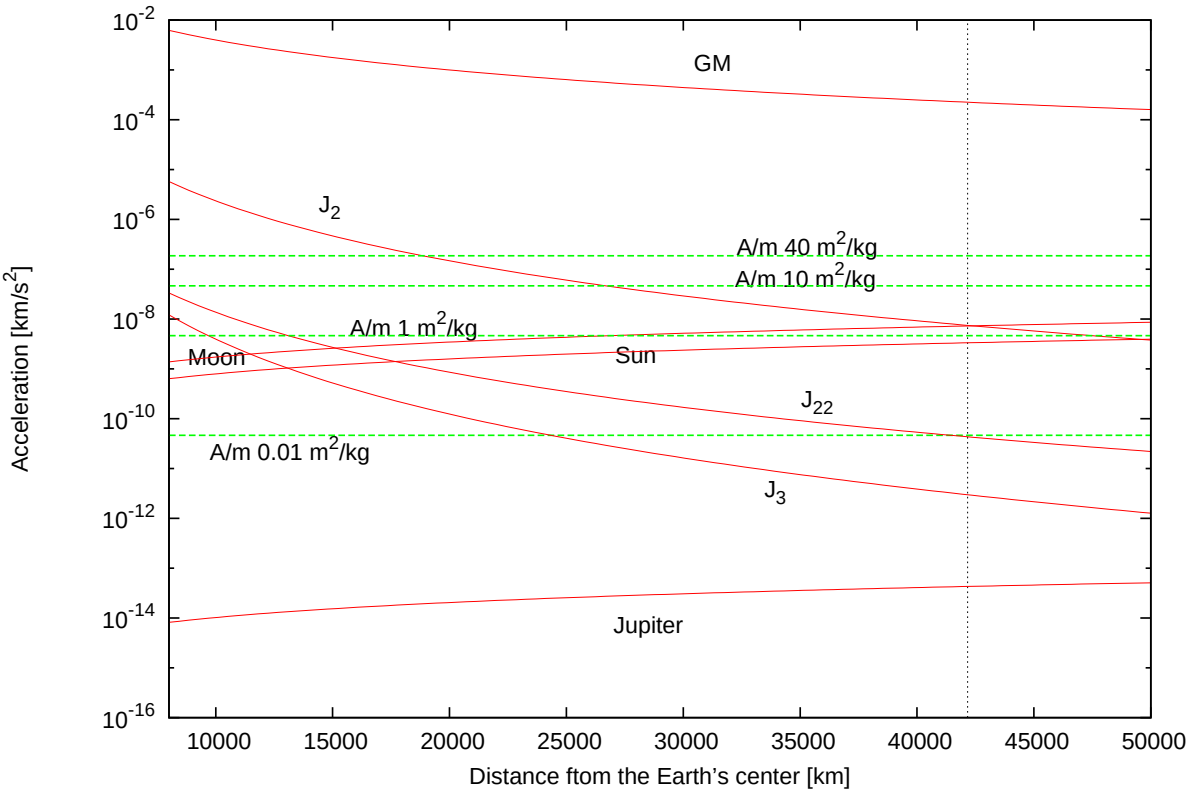

Figure 3.2: We show the order of magnitude of the main perturbations acting on space debris orbits [solid curves]. Additionally, we plot the order of magnitude of the direct radiation pressure perturbation for various area-to-mass ratios, namely $A/m = 0.01, 1, 10, 40\ \mathrm{m}^2/\mathrm{kg}$ [dashed curves].

tion. Regarding our approach, we will focus our efforts on the radiation pressure without taking into account the coupling between the radiation and the luni-solar effects. Consequently, this analysis will then emphasize the intrinsic effects related to radiation pressure. On the other hand, to avoid any singularity in eccentricity and inclination, the following simplified equations will be expressed using our non-singular set of variables.

As we are interested in the long-term dynamics, we average the disturbing function over the fast variable, namely the mean longitude λ. As a first approach, we average the disturbing function to the first order by dropping the fast periodic terms in the trigonometric functions. Using the non-dimensional ecliptic spherical coordinates $(\lambda_\odot, \beta_\odot)$ of the Sun instead of the before-mentioned rectangular coordinates $(X_\odot, Z_\odot, Z_\odot)$, the averaged potential expansion defined in Eq. (3.7), truncated up to degree 1 in Legendre polynomials, takes the form

$$\begin{aligned}\langle \mathcal{H}_{rp} \rangle_\lambda \;=\; -\frac{3}{2} C_r\, P_r\, \frac{A}{m} \left(\frac{a_\odot}{r_\odot}\right)^2 a\, e\, [C_1 \cos g_1 + C_2 \cos g_2 \\ + C_3 \cos g_3 - C_3 \cos g_4 + C_4 \cos g_5 + C_5 \cos g_6] \ .\end{aligned} \tag{3.9}$$

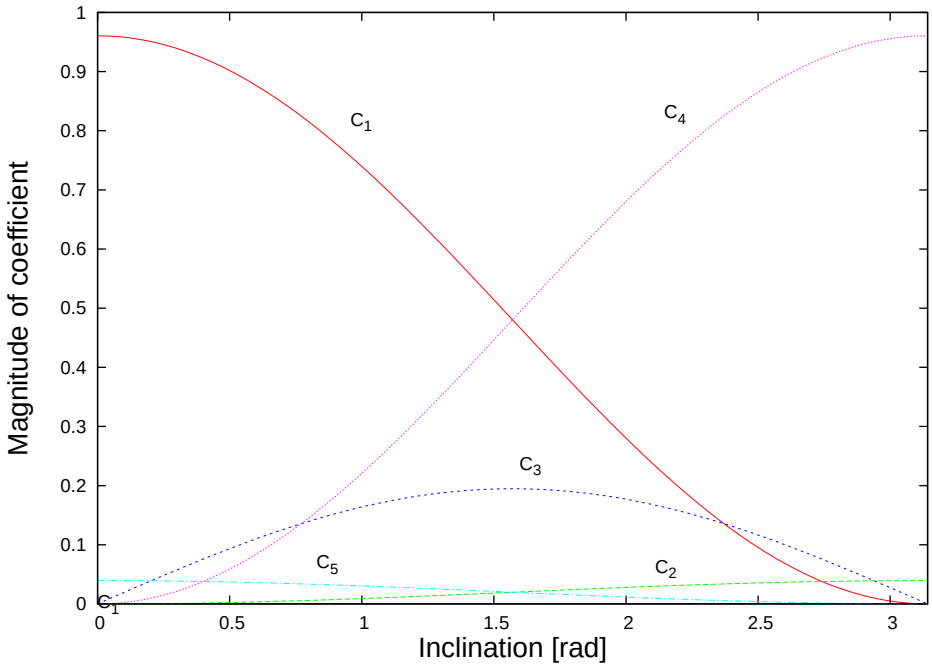

Figure 3.3: Magnitudes of coefficients $C_1,\ C_2, \cdots,\ C_5$ appearing in the averaged Hamiltonian disturbing function (3.9) as a function of the space debris orbital inclination.

This potential formulation is consistent with the Gaussian equations described in Chao (2005), where the coefficients C_i are defined by (we take the opportunity here to correct misprints that occurred in them)

$$\begin{aligned} C_1 &= \cos^2\frac{i}{2}\cos^2\frac{\epsilon}{2}\,, \\ C_2 &= \sin^2\frac{i}{2}\sin^2\frac{\epsilon}{2}\,, \\ C_3 &= \frac{1}{2}\sin i\sin\epsilon\,, \\ C_4 &= \sin^2\frac{i}{2}\cos^2\frac{\epsilon}{2}\,, \\ C_5 &= \cos^2\frac{i}{2}\sin^2\frac{\epsilon}{2}\,, \end{aligned} \tag{3.10}$$

and the angular values g_i are given by

$$\begin{aligned} g_1 &= \lambda_\odot - \varpi\,, \\ g_2 &= \lambda_\odot - \varpi + 2\Omega\,, \\ g_3 &= \lambda_\odot - \varpi + \Omega\,, \\ g_4 &= \lambda_\odot + \varpi + \Omega\,, \\ g_5 &= \lambda_\odot + \varpi - 2\Omega\,, \\ g_6 &= \lambda_\odot + \varpi\,. \end{aligned} \tag{3.11}$$

In Eqs. (3.10) and (3.11), as in Section 3.2, ϵ still denotes the obliquity of the Earth with respect to the ecliptic and ϖ denotes the longitude of perigee. The coefficients C_1 to C_5 are clearly functions of the orbital inclination. Figure 3.10 shows the orders of magnitudes of these coefficients as a function of the inclination. As shown in this figure, C_1 is the leading coefficient for small to moderate inclinations. C_2 and C_5 are very small for every value of the inclination whereas C_3 and C_4 reach relevant values for moderate to high inclinations.

The potential formulation defined in Eq. (3.9) is computed assuming that the relative motion of the Sun around the Earth is circular because of the small eccentricity of the orbit of the Earth. The angular motion of the Sun on its orbit is therefore assumed to be constant, that is $n_\odot = 2\pi/[\text{year}]$. Moreover, we assume that the Sun lies on the mean ecliptic, that is $\beta_\odot = 0$.

This potential formulation may then be expressed using the dimension-free Poincaré variables. After isolating the dominant terms (first order approximation in eccentricity and in inclination $\mathcal{O}(e, \sin i/2)$), the averaged potential takes the form

$$\begin{aligned}\langle \mathcal{H}_{rp} \rangle_\lambda \;=\; & -\mathcal{Z}_1 \left\{ (C_\odot Y_1 - S_\odot X_1) \left(1 - \frac{1}{4}\left(X_2^2 + Y_2^2\right)\right) \right. \\ & \left. + \frac{1}{4}\left[\left(Y_2^2 - X_2^2\right)(C_\odot Y_1 + S_\odot X_1)\right] - 2X_2Y_2(S_\odot Y_1 - C_\odot X_1) \right\} \\ & -\mathcal{Z}_2 \left\{ (C_\odot Y_1 + S_\odot X_1) \left(1 - \frac{1}{4}\left(X_2^2 + Y_2^2\right)\right) \right. \\ & \left. + \frac{1}{4}\left[\left(Y_2^2 - X_2^2\right)(C_\odot Y_1 - S_\odot X_1)\right] + 2X_2Y_2(S_\odot Y_1 + C_\odot X_1) \right\} \\ & -\mathcal{Z}_3 \left\{ S_\odot \left(Y_1 X_2 - X_1 Y_2\right) \right\} + \mathcal{O}(e^2, \sin^2 i/2)\,,\end{aligned} \tag{3.12}$$

where

$$\mathcal{Z} = \frac{3}{2}\, a\, C_r\, P_r\, \frac{A}{m} \left(\frac{a_\odot}{r_\odot}\right)^2, \quad C_\odot = \cos\lambda_\odot(t), \quad S_\odot = \sin\lambda_\odot(t)$$

and

$$\mathcal{Z}_1 = \mathcal{Z}\, \cos^2\frac{\epsilon}{2}, \quad \mathcal{Z}_2 = \mathcal{Z}\, \sin^2\frac{\epsilon}{2}, \quad \mathcal{Z}_3 = \mathcal{Z}\, \sin\epsilon\,.$$

3.4.1 Mid-term evolution of eccentricity and longitude of perigee

The coupled averaged equations in eccentricity and longitude of perigee due to direct solar radiation pressure have been treated by a couple of authors. The problem has been solved by Chao and Baker (1983) in the particular (e, ϕ) phase space where e is the eccentricity and $\phi = \lambda_\odot - \varpi$, that is the angular distance between the Sun and the longitude of perigee (see also Chao 2006). Afterwards, Chao and Campbell (2005) used the same (e, ϕ) formalism to explain why a Sun-pointing strategy can minimize long-term eccentricity variations for space debris located within the GEO ring, as well as for disposed satellites at 250 to 300 km above GEO. Similarly, Krivov and Getino (1997) investigated the motion of artificial satellites with large area-to-mass ratios in high altitude low inclined orbits, perturbed by solar radiation pres-

sure coupled with the Earth's oblateness. However, the derived averaged equations turn out to be singular in eccentricity, that is awkward for geostationary space debris. On the other hand, the authors represent the motion of the eccentricity and of the angle ϕ; we prefer to keep the classical eccentricity vector, linked to e and ϖ, and to introduce $\lambda_\odot$ as an external function of time. It is true that the averaged frequencies of $\lambda_\odot$ and of ϖ are very similar (equal in first approximation); however the introduction of their difference as a new angle ϕ could be confusing, introducing a kind of virtual resonance in the problem which we do not identify as a resonance in our Hamiltonian approach.

Thanks to the quasi-Hamiltonian formalism, the averaged equations of variation (w.r.t. the mean longitude λ) of the eccentricity related variables X_1, Y_1 are given by

$$\begin{aligned}
\dot{X}_1 = \frac{1}{L}\frac{\partial \langle \mathcal{H}_{rp} \rangle_\lambda}{\partial Y_1} &= -\mathcal{Z}_1/L \left[C_\odot \left(1 - \frac{1}{2} X_2^2 \right) - S_\odot \frac{1}{2} X_2 Y_2 \right] \\
&\quad -\mathcal{Z}_2/L \left[C_\odot \left(1 - \frac{1}{2} X_2^2 \right) + S_\odot \frac{1}{2} X_2 Y_2 \right] \\
&\quad -\mathcal{Z}_3/L \; S_\odot \, X_2 \, ,
\end{aligned} \tag{3.13}$$

$$\begin{aligned}
\dot{Y}_1 = -\frac{1}{L}\frac{\partial \langle \mathcal{H}_{rp} \rangle_\lambda}{\partial X_1} &= -\mathcal{Z}_1/L \left[S_\odot \left(1 - \frac{1}{2} Y_2^2 \right) - C_\odot \frac{1}{2} X_2 Y_2 \right] \\
&\quad +\mathcal{Z}_2/L \left[S_\odot \left(1 - \frac{1}{2} Y_2^2 \right) + C_\odot \frac{1}{2} X_2 Y_2 \right] \\
&\quad -\mathcal{Z}_3/L \; S_\odot \, Y_2 \, .
\end{aligned} \tag{3.14}$$

Eqs. (3.13) and (3.14) can be further reduced by neglecting the first and second order terms in X_2, Y_2. One can then integrate the equations with respect to time to obtain the solution of our so-called *simplified model* in eccentricity

$$\begin{aligned}
X_1(t) &= -\frac{\mathcal{Z}}{L\, n_\odot} \sin \lambda_\odot(t) \quad + \quad \beta_0, \\
Y_1(t) &= \frac{\mathcal{Z} \cos \epsilon}{L\, n_\odot} \cos \lambda_\odot(t) \quad + \quad \alpha_0 \, ,
\end{aligned} \tag{3.15}$$

where (α_0, β_0) are constants of integration determined from initial conditions. These equations describe an ellipse with center coordinates (α_0, β_0). In addition to the choice of non-singular variables, this simplified analytical model differs from the one developed by Chao and Baker (1983) by the presence of the term in $\sin^2 \epsilon/2$. Neglecting the terms in $\sin^2 \epsilon/2$, the ellipse becomes a circle, the radius of which is $R = (1/L\, n_\odot)\, \mathcal{Z} \cos^2 \epsilon/2$. Eqs. (3.15) show that the so-called *eccentricity vector* $(\boldsymbol{Y_1, -X_1}) \simeq (\mathbf{e} \cos(\omega + \boldsymbol{\Omega}), \mathbf{e} \, \sin(\omega + \boldsymbol{\Omega}))$ moves along this circle (counter clockwise) at a constant rate $n_\odot = 2\pi/[\text{year}]$. As a consequence, the longitude of perigee ϖ librates (Figure 3.4, left) or circulates (Figure 3.4, right) about a fixed value which depends on the initial conditions in eccentricity e_0 and in longitude of perigee ϖ_0 as well as on the radius of the circle, that is a directly proportional function of the area-to-mass ratio A/m.

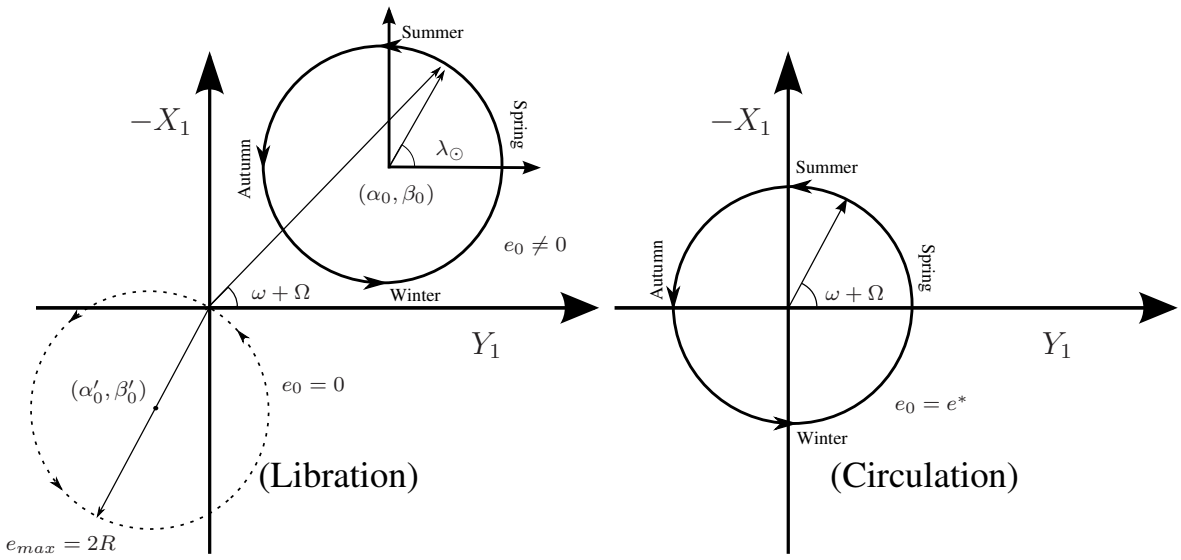

Figure 3.4: Schematic mid-term evolution (yearly oscillations) of the eccentricity vector in the $(Y_1, -X_1) \simeq (\, \mathbf{e}\, \cos(\omega + \mathbf{\Omega}), \mathbf{e}\, \sin(\omega + \mathbf{\Omega})\,)$ phase space. Depending on the initial conditions in eccentricity e_0 and longitude of perigee ϖ_0, the longitude of perigee librates [left] or circulates [right] for a fixed value of the area-to-mass ratio A/m.

To draw a parallel with our complete modeling of the radiation pressure, the mid-term evolution (several years) of the eccentricity is plotted in (Figure 3.5, top) using our semi-analytical theory. The corresponding eccentricity vector evolution is shown in (Figure 3.5, bottom). For clarity, only a subset of area-to-mass ratios are shown, namely $A/m = \ 5,\ 10,\ 20\,\mathrm{m}^2/\mathrm{kg}$. The amplitude of the mid-term oscillations, with a period of nearly one year, significantly grows from 0.1 to $\ 0.4$ with increasing area-to-mass ratio. On the other hand, the eccentricity vector defines nearly a circle with center coordinates depending on the initial conditions as well as on the area-to-mass ratios. Each circle intersects the origin of the frame of reference. Therefore, these last numerical results are in agreement with the solution of the simplified analytical model defined in Eqs. (3.15).

If we choose the initial eccentricity e_0 and the initial longitude of perigee ϖ_0 in such a way that $\alpha_0 = \beta_0 = 0$, the circle will be centered in $(Y_1, -X_1) = (0, 0)$. In that case, the module of the eccentricity vector will remain constant over time (Figure 3.4, right). The conditions leading to such an equilibrium in eccentricity can then be written as

$$\begin{aligned}
\sqrt{2P_0/L}\, \cos \varpi_0 &= \frac{\mathcal{Z} \cos^2 \epsilon/2}{L\, n_\odot} \cos \lambda_\odot(0)\,, \\
\sqrt{2P_0/L}\, \sin \varpi_0 &= \frac{\mathcal{Z} \cos^2 \epsilon/2}{L\, n_\odot} \sin \lambda_\odot(0)\,,
\end{aligned}$$

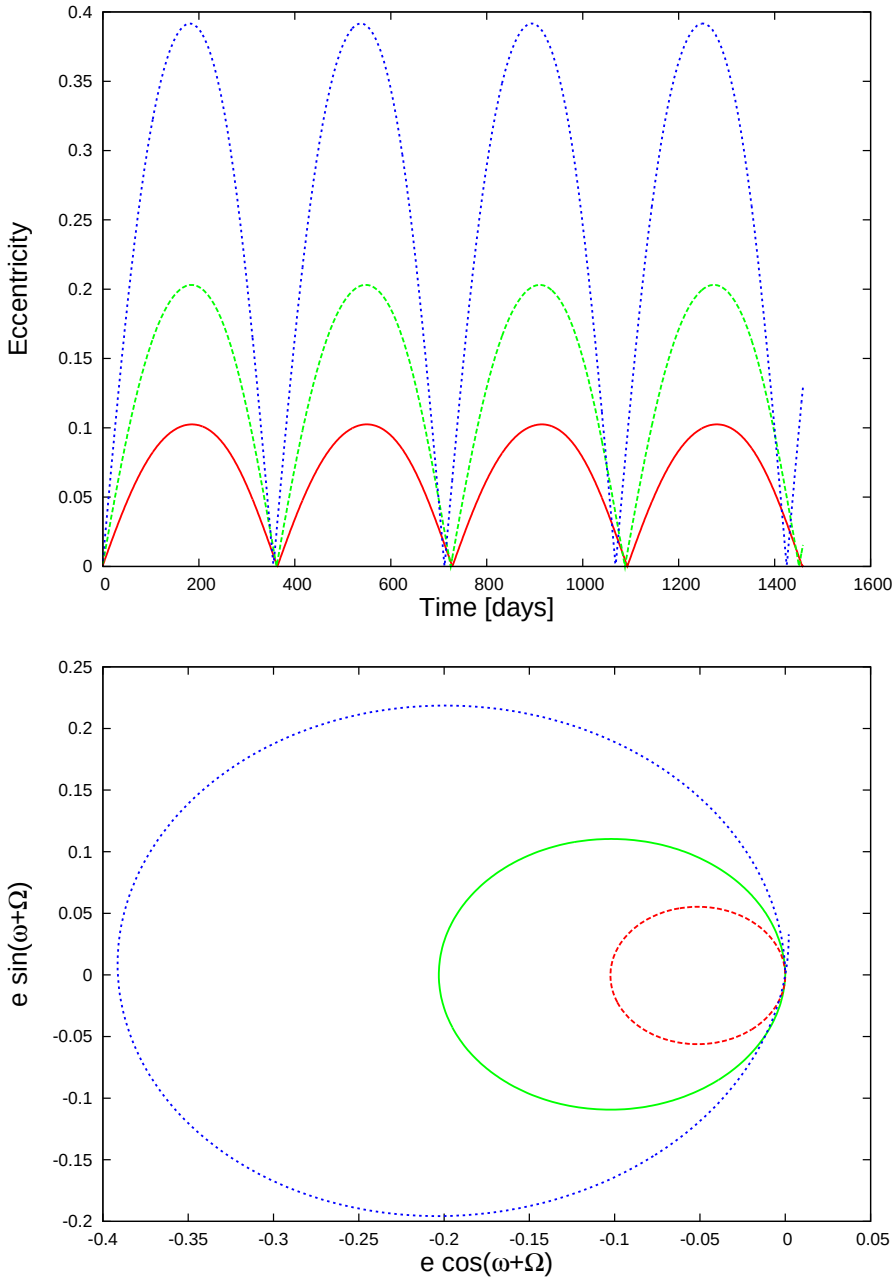

Figure 3.5: Mid-term variations (yearly oscillations) of the eccentricity and the corresponding eccentricity vector as a function of various area-to-mass ratios ($A/m = 5, 10, 20$ m^2/kg – red, green, blue line, respectively) for a fixed initial condition ($a_0 = 42\,164$ km, $e_0 = 0$, $i_0 = 0$ rad, $\Omega_0 = \omega_0 = \lambda_0 = 0$ rad). Time at epoch is 21 March 2000.

leading to

$$\begin{cases} e_0 &= \dfrac{3}{2} C_r \, P_r \, \dfrac{A}{m} \, \dfrac{1}{na \, n_\odot} \, \cos^2 \dfrac{\epsilon}{2} \underset{\text{def.}}{=} e^* \, , \\ \varpi_0 &= \lambda_\odot(0) \, . \end{cases}$$

These values are in good agreement with those of Chao and Baker (1983), where the so-called *forced eccentricity* e^* turns out to be directly related to the area-to-mass ratio of the space debris by the following equation

$$e^* \simeq 0.01 \, C_r \, \frac{A}{m} \, .$$

As a comparison with our semi-analytical model, Figure 3.6 shows the mid-term evolution of the eccentricity and the corresponding eccentricity vector evolution for a fixed value of the area-to-mass ratio ($A/m = 10 \text{ m}^2/\text{kg}$) and a fixed value of the initial conditions, that is $a_0 = 42\,164 \text{ km}, \; e_0 = 0.1, i_0 = 0 \text{ rad}, \; \Omega_0 = \omega_0 = \lambda_0 = 0 \text{ rad}$. The numerical propagations were carried out with our semi-analytical theory over 2 years. The difference between the chosen release orbits only depends on the initial *time at epoch* parameters t_0. Different initial times at epoch will induce different initial ecliptic longitudes of the Sun $\lambda_\odot(0)$. Figure 3.6 revealed a quite rich collection of behaviors depending only on the initial ecliptic longitude of the Sun, that is the initial angular distance between the Sun and the longitude of perigee. Assuming an initial time at epoch of 21 March 2000, that is adopting a Sun pointing longitude of perigee strategy ($\lambda_\odot(0) = 0$ rad), the eccentricity will remain nearly constant. In this case, the eccentricity vector moves counter-clockwise on a circle, the center coordinate of which matches nearly the center coordinate of the eccentricity vector reference frame. Assuming other initial ecliptic longitudes of the Sun, the eccentricity presents clearly a yearly variation. On the other hand, the amplitude of variations of the eccentricity is equivalent in each case, namely twice the radius of the circle in the eccentricity vector reference frame. These numerical results are over again in good agreement with our simplified analytical model.

3.4.2 Long-term evolution of inclination and longitude of the ascending node

The coupled equations in inclination and longitude of the ascending node under the influence of direct solar radiation pressure were studied by several authors (e.g. Anselmo et al., 1983). As part of this work, the authors present some results concerning the long-term variation of the inclination and longitude of the ascending node. Especially, the authors quote: "*The inclination i and the node Ω undergo no long-periodic or secular perturbation to zero order in the eccentricity*". However, this result were obtained within the context of small to moderate area-to-mass ratios. As a matter of fact, as seen previously in Subsection 3.4.1, a space debris subjected to direct solar radiation pressure presents periodic oscillations of the eccentricity with high amplitudes for moderate to high area-to-mass ratio. As a consequence, the zero order assumption in eccentricity does not hold anymore.

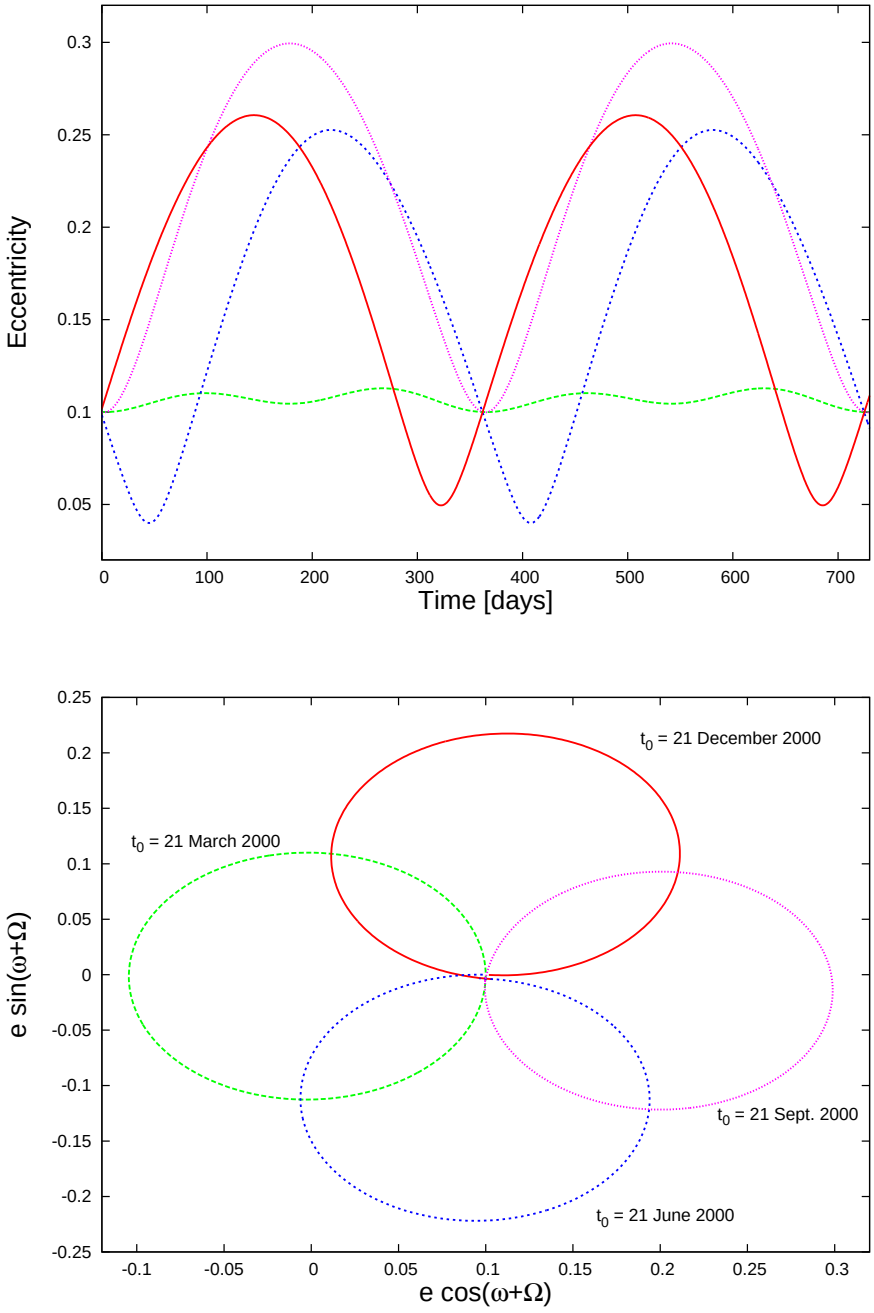

Figure 3.6: Mid-term variations (yearly oscillations) of the eccentricity and the corresponding eccentricity vector for a fixed initial condition $a_0 = 42\,164$ km, $e_0 = 0.1$, $i_0 = 0$ rad, $\Omega_0 = \omega_0 = \lambda_0 = 0$ rad and a fixed area-to-mass $A/m = 10\ \mathrm{m}^2/\mathrm{kg}$. Various initial time at epoch t_0 were used for the numerical propagations.

The direct solar radiation pressure mean potential defined in Eq. (3.12) can be differentiated to obtain the coupled averaged equations in inclination and longitude of the ascending node

$$\begin{aligned}\dot{X}_2 = \frac{1}{L}\frac{\partial \langle \mathcal{H}_{rp} \rangle_\lambda}{\partial Y_2} &= -\mathcal{Z}_1/2L\Big[- X_2\,(S_\odot Y_1 - C_\odot X_1) + 2S_\odot X_1 Y_2\Big] \\ &\quad -\mathcal{Z}_2/2L\Big[+ X_2\,(S_\odot Y_1 + C_\odot X_1) - 2S_\odot X_1 Y_2\Big] \\ &\quad +\mathcal{Z}_3/L\ S_\odot\, X_1\,,\end{aligned} \tag{3.16}$$

$$\begin{aligned}\dot{Y}_2 = -\frac{1}{L}\frac{\partial \langle \mathcal{H}_{rp} \rangle_\lambda}{\partial X_2} &= +\mathcal{Z}_1/2L\Big[- Y_2\,(S_\odot Y_1 - C_\odot X_1) - 2C_\odot X_2 Y_1\Big] \\ &\quad +\mathcal{Z}_2/2L\Big[+ Y_2\,(S_\odot Y_1 + C_\odot X_1) - 2C_\odot X_2 Y_1\Big] \\ &\quad +\mathcal{Z}_3/L\ S_\odot Y_1\,.\end{aligned} \tag{3.17}$$

After substituting the first order approximation of the eccentricity and longitude of perigee variation defined by Eqs. (3.15) into Eqs. (3.17) and (3.16), we find the doubly averaged equations with respect to the mean longitude λ and the ecliptic longitude $\lambda_\odot$, that is

$$\begin{aligned}\left\langle \dot{X}_2 \right\rangle_{\lambda_\odot} &= \frac{\mathcal{Z}}{2\,n_\odot\,L^2}\Big[\,(\mathcal{Z}_1 - \mathcal{Z}_2)\ Y_2 - \mathcal{Z}_3\Big] = \frac{1}{2\,n_\odot\,L^2}\Big[\mathcal{Z}^2\,\cos\epsilon\, Y_2 - \mathcal{Z}\mathcal{Z}_3\Big]\,, \\ \left\langle \dot{Y}_2 \right\rangle_{\lambda_\odot} &= \frac{\mathcal{Z}\,\cos\epsilon}{2\,n_\odot\,L^2}\,(\mathcal{Z}_1 + \mathcal{Z}_2)\ X_2 = -\frac{\mathcal{Z}^2\,\cos\epsilon}{2\,n_\odot\,L^2}\,X_2\,,\end{aligned} \tag{3.18}$$

where the relative motion of the Sun around the Earth is still assumed to be circular with a constant angular motion of $n_\odot = 2\pi/[\text{year}]$. This system of differential equations (3.18) is no more and no less than a harmonic oscillator expressed in the rectangular coordinates X_2

$$\left\langle \ddot{X}_2 \right\rangle_{\lambda_\odot} = -\nu_\Omega^2\, X_2 \qquad \text{with} \quad \nu_\Omega = \frac{\mathcal{Z}^2\,\cos\epsilon}{2\,n_\odot\,L^2}\,. \tag{3.19}$$

Moreover, a general solution of our second *simplified model* in inclination can be written as follows

$$\begin{aligned}\langle X_2 \rangle_{\lambda_\odot} &= -A_0 \sin(\nu_\Omega t + \theta_0)\,, \\ \langle Y_2 \rangle_{\lambda_\odot} &= \sin\epsilon - A_0 \cos(\nu_\Omega t + \theta_0) + \mathcal{O}(\epsilon^2)\,,\end{aligned} \tag{3.20}$$

where the amplitude A_0 and the phase difference θ_0 are determined from initial conditions. Eqs. (3.20) describe a circle with fixed center coordinates $(0, \sin\epsilon) = (0, \epsilon + \mathcal{O}(\epsilon^3))$ and a radius $R = A_0$. The so-called *inclination vector* $(\boldsymbol{Y_2, -X_2}) \simeq (\sin \mathbf{i}\, \cos \boldsymbol{\Omega}, \sin \mathbf{i}\, \sin \boldsymbol{\Omega})$ moves along this circle (clockwise) at a constant rate ν_Ω. Similarly to the case of the eccentricity vector presented in Eqs. (3.15), the longitude of the ascending node will librate or circulate depending only on the initial conditions in inclination i_0 and longitude of the ascending node Ω_0 (Figure 3.7, top). However, the libration regime takes place at about 0 degree. On the other hand, the amplitude A_0 of the solution (3.20), that is the radius of the circle, is independent of the area-to-mass ratio as well as of any multiplying factor present in the direct solar

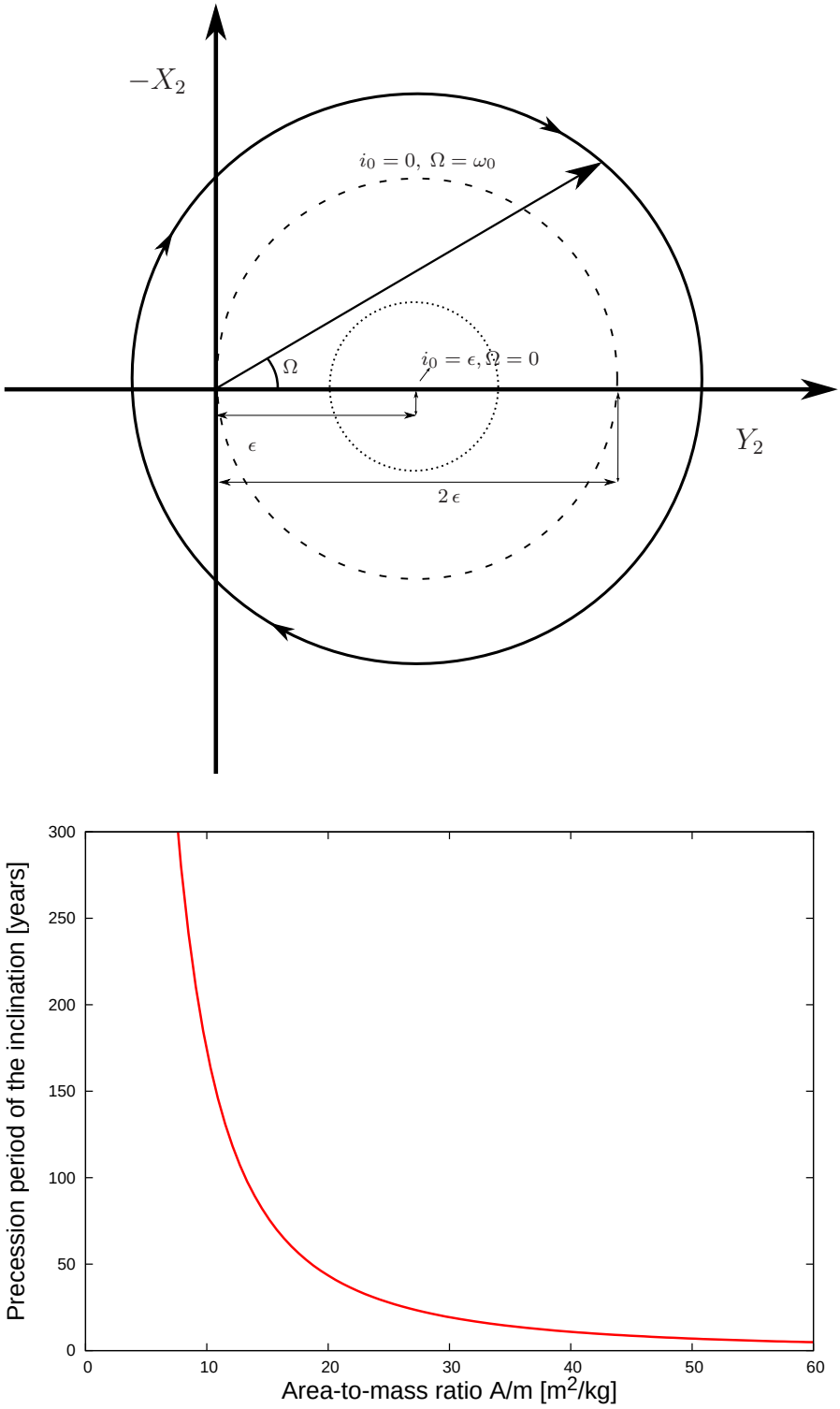

Figure 3.7: Schematic long-term evolution of the inclination vector in $(Y_2, -X_2) \simeq (\sin i\ \cos\Omega, \sin i\ \sin\Omega)$ phase space [top]. Various regimes of the inclination vector are recognizable: *circulation* [solid line] and *libration* [dashed and dotted line]. Period of precession $2\pi/\nu_\Omega$ of the inclination vector with respect to the area-to-mass ratio A/m [bottom].

radiation pressure formulation (Eq. 3.4). Indeed, the amplitude only depends on the initial conditions and on the obliquity ϵ of the Earth's orbit with respect to the ecliptic. Concerning the long-term evolution for small area-to-mass ratios (typically 0 up to $\sim 5\ \mathrm{m}^2/\mathrm{kg}$) there is no significant long-term variation of the inclination and the longitude of the ascending node over a time span of several decades. Indeed, the period of precession of the inclination vector (Figure 3.7, bottom) becomes extremely large. As a consequence, adding all the other relevant perturbations, that is the luni-solar interactions and the oblateness of the Earth, we expect that the space debris presents the behavior of a typical abandoned geosynchronous spacecraft, with a maximum inclination of 15° and a periodicity of about 54 years (Agrawal, 1986; Allen and Cook, 1964).

As a comparison with respect to the simplified analytical model in inclination, we plotted the long-term evolution (several decades) of the inclination and the corresponding inclination vector using our semi-analytical theory. The numerical propagations were carried out over a time span of 80 years using the initial conditions of a typical geosynchronous space debris. Figure 3.8 shows clearly that an increase of the area-to-mass ratio has as consequence a faster orbit pole precession. Taking into account only the effects of the direct solar radiation pressure, we also see that the maximum amplitude of the inclination, that is the amplitude of the plane motion, is independent of the area-to-mass ratio. A small wobble, with a period of approximately 1 year, is also clearly identified due to the mid-term variations present in the numerical integrations. The maximum reached by the inclination seems always to converge to the particular value of 47°, that is twice the obliquity of the Earth with respect to the ecliptic. Actually, if we choose a zero inclination i_0 as initial condition (Figure 3.7, top, dashed circle), the inclination variation can be written as

$$\sin^2 \frac{i}{2} \simeq \sin^2 \epsilon \, \sin^2 \left(\frac{\nu_\Omega t}{2} \right) .$$

In this particular case, corresponding to the initial inclination of most geosynchronous objects, the maximum value i_{max} reached by the inclination can be computed easily to obtain

$$i_{max} \simeq 2\,\epsilon\,,$$

which is in agreement with our previous numerical propagations.

Moreover, if we choose the initial inclination and longitude of node in such a way that the inclination vector matches the center coordinates of the circle, the module of the inclination as well as the longitude of the ascending node will remain constant over time. Such equilibrium conditions happen if and only if

$$i_0 = \epsilon, \qquad \Omega_0 = 0\,.$$

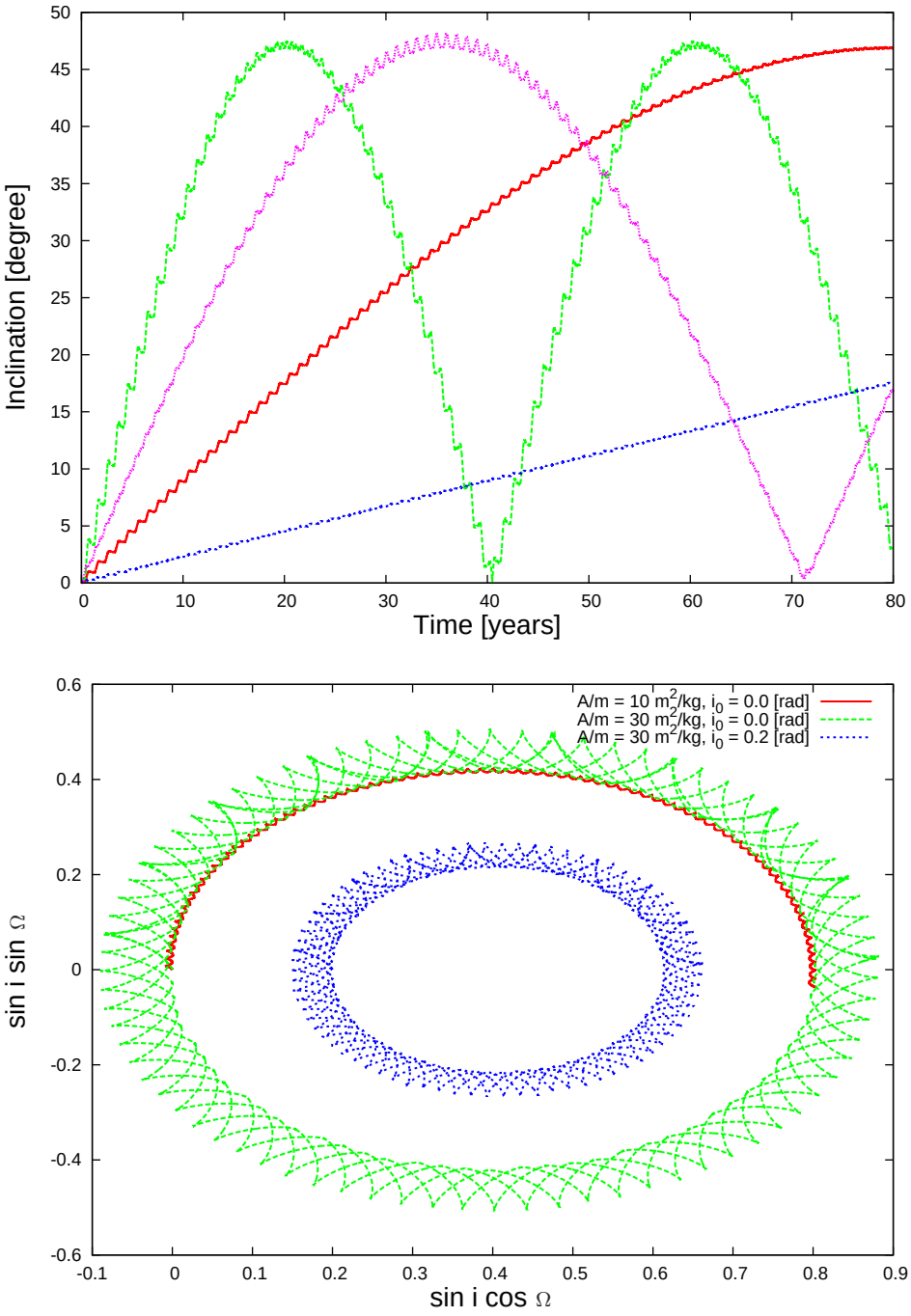

Figure 3.8: Long-term evolution of the inclination for various area-to-mass ratios ($A/m = 5, 10, 15, 20$ m^2/kg, $a_0 = 42\,164$ km, $e_0 = 0$, $i_0 = 0$ rad, $\Omega_0 = \omega_0 = \lambda_0 = 0$ rad) [top]. Long-term evolution of the inclination vector for a couple of initial conditions in inclination and area-to-mass ratios ($A/m = 10,\ 30$ m^2/kg) [bottom].

This result is in complete agreement with the fact that, considering the Gauss equations, the inclination and the node are affected only by the out-of-plane component

$$\begin{aligned} W &= \sin i \cos^2 \frac{\epsilon}{2} \sin(\lambda_\odot - \Omega) \\ &\quad - \sin i \sin^2 \frac{\epsilon}{2} \sin(\lambda_\odot + \Omega) - \cos i \sin \epsilon \sin \lambda_\odot \,, \end{aligned}$$

where this quantity is zero if and only if the inclination i is equivalent to the obliquity ϵ, and the longitude of the ascending node is equal to zero. However, let us note that this theoretical equilibrium is certainly important but to a lesser extent than the equilibrium presented in the eccentricity vector phase space. As a matter of fact, this equilibrium will be easily broken through the addition of the luni-solar perturbations, which induce important variations of the inclination and longitude of the ascending node as well. On the contrary, as explained in Anselmo and Pardini (2007a), the equilibrium in eccentricity can be used to adopt a Sun pointing perigee within the framework of eccentricity management during reorbitation (see also Delong and Frémaux, 2005). However, for typical satellites, this Sun-pointing re-orbit strategy is applicable only for small eccentricities ($e < 0.005$), but in general is inappropriate for about 8 months of the year, due to the effects of luni-solar perturbations on the evolution of the perigee altitude. In general, the perigee should be pointed towards about $90°$ or $270°$ in right ascension, and this may also correspond to sun-pointing conditions only around the solstices.

3.4.3 Long-term coupled equations between eccentricity and inclination

As shown in Subsection 3.4.2, Eqs. (3.13), (3.14) and (3.17), (3.16) are not uncoupled in the set of variables (X_1, Y_1) and (X_2, Y_2), respectively. Similarly to this latter analysis, it can be shown that the mid-term variations of the inclination related variables (X_2, Y_2) will induce additional long-term variations on the eccentricity vector by combination of mid-term periods only. The solution of this additional coupling effect between eccentricity and inclination can be written

$$\begin{aligned} X_1(t) &= -\frac{\mathcal{Z}}{L\, n_\odot} \sin \lambda_\odot(t) \quad + \quad B_0 \sin(\nu_\Omega t + \phi_0) \,, \\ Y_1(t) &= \frac{\mathcal{Z} \cos \epsilon}{L\, n_\odot} \cos \lambda_\odot(t) \quad + \quad B_0 \cos(\nu_\Omega t + \phi_0) \,, \end{aligned} \tag{3.21}$$

where the amplitude B_0 and the phase difference ϕ_0 are determined from initial conditions only. More precisely, the amplitude B_0 depends only on the initial center of coordinates (α_0, β_0) by the following relation

$$B_0 = \sqrt{\alpha_0^2 + \beta_0^2} \,.$$

Eqs. (3.21) show that the eccentricity vector always moves (counter clockwise) along a circle, defined in Eqs. (3.15), the center of coordinates of which moves (clockwise) along a great circle of radius B_0 with a proper period of $2\pi/\nu_\Omega$. The combination of mid-term and long-term variations is illustrated schematically in Figure 3.9 (top). Using our semi-analytical theory,

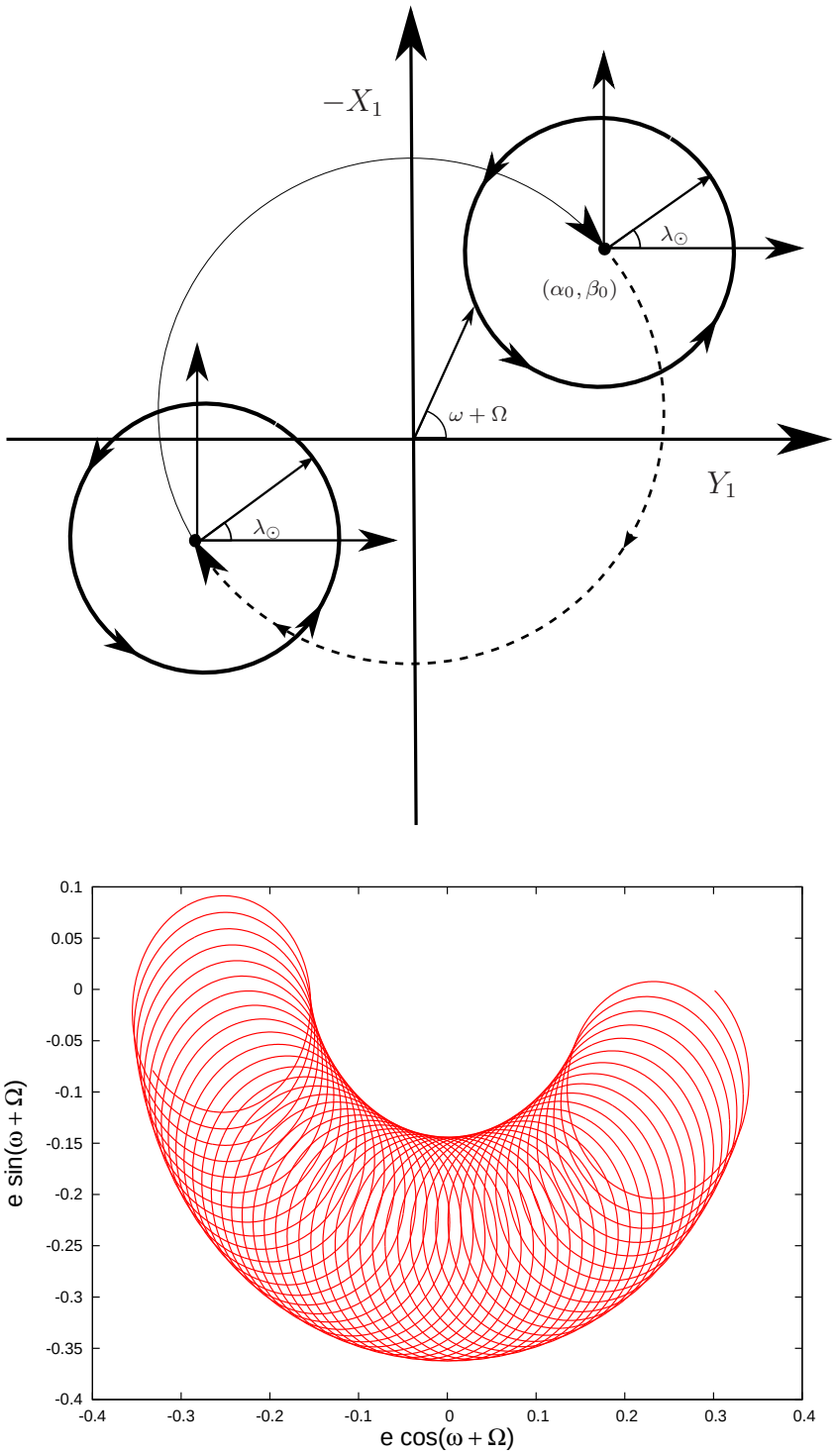

Figure 3.9: Long-term and mid-term variations of the eccentricity vector coupled with the inclination and node revolution. Theoretical evolution in the $(Y_1, -X_1) \simeq (\mathbf{e}\,\cos(\omega + \mathbf{\Omega}), \mathbf{e}\,\sin(\omega + \mathbf{\Omega}))$ [top]. Numerical propagation over 40 years of a space debris projected in the $e\cos(\omega + \Omega), e\sin(\omega + \Omega)$ phase space [bottom]. Area-to-mass ratio and initial conditions are $A/m = 10\ \mathrm{m}^2/\mathrm{kg}$ and ($a_0 = 42\,164$ km, $e_0 = 0.2,\ i_0 = 0,\ \Omega_0 = \omega_0 = M_0 = 0$ rad), respectively.

Figure 3.9 (bottom) shows the evolution, over 40 years, of the eccentricity vector of a space debris, taking into account only direct solar radiation pressure. The pattern observed is, as expected, basically produced by the superimposition of two variations, the first with a period of 1 year, associated with the solution presented in Eqs. (3.15), and the other with a period of several decades, that is the proper period $2\pi/\nu_\Omega$ of the longitude of the ascending node defined in Eq. (3.19).

3.5 Comparison of radiation pressure models – long-term analysis

The aim of the analysis presented in this section is to compare the long-term evolution of geosynchronous orbits predicted by various models for the direct solar radiation pressure. As shown in Section 3.2, the direct solar radiation pressure acceleration was given by Eq. (3.4). As a first approximation, if the Sun–space debris direction is replaced by the direction pointing from the Sun to the Earth, that is $\mathbf{r} - \mathbf{r}_\odot = -\mathbf{r}_\odot$, Eq. (3.4) becomes

$$\mathbf{a_{rp}} = -\, C_r\, P_r \left[\frac{a_\odot}{\|\mathbf{r}_\odot\|}\right]^2 \frac{A}{m}\, \frac{\mathbf{r}_\odot}{\|\mathbf{r}_\odot\|}\,. \tag{3.22}$$

This simplified acceleration may then be expressed as the gradient of the following potential

$$\mathcal{H}_{rp} = C_r\, P_r\, \frac{A}{m} \left(\frac{a_\odot}{r_\odot}\right)^2 r\, \cos\psi\,,$$

and therefore can be expanded using non-singular variables. This approximation seems consistent inasmuch as the ratio of the position vector of the space debris with respect to Sun–space debris vector may be assumed to be small ($\|\boldsymbol{r}\|/(\|\boldsymbol{r} - \boldsymbol{r_\odot}\| = 2.8 \times 10^{-4}$ for a geosynchronous space debris). Figures 3.10 and 3.11 show the differences between two mean orbits propagated with our semi-analytical theory over 54 years. The first orbit is propagated using a first degree expansion in Legendre polynomials that is making the assumption that the Sun–space debris direction coincides with the Sun–Earth direction. The second orbit is propagated using a third degree expansion in Legendre polynomials. The initial conditions are those of a perfect geostationary space debris. Figures 3.10 and 3.11 correspond to numerical propagations with a small area-to-mass ($A/m = 0.01\ \mathrm{m^2/kg}$) and a high area-to-mass ratio ($A/m = 30\ \mathrm{m^2/kg}$), respectively. Although the differences remain moderate in each case, these figures show the importance of adopting a complete expansion, when dealing with radiation pressure. Indeed, Figure 3.11 reports clearly that the order of magnitude of the error on the position may reach high values, namely hundreds of kilometers when propagating an object with extremely high area-to-mass ratios. It should however be remarked that modeling a $30\ \mathrm{m^2/kg}$ very strange object as an optically uniform sphere for several decades would affect the computations with a significant uncertainty. On the other hand, the order of magnitude of the error on the position remains moderate for small area-to-mass ratios and even if the difference in the inclination related variable ΔX_2 presents an apparent secular behavior, the

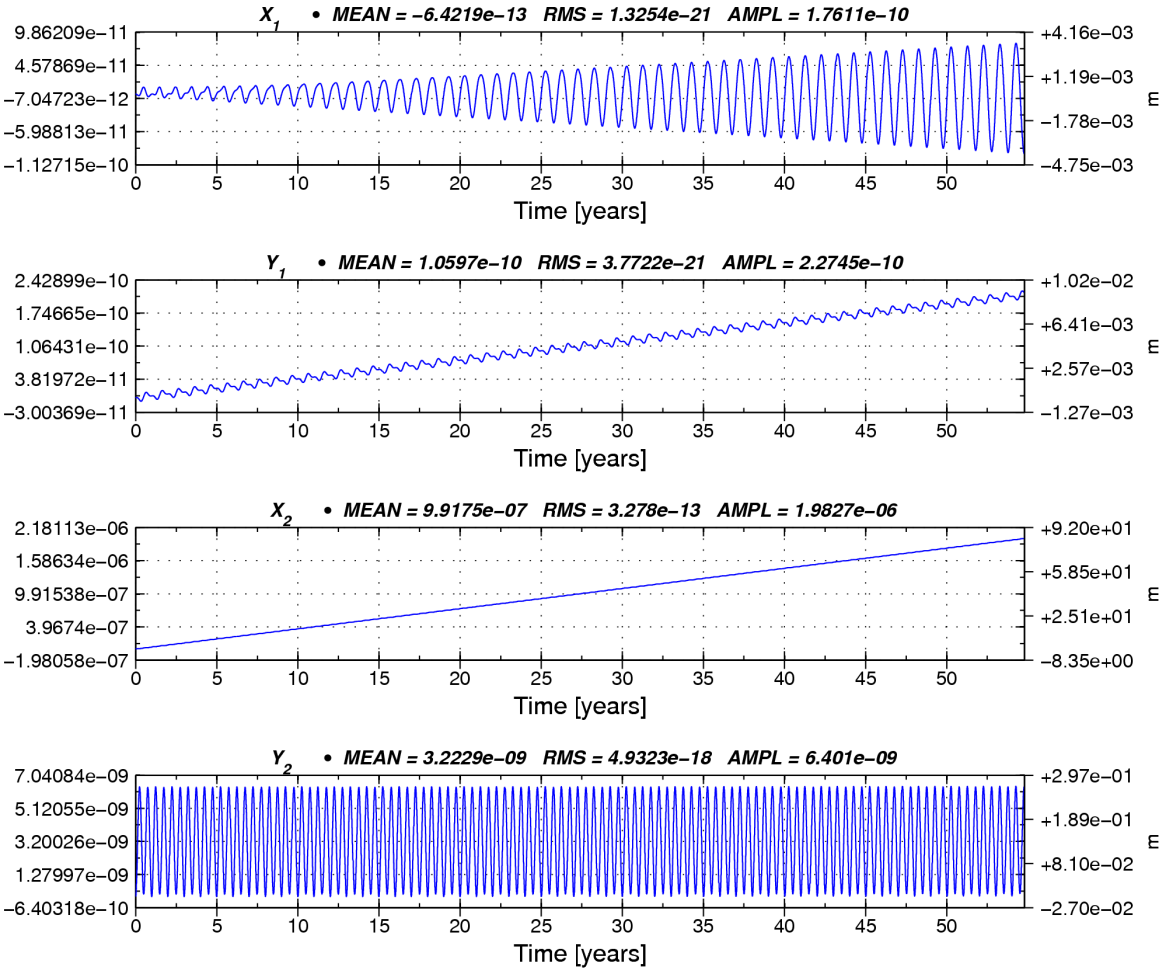

Figure 3.10: Differences between two mean orbits expressed in the non-singular and non-dimensional variables ($X_1,\ Y_1,\ X_2,\ Y_2$) and propagated with a first degree ($n_{max} = 1$) and a third degree expansion ($n_{max} = 3$) of the direct solar radiation pressure, respectively. Initial conditions are: $a_0 = 42\,164$ km, $e_0 = 0,\ i_0 = 0$ rad, $\Omega_0 = \omega_0 = \lambda_0 = 0$ rad and the area-to-mass ratio is $A/m = 0.01\ \mathrm{m}^2/\mathrm{kg}$. On each graph, the left vertical scale shows the deviations ($\Delta X_1,\ \Delta Y_1,\ \Delta X_2,\ \Delta Y_2$) and the right vertical scale shows the order of magnitude of the error on the position ($a_0\Delta X_1,\ a_0\Delta Y_1,\ a_0\Delta X_2,\ a_0\Delta Y_2$) [meter(s)].

deviation reaches at most 80 m after 54 years of propagation (see Figure 3.10).

A further simplification may be introduced, by disregarding the small eccentricity of the Earth's orbit around the Sun ($e_\oplus = 0.0167$), that is putting the geocentric vector of the Sun $\mathbf{r}_\odot = 1$ AU in Eq. (3.22), leading to the doubly simplified acceleration

$$\mathbf{a_{rp}} = -\,C_r\,P_r\frac{A}{m}\,\frac{\mathbf{r}_\odot}{\|\mathbf{r}_\odot\|}\,. \tag{3.23}$$

However, even though the correct evolution of the Sun motion in the geocentric reference frame is retained in the computation of the running Earth–Sun direction, the dynamics may

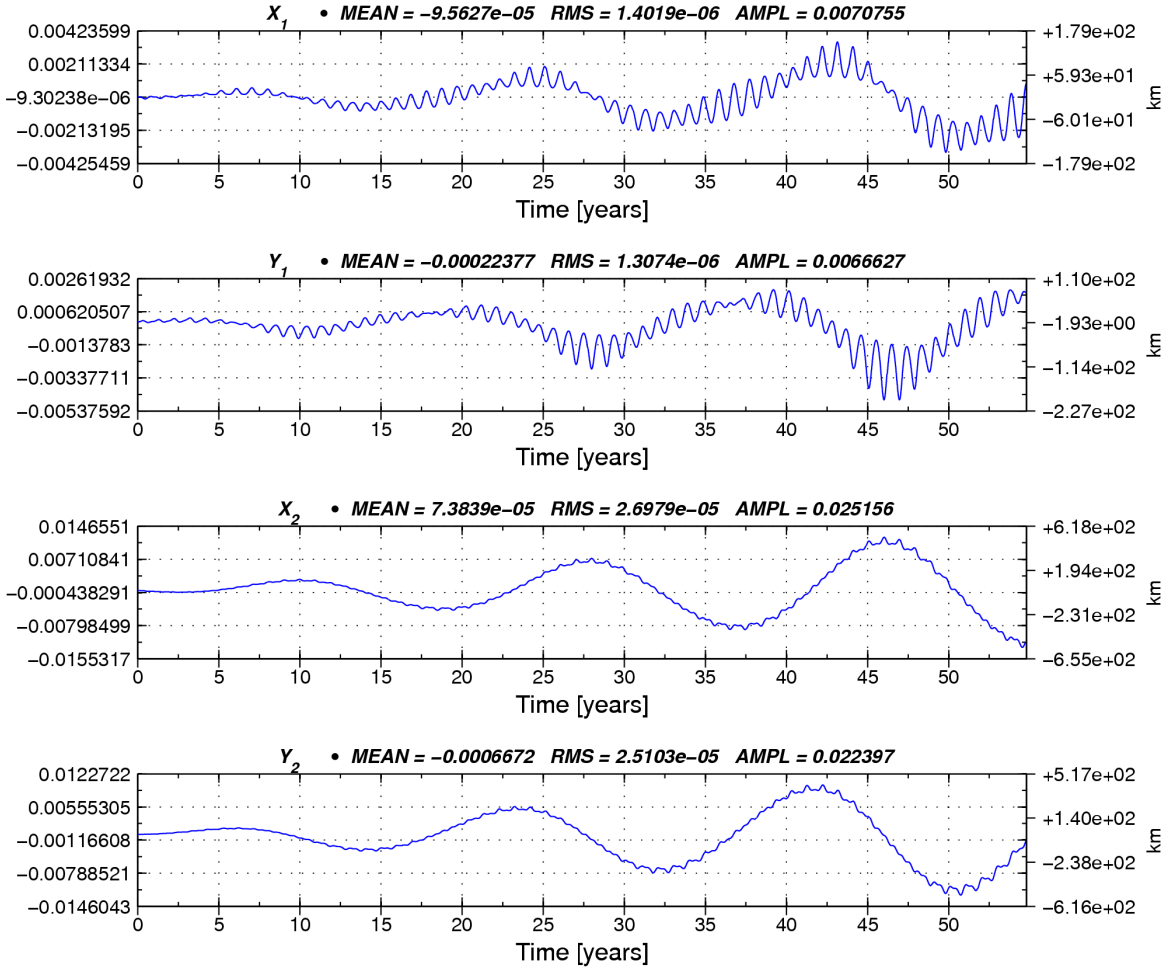

Figure 3.11: Differences between two mean orbits expressed in the non-singular and non-dimensional variables (X_1, Y_1, X_2, Y_2) and propagated with a first degree ($n_{max} = 1$) and a third degree expansion ($n_{max} = 3$) of the direct solar radiation pressure, respectively. Initial conditions are: $a_0 = 42\,164$ km, $e_0 = 0,\ i_0 = 0$ rad, $\Omega_0 = \omega_0 = \lambda_0 = 0$ rad and the area-to-mass ratio is $A/m = 30\ \mathrm{m}^2/\mathrm{kg}$. On each graph, the left vertical scale shows the deviations $(\Delta X_1,\ \Delta Y_1,\ \Delta X_2,\ \Delta Y_2)$ and the right vertical scale shows the order of magnitude of the error on the position $(a_0\Delta X_1,\ a_0\Delta Y_1,\ a_0\Delta X_2,\ a_0\Delta Y_2)$ [kilometers].

change considerably. Figure 3.12 shows the effects induced by the eccentricity of the Earth on a geosynchronous space debris, subjected only to radiation pressure, when its area-to-mass ratio reached $17\ \mathrm{m}^2/\mathrm{kg}$. First, we choose the complete model of radiation pressure defined in Eq. (3.4) to perform an orbital propagation, taking into account the variation of the distance between the Sun and the Earth. Second, we perform the same orbital propagation with the same initial conditions but using the doubly simplified radiation pressure model defined in Eq. (3.23), that is neglecting the eccentricity of the Earth. Finally, we plot the two propagated orbits as well as the difference between them. As a result, we see that the difference between the two models remains small on the inclination variation. However, the eccentricity dynamics clearly presents additional variations due to a phase difference effect, the period of which is

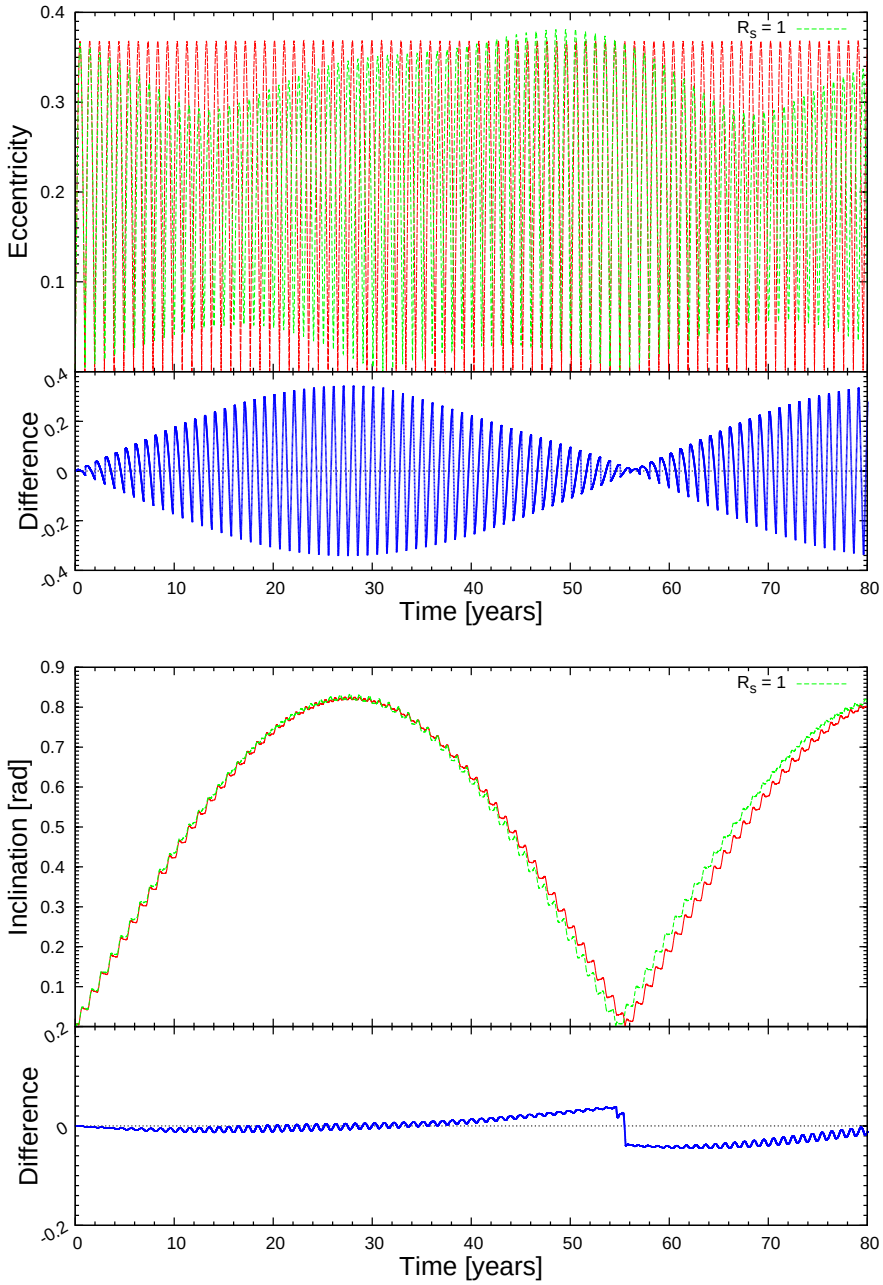

Figure 3.12: Eccentricity [top] and inclination [bottom] evolution in GEO over 80 years taking into account only direct solar radiation pressure. Orbital propagations taking into account the eccentricity of the Earth, (Eq. 3.4, complete model) [Solid curves]. Orbital propagation assuming $r_\odot = 1$ (Eq. 3.23, simplified model) [dashed curves]. Difference between the two orbital propagations [bottom curves]. Area-to-mass ratio and initial conditions are $A/m = 17\,\mathrm{m}^2/\mathrm{kg}$ and $(a_0 = 42\,164\,\mathrm{km},\ e_0 = 0,\ i_0 = 0,\ \Omega_0 = \omega_0 = M_0 = 0\,\mathrm{rad})$, respectively.

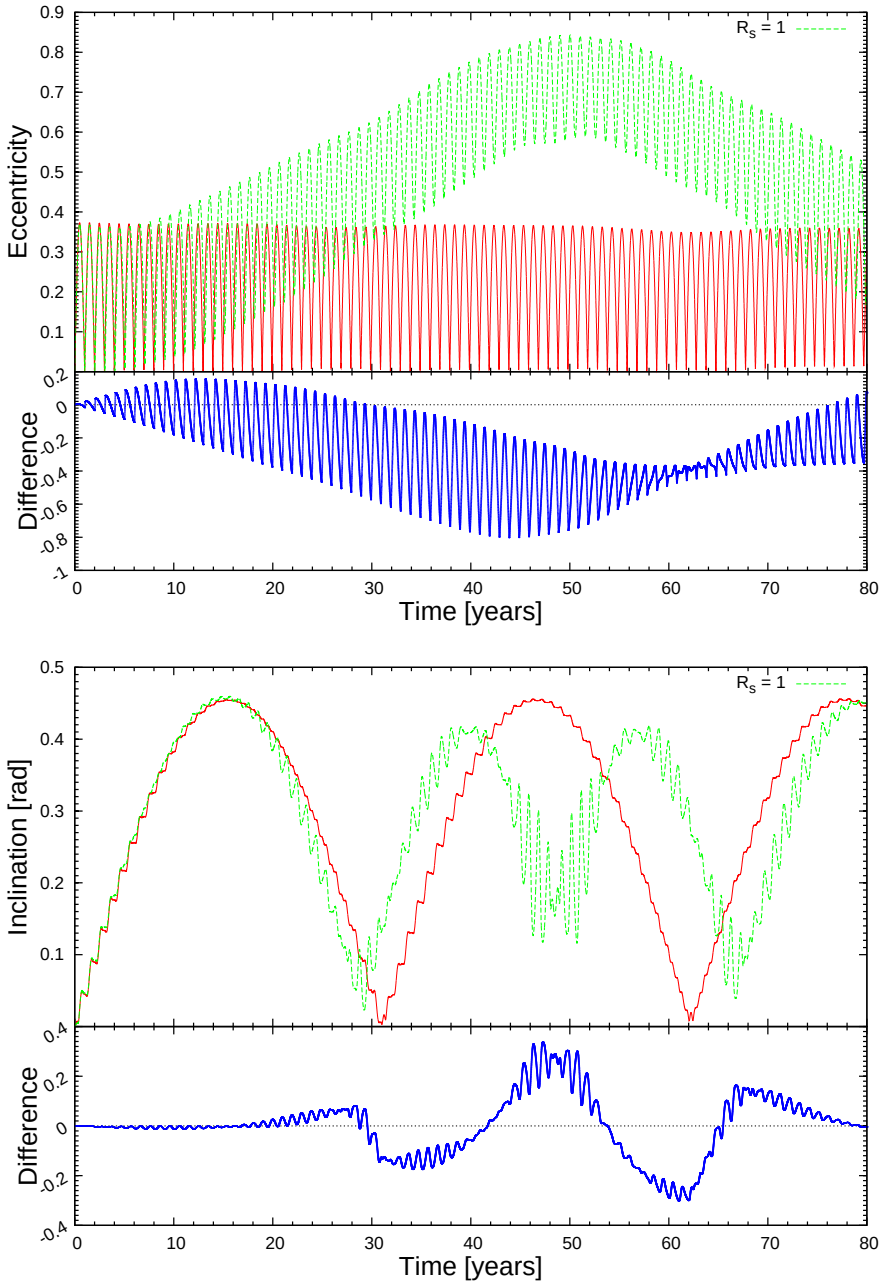

Figure 3.13: Eccentricity [top] and inclination [bottom] evolution in GEO over 80 years taking into account J_2 and direct solar radiation pressure. Orbital propagations taking into account the eccentricity of the Earth (Eq. 3.4, complete model) [Solid curves]. Orbital propagation assuming $r_\odot = 1$ (Eq. 3.23, simplified model) [dashed curves]. Difference between the two orbital propagations [bottom curves]. Area-to-mass ratio and initial conditions are $A/m = 17\,\mathrm{m}^2/\mathrm{kg}$ and $(a_0 = 42\,164\,\mathrm{km},\ e_0 = 0,\ i_0 = 0,\ \Omega_0 = \omega_0 = M_0 = 0\,\mathrm{rad})$, respectively.

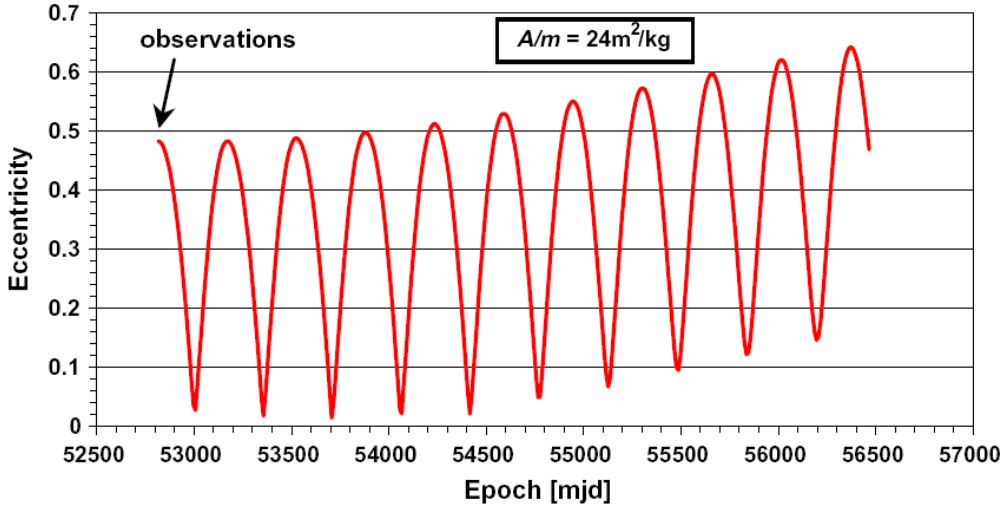

Figure 3.14: Evolution of the eccentricity for an object of the new population over ten years as computed in Schildknecht et al. (2007). The additional spurious long-periodic effect is clearly visible. [*Graphic by Schildknecht et al. (2007)*].

directly related to the period of revolution $2\pi/\nu_\Omega$ of the inclination vector. The amplitudes of these variations are on the order of the maximum eccentricity, that is 0.37. Let us remark that if we consider all the other relevant luni-solar perturbations, we can draw the same conclusion.

When considering the direct solar radiation pressure coupled with the effects induced by the second zonal harmonic of the geopotential, the differences between the complete model and the simplified one become considerable. Indeed, Figure 3.13 shows the effects induced by the eccentricity of the Earth on the same geosynchronous space debris, subjected to radiation pressure and also influenced by the second zonal harmonic J_2. In this case, the dynamics of the eccentricity as well as the dynamics of the inclination are completely different. In addition to the yearly eccentricity oscillations, obvious in all the plots, some long-term trends with high amplitudes are clearly recognizable. In this case, the coupling between radiation pressure and the oblateness of the Earth produces such a large eccentricity (Figure 3.13, top) able to induce a fictitious orbital decay (Anselmo and Pardini, 2005, 2007b). Then we can draw a conclusion: *the assumption of a fixed Sun–Earth distance, in the estimation of solar radiation pressure magnitude, introduces a significant spurious long period effect, especially when the radiation pressure is coupled with the influence of* J_2.

Consequently, these results confirm that a correct modeling of the Sun–Earth distance is very important to describe accurately the long-term evolution of geosynchronous objects, in particular if the area-to-mass ratio is large. This simplifying assumption is not considered in the numerical investigations performed by Liou and Weaver (2005) and Chao (2006). On the contrary, considering the elements provided, such a simplified assumption seems to be

adopted in Schildknecht et al. (2007), where orbital determinations provide estimates for the area-to-mass ratios of a small sample of the newly discovered population of space debris (see Figure 3.14). However, as mentioned before, a fixed value of the Sun–Earth distance induces significant spurious long-period effects, mainly affecting the eccentricity and, therefore, the orbital lifetime, but also the inclination. Consequently, this assumption might introduce important additional residuals in the restitution process of orbital elements as well as parameters such as the area-to-mass ratios.

Chapter 4

Semi-analytical investigations of high area-to-mass ratio geosynchronous space debris including Earth's shadowing effects

> *"The Kessler Syndrome is a scenario, proposed by NASA consultant Donald J. Kessler, in which the volume of space debris in Low Earth Orbit is so high that objects in orbit are frequently struck by debris, creating even more debris and a greater risk of further impacts. The implication of this scenario is that the escalating amount of debris in orbit could eventually render space exploration, and even the use of satellites, too prone to loss to be feasible for many generations."*
>
> IAF website, 2008 (Source: Kessler and Cour-Palais, 1978)

– The results of this chapter have been previously published in Valk and Lemaître (2008) –

As shown in Chapter 3, the effects of direct solar radiation pressure on the motion of a space debris, in particular those with high area-to-mass ratios, have been treated by a number of authors (Anselmo and Pardini, 2005; Chao, 2006; Liou and Weaver, 2005). As an example, we performed analytical and semi-analytical investigations which both emphasize and lead to an insightful understanding of the intrinsic effects of direct solar radiation pressure. In the latter papers as well as in Chapter 3, the authors mainly focus their attention on the long-term variations of both the eccentricity and the inclination vectors. On the other hand, the analytical investigations of direct solar radiation pressure have been derived under the assumption of full illumination by the Sun, that is not taking into account the Earth's shadowing effects on the orbital dynamics. However, most of the space debris orbiting around the Earth are subjected to eclipses of the Sun by the Earth, inducing a great fluctuation in the available solar radiation caught by the objects. Therefore, unlike the classical gravitational forces which affect the motion permanently, the solar radiation pressure perturbation has to be considered as a discontinuous function.

Usually, the Earth's shadowing effects are considered within the framework of a completely numerical integration process. For this purpose, the integration process is only performed during the sunlight portion of the orbit; the radiation pressure being obviously turned off if the radiation is blocked by the Earth between the Sun and the space debris. This approach can be realized by the introduction of a so-called *shadow function* which is equal to one if the space debris is illuminated by the Sun, and to zero if the space debris is in shadow (Ferraz-Mello, 1972).

In this chapter, and as a subsequent review of solar radiation pressure developed in Chapter 3, we will stay within the framework of a mean motion semi-analytical theory, that is only the long-term and secular effects will be derived. In other words, the resulting theory will not include any short-term effects. In practice, the theory consists of the numerical integration of the filtered equations of motion over the short periods onto which we superimpose the mean variation induced by the Earth's shadowing effects.

For the purpose of computing the effects induced by the Earth's shadow, our semi-analytical theory proposes an improvement of the analytical method developed by Aksnes (1976), where the expressions for the perturbations on the orbital elements are given. In this approach, the perturbations accounting for the direct solar radiation pressure with the Earth's shadow are computed on a revolution-by-revolution basis, retaining the original unexpanded form of the shadow function.

In this chapter, this latter approach is adopted and generalized into a more convenient non-singular formalism, particularly suitable for both near-circular and near-equatorial orbits as well as for orbits which transit periodically around null eccentricities and null inclinations.

This chapter is organized as follows. First, in Section 4.1, in opposition to the classical approach where the singular eccentric anomalies at shadow entry and shadow exit are computed, we present our algorithm allowing to compute the non-singular mean longitude at shadow entry and shadow exit.

In Section 4.2, as an extension of the semi-analytical theory developed in Chapters 2 and 3, we show how to apply the above-mentioned algorithm in order to derive the mean net change over each orbital revolution.

Finally, in Sections 4.3 and 4.4, the algorithm is applied by means of numerical integrations of the equations, averaged over the short periods, including radiation pressure with Earth's shadow, J_2, the combined Moon and Sun third-body attraction as well as the long-term effects of the 1:1 resonance occurring for geosynchronous objects. Both the numerical and semi-analytical investigations are performed within the framework of short-, mid- and long-term analyses. Subsequently, these semi-analytical investigations, which are compared with com-

pletely numerical propagations, will lead to a deep understanding of the long-term evolution of the semi-major axis.

4.1 Orbital entry and exit of a space debris from the shadow of the Earth – the algorithm

This section introduces the main algorithm previously mentioned in the introduction: considering a fixed orbit in space, characterized by a set of well-defined elements as well as by the position of the Sun with respect to the Earth, we show how to compute the mean longitudes at shadow entry λ_1 and shadow exit λ_2 of a space debris orbiting around the Earth.

For the purpose of eclipse investigations, we assume that the Earth is perfectly spherical with radius R_e (the Earth's atmosphere is neglected in the present algorithm). Moreover, we also assume that the Sun is infinitely far from the Earth, in such a way that the light rays are parallel in the neighborhood of the Earth. Under these assumptions, the boundary of the Earth's shadow is a circular cylinder with radius R_e, the axis of which is parallel to the Sun–Earth direction. Figure 4.1 illustrates the geometry of the entry and exit points of a space debris with respect to the position of the Sun and of the space debris, respectively.

The geometric constraint of the problem can be obtained by realizing that, upon entry or exit from the Earth's shadow, the angular distance ψ between the radius vector to the Sun $\boldsymbol{r}_\odot$ and the radius vector to the space debris $\boldsymbol{r}$ is solution of the following equation

$$r^2 \cos^2 \psi = r^2 - R_e^2 \,, \tag{4.1}$$

where ψ is taken within the interval $\pi/2 \leq \psi \leq 3\pi/2$, since this is the only domain where a shadow exists (Escobal, 1965). Let us remark that the scalar product of the Sun vector with the space debris vector determines the angular distance at any time

$$\cos \psi = \frac{\langle \boldsymbol{r}_\odot \cdot \boldsymbol{r} \rangle}{r_\odot \, r} \,. \tag{4.2}$$

This formulation is elementary but does not include any direct information on the space debris location on its orbits. However, considering the non-singular equinoctial orbital elements

$$\begin{array}{lll} a & h_e = e \sin(\omega + \Omega) & p_e = \tan(i/2) \sin \Omega \\ \lambda = M + \omega + \Omega & k_e = e \cos(\omega + \Omega) & q_e = \tan(i/2) \cos \Omega \,, \end{array}$$

where a is the semi-major axis, e the eccentricity, i the inclination, ω the argument of perigee, Ω the longitude of the ascending node and M the mean longitude, the radius vector $\boldsymbol{r}(x_c, y_c, z_c)$ of the space debris can be expressed in the equinoctial reference frame $(\boldsymbol{f}, \boldsymbol{g}, \boldsymbol{h})$ using the

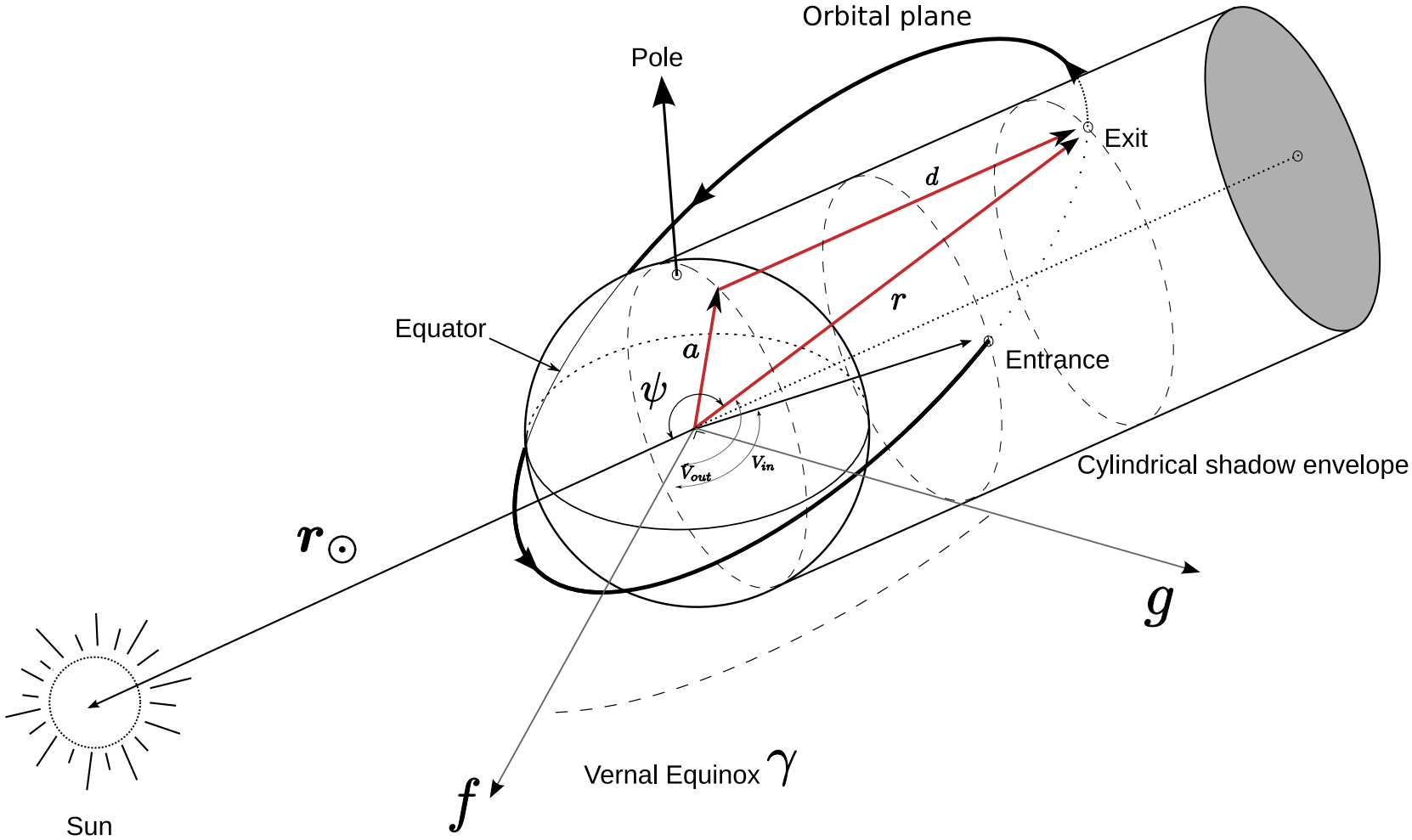

Figure 4.1: Entry and exit orbit geometry for solar radiation pressure in the non-singular equinoctial reference frame (cylindrical shadow). The Earth's shadow is supposed to be cylindrical. The true longitudes at shadow entry and shadow exit are represented by V_{in} and V_{out}, respectively.

following matrix relation

$$\begin{aligned}\begin{bmatrix} x_c \\ y_c \\ z_c \end{bmatrix} &= \frac{1}{1+p_e^2+q_e^2}\begin{bmatrix} 1-p_e^2+q_e^2 & 2p_eq_e & 2p_e \\ 2p_eq_e & 1+p_e^2-q_e^2 & -2q_e \\ -2p_e & 2q_e & 1-p_e^2-q_e^2 \end{bmatrix}\begin{bmatrix} X_e \\ Y_e \\ 0 \end{bmatrix} \\ &= \begin{bmatrix} \boldsymbol{f} & \boldsymbol{g} & \boldsymbol{h} \end{bmatrix}\begin{bmatrix} X_e \\ Y_e \\ 0 \end{bmatrix},\end{aligned}$$

where the quantities $(X_e, Y_e, 0)$ are the coordinates relative to the equinoctial reference frame, which can now be expressed either in terms of the true longitude $V = f+\omega+\Omega$ or, alternatively, of the eccentric longitude $F = E+\omega+\Omega$, where f and E are the true and eccentric anomaly, respectively. The equations are given by

$$\begin{aligned} X_e &= r\cos V &&= a\,(\,(1-h_e^2\eta)\,\cos F + h_ek_e\,\sin F - k_e)\,, \\ Y_e &= r\sin V &&= a\,(\,(1-k_e^2\eta)\,\sin F + h_ek_e\,\cos F - h_e)\,, \end{aligned} \tag{4.3}$$

making use of the auxiliary quantity (Broucke and Cefola, 1973)

$$\eta = \frac{1}{1+\sqrt{1-h_e^2-k_e^2}}\,.$$

As a consequence, the angular distance between the Sun radius vector and the space debris radius vector can be obtained as a function of the true longitude

$$\cos\psi = \beta\cos V + \xi\sin V\,, \tag{4.4}$$

where the quantities β and ξ are defined as

$$\beta = X_\odot\,f_x + Y_\odot\,f_y + Z_\odot\,f_z, \qquad \xi = X_\odot\,g_x + Y_\odot\,g_y + Z_\odot\,g_z\,,$$

where (f_x, f_y, f_z) and (g_x, g_y, g_z) are the Cartesian components of the first two equinoctial reference frame vectors, that is $\boldsymbol{f}$ and $\boldsymbol{g}$, respectively. The quantities $(X_\odot, Y_\odot, Z_\odot)$ are the Cartesian normalized components of the Sun radius vector $\boldsymbol{r}_\odot$ evaluated at some convenient time, say at the time t_i when performing the integration step in the interval $[t_i, t_{i+1}]$. Therefore, the so-called *shadow function* Σ_1 can be computed when the squares of Eqs. (4.2) and (4.4) are made equal

$$\Sigma_1 \equiv p^2(\beta\cos V + \xi\sin V)^2 + R_e^2(1 + h_e\cos V + k_e\sin V)^2 - p^2 = 0\,, \tag{4.5}$$

where we substituted the magnitude of the radius vector $\boldsymbol{r}$, using the following expressions

$$r = \frac{p}{1+k_e\cos V + h_e\sin V}, \qquad p = a(1-e^2)\,.$$

As expected, the shadow function Σ_1 is a second-order equation containing both sine and cosine values of the true longitude. Unfortunately, contrary to the results obtained by Escobal (1965) and Vallado (2001), the equation can not be converted into a simple fourth-order polynomial containing only cosine values of the true longitude because of the double products. Consequently, the equation can not be solved in closed form by quadratic radicals. Let us remark that, at this stage, we could use a numerical technique to solve the equation with respect to the angular variable ψ. However, a drawback of this technique is that the shadow function can admit at most four solutions, whereas numerical methods such as the Newton–Raphson approach (or any other iteration method) only converge to a unique root, which depends on the choice of the initial condition. Moreover, under special circumstances, the numerical convergence of the method is not systematically ensured. Therefore, our method claims to be analytical so far as we can.

Here, we propose to show how the so-called *resultant method* can be used to solve analytically our problem as a system of two algebraic equations in two variables. Let us define the two following Cartesian variables

$$x = \cos V\,, \qquad y = \sin V\,,$$

which satisfy the trivial algebraic relation $\Sigma_2 \equiv x^2 + y^2 - 1 = 0$. As a result, the shadow function Σ_1 can be written as a second-order polynomial function in the variable x

$$\Sigma_1 \equiv a_2(y)\, x^2 + a_1(y)\, x + a_0(y) = 0,$$

whose coefficients a_i are functions of the variable y

$$\begin{aligned} a_2(y) &= R_e^2 h^2 + p^2\beta^2\,, \\ a_1(y) &= 2R_e^2 h + 2R_e^2 h k_e\, y + 2p^2\beta\xi\, y\,, \\ a_0(y) &= R_e^2 k_e^2\, y^2 + 2R_e^2 k_e\, y + p^2\xi^2\, y^2 + R_e^2 - p^2\,. \end{aligned}$$

The resultant is built by computing the determinant of the 4×4 *Sylvester's matrix* (Sylvester, 1840), leading to a fourth-order polynomial function in y, namely the sine of the true longitude

$$\mathcal{R}[\Sigma_1, \Sigma_2](y) \equiv \begin{vmatrix} a_2(y) & 0 & 1 & 0 \\ a_1(y) & a_2(y) & 0 & 1 \\ a_0(y) & a_1(y) & y^2-1 & 0 \\ 0 & a_0(y) & 0 & y^2-1 \end{vmatrix} = A_4\, y^4 + A_3\, y^3 + A_2\, y^2 + A_1\, y + A_0 = 0\,,$$

where the coefficients A_i are considered to be constant during the current interval of integration and are functions of the equinoctial elements

$$\begin{aligned} A_0 &= \left(p^2\beta^2 + R_e^2 - 2\,{R_e}^2 h_e + {R_e}^2 {h_e}^2 - p^2\right)\left(p^2\beta^2 + R_e^2 + 2\,R_e^2 h_e + {R_e}^2 {h_e}^2 - p^2\right), \\ A_1 &= -4\,R_e^2\left(R_e^2 k_e {h_e}^2 - R_e^2 k_e + 2\,p^2\beta\,\xi\,h_e + p^2 k_e - k_e p^2\beta^2\right), \end{aligned}$$

$$
\begin{aligned}
A_2 &= 6\,R_e^4 {k_e}^2 - 2\,p^4\xi^2 - 2\,R_e^4 {h_e}^2 {k_e}^2 + 2\,R_e^2 p^2\xi^2 + 2\,R_e^2 {h_e}^2 p^2 - 2\,p^2\beta^2 R_e^2 \\
&\quad +2\,p^4\beta^2 - 4\,p^2\beta^2 R_e^2 {h_e}^2 + 2\,R_e^2 {h_e}^2 p^2\xi^2 + 2\,p^2\beta^2 R_e^2 {k_e}^2 - 8\,p^2\beta\,\xi\,{R_e}^2 h_e k_e \\
&\quad -2\,R_e^4 {h_e}^4 - 2\,p^4\beta^2\xi^2 - 2\,p^4\beta^4 - 2\,p^2 R_e^2 {k_e}^2 + 2\,R_e^4 {h_e}^2 , \\
A_3 &= 4\,R_e^2 \left(2\,p^2\beta\,\xi\,h_e + R_e^2 k_e {h_e}^2 - k_e p^2\beta^2 + R_e^2 {k_e}^3 + p^2\xi^2 k_e\right) , \\
A_4 &= \left(p^2\xi^2 + R_e^2 k_e^2 - 2\,R_e\,k_e\beta\,p + p^2\beta^2 + 2\,\xi\,R_e\,h_e p + R_e^2 {h_e}^2\right) \times \\
&\quad \left(p^2\xi^2 + {R_e}^2 {k_e}^2 + 2\,R_e\,k_e\beta\,p + p^2\beta^2 - 2\,\xi\,R_e\,h_e p + R_e^2 {h_e}^2\right) .
\end{aligned}
$$

The resultant $\mathcal{R}[\Sigma_1, \Sigma_2]$, as a fourth-order polynomial function, admits at most four real solutions which can be computed in closed form by quadratic radicals using the Descartes method. Moreover, by construction of the resultant polynomial function, these solutions in the sine of the true longitude are solutions of the complete system of equations. Once one has solved for these y values, one can substitute them back into the original equations and solve for the corresponding cosine values of the true longitude through the x variable. Rejection of the two additional spurious roots can be accomplished, considering the fact that only the solutions which lead to

$$\cos\psi = \beta\cos V + \xi\sin V < 0\,,$$

are of any physical meaning, because of the restriction of the interval where a shadow exists (Eq. 4.1). Let us remark that the solutions of Eq. (4.5) could also be computed within the complex formalism. Indeed, by expressing the sine and cosine functions of the true anomaly in terms of an auxiliary quantity $z = e^{iV}$, Eq. (4.5) is easily converted into a fourth-order polynomial in z, which is in turn solved for its real and imaginary part, respectively.

Finally, considering Eqs. (4.3) and solving for the sine and cosine of the eccentric longitude F, yields the following expressions

$$
\begin{aligned}
\cos F &= k_e + \frac{(1-k_e^2\eta)X_e - h_e k_e \eta Y_e}{a\sqrt{1-h_e^2-k_e^2}}, \\
\sin F &= h_e + \frac{(1-h_e^2\eta)Y_e - h_e k_e \eta X_e}{a\sqrt{1-h_e^2-k_e^2}},
\end{aligned}
$$

for determining the eccentric longitude, from which the mean longitude λ can be computed using the generalized Kepler's equation

$$\lambda = F - k_e\sin F + h_e\cos F\,.$$

4.2 Analytical averaging

As mentioned before, the approach pursued in this chapter is based on the one developed by Aksnes (1976). In this theory, the shadowing effects are not taken into account using some specific series expansion of the shadow function such in Ferraz-Mello (1972), Vashkoviak (1974) as well as in Lála and Sehnal (1969). The acceleration of the solar radiation pressure is

kept in its original form and the perturbation is computed on a revolution-by-revolution basis. Under such a formalism, the Gauss variational equations of motion are analytically integrated under the assumption that all the variables on the right-hand sides, except those depending explicitly on the position of the space debris within its orbit, are held constant. Therefore, Kozai (1961) and later Aksnes (1976) derived the perturbations suffered by a satellite that moves in sunlight from eccentric anomaly E_1 to E_2

$$
\begin{aligned}
\delta a &= 2a^3 F |\mathbf{S}\cos E + \mathbf{T}(1-e^2)\sin E|_{E1}^{E_2}\,, \\
\delta e &= a^2\, F\,(1-e^2)^{1/2}\left|\frac{1}{4}\mathbf{S}(1-e^2)^{1/2}\cos 2E + \mathbf{T}\left(\frac{3}{2}E - 2e\sin E + \frac{1}{4}\sin 2E\right)\right|_{E1}^{E_2}\,, \\
\delta i &= a^2\, F\,\mathbf{W}(1-e^2)^{-1/2}\left|\left[-\frac{3}{2}eE + (1-e^2)\sin E - \frac{e}{4}\sin 2E\right]\cos\omega\right. \\
&\quad \left. +(1-e^2)^{1/2}\left(\cos E - \frac{e}{4}\cos 2E\right)\sin\omega\right|_{E1}^{E_2}\,, \\
\sin i\,\delta\Omega &= a^2\, F\,\mathbf{W}(1-e^2)^{-1/2}\left|\left[-\frac{3}{2}eE + (1-e^2)\sin E - \frac{e}{4}\sin 2E\right]\sin\omega\right. \\
&\quad \left. -(1-e^2)^{1/2}\left(\cos E - \frac{e}{4}\cos 2E\right)\cos\omega\right|_{E1}^{E_2}\,, \\
\delta\omega &= -\cos i\delta\Omega + \frac{a^2\, F\,(1-e^2)^{1/2}}{e}\left|\mathbf{S}\left(-\frac{3}{2}E + e\sin E + \frac{1}{4}\sin 2E\right) + \right. \\
&\quad \left. \mathbf{T}(1-e^2)^{-1/2}\left(e\cos E - \frac{1}{4}\cos 2E\right)\right|_{E1}^{E_2}\,, \\
\delta M &= -(1-e^2)^{1/2}(\delta\omega + \cos i\,\delta\Omega) \\
&\quad -3a^2\, F\,\left|\mathbf{S}\left[-\frac{3}{2}eE + \left(\frac{5}{3} + \frac{2}{3}e^2\right)\sin E - \frac{5}{12}e\sin 2E\right]\right. \\
&\quad -\mathbf{T}(1-e^2)^{1/2}\left(\frac{5}{3}\cos E - \frac{5}{12}e\cos 2E\right) \\
&\quad \left. -\left[\mathbf{S}\cos E + \mathbf{T}(1-e^2)^{1/2}\sin E\right](E - e\sin E)\right|_{E1}^{E_2}\,,
\end{aligned}
$$

where $\mathbf{S} = S(0)$, $\mathbf{T} = T(0)$ and $\mathbf{W}$ are the direction cosines of the force, along the radial, along-track and cross-track direction, respectively, and evaluated at true anomaly $f = 0$ (Kozai, 1961). The angles E_1 and E_2 denote the eccentric anomalies at shadow exit and shadow entry, respectively. The author stresses that the expressions for $\delta\omega$ and δM are singular for circular orbits. Similarly, a problem appears for the expressions of $\delta\Omega$ and $\delta\omega$ for equatorial orbits. Through some corrections, the latter algorithm is also assumed to hold when the eccentricity and the inclination are zero. Actually, these singularities can be partly avoided by expanding some eccentricity denominators in powers of the eccentricity or by computing the perturbations directly in the radius vector and in the argument of latitude $u = \omega + f$ (Aksnes, 1976). However, let us remark that these new perturbation expressions always depend on the eccentric anomalies at shadow exit and shadow entry. These angular values can be theoretically determined by solving a fourth-order polynomial equation in the cosine of the eccentric anomaly, but only when the eccentricity and the inclination are not too small (Escobal, 1965).

4.2.1 Analytical evaluations of the perturbations

The solution addressed in this chapter is based on the adoption of the algorithm outlined in Section 4.1, in addition to the non-singular extension of the analytical averaging discussed in Section 4.2. In this approach, the acceleration of the solar radiation pressure including the Earth's shadowing effects is always computed on a revolution-by-revolution basis. Within our theory, the mean net change over an orbital revolution is computed by means of the osculating Hamiltonian disturbing function expressed in terms of non-singular variables. The latter disturbing function is a function of the mean longitude λ and can be therefore averaged taking into account that the space debris crosses the Earth's shadow between shadow entry λ_1 and shadow exit λ_2.

Making use of the Cartesian Poincaré variables $(X_1, Y_1, X_2, Y_2, L, \lambda)$, the osculating Hamiltonian disturbing function of the direct solar radiation pressure is given by (see Eq. 3.8, page 71)

$$\mathcal{H}_{rp} = \sum_{n=0}^{n_{max}} \frac{L^{2n}}{r_{\odot}^{n+1}} \sum_{j=0}^{N_n} \mathcal{A}_j^n(X_1, Y_1, X_2, Y_2, X_{\odot}, Y_{\odot}, Z_{\odot})\, \mathcal{B}_j^n(\lambda)\,,$$

that is a well-known Fourier series in the angular variable, namely the mean longitude λ, whose coefficients are polynomials in the Cartesian variables $X_i,\ Y_i,\ X_{\odot},\ Y_{\odot},\ Z_{\odot}$. For similar developments and further details, we refer to Chapters 2 and 3.

Thanks to the Hamiltonian formalism, the associated differential system of equations has been easily derived. More precisely, we have

$$\begin{aligned} \dot{X}_i &= \frac{1}{L}\frac{\partial \mathcal{H}}{\partial Y_i}\,, \qquad \dot{Y}_i = -\frac{1}{L}\frac{\partial \mathcal{H}}{\partial X_i}\,, \qquad i = 1, 2 \\ \dot{\lambda} &= \frac{\partial \mathcal{H}}{\partial L} - \frac{1}{2L}\left[\sum_{i=1}^{2}\frac{\partial \mathcal{H}}{\partial X_i}X_i + \sum_{i=1}^{2}\frac{\partial \mathcal{H}}{\partial Y_i}Y_i\right], \qquad \dot{L} = -\frac{\partial \mathcal{H}}{\partial \lambda}\,. \end{aligned} \tag{4.6}$$

This differential system of osculating equations can be therefore analytically integrated with respect to the mean longitude λ, if all the variables on the right-hand side in the polynomial functions are considered as constants. Subsequently, the long-term mean variations, over a complete revolution of the space debris, are given by

$$\begin{aligned} \Delta\overline{X}_i &= \frac{1}{L}\left\{\frac{\delta\overline{\mathcal{H}}_{rp}}{\delta Y_i} - \int_{\lambda_1}^{\lambda_2}\frac{\delta \mathcal{H}_{rp}}{\delta Y_i}d\lambda\right\} \\ &\underset{not}{=} \overline{\mathcal{H}}_{rp}^{Y_i} - \mathcal{S}_{rp}^{Y_i}(\lambda_1, \lambda_2)\,, \end{aligned} \tag{4.7}$$

and similarly

$$\begin{aligned} \Delta\overline{Y}_i &= -\frac{1}{L}\left\{\frac{\delta\overline{\mathcal{H}}_{rp}}{\delta X_i} - \int_{\lambda_1}^{\lambda_2}\frac{\delta \mathcal{H}_{rp}}{\delta X_i}d\lambda\right\} \\ &\underset{not}{=} \overline{\mathcal{H}}_{rp}^{X_i} - \mathcal{S}_{rp}^{X_i}(\lambda_1, \lambda_2)\,, \end{aligned} \tag{4.8}$$

where $\overline{\mathcal{H}}_{rp}$ is the first-order averaged Hamiltonian disturbing function

$$\overline{\mathcal{H}}_{rp} = \sum_{n=0}^{n_{max}} \overline{\mathcal{R}}_n = \sum_{n=0}^{n_{max}} \frac{L^{2n}}{r_{\odot}^{n+1}} \sum_{j=0}^{N_n} \mathcal{A}_j^n(X_1, Y_1, X_2, Y_2, X_{\odot}, Y_{\odot}, Z_{\odot}) \,.$$

In both Eqs. (4.7) and (4.8), the quantities $\overline{\mathcal{H}}_{rp}^{Y_i}$, $\overline{\mathcal{H}}_{rp}^{X_i}$ denote the mean variations in the orbital elements X_i and Y_i, respectively, without considering the Earth's shadowing effects, from which we subtract the mean net change $\mathcal{S}_{rp}^{Y_i}(\lambda_1, \lambda_2)$ and $\mathcal{S}_{rp}^{X_i}(\lambda_1, \lambda_2)$ when the space debris crosses the Earth's shadow between shadow entry λ_1 and shadow exit λ_2. Let us remark that, whenever the space debris does not encounter the Earth's shadow within its orbit over a revolution, the functions $\mathcal{S}_{rp}$ equal zero, by fixing, say $\lambda_1 = \lambda_2$. It is also worth noting that the mean net changes $\mathcal{S}_{rp}$ are defined as integrals of functions expanded into Fourier series. As a consequence, these integrations can be easily performed in a completely analytical way.

In addition, the long-term variation of the semi-major axis over a complete revolution is simply related to

$$\Delta\overline{L} \;=\; [\mathcal{H}_{rp}]_{\lambda_1}^{\lambda_2} = \mathcal{H}_{rp}(\lambda_2) - \mathcal{H}_{rp}(\lambda_1) \,. \tag{4.9}$$

4.2.2 How to apply the semi-analytical theory

Let us assume that a set of well-defined variables, such as Poincaré variables or equinoctial variables, are given for an initial time t_0.

1. For the purpose of numerical integration of the filtered equations of motion, we consider the differential system of equations (4.6). At each step of the integration process, the net change of the variables can be computed for all the perturbations excluding the Earth's shadowing effects.

2. By means of the algorithm mentioned before, the mean longitude at shadow entry and shadow exit are computed within the assumption that the orbit is held frozen during the integration time step.

3. From Eqs. (4.7), (4.8) and (4.9), the perturbations in the elements are computed on a revolution-by-revolution basis. If the integration time step is lower than the orbital period of the space debris, the perturbations induced by the Earth's shadow are linearized over the current integration time step.

4. Summing the latter perturbations with the perturbations obtained in the first step, gives the total perturbations in the elements.

4.3 Short- and mid-term investigations for objects with high area-to-mass ratios

In the framework of short-term investigations, numerical integrations of the osculating equations of motion, without taking into account eclipses, show that the direct solar radiation pressure mainly produces short-period effects (1 sidereal day) on the semi-major axis. These short-period effects are characterized by high amplitudes, the order of which is proportional to the area-to-mass ratio A/m. Considering the Gaussian equations of motion, the acceleration of a near-circular and near-equatorial object is given by

$$\frac{\mathrm{d}a}{\mathrm{d}t} = -C_r\, P_r\, \frac{A}{m}\, \frac{2}{n}\, \cos^2\frac{\epsilon}{2}\, \sin(\lambda_\odot - V)\,.$$

Let us recall that C_r is the non-dimensional "reflectivity" coefficient which depends on the optical properties of the space debris surface; $P_r = 4.56 \times 10^{-6}\ \mathrm{N/m^2}$ is the radiation pressure for an object located at a distance of 1 AU; ϵ is the obliquity of the Earth with respect to the ecliptic; $\lambda_\odot$ is the ecliptic longitude of the Sun and n is the mean motion, that is $2\pi/\mathrm{day}$ for geosynchronous space debris.

Consequently, a first estimation of the short-period amplitudes χ appearing in the semi-major axis can be derived

$$\chi = 2\, C_r\, P_r\, \frac{A}{m} \cos^2\frac{\epsilon}{2}\, \frac{1}{n^2}\,.$$

As a matter of fact, these high amplitude short-period effects are responsible for the long-term variations of the semi-major axis, when considering solar radiation pressure with the perturbations induced by the Earth's shadowing effects. Actually, in the latter case, the radiation pressure cannot be considered as a conservative force anymore (Milani et al., 1987), (Anselmo et al., 1983), what is due to the breakage of short-period effects during the transit time through the shadow of the Earth. On the contrary, the radiation pressure does not induce any significant short-period variation of the other orbital elements. This statement explains why radiation pressure with eclipses does not affect significantly the other orbital elements, in contrast with the variations of the semi-major axis. These remarks are in agreement with Anselmo and Pardini (2007b) where, among other results, the authors present geosynchronous objects propagations with and without eclipses.

Let us recall that in the theoretical context of classical geostationary space debris ($A/m \ll 1\ \mathrm{m^2/kg}$), the orbital plane remains reasonably close to the equatorial plane. As a consequence, the Sun moves through the orbital plane twice per year. As a matter of fact, a classical geostationary space debris will experience eclipses around the spring and autumn equinoxes. During these two eclipse seasons, the space debris transits through the Earth's shadow once per day, leading to eclipses of the Sun by the Earth. Figure 4.2 illustrates the two eclipse seasons occurring over a year.

Let us now consider the evolution of several higher area-to-mass ratio space debris subjected to solar radiation pressure with eclipses; we analyze the dynamical evolution of objects over both short-term (a few days) and mid-term (a few years) time scales.

The simulations were carried out by means of both completely numerical integrations and semi-analytical extrapolations, that is numerical integrations of the filtered equations of motion, including the Earth's shadowing effects. The chosen orbits correspond to initial geo-

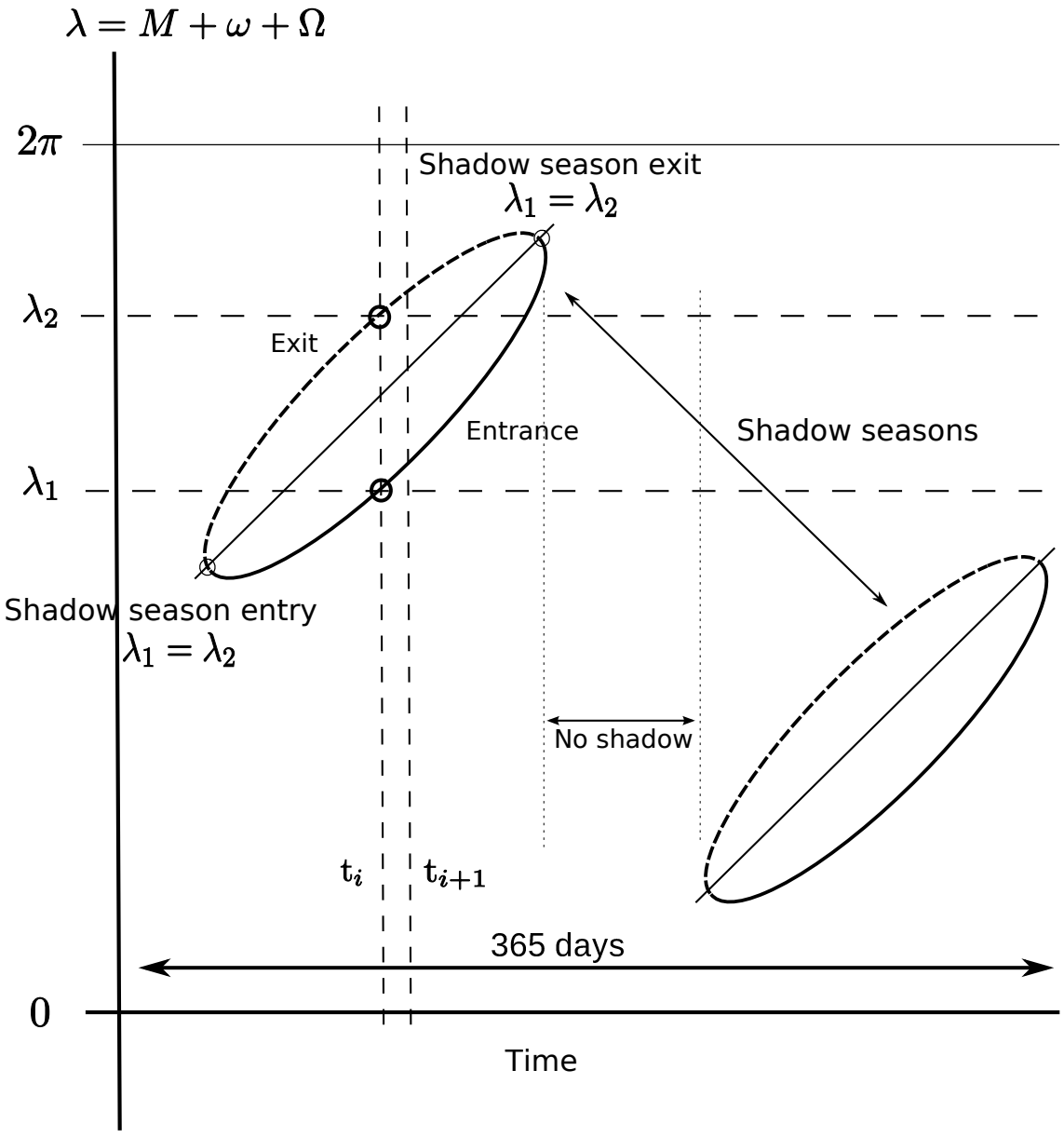

Figure 4.2: Schematic evolution of the shadow transits over a year for near-equatorial orbits. Twice per year, the Sun moves through the orbital plane of motion, leading to eclipse seasons. By means of the before-mentioned algorithm (Section 4.1), the mean longitudes at shadow entry λ_1 and shadow exit λ_2, as well as the mean change over an orbital period, are determined at each step of the integration process.

stationary space debris with area-to-mass ratios between 1 to $20\ \mathrm{m}^2/\mathrm{kg}$. The top graphs of Figure 4.3a-c shows the short-term evolution of the semi-major axis (the osculating semi-major axis obtained by numerical integration) and its mid-term evolution (obtained by the semi-analytical approach), over 5 years, for three area-to-mass ratios (5, 10 and $20\ \mathrm{m}^2/\mathrm{kg}$). The bottom graphs of the same figures show the mid-term evolution of the eccentricity for the same period.

The amplitudes of the short-term variations, observed in the osculating semi-major axis, are obviously directly proportional to the area-to-mass ratio. The sign of variation of the cumulated mean change over an eclipse season, Δa_{tot}, depends on the sign of variation of the mean eccentricity over this period. Indeed, an increase of the eccentricity induces a decrease of the mean semi-major axis during the eclipse season. Figure 4.4 represents schematically the mean and osculating semi-major axis over an eclipse season for an increasing eccentricity during a shadow transit. A similar plot could be drawn for a decreasing eccentricity, with a resulting increasing semi-major axis over an eclipse season. Let us now plot the cumulated mean change Δa_{tot} over an eclipse season with respect to the area-to-mass ratio; the behavior is clearly quadratic (Figure 4.5). Besides the understanding of the dynamics occurring in the semi-major axis, these results also report to what extent our semi-analytical theory is in good agreement with accurate numerical integrations. The theory seems to define accurately the so-called mean motion even with the simplifying assumptions which are made.

It is worth stressing that a particular attention has to be given when making comparisons between osculating orbits and mean orbits derived within the context of mean orbital theories. As shown in Figure 4.3a-c, the chosen osculating initial conditions do not have to be equal to the initial conditions given in the semi-analytical extrapolations. Indeed, the osculating initial conditions have to be computed, taking into account the presence of short-term variations. This is the reason for which we indicate the initial osculating semi-major axis on the graphs; it does not coincide with the initial mean semi-major axis and it is systematically distant from the exact equilibrium. Fortunately, thanks to the chosen Hamiltonian formalism, the conversion between osculating and averaged initial conditions can be realized within the framework of Lie transforms theory (Deprit, 1969; Deprit and Rom, 1970; Henrard, 1970). For instance, within the context of a first order averaging process over the short periods, the transformation between both the osculating and mean semi-major axis related variables L and L', is given by (expanded up to order 1)

$$L = L' - \left\{ \frac{\partial \mathcal{W}_1}{\partial \lambda} \right\} \Bigg|_{E'} ,$$

where E' stands for the complete set of mean variables and where $\mathcal{W}_1$ is the first-order generating function, that is a function of the discarded "short-periodic" terms, which is computed in the following by an analytical integration with respect to the fast angle λ (see Eq. F.6, page 178).

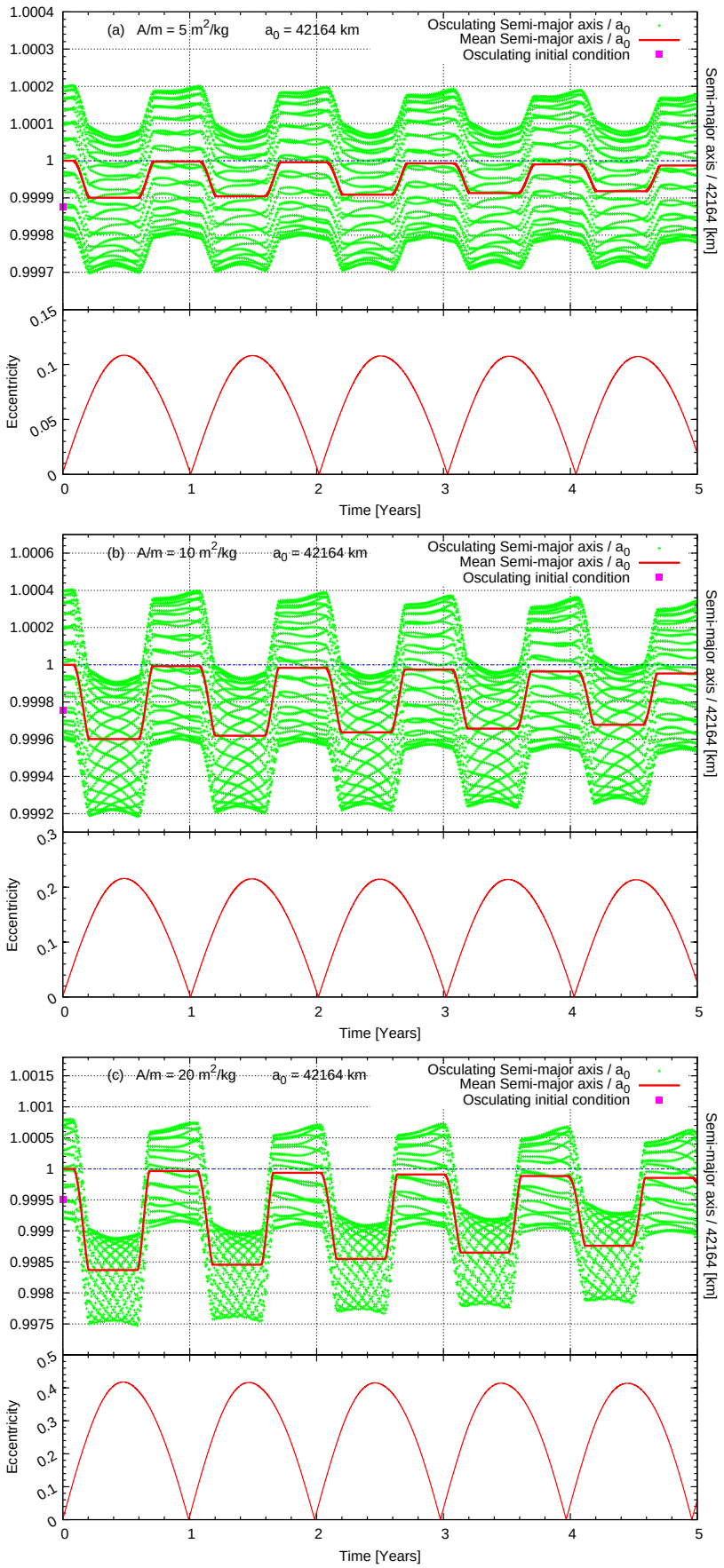

Figure 4.3: Short-term (1 day) and mid-term (a few years) evolution of the semi-major axis over 5 years. The amplitude of variation of the short periods as well as the cumulated variation Δa_{tot} over an eclipse season is represented for three area-to-mass ratios. The mid-term evolution of the eccentricity is given below for each case.

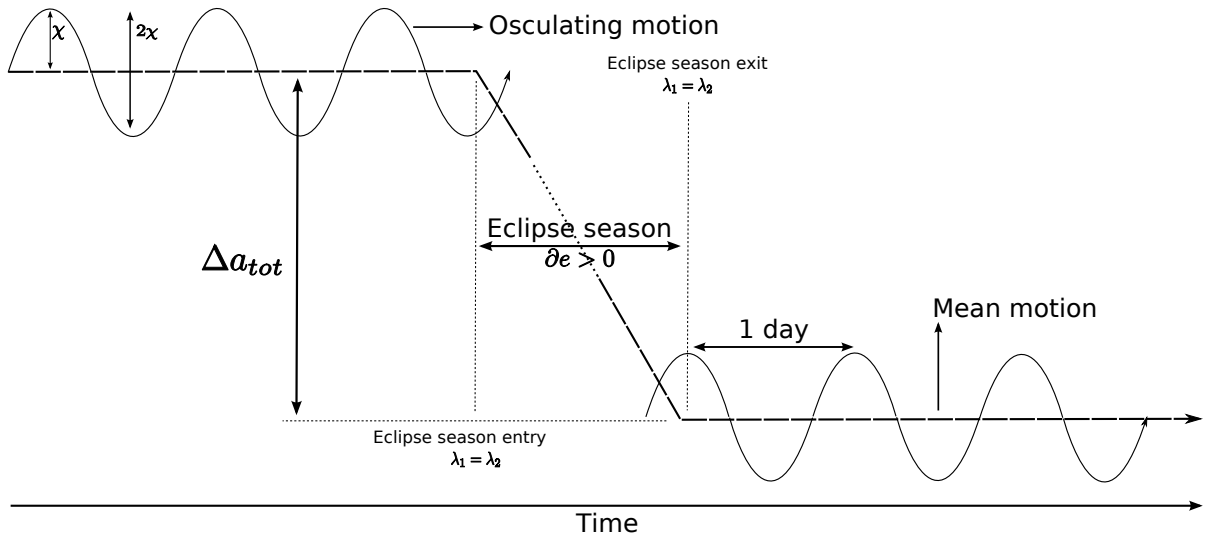

Figure 4.4: Schematic evolution of the mean and osculating semi-major axis over an eclipse season. The sign of the cumulated variation of the mean semi-major axis Δa_{tot} depends on the sign of variation of the mean eccentricity during the eclipse season.

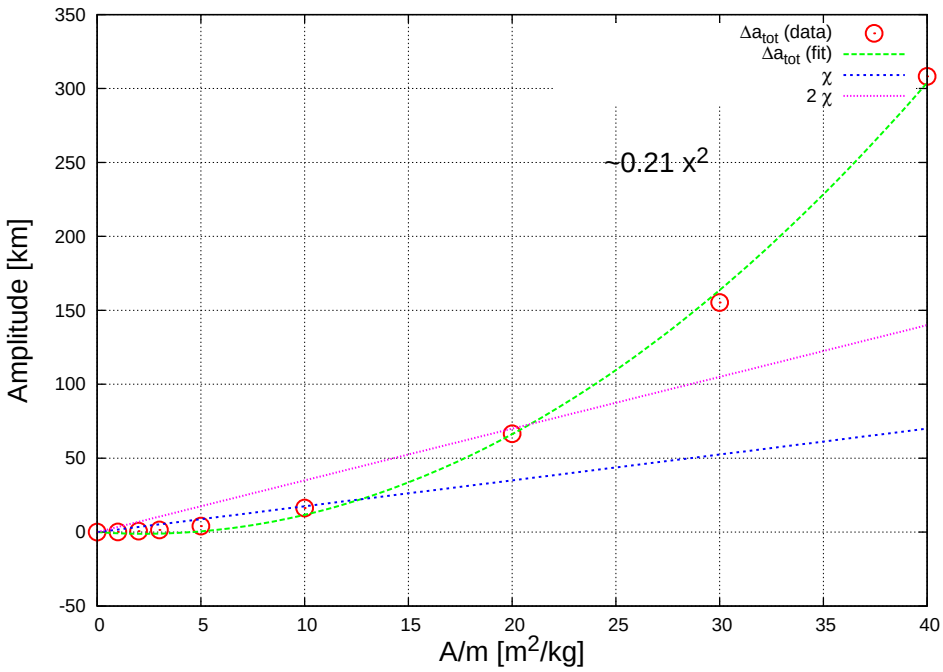

Figure 4.5: Amplitudes of both short-term variations χ and cumulated mean change over an eclipse season Δa_{tot}, as a function of the area-to-mass ratio.

Similar transformations are available for the remaining orbital elements. For further details, we refer to Appendix F (Section F.4, page 178), where such transformations between mean and osculating elements are given.

4.4 Long-term investigations for objects with high area-to-mass ratios

In Figure 4.3, besides the cumulated mean change over eclipse seasons, there is no significant long-term variation of the semi-major axis. During this 5 years period, the dates and duration of the eclipse seasons are almost the same for every year. As a consequence of the low inclination of the orbits with respect to the equatorial plane, each eclipse season lasts more or less 46 days, from February 26 to April 13 (spring eclipse season) and from August 31 to October 16 (autumn eclipse season) (Soop, 1994). Actually, even for moderate area-to-mass ratios, the radiation pressure, coupled with J_2 and the third-body attractions, induces only small to moderate variations of the inclination.

For the purpose of long-term investigations ($\sim$ 25 years) of the semi-major axis, we also performed several propagations by means of both complete numerical integrations and numerical integrations of the filtered equations of motion, including Earth's shadowing effects. The chosen model of forces included the second zonal harmonic J_2 and the luni-solar perturbations. These numerical investigations were performed for various high area-to-mass ratios.

In each case, we show both the dynamical evolution of the osculating semi-major axis and the mean semi-major axis over a period of 27 years. In addition, we plot the evolution of the eclipse seasons by means of the mean longitude at shadow entry and shadow exit, superimposed with the evolution of the longitude of the ascending node. Finally, the long-term evolution of the inclination is represented.

4.4.1 Earth's shadow, J_2, third-body – moderate area-to-mass ratios

On the one hand, for $A/m = 5\ \mathrm{m}^2/\mathrm{kg}$ (Figure 4.6), the inclination remains moderate and the eclipse seasons present a regular pattern over time. The consequence is a small to moderate long-term variation of the semi-major axis. For the sake of clarity, it is important to note that the growth of the duration of the eclipse seasons due to an increasing inclination can not explain completely the long-term evolution of the semi-major axis. In fact, in the latter case, the length of the eclipse seasons has almost increased linearly by a few days (Figure 4.7, bottom), while the semi-major axis seems to present a more intricate evolution. In particular, the cumulated variation over eclipse seasons seems to decrease in the first part of the integration process, reaches very small amplitudes after 11 years and finally increases. This specific dynamics is directly related to the asymmetry between the length of the spring eclipse seasons and the length of the autumn eclipse seasons. More precisely, the lengths of the spring eclipse seasons always seem to be greater than those of the autumn eclipse seasons (Figure 4.7, bottom). To

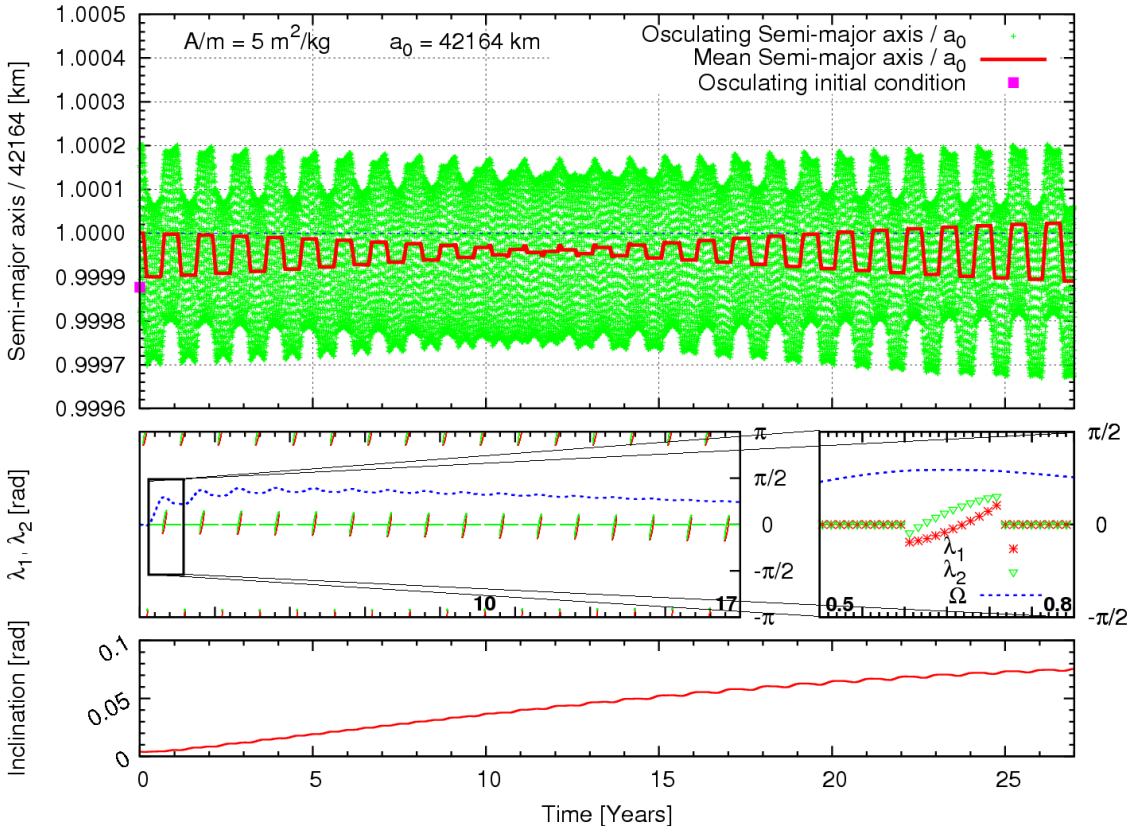

Figure 4.6: [Top] Long-term semi-major axis evolution taking into account J_2 and solar radiation pressure with Earth's shadowing effects: mean semi-major axis (solid curve), osculating semi-major axis (dotted curve). Area-to-mass ratio and mean initial conditions are $A/m = 5\ \mathrm{m}^2/\mathrm{kg}$ and $a_0 = 42\,164\ \mathrm{km},\ e_0 = 0,\ i_0 = 0,\ \Omega_0 = \omega_0 = M_0 = 0$ rad, respectively. The osculating semi-major axis initial condition is $a_0^\star = 42\,158.810\ \mathrm{km}$ (solid square). [Middle left] Mean longitudes at shadow entry λ_1 and shadow exit λ_2 superimposed with the longitude of the ascending node Ω (dashed curve). [Middle right] A blow-up of the first eclipse season. [Bottom] Long-term inclination evolution.

explain this behavior, we investigated the values of the eccentricities at both entry and exit of the eclipse seasons. As indicated in Figure 4.7 (top), it is clear that the eccentricities at both entry and exit of the eclipse seasons change over time. The eccentricities are also clearly greater during the spring seasons than during the autumn seasons, explaining the differences of duration of the seasons between spring and autumn. It is also clear that, after 11 years of integration, the eccentricities at both shadow entry and shadow exit converge to the same values, leading therefore to vanishing cumulated mean changes of the semi-major axis over the eclipse seasons.

4.4.2 Earth's shadow, J_2, third-body – high area-to-mass ratios

On the other hand, the situation is more elaborate for higher area-to-mass ratios. In this case, the inclination reaches larger values. In particular, the inclination vector nearly describes a circle with fixed center coordinates depending on the selected area-to-mass ratio. Figure 4.8

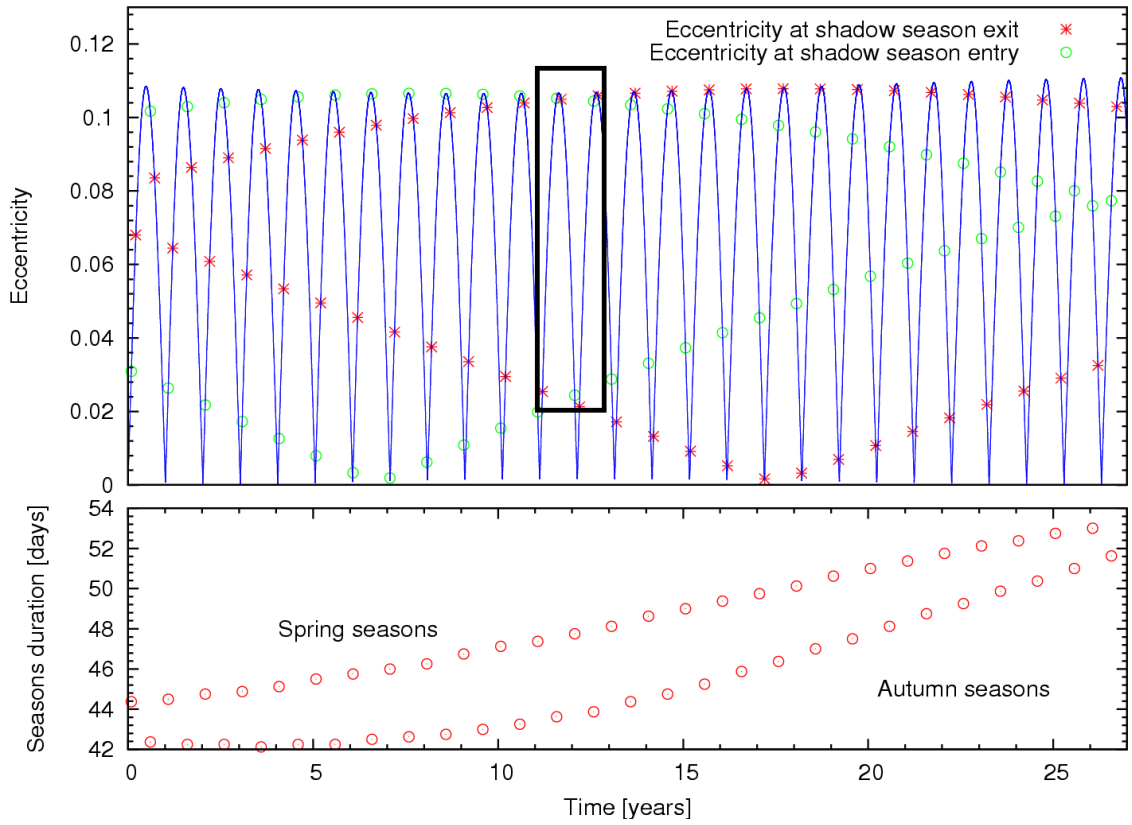

Figure 4.7: $A/m = 5\ \mathrm{m}^2/\mathrm{kg}$. [Top] Eccentricities values at both entry and exit of the eclipse seasons, superimposed with the long-term eccentricity evolution. The solid dark rectangle underlines the region where the eccentricities at both entry and exit of the eclipse seasons are similar. [Bottom] Evolution of the length of eclipse seasons.

illustrates schematically the evolution of the inclination when taking into account the second zonal harmonic J_2 and possibly the solar radiation pressure with eclipses (even if the Earth's shadowing effects do not induce significant effects on the inclination), as well as the combined Moon and Sun third-body attraction. For $A/m = 0\ \mathrm{m}^2/\mathrm{kg}$, that is not taking into account the effects of the radiation pressure, a space debris presents the behavior of a typical abandoned geosynchronous spacecraft, with a maximum inclination of 15 degrees and a periodicity of about 54 years (see Chapter 2 as well as Allen and Cook, 1964 and Agrawal, 1986). However, for $A/m = 10\ \mathrm{m}^2/\mathrm{kg}$, the inclination almost reaches the specific value corresponding to the obliquity of the Earth on the ecliptic. Let us also remark that the longitude of the ascending node always converges to zero when the inclination reaches its maximum.

As a consequence of the large variation of the inclination, both the time of the eclipse season and its total length change considerably over time (Figure 4.9, bottom).The longer is the season, the smaller is the angle between the orbital plane and the ecliptic plane. As an illustration, Figure 4.10 shows the evolution of the semi-major axis for an area-to-mass ratio equal to $10\ \mathrm{m}^2/\mathrm{kg}$. At the beginning of the integration process, the inclination remains small to moderate, leading to moderate variations of the semi-major axis such as in Figure 4.6. Moreover,

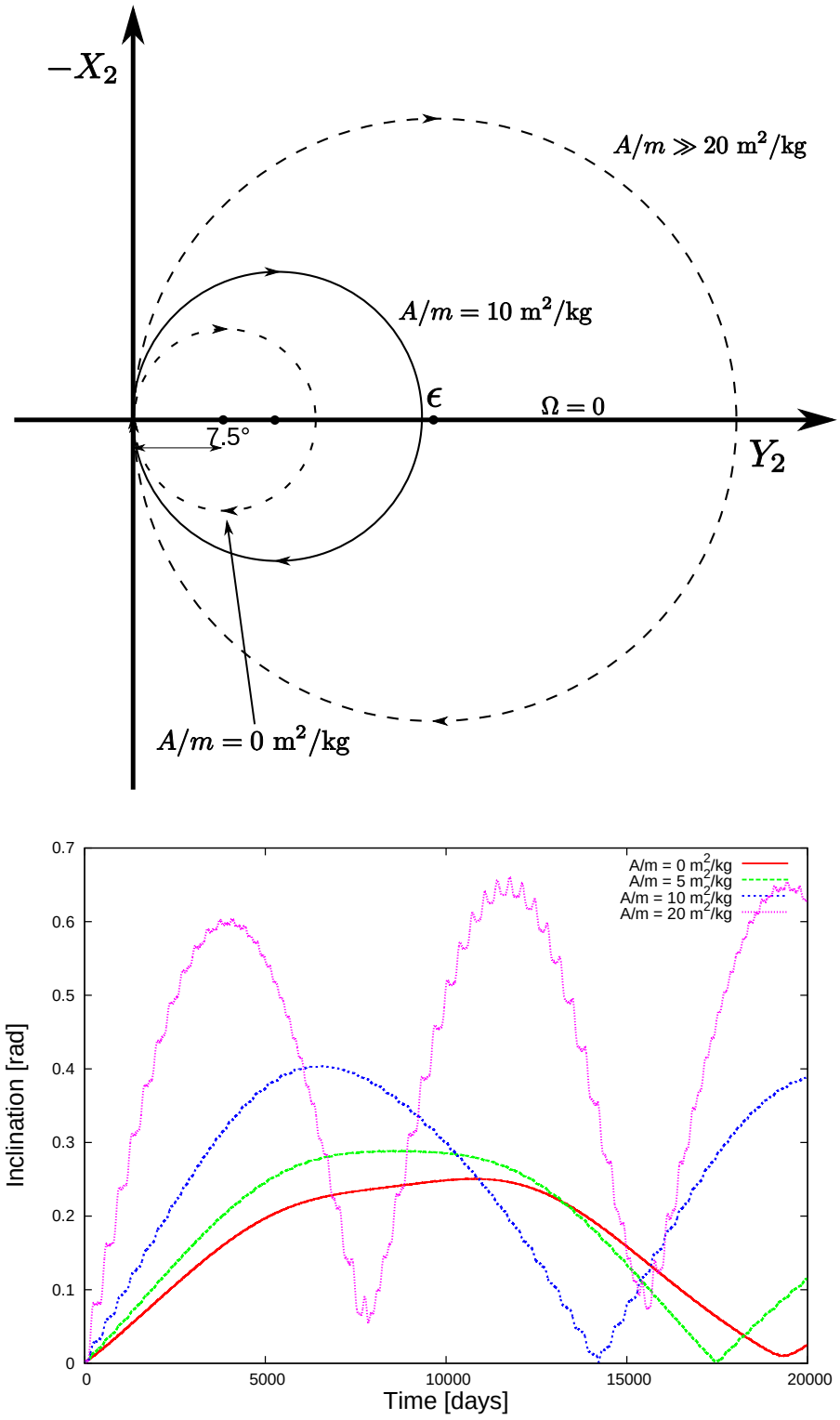

Figure 4.8: [Top] Schematic long-term evolution of the inclination vector in $(Y_2, -X_2) \simeq (\sin i \cos\Omega, \sin i \sin\Omega)$ phase space, taking into account J_2, solar radiation pressure and the combined Moon and Sun third-body attraction. [Bottom] Evolution of the inclination for various area-to-mass ratios.

the decrease of the cumulated variations on the semi-major axis, observed after 5 years, can also be explained by the evolution of the eccentricities at both entry and exit of the eclipse seasons as indicated in Figure 4.9 (top). After 20 years of integration, the inclination reaches its maximum. The eclipse seasons become "permanent" for a long time, since the orbital plane of motion is almost parallel to the ecliptic. Consequently, the semi-major axis is subjected to large variations without any conservative regime, due to the lack of a complete illumination region over successive orbital revolutions (see Figure 4.11). During this particular period, the semi-major oscillates with a period of 1 year, following what we called the *eccentricity law*, that is *increasing eccentricity during eclipse seasons leads to decreasing mean semi-major axis, and conversely*.

The patterns illustrated in Figure 4.12, corresponding to $A/m = 15\ \mathrm{m}^2/\mathrm{kg}$, mainly show the same dynamics as for $A/m = 10\ \mathrm{m}^2/\mathrm{kg}$. As expected, the amplitudes of the variation of the semi-major axis are larger than previously, what is due to a larger area-to-mass ratio. However, the large variations of the semi-major axis occur faster, since the rate of the orbital pole precession, as well as the variation of the inclination, increase with higher A/m.

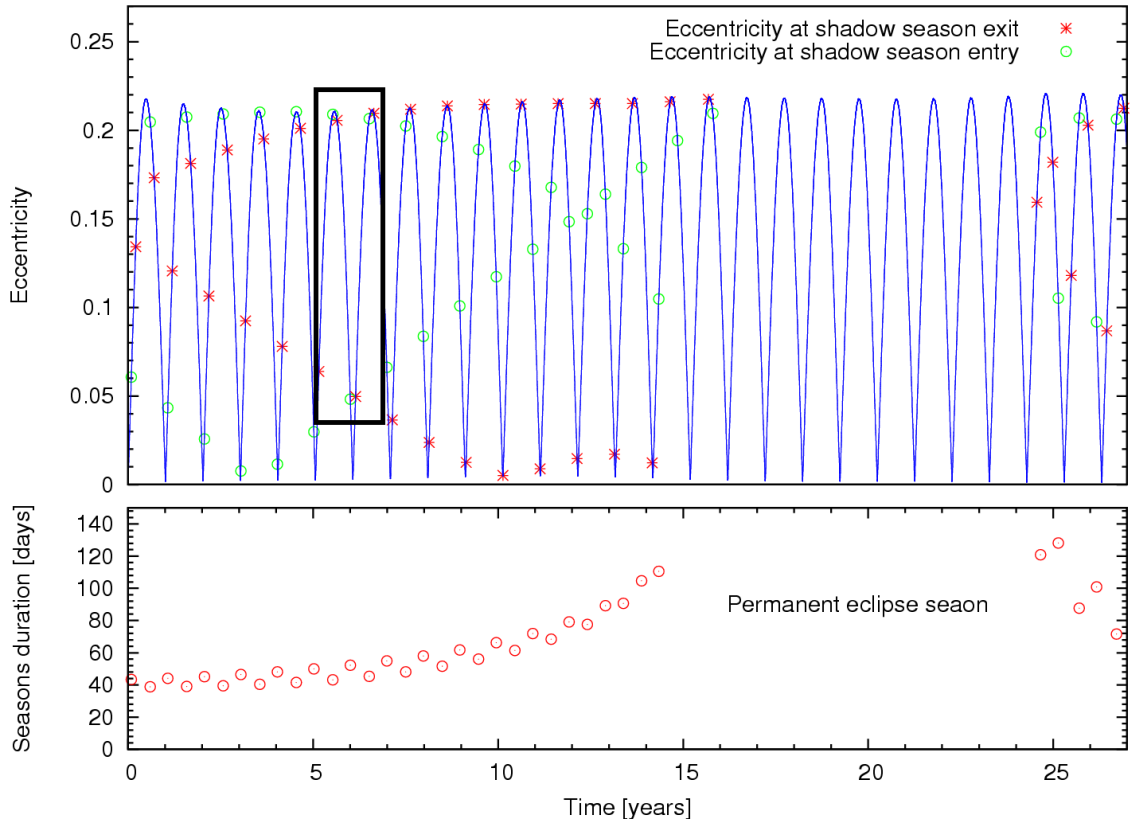

Figure 4.9: $A/m = 10\ \mathrm{m}^2/\mathrm{kg}$. [Top] Eccentricities values at both entry and exit of the eclipse seasons, superimposed with the long-term eccentricity evolution. The solid dark rectangle underlines the region where the eccentricities at both entry and exit of the eclipse seasons are similar. [Bottom] Evolution of the length of the eclipse seasons.

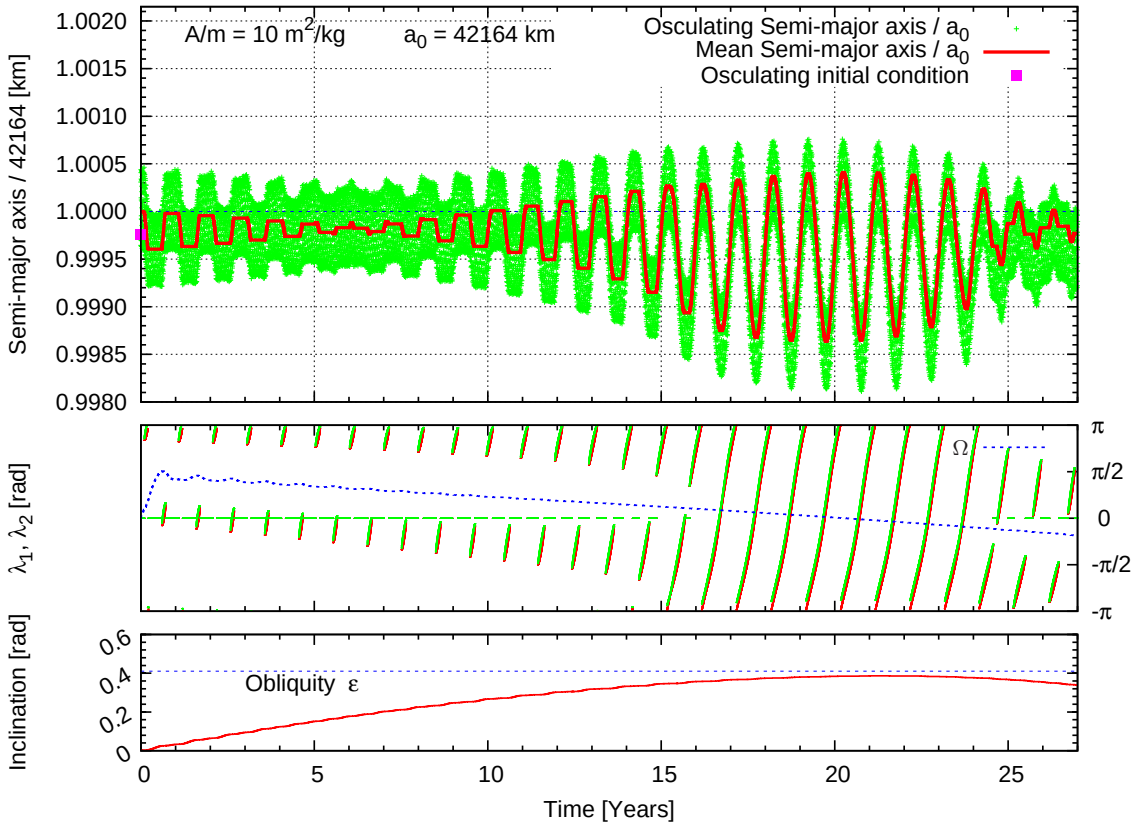

Figure 4.10: [Top] Long-term semi-major axis evolution taking into account J_2, solar radiation pressure with Earth's shadowing effects and the combined Moon and Sun third-body attraction: mean semi-major axis (solid curve), osculating semi-major axis (dotted curve). Area-to-mass ratio and mean initial conditions are $A/m = 10\ \mathrm{m}^2/\mathrm{kg}$ and $a_0 = 42\ 164\ \mathrm{km}, e_0 = 0, i_0 = 0, \omega_0 = \Omega_0 = M_0 = 0$ rad, respectively. The osculating semi-major axis initial condition is $a_0^\star = 42\ 153.621\ \mathrm{km}$ (solid square). [Middle] Mean longitudes at shadow entry λ_1 and shadow exit λ_2 superimposed with the longitude of the ascending node Ω (dashed curve). [Bottom] Long-term inclination evolution.

In all the previous investigations, our homemade semi-analytical theory gives an insightful understanding of the semi-major axis dynamics. The extrapolation of the mean motion is in complete agreement with the numerical integrations, even for longer time scales such as 25 years. Moreover, let us emphasize that the extrapolation of the mean orbital motion is considerably faster than in classical numerical integrations. Indeed, the integration of the filtered differential system of equations is made with a large integration time step of the order of the orbital period (1 day). This fact hugely reduces the time of integration as well as the round off and truncating errors (Exertier and Métris, 1995).

4.4.3 Earth's shadow, J_2, third-body and resonant effects

Finally, the patterns illustrated in Figure 4.13 (page 118) show the evolution of the semi-major axis when including the 1:1 resonance effects in addition to J_2, the radiation pressure with the Earth's shadow and the third-body attractions. The propagation is performed with an area-

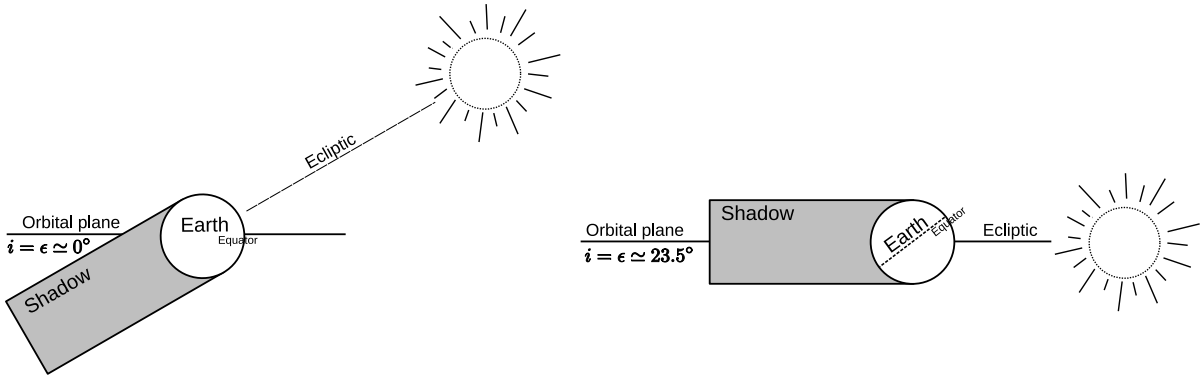

Figure 4.11: The duration of eclipse seasons depends on inclination of the space debris with respect to the orbital plane of the Sun (ecliptic). When the inclination is small, the space debris is only affected at equinox periods (short eclipse seasons) whereas it is affected at each orbital revolution when the inclination reaches a value close to the obliquity value (long eclipse seasons – "permanent" seasons).

to-mass ratio equal to $10\ \mathrm{m}^2/\mathrm{kg}$. Since the 1:1 resonance effects do not affect significantly the inclination, the eclipse seasons display partially the same evolution over time as in Figure 4.10. The inclination always reaches its maximum after 20 years of integration, leading to large yearly variations of the semi-major axis. Furthermore, the dynamics of the semi-major axis presents an additional long-term variation, clearly apparent at the beginning of the integration window. The additional period can easily be related to the long-term effects induced by the 1:1 resonance. Indeed, it is well known that geostationary objects are subjected to a long-term variation of both the semi-major axis and mean longitude (libration around stable equilibrium longitudes). Moreover, the period of variation significantly depends on the chosen initial conditions with respect to both stable and unstable equilibrium points (Chao, 2005). In this latter propagation, we consider an initial mean longitude close to the first stable equilibrium point ($\sim 75^\circ$ E). In this case, the object in consideration begins immediately to oscillate with a period close to the *proper period* of geostationary objects (see Subsection 2.6.2), that is 818.7 days even though the evolution is considerably more intricate. Let us remark that at the end of the integration interval the agreement between the mean semi-major axis and the osculating one seems to break up. However, these significant differences are not the consequences of the simplifying assumptions adopted in the semi-analytical method. Indeed, high area-to-mass space debris, subjected to both radiation pressure and the 1:1 resonance effects, seems to present highly unstable dynamics. Further investigations have to be made to quantify the order of instability as a function of both the area-to-mass ratios and the initial conditions. These further analyses should clarify the regular and chaotic components of the phase space. These investigations are the main objective of the next chapter.

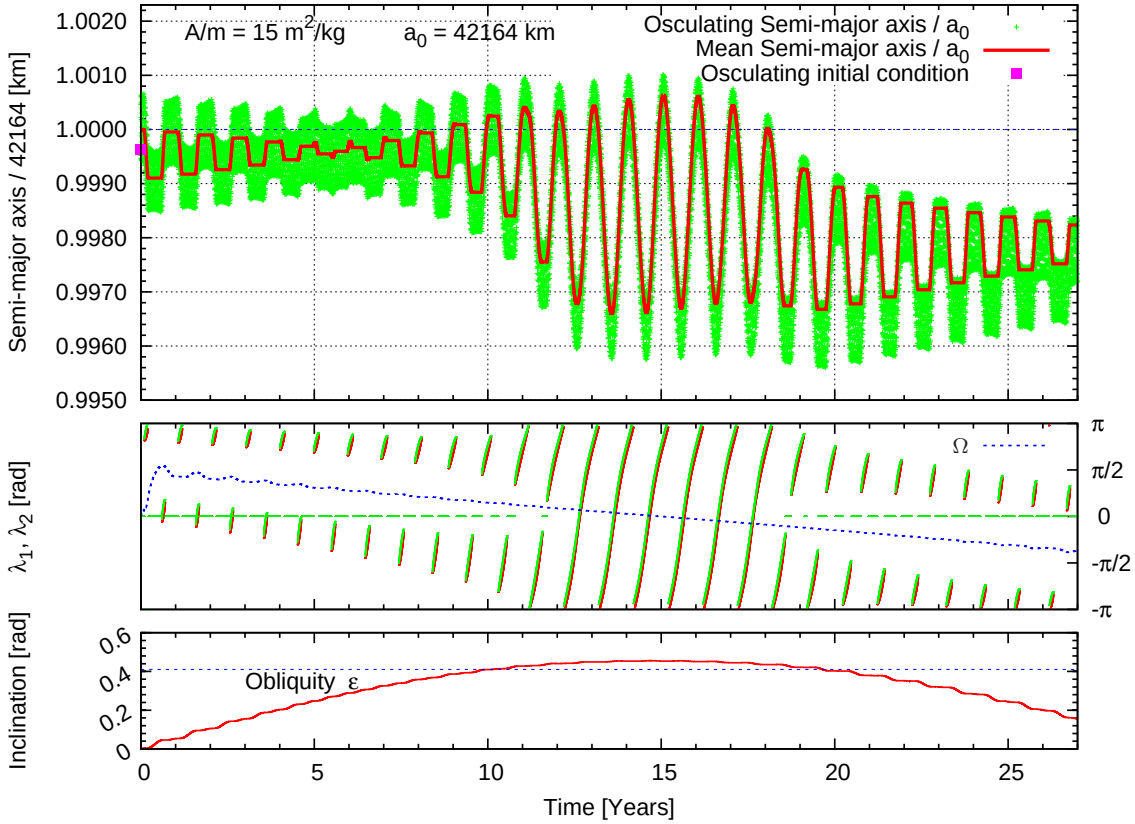

Figure 4.12: [Top] Long-term semi-major axis evolution taking into account J_2, solar radiation pressure with Earth's shadowing effects and the combined Moon and Sun third-body attraction. Area-to-mass ratio and mean initial conditions are $A/m = 15\ \mathrm{m}^2/\mathrm{kg}$ and $a_0 = 42\,164\ \mathrm{km}, e_0 = 0, i_0 = 0, \omega_0 = \Omega_0 = M_0 = 0$ rad, respectively. The osculating semi-major axis initial condition is $a_0^\star = 42\,148.432\ \mathrm{km}$. [Middle] Mean longitudes at shadow entry λ_1 and shadow exit λ_2 superimposed with the longitude of the ascending node Ω (dashed curve). [Bottom] Long-term inclination evolution.

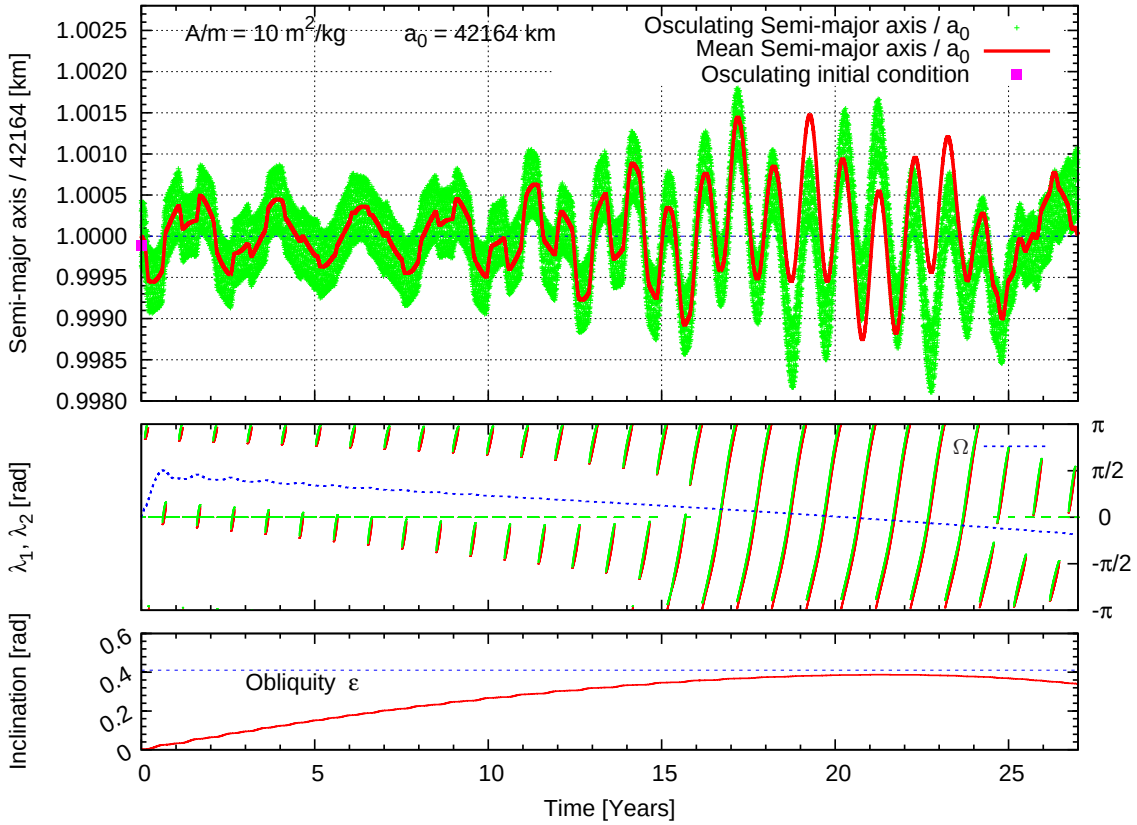

Figure 4.13: [Top] Long-term semi-major axis evolution taking into account J_2, solar radiation pressure with Earth's shadowing effects, the combined Moon and Sun third-body attraction and the 1:1 resonance induced by the C_{22} and S_{22} tesseral harmonics: mean semi-major axis (solid curve), osculating semi-major axis (dotted curve). Area-to-mass ratio and mean initial conditions are $A/m = 10\ \mathrm{m}^2/\mathrm{kg}$ and $a_0 = 42\,164\ \mathrm{km}, e_0 = 0, i_0 = 0, \omega_0 = \Omega_0 = 0, \sigma_0 = \lambda_0 - \theta_0 = 1.32$ rad, respectively. The osculating semi-major axis initial condition is $a_0^\star = 42\,153.621\ \mathrm{km}$ (solid square). [Middle] Mean longitudes at shadow entry λ_1 and shadow exit λ_2 superimposed with the longitude of the ascending node Ω (dashed curve). [Bottom] Long-term inclination evolution.

Part III

High area-to-mass ratios GEO space debris

Stability investigations

Chapter 5

Global dynamics of high area-to-mass ratios GEO space debris by means of the MEGNO indicator

"Two golf balls will soon be hit into Earth orbit from the International Space Station for a television commercial [...] The cosmonaut is a golf novice and was tutored in July by a golf instructor and a retired professional golfer [...] the ball does come equipped with a transmitter. So the satellites should be able to keep tabs on the ball...until the transmitter's batteries wear out."

NewScientist, 23 August and 17 November 2006

– The results of this chapter have been previously submitted in Valk et al. (2008) –

As mentioned in the previous chapters, the recent optical surveys in high-altitude orbits, performed by the European Space Agency 1 m telescope in Tenerife (Canary islands), have discovered a new unexpected population of 10 cm sized space debris near the geostationary region (GEO). These objects sometimes present highly eccentric orbits with eccentricities as high as 0.55 (Schildknecht et al., 2004, 2005). Following the initial guess of Liou and Weaver (2004), who suggested that this new population may be GEO objects with high area-to-mass ratios, recent numerical and analytical investigations were performed to defend this assumption (Anselmo and Pardini, 2005; Liou and Weaver, 2005). In addition, these authors and others, such as Chao (2006), Valk et al. (2007b), Valk and Lemaître (2007b), presented some detailed results concerning the short- and long-term evolution of high area-to-mass ratios geosynchronous space debris subjected to direct solar radiation pressure (see Chapter 3). More specifically, these latter authors mainly focused their attention on the long-term variation of both the eccentricity and the inclination vector. Moreover, some studies concerning the effects of the Earth's shadowing effects on the motion of such space debris were given in Chapter 4.

However, no concern about the intrinsic stability of such uncommon orbits has been given so far. In other words, up to the present, nobody ever dealt with the question to know whether these orbits are really predictable or not on the time scales of their investigations.

The objective of this chapter is basically twofold. The first goal is the investigation of the long-term stability of high area-to-mass ratios space debris subjected to the direct solar radiation pressure, by means of the MEGNO criterion (Cincotta et al., 2003). Second, while considering high area-to-mass ratios, we bring to the fore a relevant class of additional secondary structures appearing in the phase space.

This chapter is organized as follows. In Section 5.1, we focus our attention to the specification of the underlying model and we give some details about the numerical aspects of the method.

In Section 5.2, for the sake of completeness, we dwell upon the detailed definition of the *Mean Exponential Growth factor of Nearby Orbits* indicator, also providing a review of its main properties, in order to understand the behavior of the chaos indicator.

Then in Section 5.3, within the framework of the validation of our implementation, we regain the results obtained by Breiter et al. (2005a). We also discuss the significance of the time of integration, recently reported by Barrio et al. (2007).

In Section 5.4, we first apply the MEGNO technique in order to give an insightful understanding of the stability of high area-to-mass ratios space debris. More specifically, we show that the orbits of such peculiar space debris are extremely sensitive to initial conditions, especially with respect to the mean longitude and the semi-major axis. Second, we perform extended analyses, showing that the related 2-dimensional phase space is dominated by chaotic regions, in particular when the area-to-mass ratio is large. In addition, we also provide some results presenting the importance of the initial eccentricity value in the appearance of chaotic region.

Finally, in Section 5.5, we give extensive numerical and analytical investigations of the additional patterns which will be identified as secondary resonances.

5.1 The model

For the purpose of our study, we consider the modeling of a space debris subjected to the influence of the Earth's gravity field, to both the gravitational perturbations of the Sun and the Moon as well as to the direct solar radiation pressure. As a consequence the differential system of equations governing the dynamics is given by

$$\ddot{\boldsymbol{r}} = \boldsymbol{a}_{\text{pot}} + \boldsymbol{a}_{\leftmoon} + \boldsymbol{a}_{\odot} + \boldsymbol{a}_{\text{rp}} \,,$$

where $\boldsymbol{a}_{\text{pot}}$ is the acceleration induced by the Earth's gravity field, expressed as the gradient of the following potential (see Eq. 2.5, page 25)

$$U(r,\lambda,\phi) = -\frac{\mu}{r}\sum_{n=0}^{\infty}\sum_{m=0}^{n}\left(\frac{R_e}{r}\right)^n \mathcal{P}_n^m(\sin\phi)(C_{nm}\cos\, m\lambda + S_{nm}\sin\, m\lambda)\,, \tag{5.1}$$

which is subsequently expressed in Cartesian coordinates by means of the recursive Cunningham algorithm (see Appendix B, page 161).

Both the accelerations $\boldsymbol{a}_{\leftmoon}$ and $\boldsymbol{a}_{\odot}$ result from the gravity interaction with a third body of mass m_*, where $* = \leftmoon$ and $* = \odot$, and can be expressed with respect to the Earth's center of mass (see Subsection 2.2.3, page 28)

$$\boldsymbol{a}_* = -\mu_*\left(\frac{\boldsymbol{r}-\boldsymbol{r}_*}{\|\boldsymbol{r}-\boldsymbol{r}_*\|^3} + \frac{\boldsymbol{r}_*}{\|\boldsymbol{r}_*\|^3}\right)\,,$$

Regarding the direct solar radiation pressure, we assume a hypothetical spherical space debris with optical properties defined by a single scalar coefficient. The albedo of the Earth is ignored and the Earth's shadowing effects are not taken into account either. For the sake of clarity, the acceleration induced by the direct solar radiation pressure is recalled here. From Section 3.2, we have

$$\mathbf{a_{rp}} = C_r\, P_r \left[\frac{a_\odot}{\|\mathbf{r}-\mathbf{r}_\odot\|}\right]^2 \frac{A}{m}\,\frac{\mathbf{r}-\mathbf{r}_\odot}{\|\mathbf{r}-\mathbf{r}_\odot\|}\,.$$

5.2 The Mean Exponential Growth factor of Nearby Orbits

We present in this section the definition and some properties of the MEGNO criterion.

Let $\mathcal{H}(\boldsymbol{p},\boldsymbol{q})$, with $\boldsymbol{p}\in\mathbb{R}^n$, $\boldsymbol{q}\in\mathbb{T}^n$, be a n-degree of freedom Hamiltonian system and let us introduce the compact notation $\boldsymbol{x} = (\boldsymbol{p},\boldsymbol{q}) \in \mathbb{R}^{2n}$ as well as $\boldsymbol{f} = (-\partial\mathcal{H}/\partial\boldsymbol{q}, \partial\mathcal{H}/\partial\boldsymbol{p}) \in \mathbb{R}^{2n}$, then the dynamical system is described by the following set of ordinary differential equations

$$\frac{\mathrm{d}}{\mathrm{d}t}\boldsymbol{x}(t) = \boldsymbol{f}(\boldsymbol{x}(t),\boldsymbol{\alpha})\,, \qquad \boldsymbol{x}\in\mathbb{R}^{2n}\,, \tag{5.2}$$

where $\boldsymbol{\alpha}$ is a vector of parameters entirely defined by the model. Let $\phi(t) = \phi(t;\boldsymbol{x}_0,t_0)$ be a solution of the flow defined in Eq. (5.2) with initial conditions $(t_0,\boldsymbol{x}_0)$, then it has associated the Lyapunov Characteristic Number (hereafter LCN), defined by (Benettin et al., 1980a)

$$\lambda = \lim_{t\to\infty}\frac{1}{t}\,\ln\frac{\|\boldsymbol{\delta}_\phi(t)\|}{\|\boldsymbol{\delta}_\phi(t_0)\|}, \tag{5.3}$$

where $\boldsymbol{\delta}_\phi(t)$, the so-called *tangent vector*, measures the evolution of an initial small deviation $\boldsymbol{\delta}_\phi(t_0)\equiv\boldsymbol{\delta}_0$ between $\phi(t)$ and a nearby orbit, and whose evolution is given by the variational

equations (terms of order $\mathcal{O}(\boldsymbol{\delta}^2)$ are omitted)

$$\dot{\boldsymbol{\delta}}_\phi = \frac{\mathrm{d}}{\mathrm{d}t}\boldsymbol{\delta}_\phi(t) = \boldsymbol{J}(\phi(t))\,\boldsymbol{\delta}_\phi(t)\,, \quad \text{with} \quad \boldsymbol{J}(\phi(t)) = \frac{\partial \boldsymbol{f}}{\partial \boldsymbol{x}}(\phi(t))\,, \tag{5.4}$$

where $\boldsymbol{J}(\phi(t))$ is the Jacobian matrix of the differential system of equations, evaluated on the solution $\phi(t)$. Let us note that the definition of the LCN, given by Eq. (5.3), can also be written in an integral form

$$\lambda = \lim_{t\to\infty} \frac{1}{t} \int_0^t \frac{\dot{\delta}_\phi(s)}{\delta_\phi(s)}\, ds\,,$$

where $\delta_\phi = \|\boldsymbol{\delta}_\phi\|$, $\dot{\delta}_\phi = \dot{\boldsymbol{\delta}}_\phi \cdot \boldsymbol{\delta}_\phi/\delta_\phi$.

The Mean Exponential Growth factor of Nearby Orbits (hereafter MEGNO) $Y_\phi(t)$ is based on a modified time-weighted version of the integral form of the LCN (Cincotta and Simó, 2000). More precisely

$$Y_\phi(t) = \frac{2}{t} \int_0^t \frac{\dot{\delta}_\phi(s)}{\delta_\phi(s)}\, s\, ds\,,$$

as well as its corresponding mean value to get rid of the quasi-periodic oscillation possibly existing in $Y_\phi(t)$

$$\overline{Y}_\phi(t) = \frac{1}{t} \int_0^t Y_\phi(s)\, ds\,.$$

In the following we will omit the explicit dependence of Y and $\overline{Y}$ on the specific orbit ϕ, once this will be clear from the context.

Actually, this latter approach allows to study the dynamics for long time scales, where generically $\lim_{t\to\infty} Y(t)$ does not converge, while $\lim_{t\to\infty} \overline{Y}(t)$ is well defined (Cincotta et al., 2003). Consequently, the time evolution of $\overline{Y}(t)$ allows to derive the possible divergence of the norm of the tangent vector $\boldsymbol{\delta}(t)$, giving a clear indication of the character of the different orbits. Indeed, for quasi-periodic (regular) orbits, $Y(t)$ oscillates around the value 2 with a linear growth of the separation between nearby orbits. On the other hand, for chaotic (irregular) motion, the module of $\boldsymbol{\delta}$ grows exponentially with time, and $Y(t)$ oscillates around a linear divergence line. Cincotta et al. (2003) showed that, for the quasi-periodic regime, $\overline{Y}(t)$ converges to 2, that is a fixed constant, independent of the orbit. Moreover, it has been shown that ordered motions with harmonic oscillations, i.e. orbits very close to a stable periodic orbit, result asymptotically to $\overline{Y}(t) = 0$.

These latter properties can also be used to compute efficiently a good estimation of the LCN, or similarly the Lyapunov time $T_\lambda = 1/\lambda$, by means of a linear least square fit of $\overline{Y}(t)$. Indeed, in the case of an irregular orbit, the time evolution of $\overline{Y}(t)$ may be easily written as

$$\overline{Y}(t) \simeq a_\star\, t + d, \qquad t \to \infty,$$

where $a_\star$ is simply related to the LCN by the relation $a_\star = \lambda/2$ and d is close to zero.

Regarding the numerical computation of the MEGNO indicator, we adopt the same strategy as in Goździewski et al. (2001). To be specific, in addition to the numerical integrations of both the equations of motion and the first order variation equations, we consider the two additional differential equations

$$\frac{\mathrm{d}}{\mathrm{d}t}y = \frac{\dot{\boldsymbol{\delta}} \cdot \boldsymbol{\delta}}{\boldsymbol{\delta} \cdot \boldsymbol{\delta}}\, t\,, \qquad \frac{\mathrm{d}}{\mathrm{d}t}w = 2\frac{y}{t}\,, \tag{5.5}$$

which allow to derive the MEGNO indicators as

$$Y(t) = 2\, y(t)/t, \qquad \overline{Y}(t) = w(t)/t\,.$$

The MEGNO criterion, unlike the common Lyapunov variational methods, takes advantage of the whole dynamical information for the orbits and the evolution of its tangent vector, which results in shorter integration times, to achieve comparable results. Moreover, a couple of applications found in the literature (e.g. Goździewski et al. 2001; Goździewski 2003; Goździewski et al. 2008; Cincotta and Simó 2000; Breiter et al. 2005a; Breiter et al. 2005b) justify and confirm that the MEGNO is relevant, reliable and provides an efficient way for the investigation of the dynamics by detecting regular as well as stochastic regimes.

5.2.1 MEGNO and numerical integrations

As previously mentioned, in order to evaluate the MEGNO indicator, we have to integrate the differential system of equations of motion (5.2), the linear first order variational system of equations (5.4) as well as the two additional differential equations (5.5). We choose to write both the expressions of the perturbing forces and the variational system, i.e. the Jacobian matrix, in rectangular coordinates, *positions* and *velocities*. In such a way we can overcome both the null eccentricity and the null inclination singularity present in the dynamics of space debris. Moreover, the explicit analytical expressions of the vector fields allow us to avoid the difficulties inherent in the classical method of neighboring trajectories (two particles method). For further detail concerning the explicit computation of the variational system of equations, we refer to Appendix D on page 167.

In order to numerically integrate the two differential systems of equations, we adopted the variable step size Bulirsh-Stoer algorithm (see e.g. Bulirsh and Stoer, 1966; Stoer and Bulirsh, 1980). Let us note that, for the purpose of validation, the numerical integrations were also made with a couple of other numerical integrators. However, the Bulirsh-Stoer algorithm seems to be the best compromise between accuracy and efficiency. Moreover, as quoted by Wisdom (1983): *What is more important for this study, Benettin et al. (1980a,b) found that the maximum LCE did not depend on the precision of their calculation. It appears likely that as long as a certain minimum precision is kept, maximum LCE's may be accurately computed, even though it is not possible to precisely follow a specified trajectory for the required length*

of time.

Although this latter observation was formulated in the framework of both Lyapunov variational method and Hamiltonian systems, it seems that it remains relevant in the computation of the MEGNO criterion, at least in the particular case of our analysis.

5.2.2 Influence of the initial tangent vector δ_0

By construction MEGNO depends on the initial value of the tangent vector $\boldsymbol{\delta}_0$, although the latter does not influence significantly the detection of chaotic region. Nevertheless we preferred to adopt the strategy of initializing randomly the initial tangent vectors in order to avoid some parts of *artificially created zones of low MEGNO due to the proximity of* $\boldsymbol{\delta}_0$ *to the minimum Lyapunov exponent direction* (Breiter et al., 2005a). Moreover, as pointed out by Goździewski et al. (2001), the random sampling of $\boldsymbol{\delta_0}$ is relevant in the sense that different initial tangent vectors can lead to different behaviors of the MEGNO time evolution while considering the same orbit. This observation has been reported in the framework of extrasolar planetary systems and seems to be similar in the case of Earth orbiting objects, and more generally for high-dimensional dynamical systems (having more than 3 degrees of freedom).

Regarding the impact of the choice of the initial tangent vector $\boldsymbol{\delta}_0$, we performed a set of exhaustive numerical investigations of regular orbits. More specifically, we compared the time evolution of the MEGNO using different initial tangent vectors and identical generic initial conditions. The results confirm that the random choice of the initial tangent vector induces a significant random behavior in the way MEGNO approaches the limit value 2, hence preventing this information from being useful to check the stability/instability character of regular orbits. Actually, when considering a slightly perturbed two-body problem (such as the central attraction disturbed by the oblateness of the Earth), the MEGNO convergence to 2 is completely random, leading to more or less 50% of convergence of $\overline{Y}(t)$ to 2 from above and the other remaining 50% from below. This result is formally discussed in the following subsections. However, when the order of magnitude of the perturbation is larger, the result does not completely hold anymore. In particular, when considering the perturbing effects induced by the 1:1 resonance, the MEGNO evolution no longer depends on the random choice of the initial tangent vector. In this latter case, the intrinsic stability of the chosen orbits seems also to dictate the evolution of the MEGNO as reported in Cincotta et al. (2003). More specifically, the stability of the orbit seems to influence the time evolution of the MEGNO the stronger the orbit is closer to a stable or unstable equilibrium point. For instance, regarding the orbits extremely close to a stable equilibrium point, the MEGNO generally approaches slowly the limit value 2 from below even though some infrequent orbits present a MEGNO convergence from above. Conversely, the orbits initially close to the separatrices generally present a MEGNO approaching the value 2 from above.

5.2.3 MEGNO for integrable systems

In this paragraph we will study the MEGNO indicator for integrable Hamiltonian systems and we will show that generically (if the system is not isochronous) it always converges to 2, moreover the way $Y(t)$ reaches this limit value, say from higher or lower values, depends only on the choice of the initial tangent vector and not on the orbit itself.

So let us consider an integrable Hamiltonian system and assume action-angle variables, $\mathcal{H} = \mathcal{H}(\boldsymbol{p})$, where $\boldsymbol{p} \in B \subset \mathbb{R}^n$ denotes the action variables and $\boldsymbol{q} \in \mathbb{T}^n$ denotes the angle variables. Then the Hamiltonian equations are

$$\begin{aligned} \dot{\boldsymbol{p}} &= 0\,, \\ \dot{\boldsymbol{q}} &= \frac{\partial \mathcal{H}}{\partial \boldsymbol{p}} = \boldsymbol{\omega}(\boldsymbol{p})\,. \end{aligned}$$

The tangent space (to a given orbit) can be split into the action direction and angle direction, namely $\boldsymbol{\delta} = (\boldsymbol{\delta}_p, \boldsymbol{\delta}_q)$, thus the variational system can be written as

$$\begin{aligned} \dot{\boldsymbol{\delta}}_p &= 0\,, \\ \dot{\boldsymbol{\delta}}_q &= \frac{\partial^2 \mathcal{H}}{\partial \boldsymbol{p}^2}\boldsymbol{\delta}_p = M(\boldsymbol{p})\,\boldsymbol{\delta}_p\,. \end{aligned}$$

If the system is isochronous then $M \equiv 0$, thus $\boldsymbol{\delta}_p$ and $\boldsymbol{\delta}_q$ are constant and $Y(t) = 0$ for all t. On the other hand, if the system is non-isochronous we get $\boldsymbol{\delta}_p(t) = \boldsymbol{\delta}_p(0)$ and $\boldsymbol{\delta}_q(t) = \boldsymbol{\delta}_q(0) + M(\boldsymbol{p}(0))\,\boldsymbol{\delta}_p(0)t$. To simplify the notations let us introduce

$$M\left(\boldsymbol{p}(0)\right) = M_0, \quad \boldsymbol{\delta}_p(0) = \boldsymbol{\xi}_0 \text{ and } \boldsymbol{\delta}_q(0) = \boldsymbol{\eta}_0\,.$$

Using the definition of MEGNO, we get

$$Y(t) = \frac{1}{t}\int_0^t \frac{(M_0\boldsymbol{\xi}_0)^2 s + M_0\boldsymbol{\xi}_0 \cdot \boldsymbol{\eta}_0}{(\boldsymbol{\xi}_0)^2 + (\boldsymbol{\eta}_0)^2 + 2M_0\boldsymbol{\xi}_0 \cdot \boldsymbol{\eta}_0 s + (M_0\boldsymbol{\xi}_0)^2 s^2} s\; ds\,,$$

and this integral can be explicitly computed and we obtain

$$\begin{aligned} Y(t) &= 2 - \frac{M_0\boldsymbol{\xi}_0 \cdot \boldsymbol{\eta}_0}{t(M_0\boldsymbol{\xi}_0)^2}\log\left[1 + 2M_0\boldsymbol{\xi}_0 \cdot \boldsymbol{\eta}_0 t + (M_0\boldsymbol{\xi}_0)^2 t^2\right] + \\ &- \frac{2}{t}\frac{\sqrt{(M_0\boldsymbol{\xi}_0)^2 - (M_0\boldsymbol{\xi}_0 \cdot \boldsymbol{\eta}_0)^2}}{(M_0\boldsymbol{\xi}_0)^2}\left[\arctan\frac{M_0\boldsymbol{\xi}_0 \cdot \boldsymbol{\eta}_0 + (M_0\boldsymbol{\xi}_0)^2 t^2}{\sqrt{(M_0\boldsymbol{\xi}_0)^2 - (M_0\boldsymbol{\xi}_0 \cdot \boldsymbol{\eta}_0)^2}}\right. \\ &- \left.\arctan\frac{M_0\boldsymbol{\xi}_0 \cdot \boldsymbol{\eta}_0}{\sqrt{(M_0\boldsymbol{\xi}_0)^2 - (M_0\boldsymbol{\xi}_0 \cdot \boldsymbol{\eta}_0)^2}}\right]. \end{aligned} \tag{5.6}$$

One can check that the square root is well defined, i.e. positive, and thus one can cast (5.6) into

$$Y(t) = 2 - \frac{M_0\boldsymbol{\xi}_0 \cdot \boldsymbol{\eta}_0}{t}F_1(t) - \frac{1}{t}F_2(t)\,,$$

where F_1 and F_2 are positive functions and F_2 is bounded. We can then conclude that

1. if $M_0\boldsymbol{\xi}_0 \cdot \boldsymbol{\eta}_0 > 0$ then $Y(t)$ approaches 2 from below;
2. if $M_0\boldsymbol{\xi}_0 \cdot \boldsymbol{\eta}_0 < 0$ then $Y(t)$ approaches 2 from above, in fact for large t the first contribution dominates the bounded term F_2.

In this last part we will consider if and under which assumptions the previous results concerning the convergence $Y \to 2$ are still valid, for a quasi–integrable Hamiltonian system of the form $H(\boldsymbol{p}, \boldsymbol{q}, \epsilon) = H_0(\boldsymbol{p}) + \epsilon V(\boldsymbol{p}, \boldsymbol{q})$. The main idea is the following, fix $\epsilon > 0$ but small and consider a "non–chaotic"orbit ϕ_ϵ, namely an orbit without a positive Lyapunov exponent (or if you prefer with a bounded MEGNO), then if ϵ is sufficiently small this orbit is a perturbation of an orbit existing also for $\epsilon = 0$, ϕ_0, and we can check that $Y_{\phi_\epsilon} = Y_{\phi_0} + \mathcal{O}(\epsilon)$, hence the smallness of such ϵ–correction cannot change "the way Y goes to 2". More precisely the Hamilton equations are now

$$\begin{aligned} \dot{\boldsymbol{p}} &= -\frac{\partial \mathcal{H}}{\partial \boldsymbol{q}} = -\epsilon \frac{\partial V}{\partial \boldsymbol{q}} \\ \dot{\boldsymbol{q}} &= \frac{\partial \mathcal{H}}{\partial \boldsymbol{p}} = \boldsymbol{\omega}(\boldsymbol{p}) + \epsilon \frac{\partial V}{\partial \boldsymbol{p}}\,, \end{aligned}$$

and a similar decomposition can be done for the variational system

$$\begin{aligned} \dot{\boldsymbol{\delta}}_p &= -\epsilon \frac{\partial^2 V}{\partial \boldsymbol{p} \partial \boldsymbol{q}} \boldsymbol{\delta}_p - \epsilon \frac{\partial^2 V}{\partial \boldsymbol{q}^2} \boldsymbol{\delta}_q \\ \dot{\boldsymbol{\delta}}_q &= \left(\frac{\partial^2 \mathcal{H}}{\partial \boldsymbol{p}^2} + \epsilon \frac{\partial^2 V}{\partial \boldsymbol{p}^2} \right) \boldsymbol{\delta}_p + \epsilon \frac{\partial^2 V}{\partial \boldsymbol{p} \partial \boldsymbol{q}} \boldsymbol{\delta}_q\,. \end{aligned}$$

Looking for $\boldsymbol{\delta}_p$ and $\boldsymbol{\delta}_q$ as ϵ–power series, i.e. $\boldsymbol{\delta}_p = \boldsymbol{\delta}_{p,0} + \epsilon \boldsymbol{\delta}_{p,1} + \ldots$ and $\boldsymbol{\delta}_q = \boldsymbol{\delta}_{q,0} + \epsilon \boldsymbol{\delta}_{q,1} + \ldots$, and collecting together, in the definition of MEGNO, terms contributing to the same power of ϵ, we can thus get

$$\begin{aligned} Y_{\phi_\epsilon}(t) &= \frac{1}{t} \int_0^t \frac{(M_0 \boldsymbol{\delta}_{p,0})^2 s + M_0 \boldsymbol{\delta}_{p,0} \cdot \boldsymbol{\delta}_{q,0}}{(\boldsymbol{\delta}_{p,0})^2 + (\boldsymbol{\delta}_{p,0})^2 + 2 M_0 \boldsymbol{\delta}_{p,0} \cdot \boldsymbol{\delta}_{q,0} s + (M_0 \boldsymbol{\delta}_{q,0})^2 s^2} s \, ds + \mathcal{O}(\epsilon) \\ &= Y_{\phi_0}(t) + \mathcal{O}(\epsilon)\,. \end{aligned}$$

5.3 Validation of the method

To validate our method we first apply the technique on a simplified model, containing only the Earth's gravity field expanded up to the second degree and order harmonics, namely, $J_2 = -C_{20}, C_{22}$ and S_{22}. For the purpose of the analysis, we followed a set of 12 600 orbits, propagated over a 30 years time span, that is the order of 10^4 fundamental periods (1 day) empirically required by the method (Goździewski et al., 2001). As reported in Breiter et al. (2005a), a 30 years time span seems to be relatively small for long-term investigation of geosynchronous space debris. However, on the one hand, the numerical integration of variational equations in addition to the extrapolation of the orbit is quite time consuming. Indeed, the simulation with an entry-level step size of 400 seconds takes approximately 20 seconds per orbit when including only the Earth's gravity field whereas it takes 42 seconds with a complete

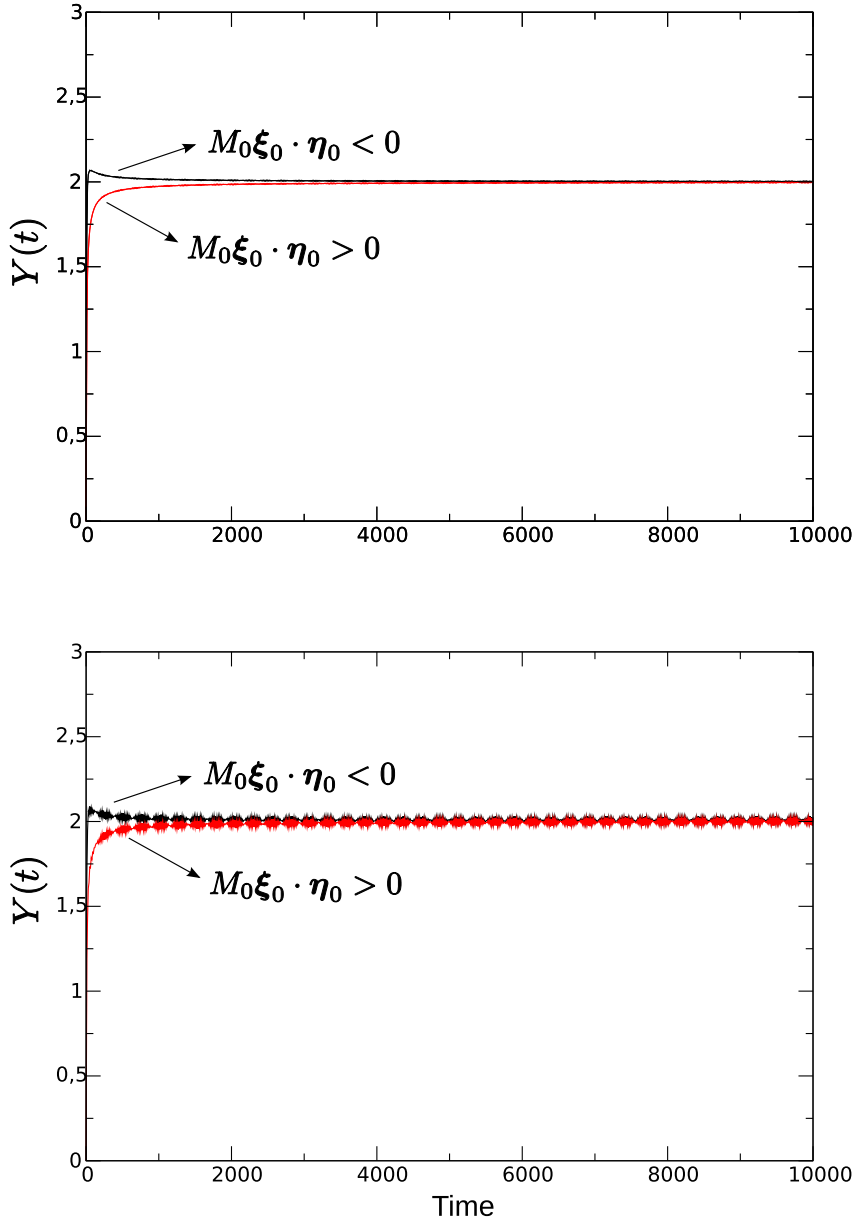

Figure 5.1: MEGNO for quasi-integrable Hamiltonian system. We consider the evolution of Y_{ϕ_ϵ} for the system: $H = p_1^2/2 + p_2 + \epsilon \cos q_1 + \epsilon \cos(q_1 - q_2)$. On the top panel $\epsilon = 10^{-4}$ while on the bottom panel $\epsilon = 10^{-3}$. In both cases ϵ is small enough to confirm the theoretical predictions, let observe that in this case the matrix M is given by $\left(\begin{smallmatrix} 1 & 0 \\ 0 & 0 \end{smallmatrix}\right)$ and thus the sign condition reads $M\boldsymbol{\delta}_{p,0} \cdot \boldsymbol{\delta}_{q,0} = \delta^1_{p,0}\delta^1_{q,0}$.

model, which is already significant when examining large sets of initial conditions (typically more than 10^4 orbits). On the other hand, the analysis of the following section will bring to the fore some indications about the Lyapunov times resulting in lower than 30 years. As a consequence, our choice of integration time can be considered as sufficiently large in the particular

case of our study.

For the purpose of this validation study, we consider a set of initial conditions defined by a mean longitude grid of 1°, spanning 90° on both sides of the first stable equilibrium point and a semi-major axis a grid of 1 km, spanning the $42\,164 \pm 35$ km range. The other fixed initial conditions are $e_0 = 0.002$ for the eccentricity, $i_0 = 0.004$ for the inclination, $\Omega_0 = \omega_0 = 0$ for the longitude of the ascending node and argument of perigee, respectively. These values have been fixed to compare our results for the nearly-geosynchronous orbits with the ones of Breiter et al. (2005a). As pointed out by Breiter et al. (2005a), due to the 1:1 resonance, good variables to present our results will be (a_0, σ_0), where a_0 is the osculating initial semi-axis and σ is the so-called resonant angle, i.e. $\sigma = \lambda - \theta$ with the sidereal time θ.

Figure 5.2 (top) shows the MEGNO values computed using 30 years of integration time. We identify clearly a blow-up of the typical double pendulum-like pattern related to the 1:1 resonance (observe the horizontal range of 180°). Both the unstable and the two stable equilibrium points are clearly visible. We observe that the phase space seems to be essentially filled in with MEGNO values $\overline{Y}(t) \simeq 2$, that is plenty of regular orbits. Moreover, the two separatrices are also identifiable and are associated with neighboring MEGNO values $2 < \overline{Y}(t) \leq 4$. Therefore, following the properties defined in Section 5.2, one could consider that these orbits are chaotic, however, we will show that this conclusion is false. Indeed, a careful identification of the MEGNO time evolution shows that the latter always approaches slowly the limit 2 from above. The closer to the separatrice, the slower the convergence. More precisely, none of the above simulated orbits presents a MEGNO time evolution around a linear divergence line, leading to the conclusion that these orbits are actually unstable periodic orbits, and as a matter of fact also regular.

To clarify this point, we performed a similar study but using a significantly longer time span, namely 300 years. The results are showed in Figure 5.2 (bottom). For the sake of comparison, the color bars have been taken identical on both plots. Let us observe that the maximum value reached by the MEGNO is 4 for the top panel and 2.5 for the bottom one. In the 300 years simulation (Figure 5.2, bottom), the MEGNO values, associated with orbits close to the separatrices, turn out to be, on average, smaller than in Figure 5.2 (top), reaching almost the limit $\overline{Y}(t) \to 2$, due to the longer time of integration. Similarly, the dark zone in the neighborhood of the stable equilibrium point corresponding to MEGNO values close to zero, is strongly shrunk, supporting the result that, in the limit of infinitely large t, only the orbit originating from the exact stable equilibrium point leads to $\overline{Y} = 0$ whereas the neighboring trajectories converge slowly to $\overline{Y}(t) = 2$.

Let us note that the importance of integration time has been recently reported by Barrio et al. (2007) in the framework of applications of the MEGNO method, and it is here confirmed. Moreover, the latter paper also underlines some spurious structures appearing in the maps of the variational chaos indicators, explaining the presence of some background patterns (Fig-

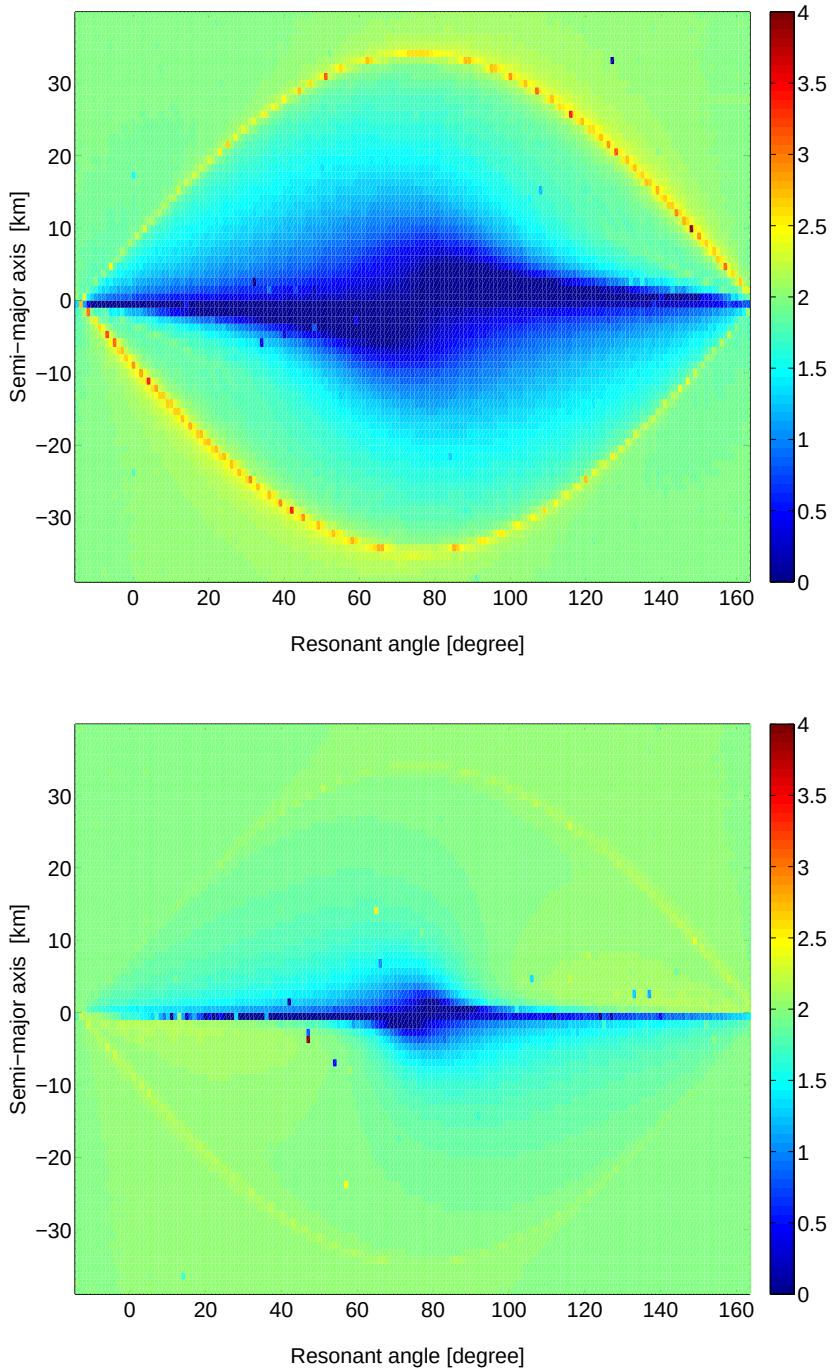

Figure 5.2: The MEGNO computed as a function of initial mean longitudes λ_0 and osculating semi-major axis a_0. The equations of motion include the central body attraction as well as the second degree and order harmonics J_2, C_{22} and S_{22}. The mean longitude grid is 1° and the semi-major axis grid is 1 km, spanning the $42\,164 \pm 35$ km range. The initial conditions are $e_0 = 0.002$, $i_0 = 0.004$, $\Omega_0 = \omega_0 = 0$. Time at epoch is 25 January 1991. The patterns have been obtained using two different integration times, $t_f = 30$ years [top] and $t_f = 300$ years [bottom].

ure 5.2), "*suggesting that the same periodic orbit is more or less regular depending on the initial conditions choice*".

5.4 High area-to-mass ratios analysis

In the particular case of classical near-geosynchronous objects, the long-term stability has been studied by computing the MEGNO indicator for a family of simulated geostationary, geosynchronous and super-geosynchronous orbits. The classical near-geosynchronous object with a period which is close to the sidereal day (1 day) is subjected to the main gravitational effects of the Earth, including the 1:1 resonance, the luni-solar perturbing effects as well as the solar radiation pressure for small area-to-mass ratio ($A/m \ll 1\ \mathrm{m}^2/\mathrm{kg}$). According to Breiter et al. (2005a) and Wytrzyszczak et al. (2007), the near-geostationary region presents chaotic orbits only very close to the separatrices due to the irregular transits between the libration and the circulation regimes. Regarding the super-geostationary orbits, all the orbits seem to be entirely regular on the time scale of the investigations, that is a few decades.

The aim of this section is to provide a more extensive analysis of the dynamics of near-geosynchronous space debris, subjected to the solar radiation pressure with high area-to-mass ratios (typically $A/m \gg 1\ \mathrm{m}^2/\mathrm{kg}$). Our main objective is to study the effects of high area-to-mass ratios on the stability of the principal periodic orbits and on the chaotic components. This analysis is divided into three parts. First, Subsection 5.4.1, we focus our attention on the sensitivity to initial conditions; then, Subsection 5.4.2, we report results of dedicated numerical analyses which emphasize the importance of the area-to-mass ratio value. Finally, in Subsection 5.4.3, we study the influence of both the initial eccentricity and time at epoch.

Let us recall that for large area-to-mass ratios, the solar radiation pressure becomes the major perturbation, by far larger than the dominant zonal gravity term J_2. In this particular case, the larger the area-to-mass ratio, the more affected the dynamics of the near-geosynchronous space debris, leading to daily high-amplitude oscillations of the semi-major axis, yearly oscillations of the eccentricity as well as long-term variations of the inclination. As an illustration, Figure 5.3 shows the orbital elements histories of the first 210 years of an initial geosynchronous high area-to-mass ratio space debris ($A/m = 10\ \mathrm{m}^2/\mathrm{kg}$). The yearly variation of the eccentricity reaches 0.2, which confirms the expected values predicted by the theories (see e.g. Anselmo and Pardini, 2005; Liou and Weaver, 2005). The inclination variation presents a well known long-term variation whose period is directly related to the area-to-mass ratio value. Regarding the argument of perigee as well as the longitude of ascending node, they both present a libration regime due to the chosen set of initial conditions. For further details, we refer to Chapter 3, where a full description of the long-term motion of high area-to-mass ratios space debris is given.

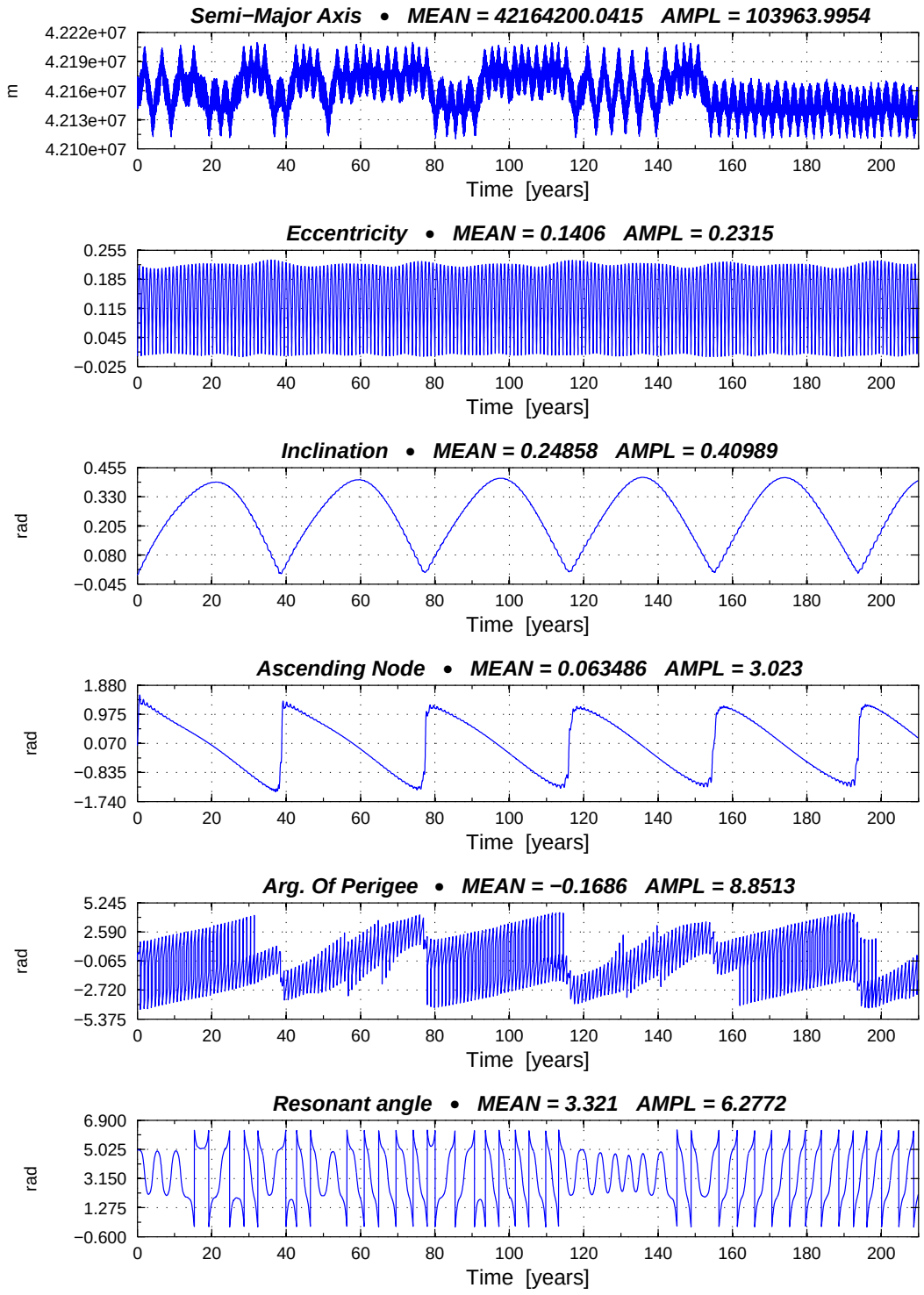

Figure 5.3: Time evolution of a typical high area-to-mass ratio space debris. Orbital elements over 210 years for a $A/m = 10\ \mathrm{m}^2/\mathrm{kg}$, initial conditions are ($a_0 = 42\,166.473$ km, $e_0 = 0.002, i_0 = 0.004$ rad, $\Omega_0 = \omega_0 = 0$ rad, $M_0 = 4.928$ rad). Time at epoch is 25 January 1991.

5.4.1 Sensitivity to initial conditions

To start with, we follow the evolution of two high area-to-mass ratio space debris ($A/m = 10\ \mathrm{m}^2/\mathrm{kg}$) defined by two sets of very close initial conditions, differing only in the 10th digits in mean longitude. Figure 5.4 shows the differences of the dynamical variables for the two orbits, confirming the hypothesis that the sensitivity to initial conditions is especially relevant for the semi-major axis and resonant angle whereas the difference between the other orbital elements remain small. Consequently, we first focus our attention on the time evolution of the semi-major axis and on the resonant angle.

As a complement to Figure 5.3, we numerically compute two orbits for two space debris with different area-to-mass ratios, $A/m = 1\ \mathrm{m}^2/\mathrm{kg}$ and $A/m = 10\ \mathrm{m}^2/\mathrm{kg}$, whose initial conditions have been chosen near the separatrices, to emphasize their chaotic behaviors. Figure 5.5 shows a blow-up of the evolution of the semi-major axis (top panels) and of the resonant angle [middle panels] over the time span of 250 years. It is clear that the semi-major axis presents some irregular components over its evolution, related to some transitions between different regimes of motion, clearly identifiable in the resonant angle plots. In addition we also computed the corresponding MEGNO time evolution. The bottom panel in each graph shows the time evolution of the MEGNO indicator as well as its corresponding mean value. First, we see that the time evolution of $\overline{Y}(t)$ presents a quasi-linear growth almost since the beginning of the integration process, leading to the conclusion that these orbits are clearly chaotic over that time scale. Therefore, we also computed the linear fit $\overline{Y}(t) \simeq a_\star\, t + d$ in both cases in order to evaluate the Lyapunov time T_λ, by means of the LCN λ or similarly the linear regression coefficients $a_\star = \lambda/2$. Let us remark that to avoid the initial transient state, the least square fits were performed on the last 85% of the time interval. This latter analysis brings to the fore the fact that larger area-to-mass ratios lead to lower Lyapunov times, i.e. larger Lyapunov Characteristic Number. Indeed, for $A/m = 1\ \mathrm{m}^2/\mathrm{kg}$, the Lyapunov time turns out to be on the order of 11 years, whereas it reaches the value $T_\lambda \simeq 3.7$ years for $A/m = 10\ \mathrm{m}^2/\mathrm{kg}$. Second, let us also remark that the behavior of the MEGNO indicator is of particular interest in these cases. A careful analysis of $Y(t)$ underlines some irregular patterns directly related to the evolution of σ, in particular when the orbits seem to transit across the separatrices. Finally, we can also highlight the fact that the sudden changes between libration and circulation regimes occur mainly when the inclination changes its sign of variation, especially at the maximum value for $A/m >> 1\ \mathrm{m}^2/\mathrm{kg}$ and at the minimum for $A/m \leq 1\ \mathrm{m}^2/\mathrm{kg}$ (Figure 5.5, top panels, dashed line), with an empirical long-term period T_Ω, that is the long-term period of the longitude of the ascending node, which decreases as A/m increases (Valk et al., 2007b).

5.4.2 Extended numerical analyses

We considered a set of $12\,600$ simulated orbits with various initial semi-major axes and mean longitudes. All the before-mentioned perturbing effects were taken into account with several values of the area-to-mass ratios regarding the solar radiation pressure. Results are reported in Figure 5.6 (in the case $A/m = 1\ \mathrm{m}^2/\mathrm{kg}$ – top left panel – we recognize the same pendulum-

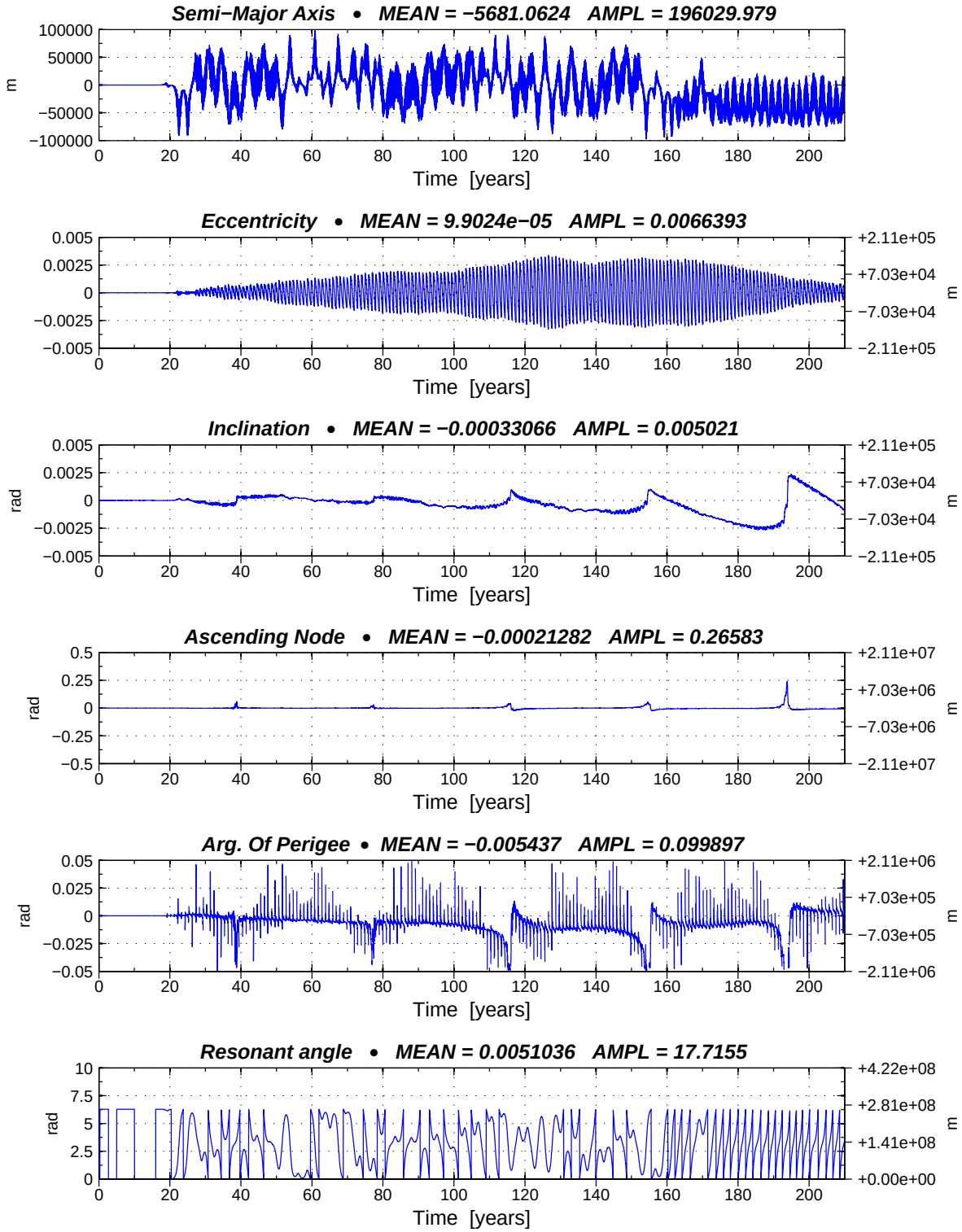

Figure 5.4: Effect of sensitivity to initial conditions for high area-to-mass ratio space debris. The figure shows the differences between two orbits with the same initial conditions ($a_0 = 42\,166.473$ km, $e_0 = 0.002, i_0 = 0.004$ rad, $\Omega_0 = \omega_0 = 0$ rad, $M_0 = 4.928$ rad) differing from the 10th digit in mean longitude λ_0. On each graph, the left vertical scale shows the deviations $(\Delta a, \Delta e, \Delta i, \Delta\Omega, \Delta\omega, \Delta\sigma)$ and the right vertical scale the order of magnitude of the difference $(-, a_0\Delta e, a_0\Delta i, a_0\Delta\Omega, a_0\Delta\omega, a_0\Delta\sigma)$ [meters]. Time at epoch is 25 January 1991.

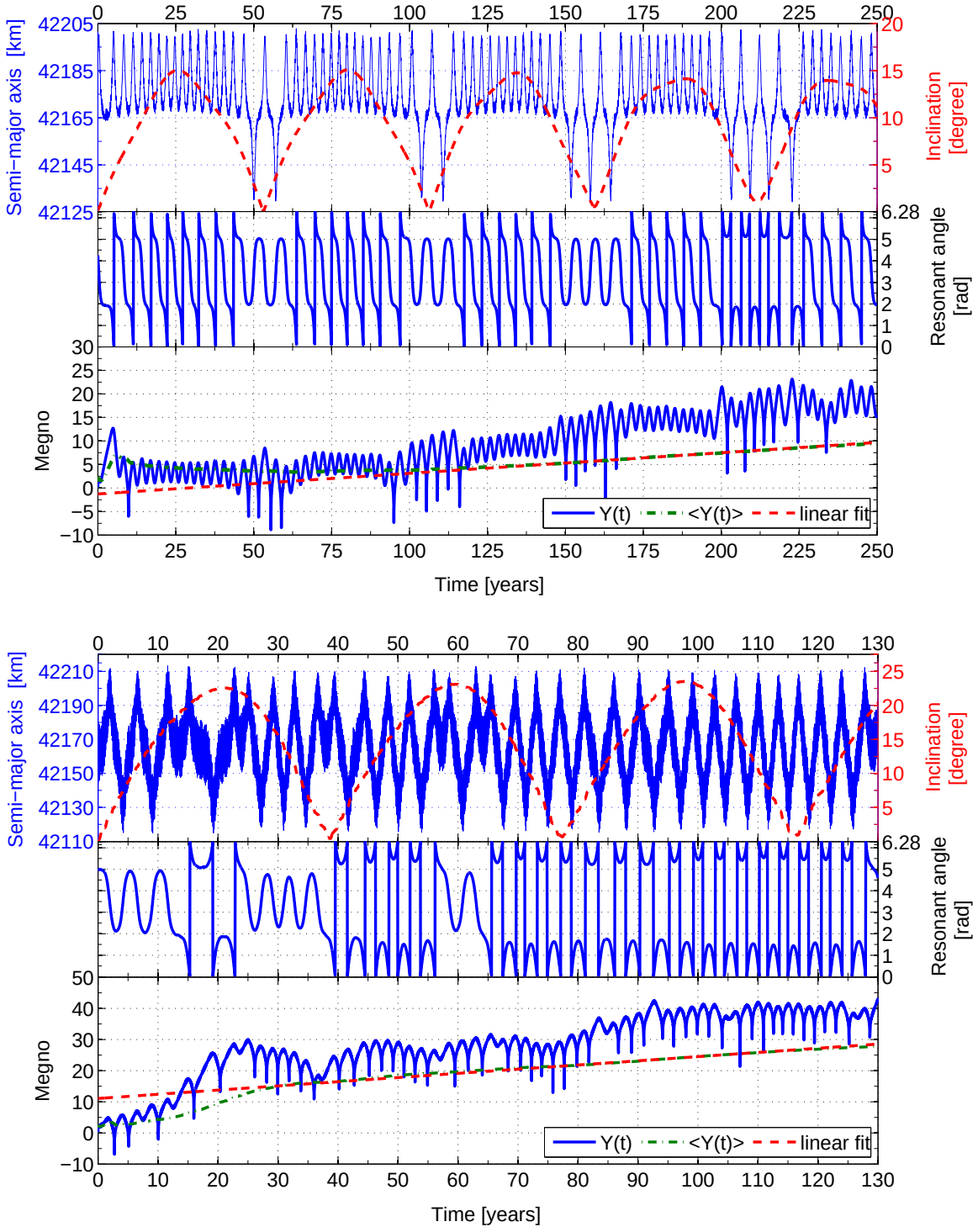

Figure 5.5: For each graph, we show the orbital evolution of the semi-major axes a (solid line) superimposed with the evolution of the inclinations (dashed line) [top panels]. The time evolution of the resonant angles [middle panels] and the time evolution of the MEGNO indicator (Y and $\overline{Y} =< Y(t) >$) as well as the corresponding linear fit $\overline{Y}(t) \simeq a_\star\, t + d$ [bottom panels]. The area-to-mass ratios are $A/m = 1\ \mathrm{m}^2/\mathrm{kg}$ in the upper panel and $A/m = 10\ \mathrm{m}^2/\mathrm{kg}$ in the lower one. The initial conditions are chosen near the separatrices. The computed linear regression coefficients are given by $a_\star = 0.043$ (for $A/m = 1\ \mathrm{m}^2/\mathrm{kg}$) and $a_\star = 0.134$ (for $A/m = 10\ \mathrm{m}^2/\mathrm{kg}$).

like pattern as in Figure 5.2). Considering the same integration time (30 years), we notice that the MEGNO values tend to be slightly larger than in Figure 5.2 (left). Moreover, some irregularly distributed MEGNO values are clearly visible close to the two saddle unstable stationary points. These results completely agree with those presented by Breiter et al. (2005a) where the solar radiation pressure was taken into account, but only for very small area-to-mass ratios (typically $0.005\ \mathrm{m}^2/\mathrm{kg}$). Indeed, our latter analysis shows that in addition to the luni-solar perturbations, the solar radiation pressure (with small to moderate area-to-mass ratios, that is $0 \leq A/m \leq 1\ \mathrm{m}^2/\mathrm{kg}$), do not change considerably the phase space pattern.

On the other hand, the remaining panels of Figure 5.6 show that the phase portrait becomes significantly more intricate with increasing area-to-mass ratios. Indeed, the width of the stochastic zone in the neighborhood of the separatrices becomes relevant with a large displacement of the separatrices on the phase plane. The larger chaotic region can readily be explained by the osculating motion of the separatrices due to the before-mentioned daily variations of the semi-major axis with respect to some mean value, as well as by the increasing amplitudes of the eccentricities. These variations lead inevitably to transits between both the regions separating libration and circulation motion for orbits initially close to the separatrices.

Moreover, it is also clear that the usual double pendulum-like phase space shows a tendency to be distorted with a apparent displacement of the unstable equilibrium points, whereas the stable equilibrium points remain almost fixed. This last result is however quite awkward insofar as there is no physical interpretation of this phenomenon. Indeed, the direct solar pressure does not depend explicitly on the resonant angle with respect to the long-term investigations and therefore can not induce a displacement of the equilibrium points in the phase space. Actually, an ingenious explanation can be found regarding the way the sampling is considered in the elaboration of the graphics. More specifically, it is worth noting that, at first, the sampling is carried out with respect to osculating initial conditions. Second, within the framework of mean-motion theory, it is well-known that, due to the short-period oscillations, the mean and the osculating initial conditions can not be considered to be equal. In other words, when considering a horizontal line in the initial conditions sampling, even though it corresponds to a fixed value of the initial osculating semi-major axis, it is actually related to various sets of mean initial semi-major axis as explained with Figure 5.7. Actually, the different initial mean longitudes induce a phase difference in the corresponding evolution of the semi-major axis, leading to different mean initial semi-major axes. Let us remark that the maximum difference between both mean semi-major axes is directly related to the order of magnitude of the short-period variations, and as a consequence, also directly related to the area-to-mas ratio.

More rigorously and as already mentioned in Chapter 4, the difference between osculating and mean initial conditions is a well-defined transformation, depending on the generating function used within the averaging process allowing to change from mean to osculating dynamics (see Appendix F.4, page 178). However, because we bound our analysis mainly to numerical simulations, we cannot access such a generating function; we can nevertheless

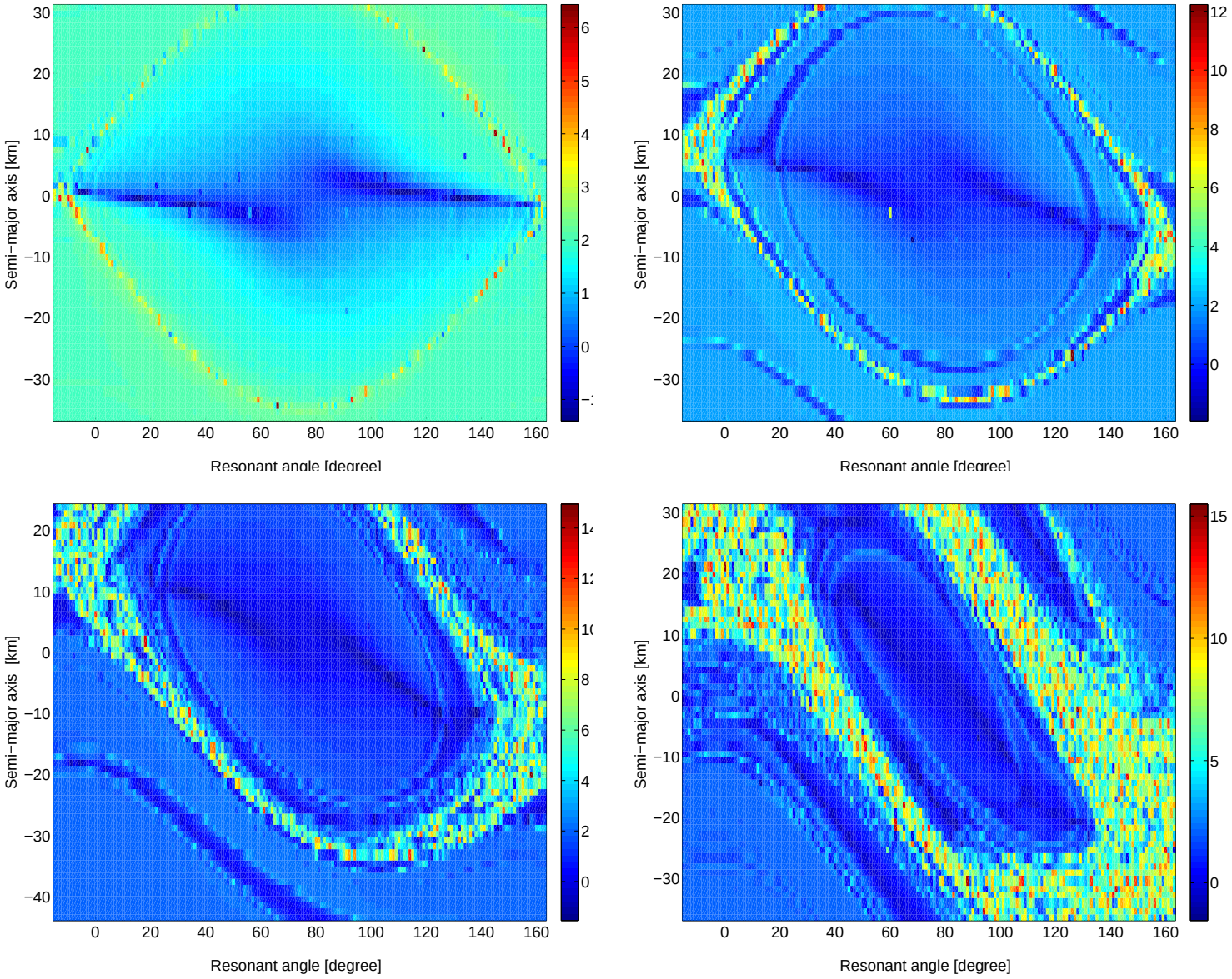

Figure 5.6: The MEGNO computed as a function of initial mean longitudes λ_0 and initial (osculating) semi-major axis a_0. The equations of motion include the central body attraction, the second degree and order harmonics J_2, C_{22} and S_{22}, the luni-solar interaction as well as the perturbing effects of the solar radiation pressure. The mean longitude grid is 1° and the semi-major axis grid is 1 km, spanning the $42\,164 \pm 35$ km range. The initial conditions are $(e_0 = 0.002, i_0 = 0.004, \Omega_0 = \omega_0 = 0)$. The integration time is 30 years from epoch fixed at 25 January 1991. The patterns have been obtained using four different area-to-mass ratios, $A/m = 1, 5, 10, 20\ \mathrm{m}^2/\mathrm{kg}$, respectively top left, top right, bottom left and bottom right panel.

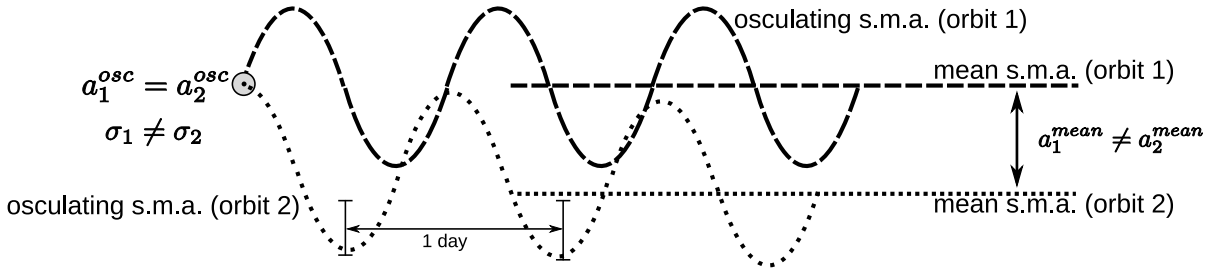

Figure 5.7: Cartoon to illustrate the difference between mean and osculating initial conditions with respect to the semi-major axis (s.m.a.) evolution. For the sake of simplicity, the mean semi-major axis does not present any long-term variation whereas the osculating semi-major axis present daily oscillations related to the direct solar pressure (the implicit underlying model is radiation pressure only). It is clear that even if the osculating initial conditions a_1^{osc} and a_2^{osc} are identical, the corresponding mean initial conditions a_1^{mean} and a_2^{mean} can be significantly different due to different initial mean longitudes (similarly different initial resonant angle values).

overcome this problem by numerically computing, for each semi-major axis osculating initial condition, the related mean initial semi-major axis, by considering the average over a short time span of 10 days. As an illustration, in Figure 5.8, we give the relation between the mean semi-major axis and the resonant angle for various values of the osculating semi-major axis ($A/m = 10\ \mathrm{m}^2/\mathrm{kg}$). The first difference is related to a semi-major axis sampling taken above the libration region, the second is related to a semi-major axis sampling which crosses the libration region and, finally, the third sampling is taken below this region. In conclusion, we clearly see that the order of magnitude of the differences is, as previously mentioned, the order of the amplitudes of the daily variations observed in the semi-major axis dynamics. Let us note that in the latter case, i.e. $A/m = 10\ \mathrm{m}^2/\mathrm{kg}$, the differences reach at most 27 km, which corresponds exactly to the difference between the stable and unstable equilibrium points, as shown in Figure 5.6 (bottom, left).

We can thus numerically apply the transformation as a post-treatment process, that is considering the MEGNO values not in the osculating initial conditions phase space, but in the mean initial conditions phase space. For the sake of comparison with Figure 5.6, we show the results once such a transformation has been applied (Figure 5.9). It is clear that now the vertical gaps between both the stable and unstable equilibrium points, are almost completely eliminated, hence these points have almost the same mean semi-major axis, getting rid of what we called the "*short-period arteface*". Let us also remark that, from now on, all the results will be shown in the mean initial conditions phase space.

5.4.3 Initial time at epoch and importance of the mean eccentricity

One should also recall that the solar radiation pressure leads to a theoretical equilibrium defined both in eccentricity e_0 and longitude of perigee ϖ_0 (see Subsection 3.4.1, page 75). The

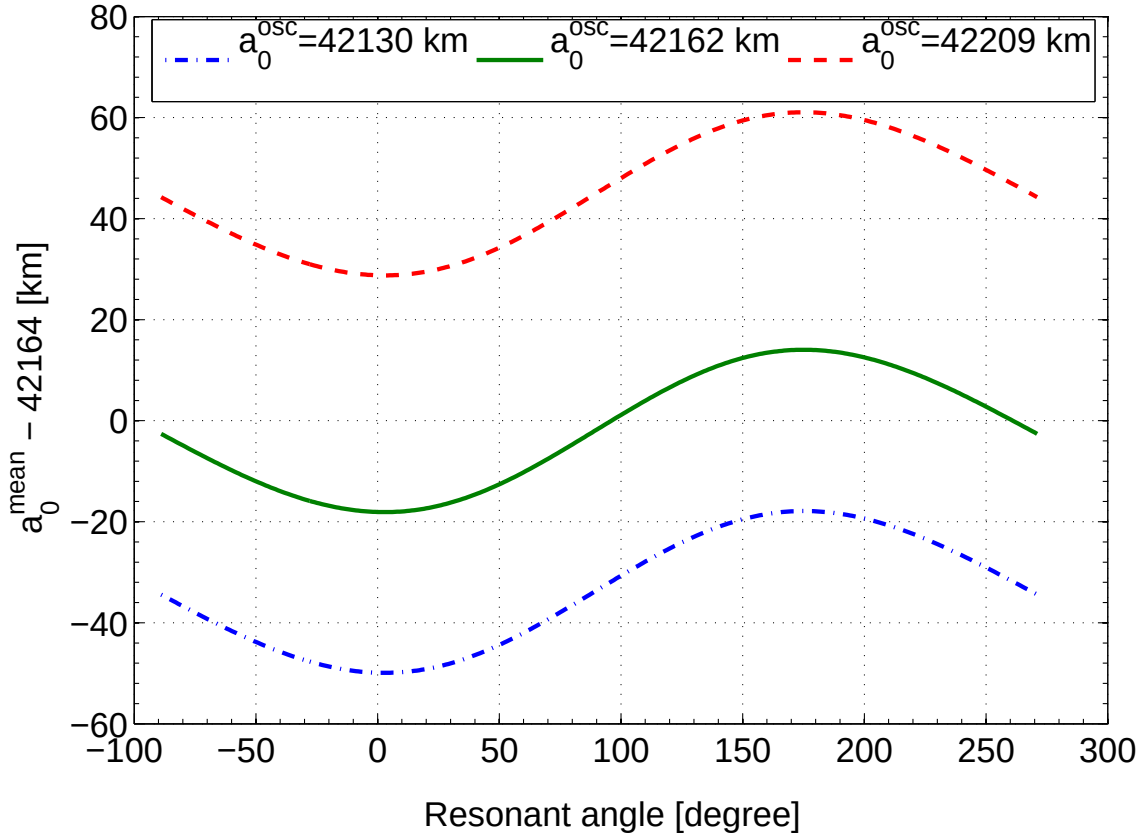

Figure 5.8: Relation between the mean semi-major axis and the resonant angle for various values of the osculating semi-major axis. The first osculating semi-major axis is taken above the libration region, the second is related to an osculating semi-major axes sampling which crosses the libration region and finally, the third sampling is taken below this region.

conditions leading to such an equilibrium were derived and are written as

$$\begin{cases} e_0 &= \dfrac{3}{2}\, C_r\, P_r\, \dfrac{A}{m}\, \dfrac{1}{n\, a\, n_\odot}\, \cos^2 \dfrac{\epsilon}{2} \simeq 0.01\, C_r\, \dfrac{A}{m}\,, \\ \varpi_0 &= \lambda_\odot(0)\,. \end{cases}$$

where n and $n_\odot$ are the angular motion of both the space debris and the Sun respectively, ϵ is the obliquity of the Earth with respect to the ecliptic and $\lambda_\odot(0)$ the initial ecliptic longitude of the Sun. If these conditions are fulfilled, it has been shown that the eccentricity vector $(e\,\cos\varpi, e\,\sin\varpi)$ remains constant leading to a fixed value of both the eccentricity and longitude of perigee. For an illustration, we refer to Figure 3.6 (page 80). Regarding this latter figure, it is clear that, apart from a phase difference, the amplitudes of variations of the eccentricities are qualitatively the same, except when adopting an initial time at epoch equal to 21 March. In this latter case, the eccentricity remains almost constant, as expected by the theory.

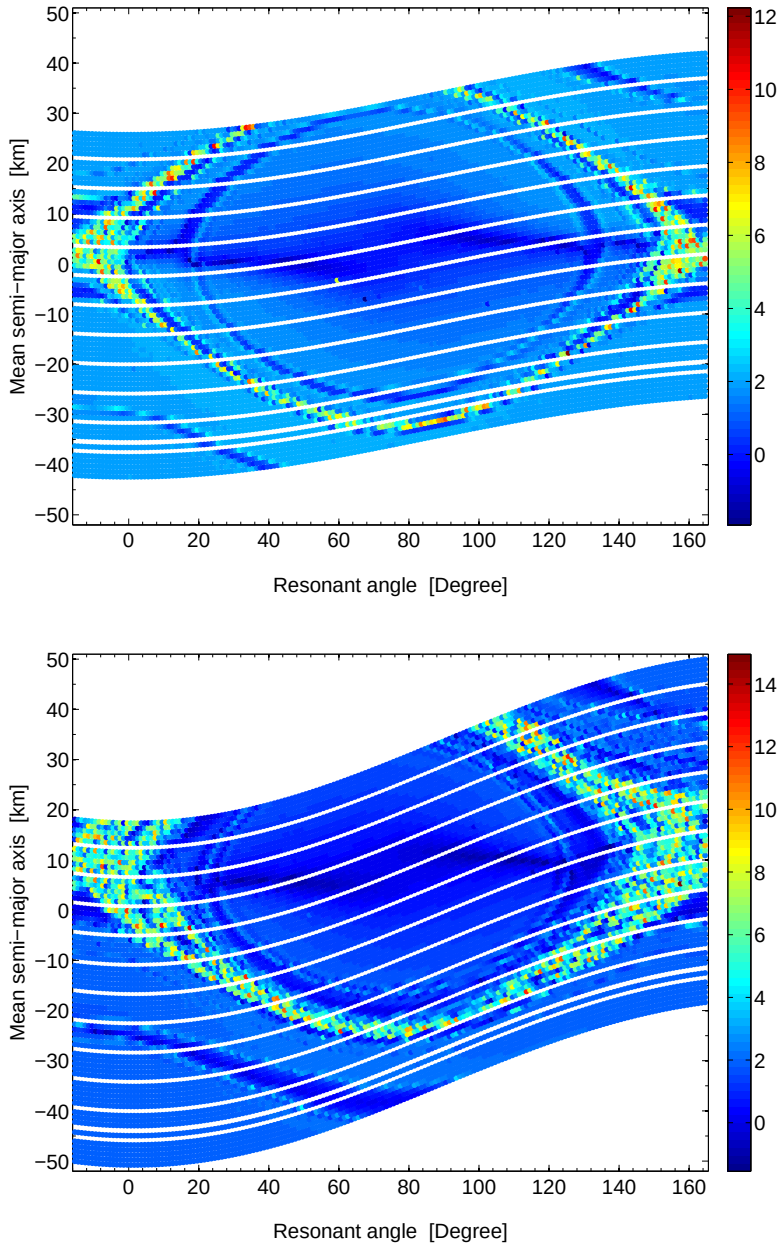

Figure 5.9: The MEGNO computed as a function of initial mean longitudes λ_0 and initial mean semi-major axes a_0. The model is the same as in Figure 5.6. The area-to-mass ratio is, $A/m = 5, 10\ \mathrm{m}^2/\mathrm{kg}$ for the top and for the bottom graph, respectively.

For the purpose of this investigation, Figure 5.10 shows the phase space in mean semi-major axis and longitude for a fixed value of the area-to-mass ratio $A/m = 10\ \mathrm{m}^2/\mathrm{kg}$ and fixed values of initial conditions, namely $e_0 = 0.1$, $i_0 = 0.004$, $\Omega_0 = \omega_0 = 0$. The differences between the two graphs only depends on the initial *time at epoch* parameter t_0. We could actually expect that different initial times at epoch, namely, different initial ecliptic longitudes of the Sun $\lambda_\odot(0)$, will reveal a quite rich collection of behaviors depending on the different states with respect to the before-mentioned *eccentricity equilibrium*. Actually,

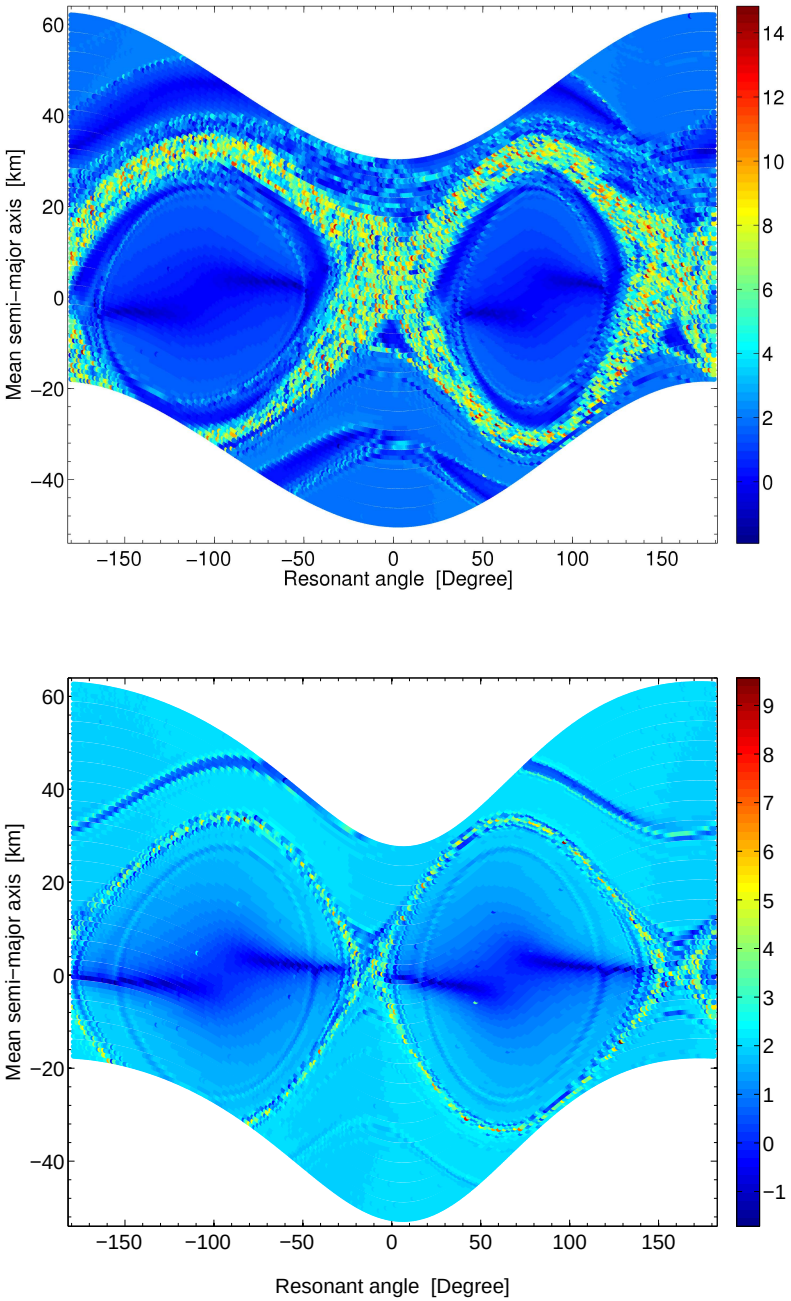

Figure 5.10: The MEGNO computed as a function of initial mean longitudes λ_0 and semi-major axis a_0. The equations of motion include the central body attraction, the second degree and order harmonics J_2, C_{22} and S_{22}, the luni-solar interaction as well as the perturbing effects of the solar radiation pressure. The mean longitude grid is 1° and the semi-major axis grid is 1 km spanning the $42\,164 \pm 35$ km range. The initial conditions are $e_0 = 0.1, i_0 = 0.004, \Omega_0 = \omega_0 = 0$ with an area-to-mass ratio $A/m = 10\ \mathrm{m}^2/\mathrm{kg}$. The patterns have been obtained using two different initial times at epoch, namely, 21 December 2000 [top], 21 March 2000 [bottom], respectively.

assuming an initial time at epoch of 21 December 2001, we see clearly that the phase space is filled by a large number of chaotic orbits (Figure 5.10, top). On the contrary, starting with an initial time at epoch of 21 March 2000, that is adopting a Sun pointing longitude of perigee ($\lambda_\odot(0) = 0$ rad), the values reached by the MEGNO tend to be lower and associated with a significantly narrower chaotic region always located close to the separatrices (Figure 5.10, bottom). In the latter case, the eccentricity presents only small yearly variations due to the proximity of the theoretical equilibrium. Therefore, these results seem to suggest that high-amplitude variations of the eccentricity increase considerably the order of magnitude of the chaotic region close to the separatrices and conversely, small eccentricity variations seem to considerably minimize the extent of chaotic regions. To justify this assumption, we performed a dedicated numerical simulation with the same set of parameters used in the one reported in Figure 5.10, but considering higher values of the initial eccentricity. Results are reported in Figure 5.11, the chosen time at epoch is 21 December 2000 and the initial eccentricities are, $e_0 = 0.2$ (top panel) and $e_0 = 0.4$ (bottom panel). In the latter case, the huge variations of the perigee altitude, induced by the large variations of the eccentricity as well as by the variations of the semi-major axis, lead to even more complicated dynamics. These results confirm thus the importance of the initial eccentricity in the appearance of chaos.

5.5 Secondary resonances

It is worth noting that inspecting Figures 5.9, 5.10 and 5.11, we clearly note the presence of some additional patterns located on both sides of the separatrices in the phase space. These never seen before regions, unexplained so far, are actually characterized by significant very low MEGNO values. Indeed, this observation underlines the fact that the dynamics of high area-to-mass ratios space debris is even more intricate than expected. In the following two paragraphs we will provide some numerical results and an analytical theory based on a simplified model, to better understand such zones.

5.5.1 Numerical investigations

We followed a large set of near-geosynchronous space debris, related to an extremely large set of initial conditions taken on both sides of the pendulum-like pattern, and for each one of the 72 000 orbits we computed the related MEGNO indicator. The initial conditions have been fixed by a mean longitude grid of 1°, spanning 360° and a semi-major axis grid of 1 km spanning the $42\,164 \pm 100$ km range, while the remaining ones and time at epoch are the same as in Figure 5.6. Moreover, as in the previous extended analyses, the model of forces also includes the central body attraction, the second degree and order harmonics J_2, C_{22} and S_{22} as well as the combined attractions of the Sun and the Moon. The perturbing effects of the direct solar radiation pressure are also considered for a high area-to-mass ratio fixed to $A/m = 10\ \mathrm{m}^2/\mathrm{kg}$. The results are reported in Figure 5.12, which is nothing but an extensive enlargement of the phase space presented in Figure 5.6 (bottom, left). This phase space widening clearly underlines the before-mentioned additional structures located at $\pm$ 40 km on each side of the

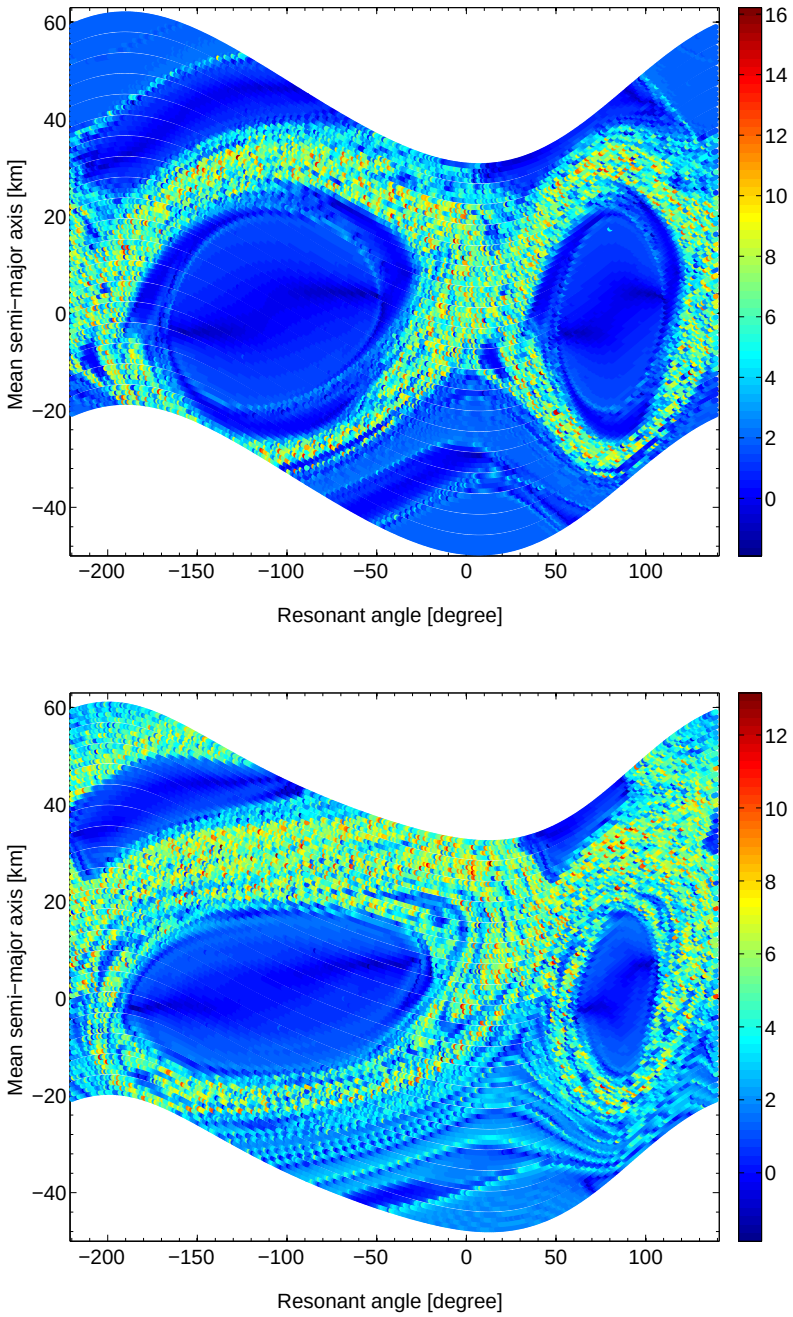

Figure 5.11: The MEGNO computed as a function of initial mean longitudes λ_0 and semi-major axis a_0. The equations of motion include the central body attraction, the second degree and order harmonics J_2, C_{22} and S_{22}, the luni-solar interaction as well as the perturbing effects of the solar radiation pressure. The mean longitude grid is 1° and the semi-major axis grid is 1 km spanning the $42\,164 \pm 35$ km range. The initial conditions are $i_0 = 0.004$, $\Omega_0 = \omega_0 = 0$ with an area-to-mass ratio $A/m = 10\ \mathrm{m}^2/\mathrm{kg}$. Time at epoch is 21 December 2000. The patterns have been obtained using two initial eccentricities, $e_0 = 0.2$ [top] and $e_0 = 0.4$ [bottom].

resonant area. Furthermore, besides these patterns, what is of special interest is that this figure also brings to the light supplementary structures located at approximately 80 km on both sides of the main resonance, suggesting that the phase space is actually foliated by a larger set of secondary structures. Moreover, the order of magnitude of these additional patterns seems to be directly related to the inverse of the distance with respect to the resonant area.

In addition, we also performed a set of similar numerical investigations, in order to distinguish qualitatively the relative relevance of some parameters such as the initial mean eccentricity and the value of the area-to-mass ratio, as well as the importance of the 1:1 resonance and of the third-body perturbations in the occurrence of such secondary structures. Even though these results are not presented here in detail, we can draw the following preliminary conclusions: the second order harmonic J_2 as well as the third-body perturbations do not seem to be really relevant and crucial in the appearance of these additional patterns. In other words, the unexpected patterns occur only when taking into account the combined effects of both the second order and degree harmonic and the direct solar pressure. As a matter of fact, the extended numerical investigations performed in Figure 5.6 (top, left) or similarly those performed in Breiter et al. (2005a) also present these structures even though they are difficult to perceive. Actually, the order of magnitude of the secondary patterns seems to be directly proportional to the area-to-mass ratio value or equivalently directly proportional to the mean value of the eccentricity. To get even more concluding results, we considered a blow-up of the phase space (dashed line rectangle in Figure 5.12) with a fairly high-resolution sampling (approximately 150 meters w.r.t. the semi-major a axis and 0.3° w.r.t. the resonant angle σ). Figure 5.13 (top) shows this phase space widening, wherein we defined a so-called *resonant angle section* (horizontal black solid line), that is the subset of orbits having the same initial resonant angle value. This resonant angle section spans the complete range in semi-major axis and passes next to the stable equilibrium point. For each orbit defined on this section, we computed the MEGNO indicator and in Figure 5.13 (middle) we report this value at the end of the simulation as a function of the semi-major axis.

To double check our results, we performed a frequency analysis investigation (Laskar et al., 1992; Laskar, 1995; Noyelles et al., 2008) aimed to study the behavior of the proper frequency of the resonant angle σ, whose results are reported in Figure 5.13 (bottom). Here one can clearly see the distinctive characteristics regarding the well-know 1:1 resonance between the mean longitude and the sidereal time. Indeed, both the MEGNO and the fundamental period show distinctively a minimum close to the stable equilibrium point. In this case, as previously mentioned in Section 5.3, the MEGNO should slowly converge to $\overline{Y}(t) = 2$ everywhere except at the equilibrium point where the limit value is $\overline{Y}(t) = 0$; this is why, using a finite integration time, we obtain such V-shaped curve, close to 0 in the center of the resonance and to 2 on the borders. It is also worth noting that the fundamental period of σ is reported to be close to 2.25 years, which is in good agreement with the well-known 818 days libration period of a typical uncontrolled near-geosynchronous object. Near the separatrices, the MEGNO clearly presents some obvious high values which confirms the presence of chaotic orbits. Here, the fundamental period reaches significant values and is as a matter of fact not well determined,

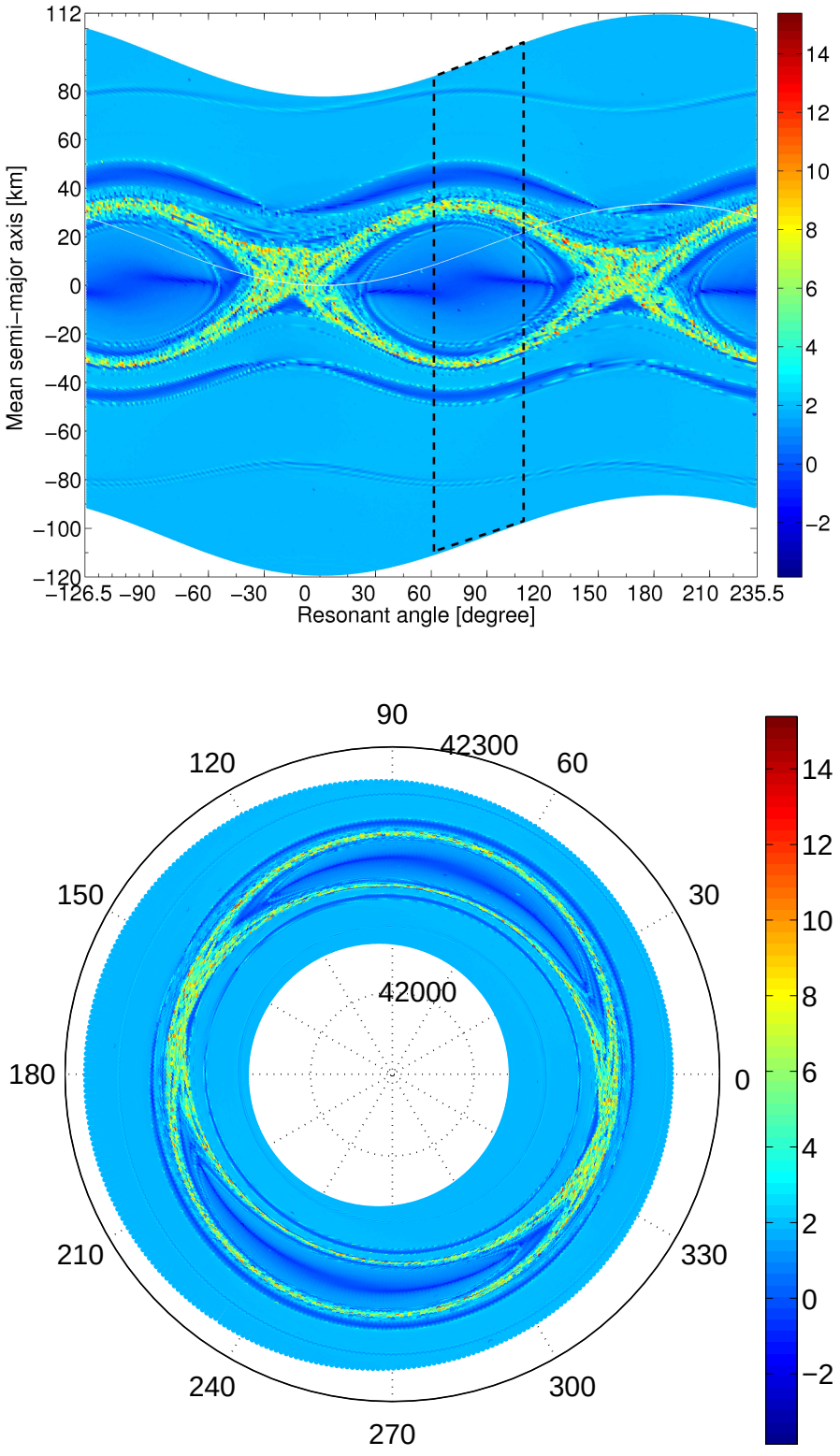

Figure 5.12: The MEGNO computed as a function of initial mean longitudes λ_0 and semi-major axis a_0. [Top] Enlargement of the complete phase space. [Bottom] Enlargement of the complete phase space shown in polar coordinates. The equations of motion include the central body attraction, the second degree and order harmonics J_2, C_{22} and S_{22} as well as the luni-solar perturbations. The mean longitude grid is 1° and the semi-major axis grid is 1 km, spanning the $42\,164 \pm 100$ km range. The initial conditions are $e_0 = 0.002$, $i_0 = 0.004$, $\Omega_0 = \omega_0 = 0$. The area-to-mass ratio is $A/m = 10\ \mathrm{m}^2/\mathrm{kg}$. Time at epoch is 25 January 1991.

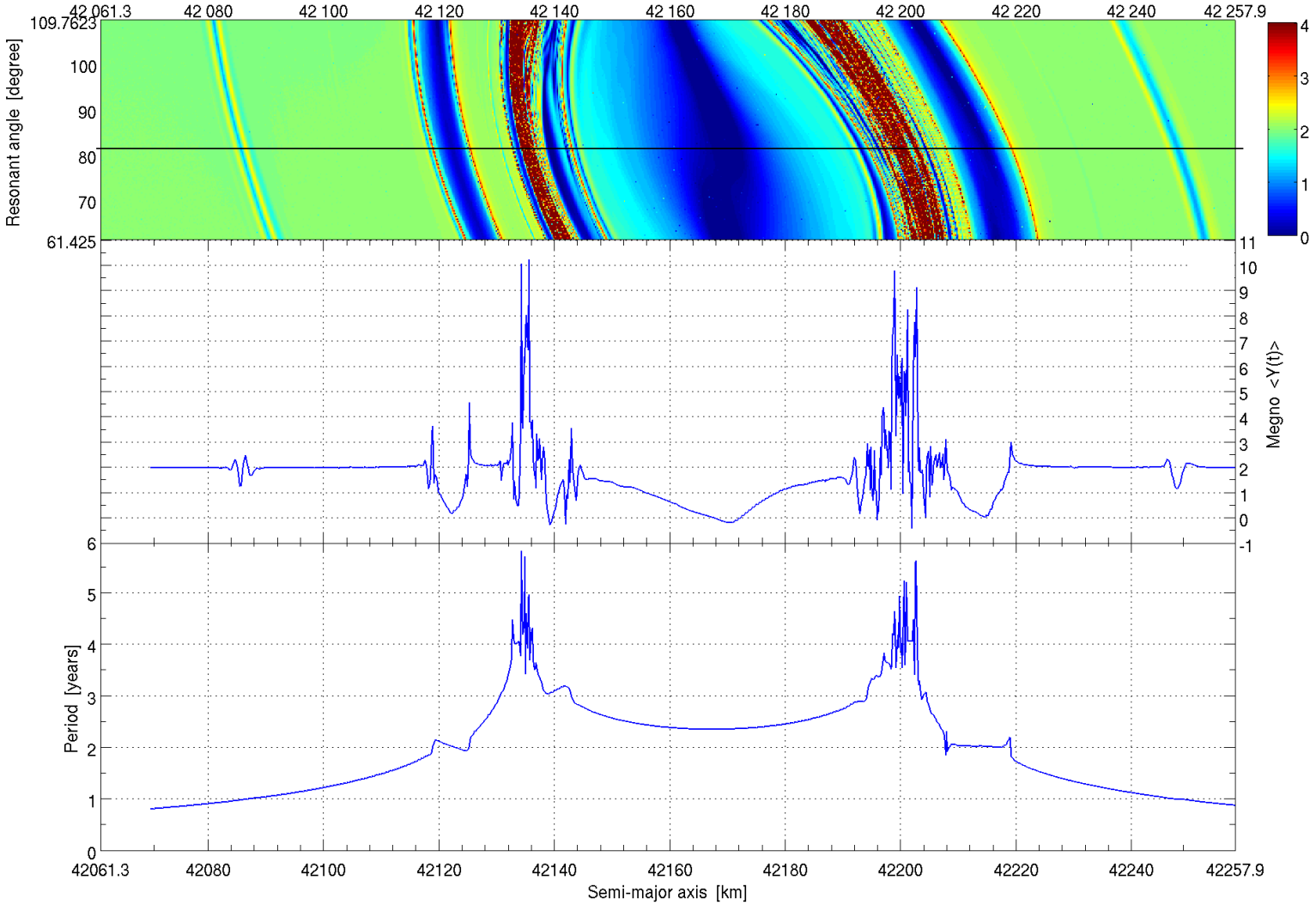

Figure 5.13: Blow-up of the phase space with the specification of a *resonant angle section* (horizontal black solid line), that is the set of orbits having the same (osculating) initial resonant angle value, near the first stable equilibrium, namely $\sigma_0^{section} = 81.67°$ (top panel). Evolution of the MEGNO with respect to the initial semi-major axis a_0 for the specified section (middle panel). The fundamental period of σ with respect to the initial semi-major axis a_0, computed by means of frequency analysis for the specified section (bottom panel). The estimation of the periods are made over a 20 years period of time.

once again supporting the result of the existence of a chaotic zone. Moreover the use of frequency analysis allows us to strongly support the hypothesis that the additional patterns are actually related to ***secondary resonances***. Indeed, if we look at the evolution of the fundamental period with respect to the semi-major axis, it is clear that the so-called secondary resonances are associated, regarding the angle σ, with periods that are commensurate with 1 year. More precisely, the major secondary resonance located at approximately 40 km on both sides of the pendulum-like pattern are related to a 2 years fundamental period of σ. Concerning the farther patterns located at $\pm$80 km, the fundamental period of σ turns out to be very close to 1 year. As a consequence, we can presumably assume that these before-mentioned secondary resonances are actually related to a commensurability between σ and the 1 year period angle $\lambda_\odot$, that is the ecliptic longitude of the Sun.

To justify this assumption, we focused our attention on the major secondary resonances located at $\pm$40 km on both sides of the pendulum-like pattern, considering the time evolution of various linear combinations between σ and $\lambda_\odot$. For this purpose, we considered various initial semi-major axes in the phase space. The results are shown in Figure 5.14. At first glance, it is apparent that three propagations stand apart from others. In the first row of Figure 5.14, that is regarding the evolution of the resonant angle σ, we clearly identify the well-know characteristics related to the primary resonance. In particular, in Figure 5.14a, that is when considering an initial semi-major axis inside the primary resonant (a_0 =42 188 km), σ shows a well-known long-periodic libration (2.25 years) whereas σ circulates outside this region. Furthermore, what is of special interest is the time evolution of both $2\sigma + \lambda_\odot$ and $2\sigma - \lambda_\odot$ shown in the second and third row, respectively. It is clear that most of the time these angles show a significant circulation regime. However, when considering an initial semi-major axis inside the major lower secondary resonance for $2\sigma - \lambda_\odot$ or similarly inside the major upper secondary resonance for $2\sigma + \lambda_\odot$, both these angles show a significant long-term evolution (Figure 5.14b,c).

5.5.2 Analytical investigation – simplified model

The presence and the location of these secondary resonances can be studied using an appropriate simplified model. Hence we model the averaged geostationary motion by a pendulum-like system, given by its Hamiltonian formulation up to order e^2 in the series expansion

$$\mathcal{H} = -\frac{\mu^2}{2L^2} - \dot{\theta}L + 3\,\frac{\mu^4}{L^6}\,R_e^2\,(1 - \frac{5}{2}\,e^2)\,S_{2200}(\Omega, \omega, M, \theta)\,,$$

where

$$S_{2200}(\Omega, \omega, M, \theta) = C_{22}\cos\,2\sigma + S_{22}\sin\,2\sigma\,.$$

In the context of direct solar radiation pressure, we can introduce the factor $\mathcal{Z}$ proportional to A/m through the eccentricity e (for further details, we refer to the averaged simplified analytical model developed in Chapter 3). In keeping with Eq. (3.15), the time evolution of both the eccentricity e and the longitude of perigee ϖ were found to be (neglecting the

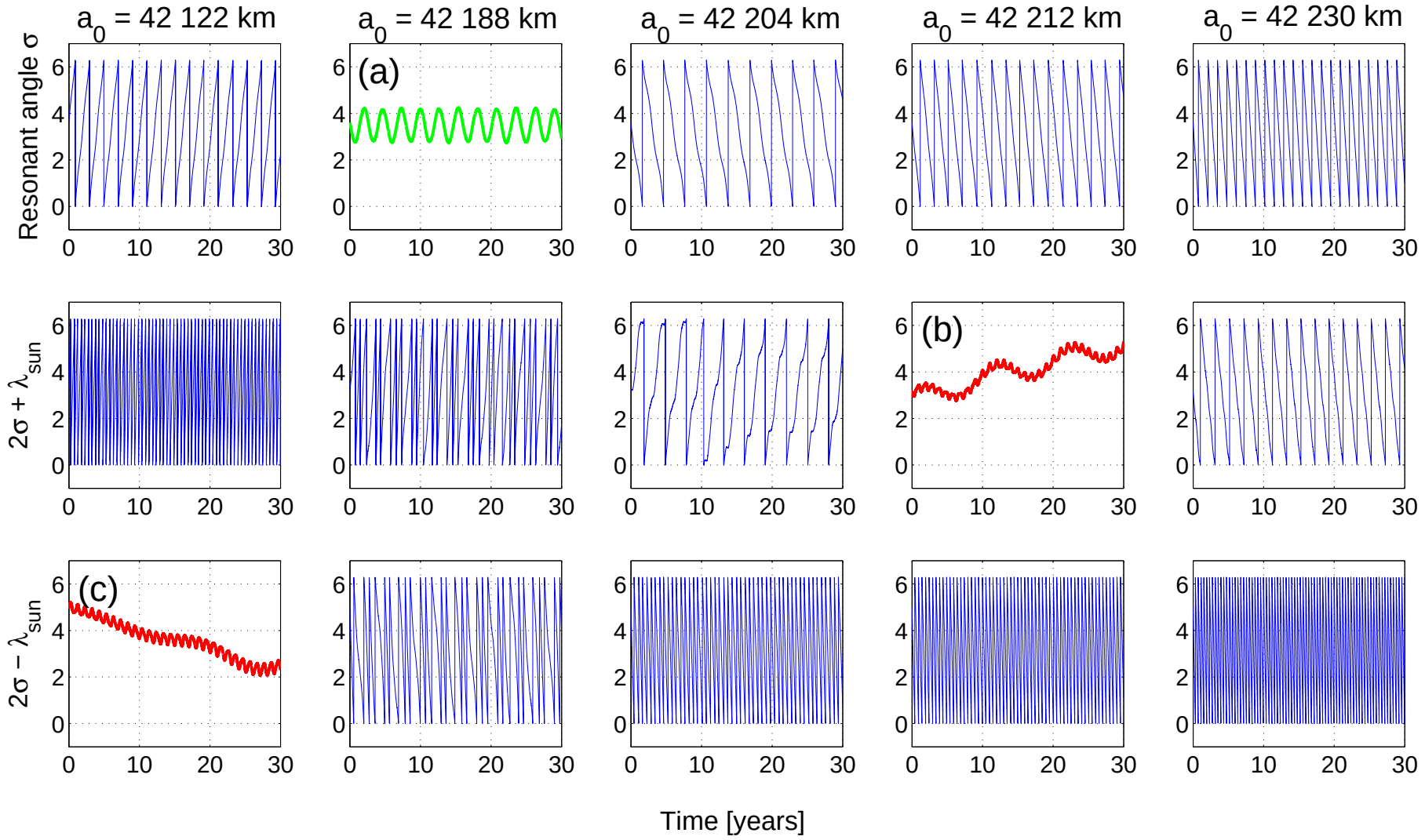

Figure 5.14: Time evolution of the angles σ, $2\sigma + \lambda_\odot$ and $2\sigma - \lambda_\odot$ (in radians) for several semi-major axes. In the lower major secondary resonance, $a_0 = 42\,122$ km. In the eye of the principal resonance, $a_0 = 42\,188$ km. Between the primary resonance and the upper secondary resonance, $a_0 = 42\,204$ km. Inside the upper major secondary resonance, $a_0 = 42\,212$ km. Outside the upper major secondary resonance, $a_0 = 42\,230$ km.

obliquity of the Earth w.r.t. to the ecliptic)

$$\begin{aligned} e\cos\varpi &= \frac{\mathcal{Z}}{L\,n_\odot}\cos\lambda_\odot + \alpha_0\,, \\ e\sin\varpi &= \frac{\mathcal{Z}}{L\,n_\odot}\sin\lambda_\odot - \beta_0\,, \end{aligned}$$

which introduces $\lambda_\odot$ in the Hamiltonian. The quantity $n_\odot$ is the mean motion of the Sun and both α_0 and β_0 are related to initial conditions with respect to the eccentricity and the longitude of perigee. Then, the resulting Hamiltonian takes the generic form

$$\mathcal{H} = -\frac{\mu^2}{2L^2} - \dot{\theta}L + \frac{F}{L^6}\,\cos(2\sigma - 2\sigma_0) - \frac{G}{L^6}\,2\cos(2\sigma - 2\sigma_0)\,\cos(\lambda_\odot + \delta)\,,$$

where δ, F, G, σ_0 are constants. A suitable transformation is then necessary to introduce action-angle variables (ψ, J) in the libration and in the circulation region of the double pendulum, in such a way any trajectory of the double pendulum is characterized by a constant action J and a corresponding constant frequency $\dot{\psi}$. Rewriting the perturbed system (because of the $\lambda_\odot$ terms) by means of these new variables and then using the expansions in Bessel functions, we could isolate any resonance of the type $k\psi \pm \lambda_\odot$, in the circulation region, for any $|k|$ and in the libration region, for $|k| \geq 3$, which corresponds to our frequency analysis. This analysis is surely promising, but it exceeds the goals of our numerical investigations.

Conclusions and Outlooks

Conclusions

The main objectives of this research work have been accomplished. Indeed, we have developed a new method especially devoted to the specific study of space debris orbiting in the neighborhood of the geostationary ring. Our approach has been motivated by the distinctive features characterizing this region. More specifically, our approach has been first developed in order to tackle the well-known problem of small-divisors arising in the numerical integrations of the equations of motion of such objects. This problem has been solved by using a set of universal elements in the framework of a quasi-Hamiltonian formalism. Moreover, our approach has also been designed as a so-called semi-analytical method, that is a procedure based on an analytical filtering of the osculating differential equations which is in turn followed by a numerical integration of the transformed equations. As a consequence of both the choice of a semi-analytical theory and the alternative selection of entirely non-singular variables, our work accounts for a new theory which ensures a high stability of the numerical integrations over periods of several dozens of years mostly because the analytical averaging process has been made once and for all, allowing an extremely fast numerical integration of a large number of orbits, without any short-period variations.

As a result of the unexpected discovery of high-area-to-mass ratio space debris presumably located in geosynchronous orbit, we seized the opportunity to extend our theory by including the solar radiation pressure acceleration. This extension has been especially intended to derive the main effects of the direct solar radiation pressure by analyzing the mid- and long-term evolution of both the eccentricity and the inclination vectors of geosynchronous space debris with high area-to-mass ratios. These last results have shown to be in good agreement with the works of Anselmo and Pardini (2005) and Chao (2006) and elaborate these results, emphasizing the importance of adopting an accurate and well-suited model. The results also confirm that such high area-to-mass ratio space debris are surely good candidates to the recently discovered debris population with mean motions of about one revolution per day and orbital eccentricities as high as 0.6.

As a second improvement of our theory, we have also presented an extension of our homemade semi-analytical theory, by developing a complete algorithm taking into account the long-term effects induced by the Earth's shadow. This algorithm was built within the context of non-singular motion and can therefore be applied to an even larger class of orbits. In all the performed investigations, we showed that our semi-analytical theory is in good agreement with numerical integrations. Furthermore, the integration of the filtered equations of motion over the short periods, coupled with our algorithm, as well as the integration of the osculating equations of motion, led also to an insightful understanding of the dynamics of the semi-major axis. We showed how both the eccentricity and the inclination induce various amplitudes of the cumulated mean variations of the semi-major axis over the eclipse seasons.

Finally, the predictability of high area-to-mass ratio space debris located near the geosynchronous region has also been investigated by means of a recent variational chaos indicator

called the MEGNO. Thanks to this highly capable technique, we have clearly identified the regular (stable) and irregular (chaotic) orbits. This efficient method allowed us to obtain a clear picture of the phase space, hence showing that chaotic regions can be particularly relevant, especially for very high area-to-mass ratios objects. Moreover, we discussed the importance of both the initial eccentricity and time at epoch in the appearance of chaos. We unveiled a relevant class of additional unexpected patterns which were identified as secondary resonances, that were numerically studied by means of both the MEGNO criterion and frequency map analysis, to eventually conclude that they involve commensurabilities between the primary resonant angle and the ecliptic longitude of the Sun. We also presented an analytical scheme that could explain their existence.

Outlooks

Regarding the elaboration of our theory, and though our semi-analytical theory has been mostly applied to the peculiar case of high area-to-mass ratio space debris, we ought to mention that our method could easily be applied to an even larger class of orbits such as LEO and MEO orbits. In this case, the theory should be adapted by considering the cross-coupling effects by means of a more rigorous averaging process to be carried out to a higher order by using the Lie algorithm. Furthermore, although we mainly considered the first major perturbations of the Earth's gravity field, the theory generally allows the inclusion of both zonal and tesseral harmonics developed up to an arbitrary degree and order.

With regard to the solar radiation pressure modeling, the theory could surely be extended by taking into account some theoretical space debris attitude motions. Indeed, the space debris have doubtlessly complex shape that could significantly affect the dynamics. Though this attitude motion as well as the shape can not be easily derived in most of the cases, it should be all-interesting to investigate to what extent the motion can be affected. These investigations could be first developed in the framework of our semi-analytic theory. Subsequently, the stability could also be investigated by using the MEGNO criterion.

Concerning the Earth's shadowing effects, our algorithm could also be improved by considering a more elaborate model. In particular, one should investigate the consequences of adopting a cylindrical boundary (where the radiation pressure is instantaneously "turning on/off") instead of taking into account the two conic boundaries with a continuous transition between the penumbra and umbra boundaries.

APPENDIX

Appendix A

List of principal symbols and notations

Symbols	Designation	Dimension
a	semi-major axis	[m]
$\boldsymbol{a}$	acceleration vector (often with subscripts)	[m s^{-2}]
a_e	Earth equatorial radius, $a_e = 6\,378\,135$ m	[m]
$a_\odot$	mean distance between the Sun and the Earth, $a_\odot = 1$ AU	[m]
A/m	area-to-mass ratio	[m^2/kg]
A	area, effective cross-section	[m^2]
$\mathcal{A}_j^{(n)}$	arbitrary polynomial function	
$\mathcal{B}_j^{(n)}$	arbitrary trigonometric function	
c	speed of light in vacuum	[m s^{-1}]
C_{nm}	geopotential harmonic coefficient	
C_r	"reflectivity" coefficient, radiation coefficient	
dV	elementary volume	[m^3]
dS	elementary surface	[m^2]
e	eccentricity	
E	eccentric anomaly	[rad], [degree]
ϵ	obliquity of the Earth w.r.t. the ecliptic	[rad], [degree]
f	true anomaly	[rad], [degree]
F_{nmp}	inclination functions	
G	Delaunay's element, $G = \sqrt{\mu\, a(1-e^2)}$	[m]
G_{npq}	eccentricity functions	
h	Planck's constant, $h = 6.62 \times 10^{-34}$ J s	[J s]
H	Delaunay's element, $H = \sqrt{\mu\, a(1-e^2)}\, \cos i$	[m]
$\mathcal{H}$	generic Hamiltonian disturbing function	
$\mathcal{H}_{3b}$	third-body Hamiltonian disturbing function	
$\mathcal{H}_{pot}$	geopotential Hamiltonian disturbing function	

continued on next page

continued from previous page

Symbols	Designation	Dimension
i	inclination	[rad], [degree]
$\boldsymbol{I}_{n\times n}$	n-dimensional identity matrix	
$\mathcal{I}$	symplectic matrix	
$\boldsymbol{J}$	Jacobian matrix	
J_n	zonal geopotential harmonic coefficient, $J_n = -C_{n0}$	
J_{nm}	geopotential harmonic coefficient, $J_{nm} = \sqrt{C_{nm}^2 + S_{nm}^2}$	
L	$L = \sqrt{\mu\, a}$, conjugate momentum w.r.t. λ	[m]
m	mass	[kg]
m_i	mass of the third body i	[kg]
M	mean anomaly	[rad], [degree]
$M_\oplus$	mass of the Earth	[kg]
n	mean orbital motion of the space debris	[rad s^{-1}]
$n_\odot$	mean motion of the Sun w.r.t. to the Earth, $n_\odot = 2\pi/[year]$	[rad s^{-1}]
p	longitude of perigee [opposite sign]	[rad], [degree]
	semi-latus rectum, $p = a\,(1 - e^2)$	[m]
P	conjugate momentum w.r.t. p, $P = L - G$	
$\mathcal{P}_n$	Legendre polynomial of degree n	
$\mathcal{P}_n^m$	Legendre functions, degree n, order m	
P_r	radiation pressure, $P_r = 4.56 \times 10^{-6}$ N/m^2	[N m^{-2}]
q	longitude of the ascending node [Opposite sign]	[rad], [degree]
Q	conjugate momentum w.r.t. q, $Q = G - H$	[m]
$\boldsymbol{r}$	geocentric vector of the space debris	[m]
r	geocentric distance of the space debris	[m]
$\boldsymbol{r}_\odot$	geocentric position of the Sun	[m]
$r_\odot$	geocentric distance of the Sun	[m]
$\boldsymbol{S}$	radial direction	
T_λ	Lyapunov time, $T_\lambda = 1/\lambda$	
$\boldsymbol{T}$	along-track direction	
U	dimension-free quantity defined by $U = \sqrt{(2P/L)}$	
V	dimension-free quantity defined by $V = \sqrt{(2Q/L)}$	
$\boldsymbol{W}$	out-of-plane direction	
$\mathcal{W}$	generating function w.r.t the averaging process	
$x,\ y,\ z$	state vector	[m]
$\bar{x},\ \bar{y},\ \bar{z}$	normalized state vector	[m]
x_1	Poincaré variables $x_1 = \sqrt{2P}\cos p$	

continued on next page

continued from previous page

Symbols	Designation	Dimension
y_1	Poincaré variables $y_1 = \sqrt{2P}\sin p$	
x_2	Poincaré variables $x_2 = \sqrt{2Q}\cos q$	
y_2	Poincaré variables $y_2 = \sqrt{2Q}\sin q$	
X_1	non-dimensional Poincaré variables $x_1 = \sqrt{2P/L}\cos p$	
Y_1	non-dimensional Poincaré variables $y_1 = \sqrt{2P/L}\sin p$	
X_2	non-dimensional Poincaré variables $x_2 = \sqrt{2Q/L}\cos q$	
Y_2	non-dimensional Poincaré variables $y_2 = \sqrt{2Q/L}\sin q$	
$X_\odot,\ Y_\odot, Z_\odot$	normalized state vector of the Sun	
$Y,\ \overline{Y}(t)$	MEGNO and its averaged value, respectively	
$\mathcal{Z}$	auxiliary quantity, $\mathcal{Z} = \frac{3}{2}\, a\, C_r\, P_r\, \frac{A}{m}\, \left(\frac{a_\odot}{r_\odot}\right)^2$	
λ	mean longitude, $\lambda = M + \Omega + \omega$	[rad], [degree]
	geocentric equatorial longitude (spherical coordinates)	[rad], [degree]
$\lambda_\odot$	ecliptic longitude of the Sun	[rad], [degree]
$\lambda^\star$	mean longitude equilibrium points w.r.t. 1:1 resonance	[rad], [degree]
$\beta_\odot$	ecliptic latitude of the Sun	[rad], [degree]
δ_{ij}	Kronecker function, $\delta_{ij} = 1$ for $i = j$, zero otherwise	
$\boldsymbol{\delta}_\phi(t),\ \boldsymbol{\delta}$	tangent vector (variational method)	
μ	gravitational constant of the Earth	[$\mathrm{m^3\,s^{-2}}$]
$\mu_{\leftmoon}$	gravitational constant of the Moon	[$\mathrm{m^3\,s^{-2}}$]
$\mu_\odot$	gravitational constant of the Sun	[$\mathrm{m^3\,s^{-2}}$]
μ_i	gravitational constant of the third body i	[$\mathrm{m^3\,s^{-2}}$]
ω	argument of perigee	[rad], [degree]
Ω	longitude of the ascending node	[rad], [degree]
θ	sidereal time	[rad], [degree]
ϖ	longitude of perigee, $\varpi = \Omega + \omega$	[rad], [degree]
σ	resonant angle, $\sigma = \lambda - \theta$	[rad], [degree]
Ψ	geocentric angle between the Sun and the space debris	[rad], [degree]
ϕ	geocentric equatorial latitude (spherical coordinates)	[rad], [degree]
$\Phi_\odot$	solar radiation constant, $\Phi_\odot$ = 1368 Watt/$\mathrm{m^2}$	[$\mathrm{Watt\,m^{-2}}$]
ν	fundamental frequency	[$\mathrm{s^{-1}}$]
$\mathbb{R}^n$	n-dimensional set of real numbers	
$\mathbb{T}^n$	n-dimensional torus	
$\dot{\circ}$	first time derivative	
$\ddot{\circ}$	second time derivative	

continued on next page

continued from previous page

Symbols	Designation	Dimension
$(\circ;\circ)$	Poisson's brackets	
$\overline{\circ}$	averaged quantity (singly averaged)	
$\widetilde{\circ}$	auxiliary quantity	
∇	gradient operator	
$\otimes$	Cartesian product	
$\langle \circ \,.\, \circ \rangle$	scalar product	
$\langle \circ \rangle_\alpha$	average w.r.t. angle α	
$\circ_\odot$	with respect to the Sun	
$\circ_\leftmoon$	with respect to the Moon	
$\circ_\oplus$	with respect to the Earth	

Appendix B

Cunningham's method

B.1 Cunningham's method

It is worth noting that in the computation of the geopotential, some recurrence relations can be used. In this section, the method is presented for the accurate and efficient computation of the forces from any number of zonal and tesseral terms in the Earth's gravitational potential.

Let us first consider the following quantities

$$\begin{aligned} V_{nm} &= \left(\frac{R_e}{r}\right)^{n+1} P_{nm}(\sin\phi)\cos m\lambda\,, \\ W_{nm} &= \left(\frac{R_e}{r}\right)^{n+1} P_{nm}(\sin\phi)\sin m\lambda\,. \end{aligned}$$

Making use of V_{nm} and W_{nm}, the Earth's gravitity potential may be written as

$$U = \frac{\mu}{R_e}\sum_{n=0}^{\infty}\sum_{m=0}^{n}(C_{nm}V_{nm} + S_{nm}W_{nm})\,,$$

where V_{nm} and W_{nm} satisfy the following recurrence relations

$$\begin{aligned} V_{mm} &= (2m-1)\left\{\frac{xR_e}{r^2}V_{m-1,m-1} - \frac{yR_e}{r^2}W_{m-1,m-1}\right\}\,, \\ W_{mm} &= (2m-1)\left\{\frac{xR_e}{r^2}W_{m-1,m-1} - \frac{yR_e}{r^2}V_{m-1,m-1}\right\} \end{aligned} \tag{B.1}$$

as well as

$$\begin{aligned} V_{n,m} &= \left(\frac{2n-1}{n-m}\right)\frac{zR_e}{r^2}\,V_{n-1,m} - \left(\frac{n+m-1}{n-m}\right)\frac{R_e}{r^2}\,V_{n-2,m}\,, \\ W_{n,m} &= \left(\frac{2n-1}{n-m}\right)\frac{zR_e}{r^2}\,W_{n-1,m} - \left(\frac{n+m-1}{n-m}\right)\frac{R_e}{r^2}\,W_{n-2,m}\,. \end{aligned} \tag{B.2}$$

Furthermore, we have

$$V_{00} = \frac{R_e}{r} \quad \text{and} \quad W_{00} = 0$$

leading to the following recursions scheme

$$\begin{array}{ccccccccc}
V_{00}, W_{00} & & & & & & & & \\
\downarrow & \searrow & & & & & & & \\
V_{10}, W_{10} & & V_{11}, W_{11} & & & & & & \\
\downarrow & & \downarrow & \searrow & & & & & \\
V_{10}, W_{10} & & V_{11}, W_{11} & & V_{22}, W_{22} & & & & \\
\downarrow & & \downarrow & & \downarrow & \searrow & & & \\
\vdots & & \vdots & & \vdots & & \ddots & & \\
\downarrow & & \downarrow & & \downarrow & & & \searrow & \\
V_{n0}, W_{n0} & & V_{n1}, W_{n1} & & V_{n2}, W_{n2} & & \dots & V_{nn}, W_{nn}\,. &
\end{array}$$

B.2 Osculating equations of motion in Cartesian coordinates

The osculating acceleration induced by the geopotential can be written as the gradient of the Earth's potential as

$$\ddot{\boldsymbol{r}} = \boldsymbol{\nabla} U\,,$$

where U is written as (see Eq. 2.5)

$$U = \frac{\mu}{r} \sum_{n=0}^{\infty} \sum_{m=0}^{n} \left(\frac{R_e}{r} \right) \mathcal{P}_n^m(\sin\phi)(C_{nm} \cos\, m\lambda + S_{nm} \sin\, m\lambda)\,.$$

Making use of the before-mentioned algorithm, the acceleration, expressed with respect to the Cartesian coordinates, can be computed as

$$\ddot{x} = \sum_{n,m} \ddot{x}_{nm}, \qquad \ddot{y} = \sum_{n,m} \ddot{y}_{nm}, \quad \ddot{z} = \sum_{n,m} \ddot{z}_{nm},$$

where

$$\begin{aligned}
\ddot{x}_{nm} \quad &\overset{m=0}{=} \quad \frac{\mu}{R_e^2} \Big\{ J_n\, V_{n+1,1} \Big\} \\
&\overset{m\geq 0}{=} \quad \frac{1}{2} \frac{\mu}{R_e^2} \Big\{ (-C_{nm}\, V_{n+1,m+1} - S_{nm}\, W_{n+1,m+1}) \\
&\qquad + \frac{(n-m+2)!}{(n-m)!}\, (C_{nm}\, V_{n+1,m-1} + S_{nm}\, W_{n+1,m-1}) \Big\},
\end{aligned}$$

$$
\begin{aligned}
\ddot{y}_{nm} &\overset{m=0}{=} \frac{\mu}{R_e^2}\left\{J_n\, W_{n+1,1}\right\} \\
&\overset{m\geq 0}{=} \frac{1}{2}\frac{\mu}{R_e^2}\Big\{\left(-C_{nm}\, W_{n+1,m+1} - S_{nm}\, V_{n+1,m+1}\right) \\
&\qquad + \frac{(n-m+2)!}{(n-m)!}\left(C_{nm}\, W_{n+1,m-1} + S_{nm}\, V_{n+1,m-1}\right)\Big\}, \\
\ddot{z}_{nm} &= \frac{\mu}{R_e^2}\Big\{(n-m+1)\left(-C_{nm}\, V_{n+1,m} - S_{nm}\, W_{n+1,m}\right)\Big\}.
\end{aligned}
$$

For further details, we refer to Cunningham (1970) or latter Montenbruck and Gill (2000) where a detailed description of the algorithm is given.

Appendix C

Eccentricity and inclination functions

C.1 Eccentricity functions

For instance, when $q = 2p - n$

$$G_{npq}(e) = \frac{1}{(1-e^2)^{n-1/2}} \sum_{d=0}^{p'-1} \left(\begin{array}{c} n-1 \\ d \end{array} \right) \left(\begin{array}{c} 2d+n-2p' \\ d \end{array} \right) \left(\frac{e}{2}\right)^{2d+n-2p'} , \qquad \text{(C.1)}$$

where $p' = p$ if $p \leq n/2$, and $p' = n - p$ if $p \geq n/2$ (Vallado, 2001). For the terms, $n - 2p + q \neq 0$, that is for the short-period terms, the development of $G_{npq}(e)$ is much more complicated, leading to an infinite series of the eccentricity. Actually, the eccentricity functions are directly related to the Hansen coefficients by

$$G_{npq} = X_{n-2p+q}^{-(n+1),(n-2p)} .$$

The third index q can be negative or positive and its magnitude determines the power of

Table C.1: Eccentricity Functions $G_{npq}(e)$ from Eq. (C.1). For a more complete list, we refer to Kaula (1966) and Chao (2005)

n	p	q	n	p	q	Eccentricity Functions, $G_{npq}(e)$
2	0	-2	2	2	2	0
2	0	-1	2	2	1	$-e/2 + e^3/16 + \cdots$
2	0	0	2	2	0	$1 - 5\,e^2/2 + 13\,e^4/16 + \cdots$
2	0	1	2	2	-1	$7e/2 - 123\,e^3/16 + \cdots$
2	0	2	2	2	-2	$17\,e^2/2 - 115\,e^4/6 + \cdots$
2	1	-2	2	1	2	$9\,e^2/4 + 7\,e^4/4 + \cdots$
2	1	-1	2	1	1	$3\,e/2 + 27\,e^3/16 + \cdots$
			2	1	0	$(1-e^2)^{-3/2}$

the eccentricity of the first term of the infinite series. Thanks to the properties of the Hansen coefficients, some symmetries are found in most of the terms, and some terms are represented in closed-form functions of the eccentricity as shown in Eq. (C.1) (Chao, 2005). Table C.1 shows the expressions for G_{npq} with npq values up to 222.

C.2 Inclination functions

Unlike the eccentricity functions, the inclination functions are always expressed in closed-form series of the inclination by the following relation (Zarrouati, 1987)

$$F_{nmp}(i) = \frac{(-1)^{\lceil n-m/2 \rceil}(n+m)!}{2^n!} \begin{pmatrix} n \\ p \end{pmatrix} \sum_{j=\sup\{0,2p-n-m\}}^{\inf\{n-m,2p\}} (-1)^j \begin{pmatrix} 2p \\ j \end{pmatrix} \times \begin{pmatrix} 2n-2p \\ n-m-j \end{pmatrix} (\cos i/2)^{n+m-2p+2j} (\sin i/2)^{n-m+2p-2j} . \tag{C.2}$$

Table C.2 shows the expressions for F_{nmp} with nmp values up to 222.

Table C.2: Inclination Functions $F_{nmp}(i)$ from Eq. (C.2). For a more complete list, we refer to Kaula (1966) and Chao (2005)

n	m	p	Inclination Functions, $F_{nmp}(i)$
2	0	0	$-(3/8)\,\sin^2 i$
2	0	1	$(3/4)\,\sin^2 i - (1/2)$
2	0	2	F_{200}
2	1	0	$(3/4)\,\sin i\,(1+\cos i)$
2	1	1	$-(3/2)\,\sin i\,\cos i$
2	1	2	$-(3/4)\,\sin i\,(1-\cos i)$
2	2	0	$(3/4)\,(1+\cos i)^2$
2	2	1	$(3/2)\,\sin^2 i$
2	2	2	$(3/4)\,(1-\cos i)^2$

Appendix D

Variational equations – linearization

In order to measure the possible exponential divergence in the framework of stability investigations, the equations of motion are linearized. Linearization explores the dynamics of the solution flow locally around a given initial condition. More specifically, consider the set of differential equations

$$\frac{\mathrm{d}}{\mathrm{d}t}\boldsymbol{x}(t) = \boldsymbol{f}(\boldsymbol{x}(t), \boldsymbol{\alpha}), \qquad \boldsymbol{x} \in \mathbb{R}^n\,, \tag{D.1}$$

where $\boldsymbol{x}$ represents a point in a n-dimensional space and $\boldsymbol{\alpha}$ is a vector of parameters entirely defined by the model. Let $\boldsymbol{x_0}$ be an initial point close to $\boldsymbol{x}$. Let $\boldsymbol{x_0}(t)$ be the trajectory arising from the initial point $\boldsymbol{x_0}$. Since we assume that $\boldsymbol{x}$ is close to $\boldsymbol{x_0}$, we can use a Taylor series expansion to write

$$\boldsymbol{f}(\boldsymbol{x}) = \boldsymbol{f}(\boldsymbol{x_0}) + \left.\frac{\mathrm{d}f(\boldsymbol{x})}{\mathrm{d}\boldsymbol{x}}\right|_{\boldsymbol{x_0}} (\boldsymbol{x} - \boldsymbol{x_0}) + \cdots\,.$$

We now find that the rate of change of the distance between the two trajectories is given by

$$\frac{\mathrm{d}\boldsymbol{\delta}}{\mathrm{d}t} = \dot{\boldsymbol{x}} - \dot{\boldsymbol{x}}_0 = \boldsymbol{f}(\boldsymbol{x}) - \boldsymbol{f}(\boldsymbol{x_0})\,.$$

Consequently, we can now write readily the so-called first order *variation system of equations*

$$\dot{\boldsymbol{\delta}} = \frac{\mathrm{d}\boldsymbol{\delta}}{\mathrm{d}t} = \left.\frac{\mathrm{d}\boldsymbol{f}}{\mathrm{d}\boldsymbol{x}}\right|_{\boldsymbol{x_0}} (\boldsymbol{x} - \boldsymbol{x_0}) = \boldsymbol{J}(t)\,\boldsymbol{\delta}(t)\,, \tag{D.2}$$

which is found by keeping only the linear terms in $\boldsymbol{\delta}$ and subtracting equation (D.1). In Eq. (D.2), $\boldsymbol{J}(t)$ is the Jacobian matrix. This is a $n \times n$ time-dependent matrix. In practice, the Jacobian matrix is unknown and its components must be computed numerically.

It has to be noted that the equations have to be integrated simultaneously with the state vector solution of Eq. (D.1). Indeed, the state vector, that is, in practice, the position and the velocity of the space debris, is required in order to evaluate the components of the Jacobian matrix, that is the partial derivatives of the accelerations. The variational equations are usually numerically integrated with the same algorithm used for integrating the equations of motion. In order to reduce the computational cost and since accuracy requirements for the

partial derivatives are generally more relaxed than for the trajectory itself (Montenbruck and Gill, 2000), the force model used to integrate the variational equations are most often reduced from that used to integrate the equations of motion. Let us remark that since equation (D.2) is a first order linear differential system of equations, the absolute length of the initial vector $\boldsymbol{\delta}$ is irrelevant. A new displacement vector $\boldsymbol{\delta}'$, which is initially related to $\boldsymbol{\delta}$ by $\boldsymbol{\delta} = k\,\boldsymbol{\delta}'$, where k is a scale factor, will always be related to $\boldsymbol{\delta}$ by the same relation $\boldsymbol{\delta}'(t) = k\,\boldsymbol{\delta}(t)$. "*The original vector $\boldsymbol{\delta}$ must be infinitesimally small so that the linear approximation is valid. However, after linearization the scale factor k is arbitrary and may be chosen to make $\boldsymbol{\delta}'$ computationally convenient, i.e. of order unity*" (Wisdom, 1983).

Hereafter, we present the partial derivatives of the acceleration for the geopotential, the luni-solar attraction and the direct solar radiation pressure, respectively.

D.1 Geopotential

D.1.1 The Two-Body problem – central term

The most important contribution to the variational equations arises from the central term of the Earth's gravitational field (Cunningham, 1970; Montenbruck and Gill, 2000)

$$\ddot{\boldsymbol{r}} = -\frac{\mu}{r^3}\boldsymbol{r}\,,$$

where $\boldsymbol{r}$ is the position vector of the object in consideration. Making use of the following relation

$$\frac{\partial r^n}{\partial \boldsymbol{r}} = \frac{\partial (x^2+y^2+z^2)^{n/2}}{\partial \boldsymbol{r}} = n\,r^{n-2}\,\boldsymbol{r}^T\,,$$

it follows that

$$\begin{aligned}\frac{\partial \ddot{\boldsymbol{r}}}{\partial \boldsymbol{r}} &= \frac{\mu}{r^5}\begin{pmatrix} 3x^2-r^2 & 3xy & 3xz \\ 3yx & 3y^2-r^2 & 3yz \\ 3zx & 3zy & 3z^2-r^2 \end{pmatrix} \\ &= -\frac{\mu}{r^3}\left\{\boldsymbol{I}_{3\times 3} - \frac{3}{r^2}\,\boldsymbol{r}\otimes\boldsymbol{r}^T\right\}\,,\end{aligned} \tag{D.3}$$

where $\boldsymbol{r}\otimes\boldsymbol{r}^T$ is Cartesian product, or outer product, of the column array $\boldsymbol{r}$ with its transpose $\boldsymbol{r}^T$ and $\boldsymbol{I}_{3\times 3}$ is the 3-dimensional identity matrix. Eq. (D.3) shows that the gravity gradient is symmetric with respect to the main diagonal and that the sum of the diagonal elements is zero. Actually, this property is independent of the form of the potential U taken into consideration. As a consequence, the number of independent components that have to be computed reduces significantly from nine to five.

D.1.2 Variational equations for the terms of degree n and order m

In an Earth-fixed reference frame, when taking into account an expansion of the geopotential up to degree n and order m, the partial derivatives can be computed from

$$\frac{\partial \ddot{\boldsymbol{r}}}{\partial \boldsymbol{r}} = \sum_{n,m} \frac{\partial \ddot{\boldsymbol{r}}_{nm}}{\partial \boldsymbol{r}}\,, \tag{D.4}$$

where the partial derivatives appearing in the right-hand side of Eq. (D.4) are given by (Montenbruck and Gill, 2000)

$$\begin{aligned}
\frac{\partial \ddot{x}_{nm}}{\partial x} &\overset{(m=0)}{=} \frac{\mu}{R_e^3}\,\frac{1}{2}\left\{(-J_n\,V_{n+2,2}) - \frac{(n+2)!}{n!}\,(-J_n\,V_{n+2,0})\right\} \\
&\overset{(m=1)}{=} \frac{\mu}{R_e^3}\,\frac{1}{4}\left\{(C_{n1}\,V_{n+2,3} + S_{n1}\,W_{n+2,3})\right. \\
&\qquad \left. + \frac{(n+1)!}{(n-1)!}\,(-3C_{n2}\,V_{n+2,1} - S_{n1}\,W_{n+2,1})\right\} \\
&\overset{(m>1)}{=} \frac{\mu}{R_e^3}\,\frac{1}{4}\left\{(C_{nm}\,V_{n+2,m+2} + S_{nm}\,W_{n+2,m+2})\right. \\
&\qquad + 2\,\frac{(n-m+2)!}{(n-m)!}\,(-C_{nm}\,V_{n+2,m} - S_{nm}\,W_{n+2,m})\Big\} \\
&\qquad \left. + \frac{(n-m+4)!}{(n-m)!}\,(+C_{nm}\,V_{n+2,m-2} + S_{nm}\,W_{n+2,m-2})\right\}.
\end{aligned} \tag{D.5}$$

Similarly, we have

$$\begin{aligned}
\frac{\partial \ddot{x}_{nm}}{\partial y} &\overset{(m=0)}{=} \frac{\mu}{R_e^3}\,\frac{1}{2}\left\{(-J_n\,W_{n+2,2})\right. \\
&\overset{(m=1)}{=} \frac{\mu}{R_e^3}\,\frac{1}{4}\left\{(C_{n1}\,W_{n+2,3} - S_{n1}\,V_{n+2,3})\right. \\
&\qquad \left. + \frac{(n+1)!}{(n-1)!}\,(-C_{n1}\,W_{n+2,1} - S_{n1}\,V_{n+2,1})\right\} \\
&\overset{(m>1)}{=} \frac{\mu}{R_e^3}\,\frac{1}{4}\left\{(C_{nm}\,W_{n+2,m+2} - S_{nm}\,V_{n+2,m+2})\right. \\
&\qquad \left. + \frac{(n-m+4)!}{(n-m)!}\,(-C_{nm}\,W_{n+2,m-2} + S_{nm}\,W_{n+2,m-2})\right\}
\end{aligned}$$

and

$$\begin{aligned}\frac{\partial \ddot{x}_{nm}}{\partial z} &\overset{(m=0)}{=} \frac{\mu}{R_e^3}\left\{(n+1)\,(-J_n\,V_{n+2,1})\right\}\\ &\overset{(m>0)}{=} \frac{\mu}{R_e^3}\Big\{\frac{n-m+1}{2}\,(C_{nm}\,V_{n+2,m+1}+S_{nm}\,W_{n+2,m+1})\\ &\quad+\frac{(n-m+3)}{2(n-m)}\,(-C_{nm}\,V_{n+2,m-1}-S_{nm}\,W_{n+2,m-1})\Big\}\end{aligned}$$

and

$$\begin{aligned}\frac{\partial \ddot{y}_{nm}}{\partial z} &\overset{(m=0)}{=} \frac{\mu}{R_e^3}\left\{(n+1)\,(-J_n\,W_{n+2,1})\right\}\\ &\overset{(m>0)}{=} \frac{\mu}{R_e^3}\Big\{\frac{n-m+1}{2}\,(C_{nm}\,W_{n+2,m+1}-S_{nm}\,V_{n+2,m+1})\\ &\quad+\frac{(n-m+3)}{2(n-m)}\,(+C_{nm}\,W_{n+2,m-1}-S_{nm}\,V_{n+2,m-1})\Big\}\end{aligned}$$

and finally

$$\frac{\partial \ddot{z}_{nm}}{\partial z} = \frac{\mu}{R_e^3}\left\{\frac{(n-m+2)!}{(n-m)!}\,(+C_{nm}\,V_{n+2,m}+S_{nm}\,W_{n+2,m})\right\}\ , \tag{D.6}$$

where the quantities V_{nm}, W_{nm} are defined in Eqs. (B.1) and (B.2) whereas C_{nm} and S_{nm} are the well known geopotential coefficients defined in Eq. (2.6). Let us note that these accelerations are derived under the assumption of a non-rotating Earth. Due to the Earth's rotation, some additional corrections have to be considered. More specifically, the transformation between the space-fixed "*sf*" and the Earth-fixed "*ef*" reference frame are given by

$$\left(\frac{\partial \ddot{\boldsymbol{r}}}{\partial \boldsymbol{r}}\right)_{sf} = \boldsymbol{U}^{-1}(t)\,\left(\frac{\partial \ddot{\boldsymbol{r}}}{\partial \boldsymbol{r}}\right)_{ef}\boldsymbol{U}(t)\,. \tag{D.7}$$

However, in practice, the Earth-fixed components may be computed by evaluating the derivatives (D.5), ..., (D.6) with the Earth-fixed coordinates defined by

$$\boldsymbol{r}_{ef} = \boldsymbol{U}(t)\,\boldsymbol{r}_{sf}\,.$$

Finally, it has to be noted that both $(\partial\ddot{\boldsymbol{r}}/\partial\boldsymbol{r})_{sf}$ and $(\partial\ddot{\boldsymbol{r}}/\partial\boldsymbol{r})_{ef}$ are partial derivatives of the acceleration defined in inertial reference frames which are rotated each other by a given rotation matrix $\boldsymbol{U}(t)$. Actually, the acceleration in a rotating reference frame is different by Coriolis and centrifugal terms. For further details, we refer for instance to Montenbruck and Gill (2000).

Finally, since the acceleration induced by the Earth's gravity field is independent of the velocity of the space debris, we only have to compute the partial derivatives with respect to the position of the space debris. Consequently, the complete Jacobian matrix needed in the

variational equations is given by

$$\boldsymbol{J}(t) = \begin{pmatrix} 0 & 0 & 0 & 1 & 0 & 0 \\ 0 & 0 & 0 & 0 & 1 & 0 \\ 0 & 0 & 0 & 0 & 0 & 1 \\ \dfrac{\partial \ddot{x}_{nm}}{\partial x} & \dfrac{\partial \ddot{x}_{nm}}{\partial y} & \dfrac{\partial \ddot{x}_{nm}}{\partial z} & 0 & 0 & 0 \\ \dfrac{\partial \ddot{x}_{nm}}{\partial y} & -\dfrac{\partial \ddot{x}_{nm}}{\partial y} - \dfrac{\partial \ddot{z}_{nm}}{\partial z} & \dfrac{\partial \ddot{y}_{nm}}{\partial z} & 0 & 0 & 0 \\ \dfrac{\partial \ddot{x}_{nm}}{\partial z} & \dfrac{\partial \ddot{y}_{nm}}{\partial z} & \dfrac{\partial \ddot{z}_{nm}}{\partial z} & 0 & 0 & 0 \end{pmatrix} .$$

D.2 Third-body variational equations

Since, the indirect term $\boldsymbol{r}_\odot / \|\boldsymbol{r}_\odot\|^3$ is independent of the satellite position, the corresponding partial derivative is zero. As a consequence, only the partial derivatives of the direct part remains, leading to

$$\frac{\partial \ddot{\boldsymbol{r}}}{\partial \boldsymbol{r}} = -\mu_i \left(\frac{1}{\|\boldsymbol{r} - \boldsymbol{r}_i\|} \boldsymbol{I}_{3\times 3} - \frac{3}{\|\boldsymbol{r} - \boldsymbol{r}_i\|^5} (\boldsymbol{r} - \boldsymbol{r}_i) \otimes (\boldsymbol{r} - \boldsymbol{r}_i)^T \right) ,$$

where μ_i is the gravitational constant of the third body. Notice that, because the acceleration is also independent of the velocity, the partial derivatives are zero, that is

$$\frac{\partial \ddot{\boldsymbol{r}}}{\partial \dot{\boldsymbol{r}}} = 0 .$$

D.3 Radiation pressure variational equations

Similarly, the partial derivatives of the direct solar radiation pressure can be easily derived. The computation yields

$$\frac{\partial \ddot{\boldsymbol{r}}}{\partial \boldsymbol{r}} = P_r \, C_r \, \frac{A}{m} \left(\frac{1}{\|\boldsymbol{r} - \boldsymbol{r}_\odot\|} \boldsymbol{I}_{3\times 3} - \frac{3}{\|\boldsymbol{r} - \boldsymbol{r}_\odot\|^5} (\boldsymbol{r} - \boldsymbol{r}_\odot) \otimes (\boldsymbol{r} - \boldsymbol{r}_\odot)^T \right) .$$

Over again, the partial derivatives with respect to the velocity is zero, leading to

$$\frac{\partial \ddot{\boldsymbol{r}}}{\partial \dot{\boldsymbol{r}}} = 0 .$$

Appendix E

The perturbed equations

E.1 The Gauss perturbation equations

For many applications, it is convenianent to express the rates of change of the elements explicitly in terms of the disturbing accelerations. The asset of the Gaussian perturbed equations is for non-conservative forces because it's directly expressed from the disturbing forces. However, let us also remark that this formulation also works for conservative forces bacause the forces are simply gradients of the potential functions (Vallado, 2001).

Let us now present the rates of changes of the Keplerian elements using a disturbing acceleration $a_{\mathcal{R}} = (a_S, a_T, a_W)$ expressed in terms of its radial (a_S), transversal (along-track) (a_T) and out-of-plane components (a_W) in the orbit oriented system

$$
\begin{aligned}
\frac{\mathrm{d}a}{\mathrm{d}t} &= \frac{2}{n\sqrt{1-e^2}}\left\{e\sin f\, a_S + \frac{p}{r}\, a_T\right\}, \\
\frac{\mathrm{d}e}{\mathrm{d}t} &= \frac{\sqrt{1-e^2}}{n\,a}\left\{\sin f\, a_S + \left(\cos f + \frac{e+\cos f}{1+e\cos f}\right)\, a_T\right\}, \\
\frac{\mathrm{d}i}{\mathrm{d}t} &= \frac{r\,\cos(\omega+f)}{n\,a^2\sqrt{1-e^2}}\, a_W, \\
\frac{\mathrm{d}\Omega}{\mathrm{d}t} &= \frac{r\,\sin(\omega+f)}{n\,a^2\sqrt{1-e^2}\,\sin i}\, a_W, \\
\frac{\mathrm{d}\omega}{\mathrm{d}t} &= \frac{\sqrt{1-e^2}}{n\,a\,e}\left\{-\cos f\, a_S + \sin f\left(1+\frac{r}{p}\right)\, a_T\right\} - \frac{r\,\sin(\omega+f)}{n\,a^2\sqrt{1-e^2}\,\sin i}\, a_W, \\
\frac{\mathrm{d}M}{\mathrm{d}t} &= \frac{1}{n\,a^2\,e}\Big\{\,(p\,\cos f - 2\,e\,r)\; a_S - (p+r)\,\sin f\, a_T\Big\}.
\end{aligned}
$$

E.2 The Lagrange Perturbation Equations

If the perturbing acceleration $a_{\mathcal{R}}$ (more precesly the related force $F_{\mathcal{R}}$) may be represented as the gradient of the scalar perturbation function $\mathcal{R}$, that is $F_{\mathcal{R}} = \boldsymbol{\nabla}\mathcal{R}$, the rate of change of the osculating Keplerian elements as a function of the derivatives $\partial\mathcal{R}/\partial a$, $\partial\mathcal{R}/\partial e$, $\partial\mathcal{R}/\partial i$, $\partial\mathcal{R}/\partial\Omega$, $\partial\mathcal{R}/\partial\omega$, $\partial\mathcal{R}/\partial M$ is given by

$$
\begin{aligned}
\frac{\mathrm{d}a}{\mathrm{d}t} &= -\frac{2}{na}\,\frac{\partial\mathcal{R}}{\partial M}\,,\\
\frac{\mathrm{d}e}{\mathrm{d}t} &= -\frac{1-e^2}{n\,a^2\,e}\,\frac{\partial\mathcal{R}}{\partial M} + \frac{\sqrt{1-e^2}}{n\,a^2\,e}\,\frac{\partial\mathcal{R}}{\partial\omega}\,,\\
\frac{\mathrm{d}i}{\mathrm{d}t} &= -\frac{\cos i}{n\,a^2\,\sqrt{1-e^2}\,\sin i}\,\frac{\partial\mathcal{R}}{\partial M} + \frac{\sqrt{1-e^2}}{n\,a^2\,e}\,\frac{\partial\mathcal{R}}{\partial\omega} + \frac{1}{n\,a^2\,\sqrt{1-e^2}\,\sin i}\,\frac{\partial\mathcal{R}}{\partial\Omega}\,,\\
\frac{\mathrm{d}\Omega}{\mathrm{d}t} &= -\frac{1}{n\,a^2\,\sqrt{1-e^2}\,\sin i}\,\frac{\partial\mathcal{R}}{\partial i}\,,\\
\frac{\mathrm{d}\omega}{\mathrm{d}t} &= \frac{\cos i}{n\,a^2\,\sqrt{1-e^2}\,\sin i}\,\frac{\partial\mathcal{R}}{\partial i} - \frac{\sqrt{1-e^2}}{n\,a^2\,e}\,\frac{\partial\mathcal{R}}{\partial e}\,,\\
\frac{\mathrm{d}M}{\mathrm{d}t} &= n + \frac{1-e^2}{n\,a^2\,e}\,\frac{\partial\mathcal{R}}{\partial e} + \frac{2}{n\,a}\,\frac{\partial\mathcal{R}}{\partial a}\,.
\end{aligned}
$$

Appendix F

Lie transforms and computational algorithm

F.1 Symplectic Lie Transforms

Let us consider a x to y transformation $\mathcal{X}$, close to the identity and developed as a power series expansion of a small parameter ϵ

$$x = \mathcal{X}(y, \epsilon) = y + \epsilon \mathcal{X}_1(y) + \epsilon^2 \mathcal{X}_2(y) + \dots . \tag{F.1}$$

For ϵ sufficiently small, the transformation is always invertible

$$y = \mathcal{Y}(x, \epsilon) = x + \epsilon \mathcal{Y}_1(x) + \epsilon^2 \mathcal{Y}_2(x) + \dots .$$

Let us remark that the before-mentioned transformation can also be defined as being the solution at "*time*" ϵ of an auxiliary n-dimensional system of differential equations

$$\frac{dx}{d\epsilon} = \mathcal{W}(x, \epsilon)$$

for the initial condition $x(\epsilon = 0) = y$. Therefore, the ϵ-dependent transformation is considered to be the flow spawn by a non-autonomous differential system of equations. Let us remark that it is always possible when considering a *generating vector field*

$$\mathcal{W}(x, \epsilon) = \left[\frac{\partial \mathcal{X}(y, \epsilon)}{\partial \epsilon} \right]_{y = \mathcal{Y}(x, \epsilon)} .$$

If we wish to generate a canonical transformation it is sufficient to define the system of differential equations

$$\dot{x} = \mathcal{I} \mathcal{H}_x^T ,$$

where $\mathcal{I}$ is the well-known symplectic matrix and (q_i, p_i) are the variables and momenta, respectivaly. As a consequence, it restricts the Lie transforms group to the subgroup of symplectic Lie transforms. For this purpose, it is sufficient and necessary to impose the generating

vector field $\mathcal{W}$ to be a Hamiltonian field, that is the product of the symplectic matrix $\mathcal{I}$ by the gradient of a Hamiltonian function

$$\mathcal{W} = \mathcal{I}\mathcal{W}_x^T \, .$$

Therefore, let us define the Lie transforms (F.1) as the solution of an auxiliary Hamiltonian differential system

$$\frac{dx}{d\epsilon} = \mathcal{I}\mathcal{W}_x^T \, .$$

F.2 Computational algorithm

Let us develop the function $f(\mathcal{X}(y,\epsilon),\epsilon)$ as a powers series expansion of ϵ about $\epsilon = 0$. We find that the transformation $g(y,\epsilon)$ of any analytical function $f(x,\epsilon)$, using the before-mentioned transformation (F.1), spawn by the generating vector field (F.1), is given by

$$g(y,\epsilon) = f(\mathcal{X}(y,\epsilon),\epsilon) = \sum_{i\geq 0} \frac{\epsilon^i}{i!} \left[D^i f(x,\epsilon)\right]_{x=y;\epsilon=0} \, , \tag{F.2}$$

where the differential operator D is defined by

$$Df(x,\epsilon) = \frac{\partial f}{\partial \epsilon} + \frac{\partial f}{\partial x}\mathcal{I}\mathcal{W}_x^T = \frac{\partial f}{\partial \epsilon} + (f;\mathcal{W}) \, , \tag{F.3}$$

and where $(f;\mathcal{W})$ corresponds to the Poisson brackets of the two functions, that is

$$(f\ ;\ \mathcal{W}) \equiv f_x \mathcal{I}\mathcal{W}_x^T = \sum_i \left(\frac{\partial f}{\partial q_i}\frac{\partial \mathcal{W}}{\partial p_i} - \frac{\partial \mathcal{W}}{\partial q_i}\frac{\partial f}{\partial p_i} \right) \, .$$

Consequently, following Eqs. (F.2) and (F.3), it is possible to write a simple computational algorithm.

First, let us consider the analytical function

$$f(x,\epsilon) = \sum_{i=0} \frac{\epsilon^i}{i!} f_i^{(0)}(x)$$

as well as the generating vector field

$$\mathcal{W} = \sum_{i=0} \frac{\epsilon^i}{i!} \mathcal{W}_{i+1}(x) \, . \tag{F.4}$$

Second, we successively construct the intermediate function $f_i^{(j)}(x)$

$$\frac{d^j}{d\epsilon^j} f(\mathcal{X}(y,\epsilon),\epsilon) = \sum_{i=0} \frac{\epsilon^i}{i!} f_i^{(j)}(x)$$

using the following recurrence formula

$$f_i^{(j)} = f_{i+1}^{(j-1)} + \sum_{k=0}^{i} C_i^k \left(f_{i-k}^{(j-1)} \; ; \; \mathcal{W}_{k+1} \right) , \tag{F.5}$$

where C_i^k stands for the binomial coefficients in the indices (i, k)

$$C_i^k = \left(\begin{array}{c} i \\ k \end{array} \right) = \frac{i!}{k!(i-k)!} .$$

Finally, the transformation $g(y, \epsilon)$ of the function $f(x, \epsilon)$ is given by

$$g(y, \epsilon) = \sum_{i=0} \frac{\epsilon^i}{i!} \left[f_0^{(i)}(x) \right]_{x=y} .$$

The recursion (F.5) is easily visualized in Figure F.1. Indeed, the construction is reminiscent of that of Pascal's triangle. For instance, assume that all the elements of the first three lines have been computed. The filling of the fourth row begins with the computation of $f_2^{(1)}$ which involves only the elements above and including $f_3^{(0)}$ on the column passing through $f_3^{(0)}$. Then one is ready to compute $f_1^{(2)}$, which involves $f_2^{(1)}$ and the elements above it on the column passing through $f_2^{(1)}$. Finally, the algorithm ends with the computation of $f_0^{(3)}$, involving $f_1^{(2)}$ and $f_0^{(2)}$.

$$\begin{array}{ccccccc}
f_0^{(0)} & & & & & & \\
f_1^{(0)} & f_0^{(1)} & & & & & \\
f_2^{(0)} & f_1^{(1)} & f_0^{(2)} & & & & \\
f_3^{(0)} & f_2^{(1)} & f_1^{(2)} & f_0^{(3)} & & & \\
f_4^{(0)} & f_3^{(1)} & f_2^{(2)} & f_1^{(3)} & f_0^{(4)} & & \\
\vdots & \vdots & \vdots & \vdots & \vdots & \ddots &
\end{array}$$

Figure F.1: Recursive transformation of an analytic function under Lie transform, better known as *the Lie triangle*

F.3 Homologic equation

In the framework of Hamiltonian system, the before-mentioned Lie algorithm consists in resolving, at each order k, the following *homologic equation*

$$\mathcal{H}_0^{(k)} - \widetilde{\mathcal{H}}_0^{(k)} = \left(\mathcal{H}_0^{(0)}\ ;\ \mathcal{W}_k\right) = -\sum_{i=1}^{n} \omega_i \frac{\partial \mathcal{W}_k}{\partial q_i}\,, \tag{F.6}$$

where $\omega_i = \dfrac{\partial \mathcal{H}_0^{(0)}}{\partial p_i}$ and $\widetilde{\mathcal{H}}_0^{(k)}$ is a known quantity and where $\mathcal{H}_0^{(0)}$ depends only on the momenta q_i. In order to find the generating function, we have to proceed to an integration with respect to the angle q_i. For this purpose, let us consider the Fourier series expansion of the first term in Eq. (F.6). We have

$$\widetilde{\mathcal{H}}_0^{(k)} - \mathcal{H}_0^{(k)} = \sum_{i_1,i_2,\ldots,i_n} \left[C_{i_1,i_2,\ldots,i_n} \cos\left(\sum_{l=1}^{n} i_l q_l\right) + S_{i_1,i_2,\ldots,i_n} \sin\left(\sum_{l=1}^{n} i_l q_l\right)\right]\,,$$

leading formally to

$$\mathcal{W}_k = \sum_{i_1,i_2,\ldots,i_n} \left[\frac{C_{i_1,i_2,\ldots,i_n} \sin\left(\sum_{l=1}^{n} i_l q_l\right)}{i_1\omega_1 + \ldots + i_n\omega_n} - \frac{S_{i_1,i_2,\ldots,i_n} \cos\left(\sum_{l=1}^{n} i_l q_l\right)}{i_1\omega_1 + \ldots + i_n\omega_n}\right]\,.$$

In order to ensure the existence of the generating function $\mathcal{W}$, it would be relevant to inspect that no denominator is close to zero. It can happen if all the arguments i_n are zero $(i_1 = i_2 = \cdots = i_n = 0)$ as well as in the case of resonances (more precisely, close to an exact resonance). In either case, the incriminated terms have to be included into the new Hamiltonian $\mathcal{H}_0^{(k)}$, the other terms being integrated to form the generating function of the transformation. In this latter case, it is sufficient to choose

$$\mathcal{H}_0^{(k)} = \langle \widetilde{\mathcal{H}}_0^{(k)} \rangle\,,$$

where $\langle\ \cdot\ \rangle$ stands for the mean value with respect to some assigned angles if the specific requirement of the transformation is the suppression of some or all periodic terms.

F.4 Transformation between mean and osculating elements

The osculating elements (q_i, p_i) can be deduced from the mean elments (q_i', p_i') by a canonical transformation induced by the generating function $\mathcal{W}$ developed in powers of the small parameter ϵ (see Eq. F.4) and computed during the averaging process. In keeping with Deprit (1969),

Deprit and Rom (1970) and Henrard (1970), such a transformation is given by (up to order 2)

$$\begin{aligned} q_i &= q'_i + \left\{ \epsilon \frac{\partial \mathcal{W}_1}{\partial p_i} + \frac{\epsilon^2}{2} \left[\frac{\partial \mathcal{W}_2}{\partial p_i} + \left(\frac{\partial \mathcal{W}_1}{\partial p_i} \; ; \; \mathcal{W}_1 \right) \right] \right\} \Bigg|_{(q',p')} + \mathcal{O}(\epsilon^3) \, , \\ p_i &= p'_i - \left\{ \epsilon \frac{\partial \mathcal{W}_1}{\partial q_i} + \frac{\epsilon^2}{2} \left[\frac{\partial \mathcal{W}_2}{\partial q_i} + \left(\frac{\partial \mathcal{W}_1}{\partial q_i} \; ; \; \mathcal{W}_1 \right) \right] \right\} \Bigg|_{(q',p')} + \mathcal{O}(\epsilon^3) \, , \end{aligned} \tag{F.7}$$

where q_i and p_i are the variables and their conjutated momenta, respectively. Although the presented formulae were truncated to the second order, they are easily generalized to any order. At this point, it is worth stressing that the right-hand sides appearing in Eqs. (F.7) are evaluted in the mean elements (q'_i, p'_i).

Practically, in the framework of a first order averaging process over the short periods, the transformation simply reads as

$$\begin{aligned} q_i &= q'_i + \left\{ \epsilon \frac{\partial \mathcal{W}_1}{\partial p_i} \right\} \Bigg|_{(v',V')} + \mathcal{O}(\epsilon^2) \, , \\ p_i &= p'_i - \left\{ \epsilon \frac{\partial \mathcal{W}_1}{\partial q_i} \right\} \Bigg|_{(v',V')} + \mathcal{O}(\epsilon^2) \, , \end{aligned}$$

where $\mathcal{W}_1$ is the first-order generating function, that is a function of the discarded "short-periodic" terms, which is computed following Eq. (F.6) by an analytical integration with respect to the fast angle, namely the mean longitude λ or equivalently, for resonant motion, with respect to the sidereal time θ.

Appendix G

Characteristic series expansion

In the following 4-order series expansion, the distance unit is equal to the mean geostationary radius, i.e 42 164 km. Furthermore, the gravitational constant of the Earth is set to $\mu = 1$.

G.1 Third-body averaged disturbing function $\mathcal{H}_i$

The third-boby disturbing function (3-degree expansion in Legendre polynomials) is given for the particular case of the Sun attraction.

λ	θ	X_1	Y_1	X_2	Y_2	L	$X_{☾}$	$Y_{☾}$	$Z_{☾}$	$r_{☾}$	$X_{\odot}$	$Y_{\odot}$	$Z_{\odot}$	$r_{\odot}$	Coefficient
cos (0	0)	(0	0	0	0	4	0	0	0	0	0	0	0	-3)	-0.1664730190000000D+06
cos (0	0)	(0	0	0	0	4	0	0	0	0	0	2	0	-3)	0.2497095285000000D+06
cos (0	0)	(0	0	0	0	4	0	0	0	0	2	0	0	-3)	0.2497095285000000D+06
cos (0	0)	(0	0	0	1	4	0	0	0	0	0	1	1	-3)	0.4994190570000000D+06
cos (0	0)	(0	0	0	2	4	0	0	0	0	0	0	2	-3)	0.2497095285000000D+06
cos (0	0)	(0	0	0	2	4	0	0	0	0	0	2	0	-3)	-0.2497095285000000D+06
cos (0	0)	(0	0	0	3	4	0	0	0	0	0	1	1	-3)	-0.3121369106250000D+06
cos (0	0)	(0	0	0	4	4	0	0	0	0	0	0	2	-3)	-0.6242738212500000D+05
cos (0	0)	(0	0	0	4	4	0	0	0	0	0	2	0	-3)	0.6242738212500000D+05
cos (0	0)	(0	0	1	0	4	0	0	0	0	1	0	1	-3)	0.4994190570000000D+06
cos (0	0)	(0	0	1	1	4	0	0	0	0	1	1	0	-3)	-0.4994190570000000D+06
cos (0	0)	(0	0	1	2	4	0	0	0	0	1	0	1	-3)	-0.3121369106250000D+06
cos (0	0)	(0	0	1	3	4	0	0	0	0	1	1	0	-3)	0.1248547642500000D+06
cos (0	0)	(0	0	2	0	4	0	0	0	0	0	0	2	-3)	0.2497095285000000D+06
cos (0	0)	(0	0	2	0	4	0	0	0	0	2	0	0	-3)	-0.2497095285000000D+06
cos (0	0)	(0	0	2	1	4	0	0	0	0	0	1	1	-3)	-0.3121369106250000D+06
cos (0	0)	(0	0	2	2	4	0	0	0	0	0	0	2	-3)	-0.1248547642500000D+06
cos (0	0)	(0	0	2	2	4	0	0	0	0	0	2	0	-3)	0.6242738212500000D+05
cos (0	0)	(0	0	2	2	4	0	0	0	0	2	0	0	-3)	0.6242738212500000D+05
cos (0	0)	(0	0	3	0	4	0	0	0	0	1	0	1	-3)	-0.3121369106250000D+06
cos (0	0)	(0	0	3	1	4	0	0	0	0	1	1	0	-3)	0.1248547642500000D+06

continued on next page

continued from previous page

λ	θ	X_1	Y_1	X_2	Y_2	L	$X_☾$	$Y_☾$	$Z_☾$	$r_☾$	$X_\odot$	$Y_\odot$	$Z_\odot$	$r_\odot$	Coefficient
cos (0	0)	(0	0	4	0	4	0	0	0	0	0	0	2	-3)	-0.6242738212500000D+05
cos (0	0)	(0	0	4	0	4	0	0	0	0	2	0	0	-3)	0.6242738212500000D+05
cos (0	0)	(0	1	0	0	6	0	0	0	0	1	0	0	-4)	0.1248547642500000D+07
cos (0	0)	(0	1	0	0	6	0	0	0	0	1	2	0	-4)	-0.1560684553125000D+07
cos (0	0)	(0	1	0	0	6	0	0	0	0	3	0	0	-4)	-0.1560684553125000D+07
cos (0	0)	(0	1	0	1	6	0	0	0	0	1	1	1	-4)	-0.3121369106250000D+07
cos (0	0)	(0	1	0	2	6	0	0	0	0	1	0	2	-4)	-0.1560684553125000D+07
cos (0	0)	(0	1	0	2	6	0	0	0	0	1	2	0	-4)	0.1560684553125000D+07
cos (0	0)	(0	1	0	3	6	0	0	0	0	1	1	1	-4)	0.1950855691406250D+07
cos (0	0)	(0	1	1	0	6	0	0	0	0	0	0	1	-4)	0.1248547642500000D+07
cos (0	0)	(0	1	1	0	6	0	0	0	0	0	2	1	-4)	-0.1560684553125000D+07
cos (0	0)	(0	1	1	0	6	0	0	0	0	2	0	1	-4)	-0.4682053659375000D+07
cos (0	0)	(0	1	1	1	6	0	0	0	0	0	1	0	-4)	-0.6242738212500000D+06
cos (0	0)	(0	1	1	1	6	0	0	0	0	0	1	2	-4)	-0.3121369106250000D+07
cos (0	0)	(0	1	1	1	6	0	0	0	0	0	3	0	-4)	0.7803422765625000D+06
cos (0	0)	(0	1	1	1	6	0	0	0	0	2	1	0	-4)	0.3901711382812500D+07
cos (0	0)	(0	1	1	2	6	0	0	0	0	0	0	1	-4)	-0.1560684553125000D+06
cos (0	0)	(0	1	1	2	6	0	0	0	0	0	0	3	-4)	-0.1560684553125000D+07
cos (0	0)	(0	1	1	2	6	0	0	0	0	0	2	1	-4)	0.3316454675390625D+07
cos (0	0)	(0	1	1	2	6	0	0	0	0	2	0	1	-4)	0.2145941260546875D+07
cos (0	0)	(0	1	2	0	6	0	0	0	0	1	0	0	-4)	-0.6242738212500000D+06
cos (0	0)	(0	1	2	0	6	0	0	0	0	1	0	2	-4)	-0.4682053659375000D+07
cos (0	0)	(0	1	2	0	6	0	0	0	0	1	2	0	-4)	0.7803422765625000D+06
cos (0	0)	(0	1	2	0	6	0	0	0	0	3	0	0	-4)	0.2341026829687500D+07
cos (0	0)	(0	1	2	1	6	0	0	0	0	1	1	1	-4)	0.8193593903906250D+07
cos (0	0)	(0	1	3	0	6	0	0	0	0	0	0	1	-4)	-0.1560684553125000D+06
cos (0	0)	(0	1	3	0	6	0	0	0	0	0	0	3	-4)	-0.1560684553125000D+07
cos (0	0)	(0	1	3	0	6	0	0	0	0	0	2	1	-4)	0.1950855691406250D+06
cos (0	0)	(0	1	3	0	6	0	0	0	0	2	0	1	-4)	0.5267310366796875D+07
cos (0	0)	(0	2	0	0	4	0	0	0	0	0	0	0	-3)	-0.2497095285000000D+06
cos (0	0)	(0	2	0	0	4	0	0	0	0	0	2	0	-3)	-0.2497095285000000D+06
cos (0	0)	(0	2	0	0	4	0	0	0	0	2	0	0	-3)	0.9988381140000001D+06
cos (0	0)	(0	2	0	1	4	0	0	0	0	0	1	1	-3)	-0.3745642927500000D+06
cos (0	0)	(0	2	0	2	4	0	0	0	0	0	0	2	-3)	-0.1248547642500000D+06
cos (0	0)	(0	2	0	2	4	0	0	0	0	0	2	0	-3)	0.1248547642500000D+06
cos (0	0)	(0	2	1	0	4	0	0	0	0	1	0	1	-3)	0.2122530992250000D+07
cos (0	0)	(0	2	1	1	4	0	0	0	0	1	1	0	-3)	-0.9988381140000001D+06
cos (0	0)	(0	2	2	0	4	0	0	0	0	0	0	2	-3)	0.1123692878250000D+07
cos (0	0)	(0	2	2	0	4	0	0	0	0	2	0	0	-3)	-0.1123692878250000D+07
cos (0	0)	(0	3	0	0	6	0	0	0	0	1	0	0	-4)	0.7803422765625000D+06
cos (0	0)	(0	3	0	0	6	0	0	0	0	1	2	0	-4)	0.1755770122265625D+07
cos (0	0)	(0	3	0	0	6	0	0	0	0	3	0	0	-4)	-0.1885827168359375D+07
cos (0	0)	(0	3	0	1	6	0	0	0	0	1	1	1	-4)	0.2731197967968750D+07
cos (0	0)	(0	3	1	0	6	0	0	0	0	0	0	1	-4)	0.1092479187187500D+07
cos (0	0)	(0	3	1	0	6	0	0	0	0	0	2	1	-4)	0.1365598983984375D+07

continued on next page

continued from previous page

λ	θ	X_1	Y_1	X_2	Y_2	L	$X_{\mathbb{C}}$	$Y_{\mathbb{C}}$	$Z_{\mathbb{C}}$	$r_{\mathbb{C}}$	$X_\odot$	$Y_\odot$	$Z_\odot$	$r_\odot$	Coefficient
cos (0	0)	(0	3	1	0	6	0	0	0	0	2	0	1	-4)	-0.6827994919921875D+07
cos (0	0)	(0	4	0	0	4	0	0	0	0	0	0	0	-3)	0.6242738212500000D+05
cos (0	0)	(0	4	0	0	4	0	0	0	0	0	2	0	-3)	0.6242738212500000D+05
cos (0	0)	(0	4	0	0	4	0	0	0	0	2	0	0	-3)	-0.2497095285000000D+06
cos (0	0)	(1	0	0	0	6	0	0	0	0	0	1	0	-4)	-0.1248547642500000D+07
cos (0	0)	(1	0	0	0	6	0	0	0	0	0	3	0	-4)	0.1560684553125000D+07
cos (0	0)	(1	0	0	0	6	0	0	0	0	2	1	0	-4)	0.1560684553125000D+07
cos (0	0)	(1	0	0	1	6	0	0	0	0	0	0	1	-4)	-0.1248547642500000D+07
cos (0	0)	(1	0	0	1	6	0	0	0	0	0	2	1	-4)	0.4682053659375000D+07
cos (0	0)	(1	0	0	1	6	0	0	0	0	2	0	1	-4)	0.1560684553125000D+07
cos (0	0)	(1	0	0	2	6	0	0	0	0	0	1	0	-4)	0.6242738212500000D+06
cos (0	0)	(1	0	0	2	6	0	0	0	0	0	1	2	-4)	0.4682053659375000D+07
cos (0	0)	(1	0	0	2	6	0	0	0	0	0	3	0	-4)	-0.2341026829687500D+07
cos (0	0)	(1	0	0	2	6	0	0	0	0	2	1	0	-4)	-0.7803422765625000D+06
cos (0	0)	(1	0	0	3	6	0	0	0	0	0	0	1	-4)	0.1560684553125000D+06
cos (0	0)	(1	0	0	3	6	0	0	0	0	0	0	3	-4)	0.1560684553125000D+07
cos (0	0)	(1	0	0	3	6	0	0	0	0	0	2	1	-4)	-0.5267310366796875D+07
cos (0	0)	(1	0	0	3	6	0	0	0	0	2	0	1	-4)	-0.1950855691406250D+06
cos (0	0)	(1	0	1	0	6	0	0	0	0	1	1	1	-4)	0.3121369106250000D+07
cos (0	0)	(1	0	1	1	6	0	0	0	0	1	0	0	-4)	0.6242738212500000D+06
cos (0	0)	(1	0	1	1	6	0	0	0	0	1	0	2	-4)	0.3121369106250000D+07
cos (0	0)	(1	0	1	1	6	0	0	0	0	1	2	0	-4)	-0.3901711382812500D+07
cos (0	0)	(1	0	1	1	6	0	0	0	0	3	0	0	-4)	-0.7803422765625000D+06
cos (0	0)	(1	0	1	2	6	0	0	0	0	1	1	1	-4)	-0.8193593903906250D+07
cos (0	0)	(1	0	2	0	6	0	0	0	0	0	1	2	-4)	0.1560684553125000D+07
cos (0	0)	(1	0	2	0	6	0	0	0	0	2	1	0	-4)	-0.1560684553125000D+07
cos (0	0)	(1	0	2	1	6	0	0	0	0	0	0	1	-4)	0.1560684553125000D+06
cos (0	0)	(1	0	2	1	6	0	0	0	0	0	0	3	-4)	0.1560684553125000D+07
cos (0	0)	(1	0	2	1	6	0	0	0	0	0	2	1	-4)	-0.2145941260546875D+07
cos (0	0)	(1	0	2	1	6	0	0	0	0	2	0	1	-4)	-0.3316454675390625D+07
cos (0	0)	(1	0	3	0	6	0	0	0	0	1	1	1	-4)	-0.1950855691406250D+07
cos (0	0)	(1	1	0	0	4	0	0	0	0	1	1	0	-3)	-0.2497095285000000D+07
cos (0	0)	(1	1	0	1	4	0	0	0	0	1	0	1	-3)	-0.2497095285000000D+07
cos (0	0)	(1	1	0	2	4	0	0	0	0	1	1	0	-3)	0.1248547642500000D+07
cos (0	0)	(1	1	1	0	4	0	0	0	0	0	1	1	-3)	-0.2497095285000000D+07
cos (0	0)	(1	1	1	1	4	0	0	0	0	0	0	2	-3)	-0.2497095285000000D+07
cos (0	0)	(1	1	1	1	4	0	0	0	0	0	2	0	-3)	0.1248547642500000D+07
cos (0	0)	(1	1	1	1	4	0	0	0	0	2	0	0	-3)	0.1248547642500000D+07
cos (0	0)	(1	1	2	0	4	0	0	0	0	1	1	0	-3)	0.1248547642500000D+07
cos (0	0)	(1	2	0	0	6	0	0	0	0	0	1	0	-4)	-0.7803422765625000D+06
cos (0	0)	(1	2	0	0	6	0	0	0	0	0	3	0	-4)	-0.1755770122265625D+07
cos (0	0)	(1	2	0	0	6	0	0	0	0	2	1	0	-4)	0.9169021749609375D+07
cos (0	0)	(1	2	0	1	6	0	0	0	0	0	0	1	-4)	-0.1092479187187500D+07
cos (0	0)	(1	2	0	1	6	0	0	0	0	0	2	1	-4)	-0.4096796951953125D+07
cos (0	0)	(1	2	0	1	6	0	0	0	0	2	0	1	-4)	0.9559192887890626D+07

continued on next page

continued from previous page

λ	θ	X_1	Y_1	X_2	Y_2	L	$X_{☾}$	$Y_{☾}$	$Z_{☾}$	$r_{☾}$	$X_{\odot}$	$Y_{\odot}$	$Z_{\odot}$	$r_{\odot}$	Coefficient
cos (0	0)	(1	2	1	0	6	0	0	0	0	1	1	1	-4)	0.1911838577578125D+08
cos (0	0)	(1	3	0	0	4	0	0	0	0	1	1	0	-3)	0.6242738212500000D+06
cos (0	0)	(2	0	0	0	4	0	0	0	0	0	0	0	-3)	-0.2497095285000000D+06
cos (0	0)	(2	0	0	0	4	0	0	0	0	0	2	0	-3)	0.9988381140000001D+06
cos (0	0)	(2	0	0	0	4	0	0	0	0	2	0	0	-3)	-0.2497095285000000D+06
cos (0	0)	(2	0	0	1	4	0	0	0	0	0	1	1	-3)	0.2122530992250000D+07
cos (0	0)	(2	0	0	2	4	0	0	0	0	0	0	2	-3)	0.1123692878250000D+07
cos (0	0)	(2	0	0	2	4	0	0	0	0	0	2	0	-3)	-0.1123692878250000D+07
cos (0	0)	(2	0	1	0	4	0	0	0	0	1	0	1	-3)	-0.3745642927500000D+06
cos (0	0)	(2	0	1	1	4	0	0	0	0	1	1	0	-3)	-0.9988381140000001D+06
cos (0	0)	(2	0	2	0	4	0	0	0	0	0	0	2	-3)	-0.1248547642500000D+06
cos (0	0)	(2	0	2	0	4	0	0	0	0	2	0	0	-3)	0.1248547642500000D+06
cos (0	0)	(2	1	0	0	6	0	0	0	0	1	0	0	-4)	0.7803422765625000D+06
cos (0	0)	(2	1	0	0	6	0	0	0	0	1	2	0	-4)	-0.9169021749609375D+07
cos (0	0)	(2	1	0	0	6	0	0	0	0	3	0	0	-4)	0.1755770122265625D+07
cos (0	0)	(2	1	0	1	6	0	0	0	0	1	1	1	-4)	-0.1911838577578125D+08
cos (0	0)	(2	1	1	0	6	0	0	0	0	0	0	1	-4)	0.1092479187187500D+07
cos (0	0)	(2	1	1	0	6	0	0	0	0	0	2	1	-4)	-0.9559192887890626D+07
cos (0	0)	(2	1	1	0	6	0	0	0	0	2	0	1	-4)	0.4096796951953125D+07
cos (0	0)	(2	2	0	0	4	0	0	0	0	0	0	0	-3)	0.1248547642500000D+06
cos (0	0)	(2	2	0	0	4	0	0	0	0	0	2	0	-3)	-0.1872821463750000D+06
cos (0	0)	(2	2	0	0	4	0	0	0	0	2	0	0	-3)	-0.1872821463750000D+06
cos (0	0)	(3	0	0	0	6	0	0	0	0	0	1	0	-4)	-0.7803422765625000D+06
cos (0	0)	(3	0	0	0	6	0	0	0	0	0	3	0	-4)	0.1885827168359375D+07
cos (0	0)	(3	0	0	0	6	0	0	0	0	2	1	0	-4)	-0.1755770122265625D+07
cos (0	0)	(3	0	0	1	6	0	0	0	0	0	0	1	-4)	-0.1092479187187500D+07
cos (0	0)	(3	0	0	1	6	0	0	0	0	0	2	1	-4)	0.6827994919921875D+07
cos (0	0)	(3	0	0	1	6	0	0	0	0	2	0	1	-4)	-0.1365598983984375D+07
cos (0	0)	(3	0	1	0	6	0	0	0	0	1	1	1	-4)	-0.2731197967968750D+07
cos (0	0)	(3	1	0	0	4	0	0	0	0	1	1	0	-3)	0.6242738212500000D+06
cos (0	0)	(4	0	0	0	4	0	0	0	0	0	0	0	-3)	0.6242738212500000D+05
cos (0	0)	(4	0	0	0	4	0	0	0	0	0	2	0	-3)	-0.2497095285000000D+06
cos (0	0)	(4	0	0	0	4	0	0	0	0	2	0	0	-3)	0.6242738212500000D+05

G.2 Direct solar radiation pressure disturbing function $\mathcal{H}_{rp}$

λ	θ	X_1	Y_1	X_2	Y_2	L	$X_{☾}$	$Y_{☾}$	$Z_{☾}$	$r_{☾}$	$X_{\odot}$	$Y_{\odot}$	$Z_{\odot}$	$r_{\odot}$	Coefficient
cos (0	0)	(0	0	0	0	0	0	0	0	0	0	0	0	-1)	0.2574575394591462D+03
cos (0	0)	(0	0	0	0	4	0	0	0	0	0	0	0	-3)	-0.1287287697295731D+03
cos (0	0)	(0	0	0	0	4	0	0	0	0	0	2	0	-3)	0.1930931545943597D+03
cos (0	0)	(0	0	0	0	4	0	0	0	0	2	0	0	-3)	0.1930931545943597D+03
cos (0	0)	(0	0	0	1	4	0	0	0	0	0	1	1	-3)	0.3861863091887194D+03
cos (0	0)	(0	0	0	2	4	0	0	0	0	0	0	2	-3)	0.1930931545943597D+03
cos (0	0)	(0	0	0	2	4	0	0	0	0	0	2	0	-3)	-0.1930931545943597D+03
cos (0	0)	(0	0	0	3	4	0	0	0	0	0	1	1	-3)	-0.2413664432429496D+03

continued on next page

continued from previous page

λ	θ	X_1	Y_1	X_2	Y_2	L	$X_{☾}$	$Y_{☾}$	$Z_{☾}$	$r_{☾}$	$X_{\odot}$	$Y_{\odot}$	$Z_{\odot}$	$r_{\odot}$	Coefficient
cos (0	0)	(0	0	0	4	4	0	0	0	0	0	0	2	-3)	-0.4827328864858993D+02
cos (0	0)	(0	0	0	4	4	0	0	0	0	0	2	0	-3)	0.4827328864858993D+02
cos (0	0)	(0	0	1	0	4	0	0	0	0	1	0	1	-3)	0.3861863091887194D+03
cos (0	0)	(0	0	1	1	4	0	0	0	0	1	1	0	-3)	-0.3861863091887194D+03
cos (0	0)	(0	0	1	2	4	0	0	0	0	1	0	1	-3)	-0.2413664432429496D+03
cos (0	0)	(0	0	1	3	4	0	0	0	0	1	1	0	-3)	0.9654657729717985D+02
cos (0	0)	(0	0	2	0	4	0	0	0	0	0	0	2	-3)	0.1930931545943597D+03
cos (0	0)	(0	0	2	0	4	0	0	0	0	2	0	0	-3)	-0.1930931545943597D+03
cos (0	0)	(0	0	2	1	4	0	0	0	0	0	1	1	-3)	-0.2413664432429496D+03
cos (0	0)	(0	0	2	2	4	0	0	0	0	0	0	2	-3)	-0.9654657729717985D+02
cos (0	0)	(0	0	2	2	4	0	0	0	0	0	2	0	-3)	0.4827328864858993D+02
cos (0	0)	(0	0	2	2	4	0	0	0	0	2	0	0	-3)	0.4827328864858993D+02
cos (0	0)	(0	0	3	0	4	0	0	0	0	1	0	1	-3)	-0.2413664432429496D+03
cos (0	0)	(0	0	3	1	4	0	0	0	0	1	1	0	-3)	0.9654657729717985D+02
cos (0	0)	(0	0	4	0	4	0	0	0	0	0	0	2	-3)	-0.4827328864858993D+02
cos (0	0)	(0	0	4	0	4	0	0	0	0	2	0	0	-3)	0.4827328864858993D+02
cos (0	0)	(0	1	0	0	2	0	0	0	0	1	0	0	-2)	-0.3861863091887194D+03
cos (0	0)	(0	1	0	0	6	0	0	0	0	1	0	0	-4)	0.9654657729717985D+03
cos (0	0)	(0	1	0	0	6	0	0	0	0	1	2	0	-4)	-0.1206832216214748D+04
cos (0	0)	(0	1	0	0	6	0	0	0	0	3	0	0	-4)	-0.1206832216214748D+04
cos (0	0)	(0	1	0	1	6	0	0	0	0	1	1	1	-4)	-0.2413664432429496D+04
cos (0	0)	(0	1	0	2	6	0	0	0	0	1	0	2	-4)	-0.1206832216214748D+04
cos (0	0)	(0	1	0	2	6	0	0	0	0	1	2	0	-4)	0.1206832216214748D+04
cos (0	0)	(0	1	0	3	6	0	0	0	0	1	1	1	-4)	0.1508540270268435D+04
cos (0	0)	(0	1	1	0	2	0	0	0	0	0	0	1	-2)	-0.3861863091887194D+03
cos (0	0)	(0	1	1	0	6	0	0	0	0	0	0	1	-4)	0.9654657729717985D+03
cos (0	0)	(0	1	1	0	6	0	0	0	0	0	2	1	-4)	-0.1206832216214748D+04
cos (0	0)	(0	1	1	0	6	0	0	0	0	2	0	1	-4)	-0.3620496648644244D+04
cos (0	0)	(0	1	1	1	2	0	0	0	0	0	1	0	-2)	0.1930931545943597D+03
cos (0	0)	(0	1	1	1	6	0	0	0	0	0	1	0	-4)	-0.4827328864858993D+03
cos (0	0)	(0	1	1	1	6	0	0	0	0	0	1	2	-4)	-0.2413664432429496D+04
cos (0	0)	(0	1	1	1	6	0	0	0	0	0	3	0	-4)	0.6034161081073740D+03
cos (0	0)	(0	1	1	1	6	0	0	0	0	2	1	0	-4)	0.3017080540536870D+04
cos (0	0)	(0	1	1	2	2	0	0	0	0	0	0	1	-2)	0.4827328864858993D+02
cos (0	0)	(0	1	1	2	6	0	0	0	0	0	0	1	-4)	-0.1206832216214748D+03
cos (0	0)	(0	1	1	2	6	0	0	0	0	0	0	3	-4)	-0.1206832216214748D+04
cos (0	0)	(0	1	1	2	6	0	0	0	0	0	2	1	-4)	0.2564518459456340D+04
cos (0	0)	(0	1	1	2	6	0	0	0	0	2	0	1	-4)	0.1659394297295279D+04
cos (0	0)	(0	1	2	0	2	0	0	0	0	1	0	0	-2)	0.1930931545943597D+03
cos (0	0)	(0	1	2	0	6	0	0	0	0	1	0	0	-4)	-0.4827328864858993D+03
cos (0	0)	(0	1	2	0	6	0	0	0	0	1	0	2	-4)	-0.3620496648644244D+04
cos (0	0)	(0	1	2	0	6	0	0	0	0	1	2	0	-4)	0.6034161081073740D+03
cos (0	0)	(0	1	2	0	6	0	0	0	0	3	0	0	-4)	0.1810248324322122D+04
cos (0	0)	(0	1	2	1	6	0	0	0	0	1	1	1	-4)	0.6335869135127426D+04
cos (0	0)	(0	1	3	0	2	0	0	0	0	0	0	1	-2)	0.4827328864858993D+02

continued on next page

continued from previous page

λ	θ	X_1	Y_1	X_2	Y_2	L	$X_☾$	$Y_☾$	$Z_☾$	$r_☾$	$X_\odot$	$Y_\odot$	$Z_\odot$	$r_\odot$	Coefficient
cos (0	0)	(0	1	3	0	6	0	0	0	0	0	0	1	-4)	-0.1206832216214748D+03
cos (0	0)	(0	1	3	0	6	0	0	0	0	0	0	3	-4)	-0.1206832216214748D+04
cos (0	0)	(0	1	3	0	6	0	0	0	0	0	2	1	-4)	0.1508540270268435D+03
cos (0	0)	(0	1	3	0	6	0	0	0	0	2	0	1	-4)	0.4073058729724775D+04
cos (0	0)	(0	2	0	0	4	0	0	0	0	0	0	0	-3)	-0.1930931545943597D+03
cos (0	0)	(0	2	0	0	4	0	0	0	0	0	2	0	-3)	-0.1930931545943597D+03
cos (0	0)	(0	2	0	0	4	0	0	0	0	2	0	0	-3)	0.7723726183774388D+03
cos (0	0)	(0	2	0	1	4	0	0	0	0	0	1	1	-3)	-0.2896397318915396D+03
cos (0	0)	(0	2	0	2	4	0	0	0	0	0	0	2	-3)	-0.9654657729717985D+02
cos (0	0)	(0	2	0	2	4	0	0	0	0	0	2	0	-3)	0.9654657729717985D+02
cos (0	0)	(0	2	1	0	4	0	0	0	0	1	0	1	-3)	0.1641291814052057D+04
cos (0	0)	(0	2	1	1	4	0	0	0	0	1	1	0	-3)	-0.7723726183774388D+03
cos (0	0)	(0	2	2	0	4	0	0	0	0	0	0	2	-3)	0.8689191956746187D+03
cos (0	0)	(0	2	2	0	4	0	0	0	0	2	0	0	-3)	-0.8689191956746187D+03
cos (0	0)	(0	3	0	0	2	0	0	0	0	1	0	0	-2)	0.4827328864858993D+02
cos (0	0)	(0	3	0	0	6	0	0	0	0	1	0	0	-4)	0.6034161081073740D+03
cos (0	0)	(0	3	0	0	6	0	0	0	0	1	2	0	-4)	0.1357686243241591D+04
cos (0	0)	(0	3	0	0	6	0	0	0	0	3	0	0	-4)	-0.1458255594592820D+04
cos (0	0)	(0	3	0	1	6	0	0	0	0	1	1	1	-4)	0.2111956378375809D+04
cos (0	0)	(0	3	1	0	2	0	0	0	0	0	0	1	-2)	-0.4827328864858993D+02
cos (0	0)	(0	3	1	0	6	0	0	0	0	0	0	1	-4)	0.8447825513503237D+03
cos (0	0)	(0	3	1	0	6	0	0	0	0	0	2	1	-4)	0.1055978189187904D+04
cos (0	0)	(0	3	1	0	6	0	0	0	0	2	0	1	-4)	-0.5279890945939523D+04
cos (0	0)	(0	4	0	0	4	0	0	0	0	0	0	0	-3)	0.4827328864858993D+02
cos (0	0)	(0	4	0	0	4	0	0	0	0	0	2	0	-3)	0.4827328864858993D+02
cos (0	0)	(0	4	0	0	4	0	0	0	0	2	0	0	-3)	-0.1930931545943597D+03
cos (0	0)	(1	0	0	0	2	0	0	0	0	0	1	0	-2)	0.3861863091887194D+03
cos (0	0)	(1	0	0	0	6	0	0	0	0	0	1	0	-4)	-0.9654657729717985D+03
cos (0	0)	(1	0	0	0	6	0	0	0	0	0	3	0	-4)	0.1206832216214748D+04
cos (0	0)	(1	0	0	0	6	0	0	0	0	2	1	0	-4)	0.1206832216214748D+04
cos (0	0)	(1	0	0	1	2	0	0	0	0	0	0	1	-2)	0.3861863091887194D+03
cos (0	0)	(1	0	0	1	6	0	0	0	0	0	0	1	-4)	-0.9654657729717985D+03
cos (0	0)	(1	0	0	1	6	0	0	0	0	0	2	1	-4)	0.3620496648644244D+04
cos (0	0)	(1	0	0	1	6	0	0	0	0	2	0	1	-4)	0.1206832216214748D+04
cos (0	0)	(1	0	0	2	2	0	0	0	0	0	1	0	-2)	-0.1930931545943597D+03
cos (0	0)	(1	0	0	2	6	0	0	0	0	0	1	0	-4)	0.4827328864858993D+03
cos (0	0)	(1	0	0	2	6	0	0	0	0	0	1	2	-4)	0.3620496648644244D+04
cos (0	0)	(1	0	0	2	6	0	0	0	0	0	3	0	-4)	-0.1810248324322122D+04
cos (0	0)	(1	0	0	2	6	0	0	0	0	2	1	0	-4)	-0.6034161081073740D+03
cos (0	0)	(1	0	0	3	2	0	0	0	0	0	0	1	-2)	-0.4827328864858993D+02
cos (0	0)	(1	0	0	3	6	0	0	0	0	0	0	1	-4)	0.1206832216214748D+03
cos (0	0)	(1	0	0	3	6	0	0	0	0	0	0	3	-4)	0.1206832216214748D+04
cos (0	0)	(1	0	0	3	6	0	0	0	0	0	2	1	-4)	-0.4073058729724775D+04
cos (0	0)	(1	0	0	3	6	0	0	0	0	2	0	1	-4)	-0.1508540270268435D+03
cos (0	0)	(1	0	1	0	6	0	0	0	0	1	1	1	-4)	0.2413664432429496D+04

continued on next page

continued from previous page

λ	θ	X_1	Y_1	X_2	Y_2	L	$X_{☾}$	$Y_{☾}$	$Z_{☾}$	$r_{☾}$	$X_{\odot}$	$Y_{\odot}$	$Z_{\odot}$	$r_{\odot}$	Coefficient
cos (0	0)	(1	0	1	1	2	0	0	0	0	1	0	0	-2)	-0.1930931545943597D+03
cos (0	0)	(1	0	1	1	6	0	0	0	0	1	0	0	-4)	0.4827328864858993D+03
cos (0	0)	(1	0	1	1	6	0	0	0	0	1	0	2	-4)	0.2413664432429496D+04
cos (0	0)	(1	0	1	1	6	0	0	0	0	1	2	0	-4)	-0.3017080540536870D+04
cos (0	0)	(1	0	1	1	6	0	0	0	0	3	0	0	-4)	-0.6034161081073740D+03
cos (0	0)	(1	0	1	2	6	0	0	0	0	1	1	1	-4)	-0.6335869135127426D+04
cos (0	0)	(1	0	2	0	6	0	0	0	0	0	1	2	-4)	0.1206832216214748D+04
cos (0	0)	(1	0	2	0	6	0	0	0	0	2	1	0	-4)	-0.1206832216214748D+04
cos (0	0)	(1	0	2	1	2	0	0	0	0	0	0	1	-2)	-0.4827328864858993D+02
cos (0	0)	(1	0	2	1	6	0	0	0	0	0	0	1	-4)	0.1206832216214748D+03
cos (0	0)	(1	0	2	1	6	0	0	0	0	0	0	3	-4)	0.1206832216214748D+04
cos (0	0)	(1	0	2	1	6	0	0	0	0	0	2	1	-4)	-0.1659394297295279D+04
cos (0	0)	(1	0	2	1	6	0	0	0	0	2	0	1	-4)	-0.2564518459456340D+04
cos (0	0)	(1	0	3	0	6	0	0	0	0	1	1	1	-4)	-0.1508540270268435D+04
cos (0	0)	(1	1	0	0	4	0	0	0	0	1	1	0	-3)	-0.1930931545943597D+04
cos (0	0)	(1	1	0	1	4	0	0	0	0	1	0	1	-3)	-0.1930931545943597D+04
cos (0	0)	(1	1	0	2	4	0	0	0	0	1	1	0	-3)	0.9654657729717985D+03
cos (0	0)	(1	1	1	0	4	0	0	0	0	0	1	1	-3)	-0.1930931545943597D+04
cos (0	0)	(1	1	1	1	4	0	0	0	0	0	0	2	-3)	-0.1930931545943597D+04
cos (0	0)	(1	1	1	1	4	0	0	0	0	0	2	0	-3)	0.9654657729717985D+03
cos (0	0)	(1	1	1	1	4	0	0	0	0	2	0	0	-3)	0.9654657729717985D+03
cos (0	0)	(1	1	2	0	4	0	0	0	0	1	1	0	-3)	0.9654657729717985D+03
cos (0	0)	(1	2	0	0	2	0	0	0	0	0	1	0	-2)	-0.4827328864858993D+02
cos (0	0)	(1	2	0	0	6	0	0	0	0	0	1	0	-4)	-0.6034161081073740D+03
cos (0	0)	(1	2	0	0	6	0	0	0	0	0	3	0	-4)	-0.1357686243241591D+04
cos (0	0)	(1	2	0	0	6	0	0	0	0	2	1	0	-4)	0.7090139270261644D+04
cos (0	0)	(1	2	0	1	2	0	0	0	0	0	0	1	-2)	0.4827328864858993D+02
cos (0	0)	(1	2	0	1	6	0	0	0	0	0	0	1	-4)	-0.8447825513503237D+03
cos (0	0)	(1	2	0	1	6	0	0	0	0	0	2	1	-4)	-0.3167934567563713D+04
cos (0	0)	(1	2	0	1	6	0	0	0	0	2	0	1	-4)	0.7391847324315332D+04
cos (0	0)	(1	2	1	0	6	0	0	0	0	1	1	1	-4)	0.1478369464863066D+05
cos (0	0)	(1	3	0	0	4	0	0	0	0	1	1	0	-3)	0.4827328864858993D+03
cos (0	0)	(2	0	0	0	4	0	0	0	0	0	0	0	-3)	-0.1930931545943597D+03
cos (0	0)	(2	0	0	0	4	0	0	0	0	0	2	0	-3)	0.7723726183774388D+03
cos (0	0)	(2	0	0	0	4	0	0	0	0	2	0	0	-3)	-0.1930931545943597D+03
cos (0	0)	(2	0	0	1	4	0	0	0	0	0	1	1	-3)	0.1641291814052057D+04
cos (0	0)	(2	0	0	2	4	0	0	0	0	0	0	2	-3)	0.8689191956746187D+03
cos (0	0)	(2	0	0	2	4	0	0	0	0	0	2	0	-3)	-0.8689191956746187D+03
cos (0	0)	(2	0	1	0	4	0	0	0	0	1	0	1	-3)	-0.2896397318915396D+03
cos (0	0)	(2	0	1	1	4	0	0	0	0	1	1	0	-3)	-0.7723726183774388D+03
cos (0	0)	(2	0	2	0	4	0	0	0	0	0	0	2	-3)	-0.9654657729717985D+02
cos (0	0)	(2	0	2	0	4	0	0	0	0	2	0	0	-3)	0.9654657729717985D+02
cos (0	0)	(2	1	0	0	2	0	0	0	0	1	0	0	-2)	0.4827328864858993D+02
cos (0	0)	(2	1	0	0	6	0	0	0	0	1	0	0	-4)	0.6034161081073740D+03
cos (0	0)	(2	1	0	0	6	0	0	0	0	1	2	0	-4)	-0.7090139270261644D+04

continued on next page

continued from previous page

λ	θ	X_1	Y_1	X_2	Y_2	L	$X_☾$	$Y_☾$	$Z_☾$	$r_☾$	$X_\odot$	$Y_\odot$	$Z_\odot$	$r_\odot$	Coefficient
cos (0	0)	(2	1	0	0	6	0	0	0	0	3	0	0	-4)	0.1357686243241591D+04
cos (0	0)	(2	1	0	1	6	0	0	0	0	1	1	1	-4)	-0.1478369464863066D+05
cos (0	0)	(2	1	1	0	2	0	0	0	0	0	0	1	-2)	-0.4827328864858993D+02
cos (0	0)	(2	1	1	0	6	0	0	0	0	0	0	1	-4)	0.8447825513503237D+03
cos (0	0)	(2	1	1	0	6	0	0	0	0	0	2	1	-4)	-0.7391847324315332D+04
cos (0	0)	(2	1	1	0	6	0	0	0	0	2	0	1	-4)	0.3167934567563713D+04
cos (0	0)	(2	2	0	0	4	0	0	0	0	0	0	0	-3)	0.9654657729717985D+02
cos (0	0)	(2	2	0	0	4	0	0	0	0	0	2	0	-3)	-0.1448198659457698D+03
cos (0	0)	(2	2	0	0	4	0	0	0	0	2	0	0	-3)	-0.1448198659457698D+03
cos (0	0)	(3	0	0	0	2	0	0	0	0	0	1	0	-2)	-0.4827328864858993D+02
cos (0	0)	(3	0	0	0	6	0	0	0	0	0	1	0	-4)	-0.6034161081073740D+03
cos (0	0)	(3	0	0	0	6	0	0	0	0	0	3	0	-4)	0.1458255594592820D+04
cos (0	0)	(3	0	0	0	6	0	0	0	0	2	1	0	-4)	-0.1357686243241591D+04
cos (0	0)	(3	0	0	1	2	0	0	0	0	0	0	1	-2)	0.4827328864858993D+02
cos (0	0)	(3	0	0	1	6	0	0	0	0	0	0	1	-4)	-0.8447825513503237D+03
cos (0	0)	(3	0	0	1	6	0	0	0	0	0	2	1	-4)	0.5279890945939523D+04
cos (0	0)	(3	0	0	1	6	0	0	0	0	2	0	1	-4)	-0.1055978189187904D+04
cos (0	0)	(3	0	1	0	6	0	0	0	0	1	1	1	-4)	-0.2111956378375809D+04
cos (0	0)	(3	1	0	0	4	0	0	0	0	1	1	0	-3)	0.4827328864858993D+03
cos (0	0)	(4	0	0	0	4	0	0	0	0	0	0	0	-3)	0.4827328864858993D+02
cos (0	0)	(4	0	0	0	4	0	0	0	0	0	2	0	-3)	-0.1930931545943597D+03
cos (0	0)	(4	0	0	0	4	0	0	0	0	2	0	0	-3)	0.4827328864858993D+02

G.3 Second degree and order disturbing function $\mathcal{H}_{J_{22}}$

σ	θ	X_1	Y_1	X_2	Y_2	L	$X_☾$	$Y_☾$	$Z_☾$	$r_☾$	$X_\odot$	$Y_\odot$	$Z_\odot$	$r_\odot$	Coefficient
cos (2	0)	(0	0	0	0	-6	0	0	0	0	0	0	0	0)	0.1080907167254767D-06
cos (2	0)	(0	0	0	2	-6	0	0	0	0	0	0	0	0)	-0.5404535836273835D-07
cos (2	0)	(0	0	0	4	-6	0	0	0	0	0	0	0	0)	0.6755669795342294D-08
cos (2	0)	(0	0	2	0	-6	0	0	0	0	0	0	0	0)	-0.5404535836273835D-07
cos (2	0)	(0	0	2	2	-6	0	0	0	0	0	0	0	0)	0.1351133959068459D-07
cos (2	0)	(0	0	4	0	-6	0	0	0	0	0	0	0	0)	0.6755669795342294D-08
cos (2	0)	(0	2	0	0	-6	0	0	0	0	0	0	0	0)	-0.2702267918136917D-06
cos (2	0)	(0	2	0	2	-6	0	0	0	0	0	0	0	0)	0.2296927730416380D-06
cos (2	0)	(0	2	1	1	-6	0	0	0	0	0	0	0	0)	0.1396098432635950D-06
cos (2	0)	(0	2	2	0	-6	0	0	0	0	0	0	0	0)	-0.1351133959068460D-07
cos (2	0)	(0	4	0	0	-6	0	0	0	0	0	0	0	0)	0.1553804052928729D-06
cos (2	0)	(1	1	0	2	-6	0	0	0	0	0	0	0	0)	-0.1396098432635950D-06
cos (2	0)	(1	1	1	1	-6	0	0	0	0	0	0	0	0)	0.4864082252646452D-06
cos (2	0)	(1	1	2	0	-6	0	0	0	0	0	0	0	0)	0.1396098432635950D-06
cos (2	0)	(2	0	0	0	-6	0	0	0	0	0	0	0	0)	-0.2702267918136917D-06
cos (2	0)	(2	0	0	2	-6	0	0	0	0	0	0	0	0)	-0.1351133959068460D-07
cos (2	0)	(2	0	1	1	-6	0	0	0	0	0	0	0	0)	-0.1396098432635950D-06

continued on next page

continued from previous page

σ	θ	X_1	Y_1	X_2	Y_2	L	$X_{☾}$	$Y_{☾}$	$Z_{☾}$	$r_{☾}$	$X_{\odot}$	$Y_{\odot}$	$Z_{\odot}$	$r_{\odot}$	Coefficient
cos (2	0)	(2	0	2	0	-6	0	0	0	0	0	0	0	0)	0.2296927730416380D-06
cos (2	0)	(2	2	0	0	-6	0	0	0	0	0	0	0	0)	0.3107608105857458D-06
cos (2	0)	(4	0	0	0	-6	0	0	0	0	0	0	0	0)	0.1553804052928729D-06
sin (2	0)	(0	0	0	0	-6	0	0	0	0	0	0	0	0)	-0.6204881922826443D-07
sin (2	0)	(0	0	0	2	-6	0	0	0	0	0	0	0	0)	0.3102440961413221D-07
sin (2	0)	(0	0	0	4	-6	0	0	0	0	0	0	0	0)	-0.3878051201766527D-08
sin (2	0)	(0	0	2	0	-6	0	0	0	0	0	0	0	0)	0.3102440961413221D-07
sin (2	0)	(0	0	2	2	-6	0	0	0	0	0	0	0	0)	-0.7756102403533053D-08
sin (2	0)	(0	0	4	0	-6	0	0	0	0	0	0	0	0)	-0.3878051201766527D-08
sin (2	0)	(0	2	0	0	-6	0	0	0	0	0	0	0	0)	0.1551220480706611D-06
sin (2	0)	(0	2	0	2	-6	0	0	0	0	0	0	0	0)	-0.1318537408600619D-06
sin (2	0)	(0	2	1	1	-6	0	0	0	0	0	0	0	0)	0.2432041126323226D-06
sin (2	0)	(0	2	2	0	-6	0	0	0	0	0	0	0	0)	0.7756102403533053D-08
sin (2	0)	(0	4	0	0	-6	0	0	0	0	0	0	0	0)	-0.8919517764063013D-07
sin (2	0)	(1	1	0	2	-6	0	0	0	0	0	0	0	0)	-0.2432041126323226D-06
sin (2	0)	(1	1	1	1	-6	0	0	0	0	0	0	0	0)	-0.2792196865271899D-06
sin (2	0)	(1	1	2	0	-6	0	0	0	0	0	0	0	0)	0.2432041126323226D-06
sin (2	0)	(2	0	0	0	-6	0	0	0	0	0	0	0	0)	0.1551220480706611D-06
sin (2	0)	(2	0	0	2	-6	0	0	0	0	0	0	0	0)	0.7756102403533053D-08
sin (2	0)	(2	0	1	1	-6	0	0	0	0	0	0	0	0)	-0.2432041126323226D-06
sin (2	0)	(2	0	2	0	-6	0	0	0	0	0	0	0	0)	-0.1318537408600619D-06
sin (2	0)	(2	2	0	0	-6	0	0	0	0	0	0	0	0)	-0.1783903552812603D-06
sin (2	0)	(4	0	0	0	-6	0	0	0	0	0	0	0	0)	-0.8919517764063013D-07

Appendix H

Admissible regions: nodal distances and elongations

The beginning of my research work has been originally devoted to the most recent theories which were developed within the context of near-Earth asteroids orbital determination. Especially, we investigated the new techniques which are well-suited even if the astrometry information is not enough to compute an orbit and/or perform an identification with an already discovered object. In particular, we focused on the theory developed in Milani et al. (2004a) where the so-called *Admissible region* is introduced.

This Ph.D manuscript gives us the opportunity to present our personal contribution to the above-mentioned theory which is all the more important as it has been recently adapted to the main problem of orbit determination of the space debris population. For further details, we refer to Tommei et al. (2007).

The results of this appendix have been previously published in Valk and Lemaître (2007a)

When a non identified object is observed, the first reaction of the scientific community is to try to determine its orbit. Unfortunately, for the data collected on very short periods of time, the arc of observation is not large enough to give any estimation of the curvature; the determination of the orbit is impossible, using traditional methods of orbital determination, such as the Gauss method. If we intend to build a complete catalog of such objects, the conclusion is easy: this object is rejected, and the observers hope to be luckier a few months or years later, to re-observe the same body, on a larger timescale. However, in many cases, the right ascension, the declination and their instantaneous time derivatives are measured.

For the last few years, associations like Space Guard or the specialists of the Near-Earth Asteroids (Minor Planet Center[1] or NEODYS group[2]) have a completely different point of

[1] http://cfa-www.harvard.edu/iau/mpc.html
[2] http://newton.dm.unipi.it/cgi-bin/neodys/neoibo

view concerning these unexpected observed objects. The main question is not only the improvement of their orbit, but also the potential hazard that they represent for the Earth: could this unknown body becomes dangerous for us, in a delay of one or two hundreds years ?

Virtually, this too short arc (TSA) corresponds to an infinity of orbits. We assume, because it is true in many cases, that its right ascension α and declination δ are know, as well as their time derivatives; on the opposite, there is no data concerning either their distance to the Earth or the time derivative of this distance. Consequently, on a set of six variables $(\alpha, \delta, \dot{\alpha}, \dot{\delta}, r, \dot{r})$, the first four are determined with a specific accuracy, while the last two are completely arbitrary. This means that the object lies in a 2 dimensional subspace of a general 6 dimensional space.

This idea was introduced by Milani et al. (2004a) and pushed further on in Milani et al. (2004b), Gronchi et al. (2004), Milani et al. (2005) and Milani and Knežević (2005). This incomplete set of data (2 angles and 2 time derivatives) is called an "*attributable*" by the authors mentioned above and this denomination is conserved here. Thanks to reasonable hypotheses (the fact that the object belongs to the Solar System, or that it is not a satellite of the Earth), Milani et al. (2004a) proved that this region, in the plane $(r, \dot{r})$, could be closed and formed of one or two connected sets. Curves of constant values of the osculating Keplerian elements can be drawn on this region.

Unfortunately, if a second observation is not available, the admissible region is still very large; one of the challenges is to follow the propagation of this admissible region, by means of linear and non linear techniques, in order to compare its evolution with a potential new arc.

Our purpose here is to concentrate on some aspects of the initial admissible region. Firstly, we recalculate one of its boundaries, for the short distances to the Earth, introducing the hyperbolic shape of the orbit instead of its linear approximation; secondly, we introduce, on the admissible zone, and in complement of the Keplerian elements information, the nodal distances, corresponding to the intersections of the Earth and potential Earth's impactors orbits. We present different situations, where the singularity in inclination is inside or outside the admissible region, following the chosen attributable. These curves could be very interesting in the context of propagation of the motions, reducing the dimension of the admissible region (dimension one instead of two). Thirdly we introduce the concept of elongations on the graphics.

H.1 The admissible region

Let $\vec{P}_{\mathcal{A}}$ and $\vec{V}_{\mathcal{A}}$ be the heliocentric position and velocity vectors of a celestial body $\mathcal{A}$ at a reference time t. At the same time, the position vector $\vec{P}_{\oplus}$ and the velocity vector $\vec{V}_{\oplus}$ of the Earth are well known.

The heliocentric energy per unit mass of $\mathcal{A}$ is given by

$$E_\odot = \frac{1}{2}\|\vec{V}_\mathcal{A}\|^2 - k_\odot^2 \frac{1}{\|\vec{P}_\mathcal{A}\|} \tag{H.1}$$

and its geocentric energy takes the form

$$E_\oplus = \frac{1}{2}\|\vec{V}_\mathcal{A} - \vec{V}_\oplus\|^2 - k_\oplus^2 \frac{1}{\|\vec{P}_\mathcal{A} - \vec{P}_\oplus\|}\,, \tag{H.2}$$

where $m_\oplus$ and $m_\odot$ are the masses of the Earth and of the Sun respectively. Gauss' constant is defined by: $k_\odot = \sqrt{Gm_\odot} = 0.01720209895$ and $k_\oplus^2 = k_\odot^2 \frac{m_\oplus}{m_\odot}$. The solar mass is taken as the mass unit, the mean semi-major axis of the Earth orbit is the distance unit (AU) and the average day is the time unit.

An attributable is defined as a fourth dimension vector

$$\vec{A} = (\alpha, \delta, \dot{\alpha}, \dot{\delta}) \;\in\; [-\pi, \pi[\,\times\,]-\frac{\pi}{2}, \frac{\pi}{2}[\,\times \mathbb{R}^2 \tag{H.3}$$

computed at the time t and to which an apparent magnitude M can be associated. We use the classical geocentric equatorial coordinates (α, δ) with α, the right ascension, and δ, the declination. The position vector $\vec{P}_\mathcal{A}$ can be expressed as

$$\vec{P}_\mathcal{A} = \vec{P}_\oplus + r\ \vec{u} \tag{H.4}$$

where r is the geocentric distance of the body $\mathcal{A}$ and $\vec{u}$ is the unit vector in the direction of the observation

$$\vec{u} = (\cos\alpha\cos\delta, \sin\alpha\cos\delta, \sin\delta). \tag{H.5}$$

The first time derivative of equation (H.4) gives the velocity vector

$$\vec{V}_\mathcal{A} = \vec{V}_\oplus + \dot{r}\ \vec{u} + r\ \dot{\alpha}\ \vec{u}_\alpha + r\ \dot{\delta}\ \vec{u}_\delta, \tag{H.6}$$

where

$$\vec{u}_\alpha = (-\sin\alpha\cos\delta, \cos\alpha\cos\delta, 0) \tag{H.7}$$

$$\vec{u}_\delta = (-\cos\alpha\sin\delta, -\sin\alpha\sin\delta, \cos\delta)\,. \tag{H.8}$$

The geocentric position and velocity vectors can be computed as functions of r and $\dot{r}$

$$\|\vec{P}_\mathcal{A} - \vec{P}_\oplus\|^2 = r^2 \tag{H.9}$$

$$\|\vec{V}_\mathcal{A} - \vec{V}_\oplus\|^2 = \dot{r}^2 + r^2\ \dot{\alpha}^2\ \cos^2\delta + r^2\ \dot{\delta}^2 = \dot{r}^2 + r^2\eta^2\,, \tag{H.10}$$

where

$$\eta = \sqrt{\dot{\alpha}^2\cos^2\delta + \dot{\delta}^2} \tag{H.11}$$

is the proper motion. The energies are given by

$$E_\oplus = \frac{1}{2}\left[\dot{r}^2 + r^2\,\eta^2 - \frac{2k_\oplus^2}{r}\right] \tag{H.12}$$

and

$$E_\odot = \frac{1}{2}\left[\dot{r}^2 + c_1\,\dot{r} + W(r) - \frac{2k_\odot^2}{\sqrt{S(r)}}\right], \tag{H.13}$$

where the quantities $W(r)$ and $S(r)$ are functions of the geocentric distance r (see Milani et al. (2004a) for details).

To determine the admissible regions, let us recall the conditions chosen by Milani et al. (2004a)

1. $\mathcal{A}$ is not a satellite of the Earth

$$\mathcal{D}_1 = \{(r, \dot{r}) : E_\oplus \geq 0\}\ ,$$

2. $\mathcal{A}$ is not influenced by the Earth's gravity field (of radius R_{SI})

$$\mathcal{D}_2 = \{(r, \dot{r}) : r \geq R_{SI}\}\ ,$$

3. $\mathcal{A}$ is on an elliptic orbit around the Sun

$$\mathcal{D}_3 = \{(r, \dot{r}) : E_\odot \leq 0\}\ ,$$

4. $\mathcal{A}$ is obviously outside the Earth's globe (of radius $R_\oplus$)

$$\mathcal{D}_4 = \{(r, \dot{r}) : r \geq R_\oplus\}\ .$$

The admissible region is defined as

$$\mathcal{D} = \{\mathcal{D}_1 \cup \mathcal{D}_2\} \cap \mathcal{D}_3 \cap \mathcal{D}_4\,. \tag{H.14}$$

A schematic example of such a region is given in Figure H.1.

H.2 Immediate impact trajectory and inner boundary

Our first purpose is to exclude, from the admissible region $\mathcal{D}$, all the objects which are on a collision course with the Earth within a short time span; as mentioned by Milani et al. (2004a), this gives an additional boundary for the left part of the admissible region, between d_4 and d_2 where the curves d_i are the boundaries of the regions $\mathcal{D}_i$. It is based on the assumption that the

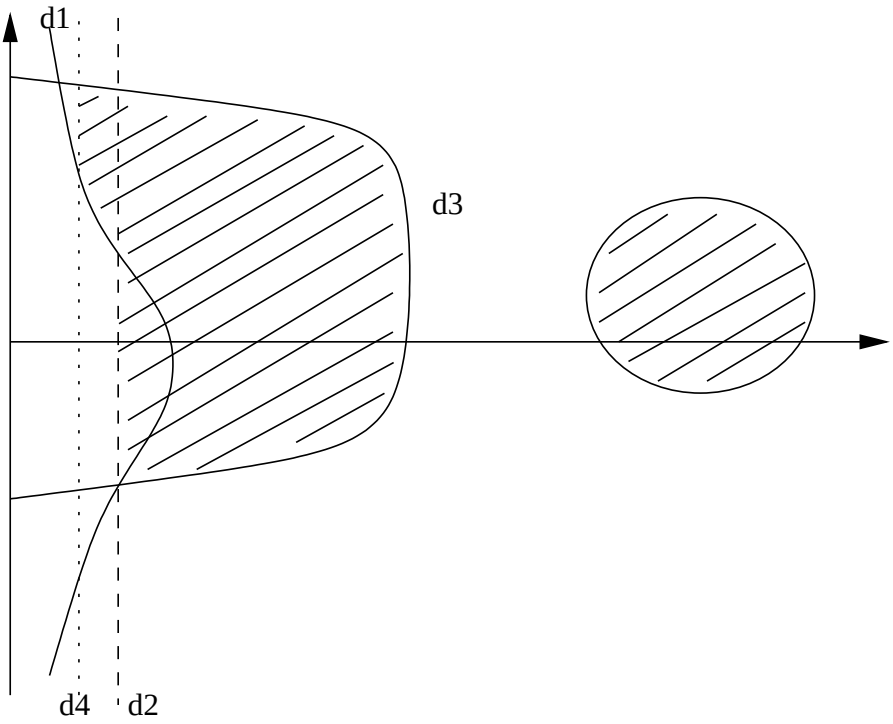

Figure H.1: The topology of an admissible region with two connected components in the plane $(r, \dot{r})$; the curves d_i, for $i = 1, 2, 3, 4$ are the boundaries of the regions $\mathcal{D}_i$.

trajectory of the body $\mathcal{A}$ is rectilinear and can be written as

$$\frac{\eta\, r^2}{|\dot{r}|} \geq R_\oplus \,, \tag{H.15}$$

where $R_\oplus = 4.26352 \times 10^{-5}$ AU. However, when the geocentric speed $\dot{r}$ is low, the hypothesis of linearity is not suitable anymore and the boundary description can be easily improved by using a two body (Keplerian) formalism: the object is assumed to move within the sphere of influence of the Earth where its orbit is only controlled by the Earth's gravity field. In this context, our new condition can be expressed as

$$q_\oplus(r, \dot{r}) - R_\oplus > 0 \,, \tag{H.16}$$

where $q_\oplus$ is the perigee corresponding to the geocentric orbit of the near-Earth object $\mathcal{A}$. This latest expression has no simple analytic form as a function of $(r, \dot{r})$, nevertheless it can be computed numerically. As it is obvious that $q_\oplus = a_\oplus\ (1 - e_\oplus)$, we compute the semi-major axis $a_\oplus$ (negative for hyperbolic orbits) and the eccentricity $e_\oplus$ by

$$a_\oplus = -\frac{k_\oplus^2}{2\ E_\oplus} \,, \qquad\qquad e_\oplus = \sqrt{1 - \frac{C_\oplus^2}{a_\oplus\ k_\oplus^2}} \,,$$

where

$$C_\oplus = \|\vec{C}_\oplus\| = \|(\vec{P}_\mathcal{A} - \vec{P}_\oplus) \times (\vec{V}_\mathcal{A} - \vec{V}_\oplus)\| = r^2\, \eta^2$$

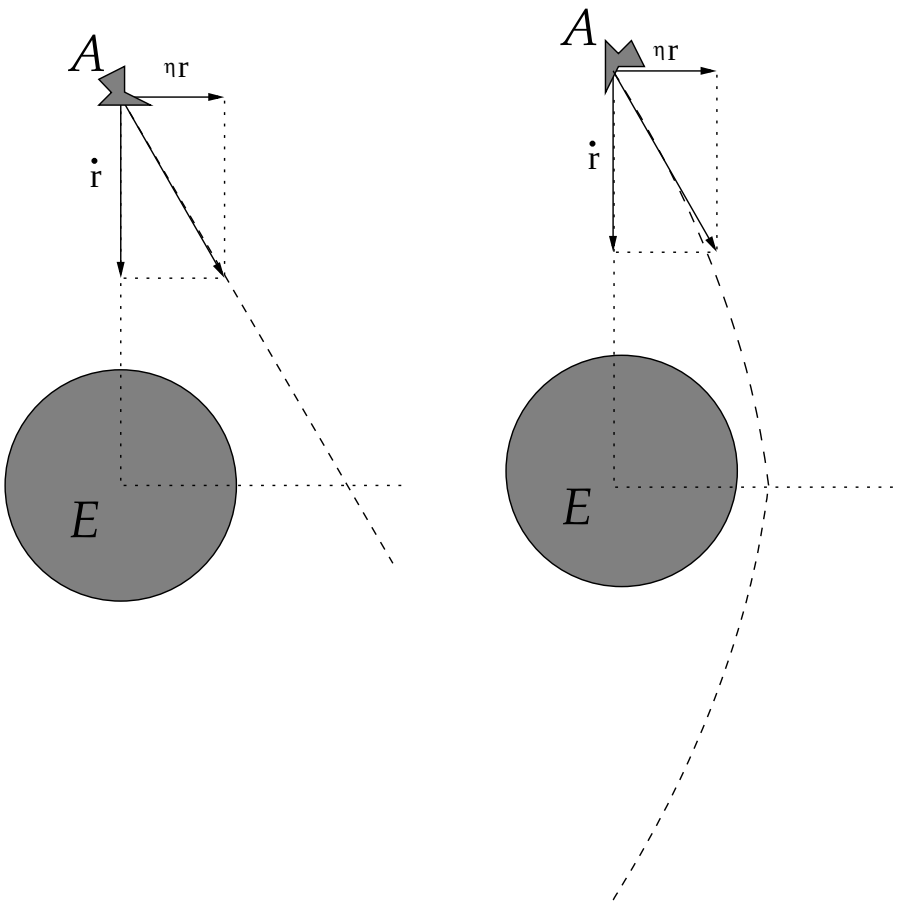

Figure H.2: Immediate impact trajectory in the linear and Keplerian cases (schematic representation).

is the norm of the angular momentum $\vec{C}_\oplus$ of the geocentric orbit. The linear and Keplerian boundaries are represented in Figure H.2 in a descriptive way and in the plane $(r, \dot{r})$ on Figure H.3. The two conditions are very similar, even if, as expected, for low radial geocentric speed $\dot{r}$, the differences are significant. Nevertheless, as already pointed out by Milani et al. (2004a), our new condition is only useful for the discovery of very small objects or of objects with a very small apparent magnitude. In other words, this condition allows to discriminate between the population of asteroids and that of future shooting stars.

A particular region appears clearly in Figure H.3, inside the green curve (geocentric energy) and to the right of the red curve (Keplerian condition): this is a region of bodies orbiting around the Earth. Of course, most of the artificial satellites have very precise orbits and do not require such a study. However, it is not always the case for space debris where orbital uncertainty is a common fact, especially in the case of uncatalogued geostationary space debris. A detailed analysis of this confined area, associated to a suitable model of propagation, would give an interesting tool to follow this population and to measure the risk for future missions.

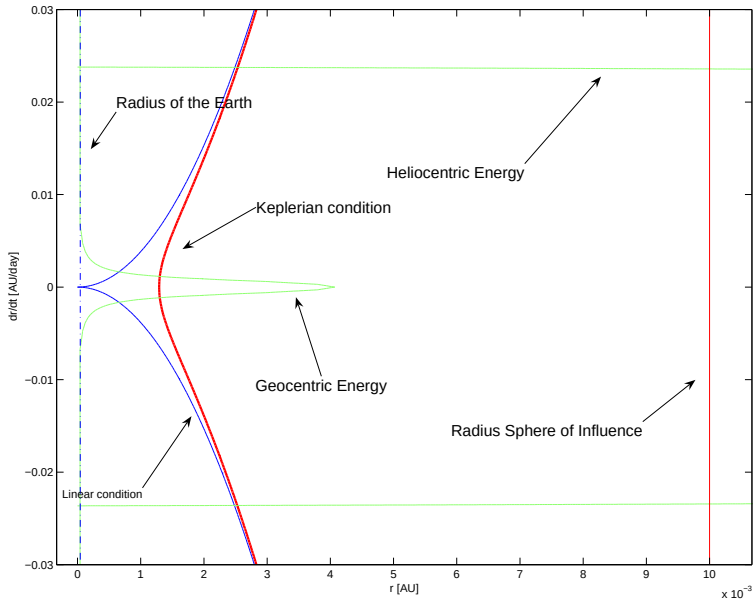

Figure H.3: Immediate impact trajectory in the linear and Keplerian cases; represented in the $(r, \dot{r})$ plane where r is given in astronomical unit.

H.3 Nodal distances

Our second purpose is to define the subset of this admissible region associated with the objects which impact the Earth. The necessary conditions for an impact between the Earth (considered on a circular heliocentric orbit) and an hypothetic object can be easily formulated: the object and the Earth should be exactly at one of the nodes of the orbit at the same time

$$\Omega - \lambda_E = \frac{\pi}{2} \mp \frac{\pi}{2} \tag{H.17}$$

$$\omega + f = \frac{\pi}{2} \mp \frac{\pi}{2}\,, \tag{H.18}$$

where λ_E is the longitude of the Earth, on its geocentric circular orbit, measured in the ecliptic plane, Ω, ω and f are respectively the longitude of the ascending node, the argument of the pericenter and the true anomaly of the heliocentric orbit of the body $\mathcal{A}$, in an ecliptic reference frame. The upper sign corresponds to an impact at the ascending node, and the lower sign to an impact at the descending node. For a collision at the ascending node, the so called *ascending nodal distance* must vanish

$$d_+ = \frac{a(1-e^2)}{1 + e\cos\omega} - a_E = 0\,, \tag{H.19}$$

where a_E is the Earth's semi-major axis, a that of the body $\mathcal{A}$ and e its eccentricity. We have a very similar condition for a collision at the descending node, for the *descending nodal distance*

$$d_- = \frac{a(1-e^2)}{1-e\cos\omega} - a_E = 0\,. \tag{H.20}$$

For any set of values of $(r, \dot{r})$ in the admissible zone, we compute numerically the orbital elements using the usual transformations

$$a = \frac{k_\odot^2}{2\,E_\odot}\,, \qquad e = \sqrt{1 - \frac{C^2}{a\,k_\odot^2}}\,, \qquad \cos i = \left(\frac{C_z}{C}\right)\,,$$

where $\vec{C} = (C_x, C_y, C_z)$ is the angular momentum of the body on its heliocentric orbit and C is its norm. $E_\odot$ is defined by the Equation (H.13). A smart way for calculating ω is to use a scalar product between the line of nodes and the Laplace vector defined by

$$\vec{q} = \vec{V}_\mathcal{A} \times \vec{C} - k_\odot^2 \frac{\vec{P}_\mathcal{A}}{\|\vec{P}_\mathcal{A}\|}\,. \tag{H.21}$$

We present two very different cases; in the first one (corresponding to the attributable $\alpha = 2.018$, $\delta = 0.204$, $\dot{\alpha} = -0.00623$ and $\dot{\delta} = 0.000302$), the level curve $i = 90°$ divides the admissible region into two parts; the level curves seem to converge towards a point located outside the admissible region. In the second one (corresponding to the attributable $\alpha = 2.018$, $\delta = -1.204$, $\dot{\alpha} = -0.0623$ and $\dot{\delta} = 0.00302$), the *convergence* point of the inclination curves is inside the admissible region. This point corresponds to a singularity: the orbit is so elliptic than it becomes a straight line; it means that the inclination is not defined anymore, the orbital plane being reduced to a line.

For both cases, the level curves of the ascending (in red) and descending (in blue) nodal distances are plotted, giving a clear idea about the location of virtual impactors in the admissible zone (Figure H.4). In the first case, on the left part of Figure H.4, the ascending and descending nodal distances curves have no intersection, except for the case $r = 0$ and $\dot{r} = 0$ (i.e. the orbit of the Earth) which is obviously common to both conditions. On the opposite, on the right part of Figure H.4, they cross several times, inside the admissible region, for different types of non circular and non coplanar orbits.

The location of the nodal distances in the admissible region is crucial to determine the potential hazard of this attributable. Indeed, it is easy to sample the curves $d_+ = 0$ or $d_- = 0$; to each point of this subset corresponds a set of six orbital elements, i.e. an orbit and an instantaneous position on this orbit. By propagating the motions of the body (on a Keplerian orbit, for the simplest case) and of the Earth, we can rapidly check whether a close encounter is scheduled or not for the next few tens of years. By close encounter, we mean that the body enters the sphere of influence of the Earth. A that moment, another analysis has to be developed, using specific variables and formulae (see for example Öpik (1976) and Valsecchi

et al. (2003)) to make the final model of approach and detect a significant probability of impact.

In a less restrictive use, this new information (the nodal distances location) may also be of great interest to improve the choice of the metric function to enhance some important subsets of the admissible region for future propagation (Milani et al., 2004a).

H.4 Circular and linear orbits

Let us draw the contour levels of the eccentricity in the admissible zone, for the two selected attributables (Figure H.5). There are two apparent centers of circular orbits: the first one coincides with the Earth itself ($r = 0$ and $\dot{r} = 0$) which is assumed to be on a circular orbit; the second one is more interesting and can be characterized as a solution of the two following equations

$$\dot{r} = -\frac{A\,r}{r+B}\,, \tag{H.22}$$

$$p_7 + 2\left[p_2\,\dot{r} + p_4\,r\,\dot{\alpha} + p_6\,r\,\dot{\delta}\right] + \dot{r}^2 + r^2\,\dot{\alpha}^2\,\cos^2\delta + r^2\dot{\delta}^2 = \frac{k^2}{\sqrt{p_0 + 2\,p_1\,r + r^2}}\,, \tag{H.23}$$

where

$$\begin{aligned} A &= p_2 + p_3\,\dot{\alpha} + p_5\,\dot{\delta} \\ B &= p_1\,, \end{aligned}$$

as well as

$$\begin{array}{lll} p_0 = \langle \vec{P}_\oplus, \vec{P}_\oplus \rangle & p_7 = \langle \vec{V}_\oplus, \vec{V}_\oplus \rangle & \\ p_1 = \langle \vec{P}_\oplus, \vec{u} \rangle & p_3 = \langle \vec{P}_\oplus, \vec{u}_\alpha \rangle & p_5 = \langle \vec{P}_\oplus, \vec{u}_\delta \rangle \\ p_2 = \langle \vec{V}_\oplus, \vec{u} \rangle & p_4 = \langle \vec{V}_\oplus, \vec{u}_\alpha \rangle & p_6 = \langle \vec{V}_\oplus, \vec{u}_\delta \rangle\,, \end{array}$$

These equations were obtained by combining two conditions characterizing circular orbits. First, the position vector $\vec{P}_\mathcal{A}$ must be perpendicular to the velocity vector $\vec{V}_\mathcal{A}$

$$\langle\, \vec{P}_\mathcal{A}, \vec{V}_\mathcal{A} \rangle = 0 \tag{H.24}$$

secondly, the orbital heliocentric velocity must correspond to

$$\| \vec{V}_\mathcal{A} \|^2 = \frac{k_\odot^2}{a}\,,$$

that is

$$\| \vec{V}_\mathcal{A} \|^2 \, \| \vec{P}_\mathcal{A} \| = k_\odot^2\,. \tag{H.25}$$

Let us notice that all the values of the eccentricities lie between 0 and 1, the values outside the admissible region correspond to hyperbolic orbits. The curve $a = 1$ (more visible on the bottom diagram) corresponds to the positions of Earth's Trojans. We plot the curves corresponding to conditions (H.24) and (H.25) in Figure H.6. The condition (H.24) describes the

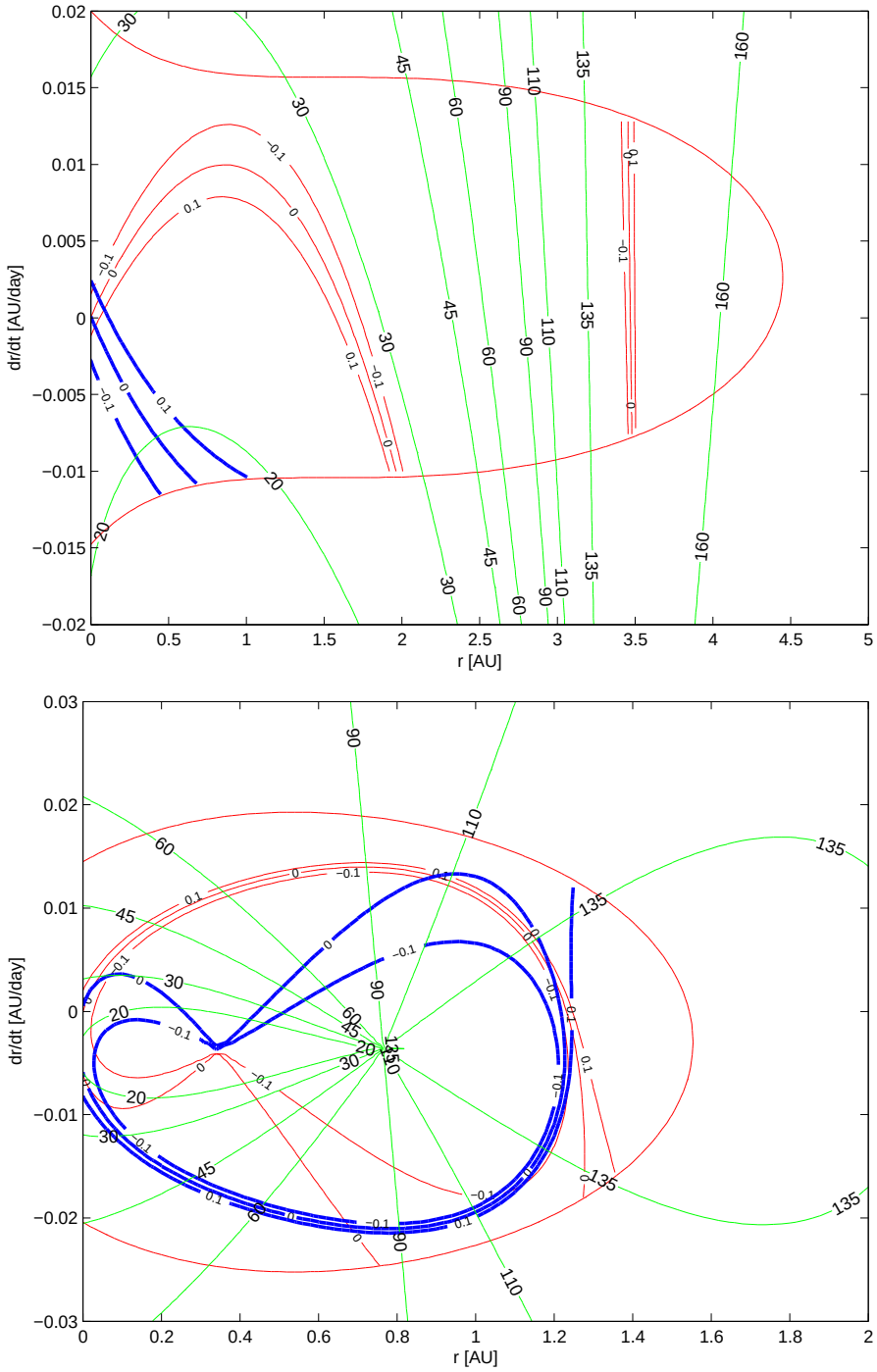

Figure H.4: Level curves of the inclination (i = 20, 30, 45, 60, 90, 110, 135, 160 degrees), of the ascending ($d_+ = -0.01, 0, 0.01$ [solid]) and descending ($d_- = -0.01, 0, 0.01$ [bold]) nodal distances for the attributable ($\alpha = 2.018$, $\delta = 0.204$, $\dot{\alpha} = -0.00623$, $\dot{\delta} = 0.000302$) [top]. ($\alpha = 2.018$, $\delta = -1.204$, $\dot{\alpha} = -0.0623$, $\dot{\delta} = 0.00302$) [bottom]. The unit is the astronomical unit.

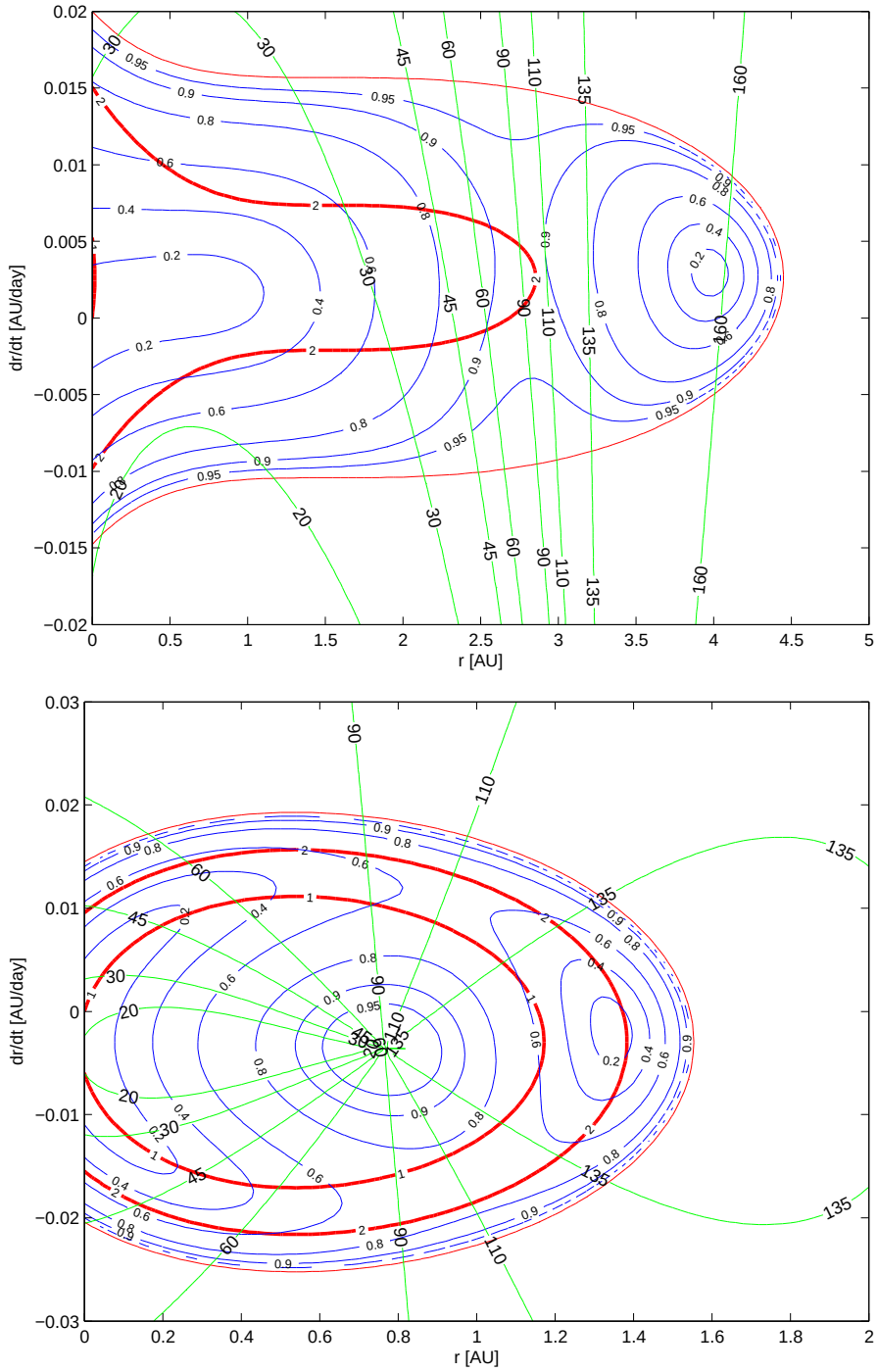

Figure H.5: Values of the eccentricity ($e = 0.2, 0.4, 0.6, 0.8, 0.9$) and of the inclination ($i = 20, 30, 45, 60, 90, 100, 135, 160$ degrees) for the two test attributables: ($\alpha = 2.018$, $\delta = 0.204$, $\dot{\alpha} = -0.00623$, $\dot{\delta} = 0.000302$) [top]. ($\alpha = 2.018$, $\delta = -1.204$, $\dot{\alpha} = -0.0623$, $\dot{\delta} = 0.00302$) [bottom]. Two level curves of the semi-major axis are also drawn corresponding to $a = 1$ AU and $a = 2$ AU [bold].

objects which are exactly at perihelion or aphelion dividing the admissible region into two distinct parts. The intersections of the curves (H.24) and (H.25) give the circular orbits in the admissible region. Beside the obvious case ($\dot{r} = 0, r = 0$), two potential circular orbits appear in the case of the first attributable and only one for the second one. The supplementary solution hidden in Figure H.5 appears clearly as shown in Figure H.6 (bottom). Let us remark that the virtual impactors detected by vanishing the nodal distances (except in the trivial case) correspond to non-circular orbits, which is obvious, the Earth moving on a circular orbit itself.

H.5 Elongations and related angular distance

Let us remind that the attributable consists of two angles and their time derivatives; usually they are connected to α, the right ascension, and δ, the declination, the geocentric equatorial coordinates, but they could also be replaced by λ and β, the ecliptic longitude and latitude of the object, or deduced from each other thanks to the relations

$$\begin{aligned} \cos\beta\cos\lambda &= \cos\delta\cos\alpha \\ \cos\beta\sin\lambda &= \sin\epsilon\sin\delta + \cos\epsilon\cos\delta\sin\alpha \\ \sin\beta &= \cos\epsilon\sin\delta - \sin\epsilon\cos\delta\sin\alpha\,, \end{aligned}$$

where ϵ is the obliquity, i.e. the angle between the ecliptic and the equatorial plane. A quantity directly linked to the attributable is the *elongation*, denoted by ϕ, the angular distance between the Sun and the body $\mathcal{A}$ as viewed from the Earth. The elongation is given by the expression

$$\cos\phi = -x_E\cos\lambda\cos\beta - y_E\sin\lambda\cos\beta\,, \tag{H.26}$$

where $(x_E, y_E, 0)$ is the heliocentric position of the Earth on its circular ecliptic orbit. For the first attributable, the elongation is $\phi = 166.87°$. This value suggests that the observations have been performed close to the opposition ($\phi = 180°$). The elongation value corresponding to the second attributable is $\phi = 91.48°$. In this particular case, the observations would have been acquired near quadrature.

Let us notice that all the virtual asteroids corresponding to the same attributable have the same elongation. On the contrary, the opposite angle θ, between the object $\mathcal{A}$ and the Earth, as viewed from the Sun, for a fixed elongation, is a function of r and its level contours are vertical lines in the admissible region, as shown in (Figure H.5). Let us remark that the two selected attributables have quite different proper motions. Indeed, we have $\eta_2 \approx 4\,\eta_1$ with $\eta_1 = 6.1 \cdot 10^{-3}$ rad/day, where η_1 and η_2 are the proper motions of the first and second attributable, respectively. On the other hand, the declination δ of the second attributable differs significantly from the first one giving to this last case a more theoretical and singular aspect. As a consequence, the internal structure of the admissible region associated to the second attributable shows several uncommon properties such as the inclination singularity, for example.

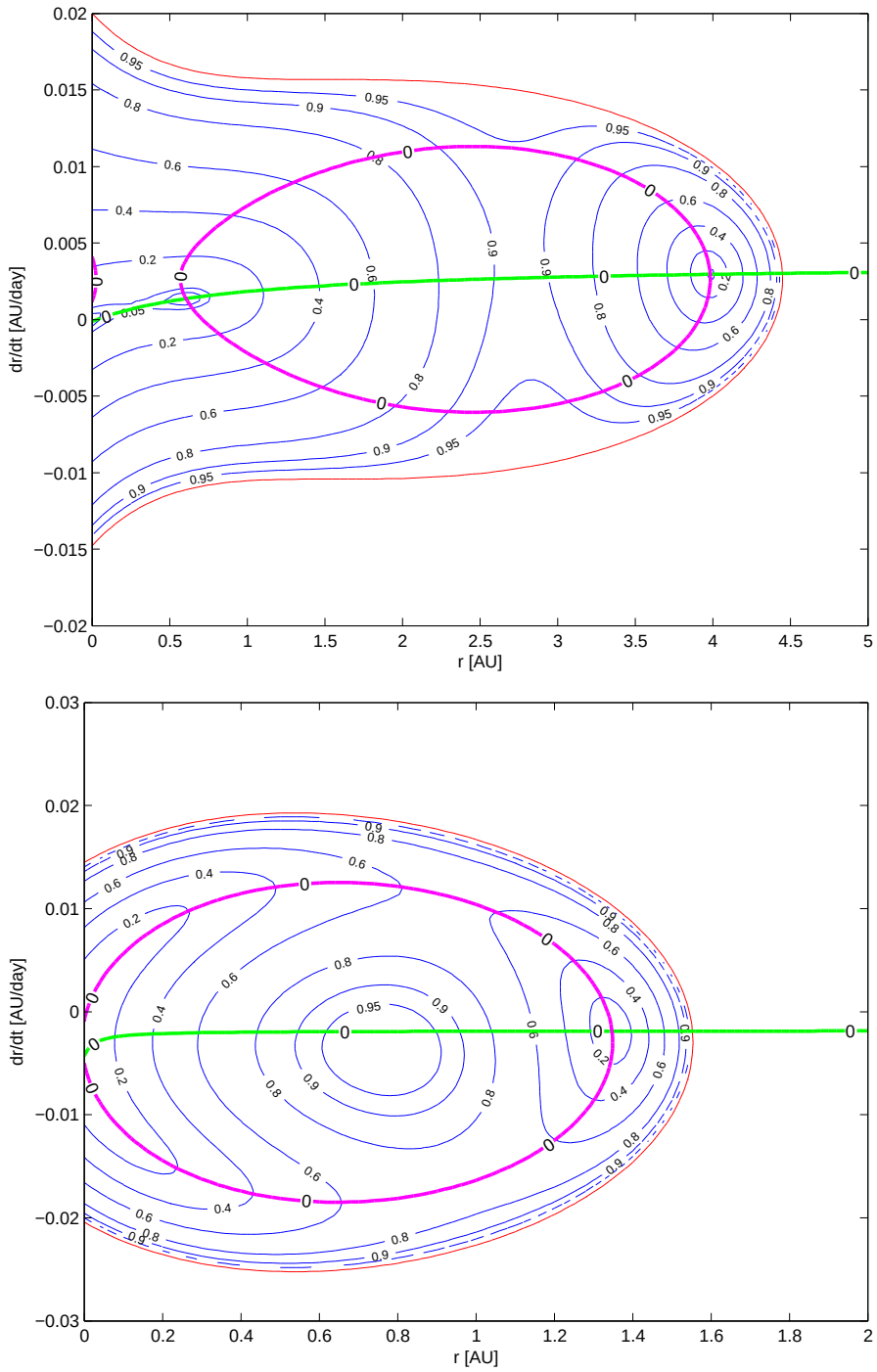

Figure H.6: Condition (H.24) and (H.25) for the two test attributables: ($\alpha = 2.018$, $\delta = 0.204$, $\dot{\alpha} = -0.00623$, $\dot{\delta} = 0.000302$) [top]. ($\alpha = 2.018$, $\delta = -1.204$, $\dot{\alpha} = -0.0623$, $\dot{\delta} = 0.00302$) [bottom].

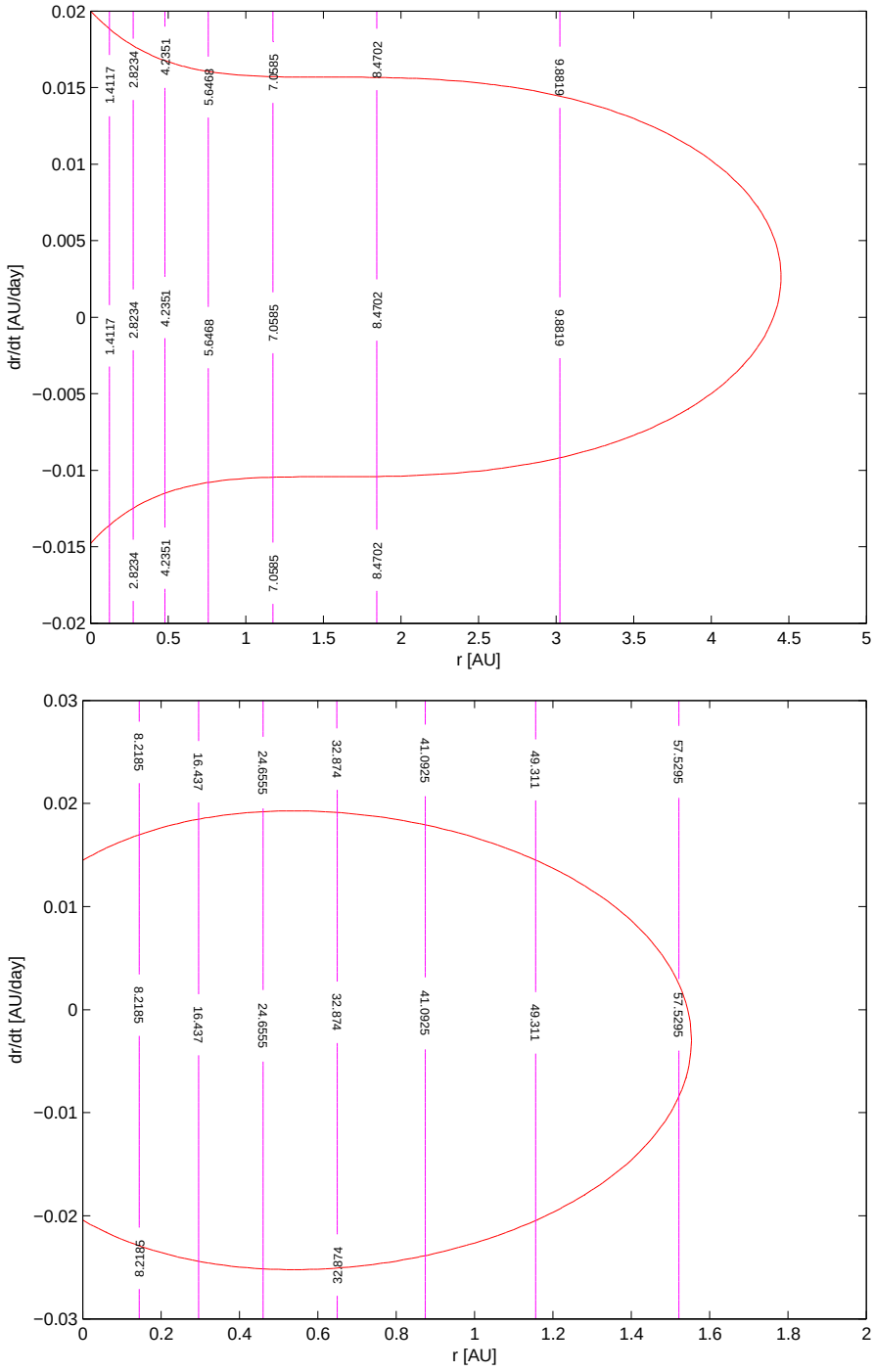

Figure H.7: The vertical lines correspond to the values of opposite angular distance θ (in degrees) for the two selected attributables.

H.6 Conclusion

The topology of the admissible region is clearly dependent on the selected attributable, as shown by our two test attributables, corresponding to two very different observations: at the opposition or at the quadrature.

We have shown that the number and the positions of the potential circular orbits, the location, the shape and the length of the ascending and descending nodal distances, the behaviour of the inclination level curves are very different from one situation to the other one and contain substantial information about any virtual body compatible with the partial set of observations.

In the search for potential impactors, we have proposed to sample the curves of zero nodal distances and to propagate this set of points for several years. This procedure reduces in a significant way the size of the admissible region and allows to use specific propagation methods, adapted to close encounters. It should be also interesting to compute the minimal orbital intersection distance (MOID) using the Öpik (1976) formalism, to have a more complete analysis about potential Earth's impactors. However, in this last case, we should check the validity of the theory by computing the Tisserand parameter.

Appendix I

Personal contributions

[Valk and Lemaître, 2007a] Valk, S., Lemaître, A. *Admissible regions for too short arcs: nodal distances and elongations*. Near Earth Objects, our Celestial Neighbors: Opportunity and Risk, Proceedings of IAU Symposium 236. Edited by G.B. Valsecchi and D. Vokrouhlický, Cambridge University Press, pp.455-464, 2007.

[Valk et al., 2007a] Valk, S., Lemaître, A., Deleflie, F. *Semi-analytical theory of mean orbital motion for geosynchronous space debris under gravitational influence*. Advances in Space Research. Submitted for publication, 2007.

[Valk et al., 2007b] Valk, S., Lemaître, A., Anselmo, L. *Analytical and semi-analytical investigations of geosynchronous space debris with high area-to-mass ratios influenced by solar radiation pressure*. Advances in Space Research 41, 1077-1090, 2007.

[Deleflie et al., 2007] Deleflie, F., Valk, S., Guzzo, M., Exertier, P., Portman, C. (2007). *Investigating the stability of the Galileo constellation in the framework of celestial mechanics*. Celestial Mechanics and Dynamical Astronomy. Submitted for publication, 2007.

[Valk and Lemaître, 2007b] Valk, S., Lemaître, A. *Analytical considerations of the space debris with high area-to-mass ratios located near the GEO region*, presented at "La Semaine de l'Astrophysique Française, Journées de la SF2A 2007", 2007.

[Valk and Lemaître, 2008] Valk, S., Lemaître, A. *Semi-analytical investigations of high area-to-mass ratio geosynchronous space debris including Earth's shadowing effects*. Advances in Space Research, 10.1016/j.asr.2008.02.010, 2008.

[Valk et al., 2008] Valk, S., Delsate, N., Lemaître, A., Carletti, T. *Global dynamics of high area-to-mass ratios geosynchronous space debris by means of the MEGNO indicator*. Advances in Space Research. Submitted for publication, 2008.

List of Figures

Bibliography

Agrawal, B. N. Design of Geosynchronous Spacecraft. Prentice-Hall, New-Jersey, 1986.

Aksnes, K. Short-period and long-period perturbations of a spherical satellite due to direct solar radiation. Celestial Mechanics and Dynamical Astronomy 13, 89–104, 1976.

Alby, F., Lansard, E., Michal, T. Collision of Cerise with Space Debris. Proceedings of the second European conference on Space Debris, ESA SP-393, pp. 589, 1997.

Allen, R.R., Cook, G.E. The long-period motion of the plane of a distant circular orbit. Proc. R. Soc. Lond., Ser. A 280, 97–109, 1964.

Anselmo, L., Bertotti, B., Farinella, P., Milani, A., Nobili, A. M. Orbital perturbations due to radiation pressure for a spacecraft of complex shape. Celestial Mechanics and Dynamical Astronomy 29, 27–43, 1983.

Anselmo L., Pardini C., Orbital Evolution of Geosynchronous Objects with High area-to-mass ratios. In Danesy, D. (Ed.), Proceedings of the Fourth European Conference on Space Debris, ESA SP-587, ESA Publications Division, Noordwijk, The Netherlands, pp. 279–284, 2005.

Anselmo, L., Pardini, C. Space debris mitigation in geosynchronous orbit. Advances in Space Research 41, 1091–1099, 2007a.

Anselmo, L., Pardini, C. Long-term evolution of High Orbits: Effects of Direct Solar Radiation Pressure and Comparison of Trajectory Propagators. *ISTI Technical Report 2007-TR-008*, PISA, Italy, 2007b.

Barrio, R., Borczyk, W., Breiter, S. Spurious structures in chaos indicators maps. Chaos, Solitons & Fractals, doi:10.1016/j.chaos.2007.09.084, 2007.

Benettin, G., Galgani, L., Giorgilli, A., Strelcyn, J.-M. Lyapunov characteristic exponents for smooth dynamical systems and for Hamiltonian systems; a method for computing all of them. Part 1: Theory. *Meccanica*, pp. 9–20, 1980a.

Benettin, G., Galgani, L., Giorgilli, A., Strelcyn, J.-M. Lyapunov characteristic exponents for smooth dynamical systems and for Hamiltonian systems; a method for computing all of them. Part 2: Numerical application. *Meccanica*, pp. 21–30, 1980b.

Beutler, G. Methods of celestial mechanics. V.1&2: Physical, mathematical, and numerical problems, Springer-Verlag, Berlin/Heidelberg, 2005.

Breiter, S. Extended Fundamental Model of Resonance. Celestial Mechanics and Dynamical Astronomy 85, 209–218, 2003.

Breiter, S., Wytrzyszczak, I., Melendo, B. Long-term predictability of orbits around the geosynchronous altitude. Advances in Space Research 35, 1313–1317, 2005a.

Breiter, S., Melendo, B., Bartczak, P., Wytrzyszczak, W. Synchronous motion in the Kinoshita problem. Application to satellites and binary asteroids. Astronomy & Astrophysics 437, 753–64, 2005b.

Broucke, R., Cefola, P. A Note on the relations between true and eccentric anomalies in the two-body problem. Celestial Mechanics 7, 388–389, 1973.

Brouwer, D., Clemence, G. M. Methods of celestial mechanics and Dynamical Astronomy. Academic Press, 1961.

Bulirsh, R., Stoer, J. Numerical treatment of ordinary differential equations by extrapolation methods. Numerishe Mathematik, Springer, Berlin/Heidelberg, 8, 1–13, 1966.

Chao, C. C., Baker, J. M. On the propagation and control of geosynchronous orbits. Journal of the Astronautical Sciences XXXI (1), 99–115, 1983.

Chao, C. C. Applied orbit perturbation and maintenance. The Aerospace Press, El Segundo, California, American Institute of Aeronautics and Astronautics, 2005.

Chao, C. C., Campbell, W. S. Long-term perigee height variations of GEO disposal orbits – a revisit. In Danesy, D. (Ed.), Proceedings of the Fourth European Conference on Space Debris, ESA SP-587, ESA Publications Division, Noordwijk, The Netherlands, pp. 303–308, 2005.

Chao, C. C. Analytical investigation of GEO debris with high area-to-mass ratio. AIAA Paper No. AIAA-2006-6514. In: Proceedings of the 2006 AIAA/AAS Astrodynamics Specialist Conference, Keystone, Colorado, 2006.

Deleflie, F. Théorie semi-analytique des mouvements quasi-circulaires moyens en mécanique spatiale – Applications aux satellites géodésiques. Phd. Dissertation, Observatoire de Paris, 2002.

Cincotta, P.M., Simó, C. Simple tools to study global dynamics in non-axisymmetric galactic potentials – I, Astron. Astrophys. Suppl. 147, 205–228, 2000.

Cincotta, P.M., Giordano, C.M., Simó, C. Phase space structure of multi-dimensional systems by means of the mean exponential growth factor of nearby orbits, Physica D 182, 151–178, 2003.

Cunningham, L.E. On the computation of the spherical harmonics terms needed during the Numerical integration of the orbital motion of an artificial satellite. Celestial Mechanics 2, 207–216, 1970.

Delong N., Frémaux C. Eccentricity management for geostationary satellites during end of life operations. In Danesy, D. (Ed.), Proceedings of the Fourthth European Conference on Space Debris, ESA SP-587, ESA Publications Division, Noordwijk, The Netherlands, pp. 297–302, 2005.

Deprit, A. Canonical transformations depending on a small parameter. Celestial Mechanics 1, 12–30, 1969

Deprit, A., Rom, A. The main problem of artificial satellite theory for small and moderate eccentricities. Celestial Mechanics 2, 166–207, 1970

Escobal, P. Methods of Orbits Determination. Robert E. Krieger publishing company Inc. (Malabar, Florida, USA), 1965.

Exertier, P., Métris, G. Semi-analytical theory of the mean orbital motion. Astronomy & Astrophysics 294, 278–286, 1995.

Ferraz Mello, S. Analytical study of the Earth's shadowing effects on satellite Orbits. Celestial Mechanics 5, 80–101, 1972.

Giacaglia, G. E. O. The equations of motion of an artificial satellite in nonsingular variables. Celestial Mechanics 15, 191–215, 1977.

Goździewski, K., Bois, E., Maciejewski, A.J., Kiseleva-Eggleton, L. Global dynamics of planetary systems with the MEGNO criterion. Astronomy & Astrophysics 378, 569–586, 2001.

Goździewski, K. Stability of the HD 12661 planetary system, Astronomy & Astrophysics 398, 1151–1161, 2003.

Goździewski, K., Breiter, S., Borczyk, W. The long-term stability of extrasolar system HD37154. Numerical study of resonance effects. Mon. Not. R. Astron. Soc. 383, 989–999, 2008.

Gronchi, J.F., Milani, A., De Michieli Vitturi, M., Knežević, Z. Orbit Determination with Very Short Arcs: Admissible Regions. *American Astronomical Society* 36, 861, 2004.

Henrard, J. On a perturbation theory using Lie transforms. Mathematics Research Laboratory, Boeing Scientific Research Laboratories. Celestial Mechanics 3, 107–120, 1970.

Henrard, J. Virtual singularities in the artificial satellite theory. Celestial Mechanics 10, 437–449, 1974.

Henrard, J., Lemaître, A. A second fundamental model for resonance. Celestial Mechanics 30, 197–218, 1983.

Henrard, J. Algebraic manipulation on computers for lunar and planetary theories. In: Proceedings of the IAU Symposium 114, Reidel, 59–62, 1986.

Henrard, J. Note on the reducing transformation and secular coupling. Celestial Mechanics 45, 327–331, 1988.

Kaula, W.M. Theory of satellite geodesy, Blaisdell Publishing Company, Waltam, MA/Toronto/London, 1966.

Kessler, D. J., Cour-Palais, B. G. Collision frequency of artificial satellites – The creation of a debris belt. Journal of Geophysical Research 10, 83, 1978.

Klinkrad H. Space Debris: Models and Risk Analysis. Springer-Verlag, Heidelberg/New York & Praxis Publishing, Chichester, UK, 2006.

Kozai, Y. Effects of solar radiation pressure on the motion of an artificial satellite. Smithsonian Astrophys Obs. Cambridge, MA (USA), Spec. Rep. No. 56, 1961.

Krivov, V., Getino, J. Orbital evolution of high-altitude balloon satellites, Astronomy & Astrophysics 318, 308–314, 1997.

Lála, P., Sehnal, L. Bulletin of the Astronomical Institutes of Czechoslovakia 20, 327-330, 1969.

Laskar, J. The chaotic motion of the solar system. A numerical estimate of the size of the chaotic zones. Icarus 88, 266–291, 1990.

Laskar, J., Froeschlé, C., Celletti, A. The measure of chaos by numerical analysis of the fundamental frequencies. Application to the standard mapping. Physica D 56, 253–269, 1992.

Laskar, J. Introduction fo frequency map analysis. In: Proceedings of 3DHAM95 NATO Advanced Institute 533, S'Agaro, pp. 134–150, 1995.

Lemoine, F.G., Kenyon, S.C., Factor, J.K., Trimmer, R., Pavlis, N.K., Chinn, D.S., Cox, C.M., Klosko, S.M., Luthcke, S.B., Torrence, M.H., Wang, Y.M., Williamson, R.G., Pavlis, E.C., Rapp, R.H., Olson, T.R. The development of the joint NASA GSFC and NIMA geopotential model EGM96. Tech. Rep. NASA/TP-1998-206861, NASA Goddard Space Flight Center, Greenbelt, Maryland, 20771 USA, 1987.

Liou, J.-C, Weaver, J.K. Orbital evolution of GEO debris with very high area-to-mass ratios, The Orbital Quarterly News, Vol. 8 issue 3, The NASA Orbital Debris Program Office, 2004.

Liou, J.-C, Weaver, J.K. Orbital dynamics of high area-to-mass ratio debris and their distribution in the geosynchronous region. In Danesy, D. (Ed.), Proceedings of the Fourth European Conference on Space Debris, ESA SP-587, ESA Publications Division, Noordwijk, The Netherlands, pp. 285–290, 2005.

McKee, M. Flying blankets threaten satellites, NewScientist, Magazine issue 2460, 2004.

Métris, G. Théorie du mouvement du satellite artificiel – Développement des équation du mouvement moyen – Application à l'étude des longues périodes. Phd. Dissertation, Observatoire de Paris, 1991.

Milani, A., Nobili, A.M., Farinella, P. Non-Gravitational Perturbations and Satellite Geodesy. Adams Hilger, Bristol, 1987.

Milani, A., Gronchi, J.F., De Michieli Vitturi, M., Knežević, Z. Orbit determination with very short arcs. I admissible regions. Celestial Mechanics and Dynamical Astronomy 90, 57–85, 2004a.

Milani, A., Gronchi, Knežević, Z., Sansaturio, M. E. Orbit Determination with Very Short Arcs: Preliminary Orbits and Identifications. American Astronomical Society 36, 862, 2004b.

Milani, A., Gronchi, G. F., Knežević, Z., Sansaturio, M. E. and Arratia, O. Orbit determination with very short arcs. Icarus 179, 350-374, 2005.

Milani, A. and Knežević, Z. From astrometry to celestial mechanics: orbit determination with Very Short Arcs. Celestial Mechanics and Dynamical Astronomy 92, 2005.

Montenbruck, O., Gill, E. Satellite orbits: models, methods, and applications. Springer, 2000.

Moons, M. Averaging approaches. In: Proceedings of the Artificial Satellite Theory Workshop, U.S.N.O. Washington D.C., 1993.

Murray, C.D., Dermott, S.F. Solar system dynamics, Cambridge University Press, Cambridge, UK, 1999.

Nacozy, P. E., Dallas, S. S. The geopotential in nonsingular orbital elements. Celestial Mechanics 15, 453–466, 1977.

Noyelles, B., Lemaître, A., Vienne, A. Titan's rotation. A 3-dimensional theory. Astronomy & Astrophysics 478, 959–970, 2008.

Öpik, E. Interplanetary Encounters, Elsevier, New York, 1976.

Pardini, C., Anselmo, L. Evolution of the debris cloud generated by the *Fengyun-1C* fragmentation event. In: Proceedings of the 20th International Symposium on Space Flight Dynamics, Annapolis, Maryland (USA), 2007.

Rossi, A. Population models of space debris. In Z. Knežević and A. Milani Ed., Proceedings of the IAU Colloquium No. 197, Dynamics of population of planetary systems, pp. 427-438, 2005

Schildknecht T., Musci R., Ploner M., Beutler, G., Flury, W., Kuusela J., Leon Cruz, J., de Fatima Dominguez Palmero, L. Optical observations of space debris in GEO and in highly-eccentric orbits, Advances in Space Research 34, 901–911, 2004.

Schildknecht, T., Musci, R. Flury, W., Kuusela, J. de Leon, J. de Fatima Dominguez Palmero, L. Optical observations of space debris in high-altitude orbits. In Danesy, D. (Ed), Proceedings of the Fourth European Conference on Space Debris, ESA SP-587, ESA Publications Divison, Noordwijk, The Netherlands, pp. 113–118, 2005.

Schildknecht, T., Musci, R., Flohrer, T. Properties of the high area-to-mass ratio space debris population at high altitudes. Advances in Space Research 41, 1039–1045, 2007.

Schildknecht, T. Optical surveys for space debris. Astron. Astrophys. Rev. 14, 41–111, 2007.

Soop, E.M. Handbook of geostationary orbits, Kluwer Academic Publishers (Dordrecht, The Netherlands) and Microcosm Inc. (Torrance, CA, USA), 1994, ISBN 0-7923-3054-4.

Standish, E.M. JPL Planetary and Lunar Ephemeris, DE405/LE405, JPL Interoffice Memorandum IOM 312.D-98-048, 1998.

Stoer, J., Bulirsch, R. Introduction to Numerical Analysis, Springer-Verlag, New York, 1980.

Sylvester, J.J. A Method of Determining By Mere Inspection the Derivatives from Two Equations of Any Degree. Phil. Mag. 16, 132–135, 1840.

The Orbital Debris Quarterly News. A publication of the NASA orbital debris program office. Vol. 12, issue 1, January 2008.

Tommei, G., Milani, A., Rossi, A. Orbit determination of space debris: admissible regions. Celestial Mechanics and Dynamical Astronomy 97, 289–304, 2007

Technical Report on Space Debris. Scientific and Technical Subcommittee of the United Nations Committee on the Peaceful Uses of Outer Space, New York, 1999.

Valk, S., Lemaître, A. Admissible regions for too short arcs: nodal distances and elongations. Near Earth Objects, our Celestial Neighbors: Opportunity and Risk, Proceedings of IAU Symposium 236. Edited by G.B. Valsecchi and D. Vokrouhlický, Cambridge University Press, pp. 455–464, 2007a.

Valk, S., Lemaître, A. Analytical considerations of the space debris with high area-to-mass ratios located near the GEO region. In: Proceeding of the “La Semaine de l’Astrophysique Française, Journées de la SF2A 2007”, 2007b.

Valk, S., Lemaître, A. Semi-analytical investigations of high area-to-mass ratio geosynchronous space debris including Earth’s shadowing effects. Advances in Space Research, 10.1016/j.asr.2008.02.010, 2008.

[Valk et al., 2007a] Valk, S., Lemaître, A., Deleflie, F. Semi-analytical theory of mean orbital motion for geosynchronous space debris under gravitational influence. Advances in Space Research. Submitted for publication, 2007.

[Valk et al., 2007b] Valk, S., Lemaître, A., Anselmo, L. Analytical and semi-analytical investigations of geosynchronous space debris with high area-to-mass ratios influenced by solar radiation pressure. Advances in Space Research 41, 1077–1090, 2007.

Valk, S., Delsate, N., Lemaître, A., Carletti, T. Global dynamics of high area-to-mass ratios geosynchronous space debris by means of the MEGNO indicator. Advances in Space Research. Submitted for publication, 2008.

Vallado, D. A. Fundamentals of astrodynamics and applications with technical contributions. Kluwer Academic Publishers, Microcosm Press, El Segundo, CA, Dordrecht, Technical contributions by Wayne D. McClain, Space Technology Library, vol. 12, 2001.

Valsecchi, G.B., Milani, A., Gronchi, G.F, and Chelsey, S.R., 2003, Resonant returns to close approaches: Analytical theory. Astronomy & Astrophysics 408, 1179–1196, 2003.

Vashkoviyak, S. N. The shadow function in the problem of influence of radiation pressure on the motion of artificial Earth satellites. Vestn. Mosk. un-ta Fiz., astron., vol. 15, 584–590, 1974.

Wisdom, J. Chaotic behavior and the origin of the 3/1 Kirkwood gap. Icarus 56, 51–74, 1983.

Wytrzyszczak, I. Non singular elements in description of the motion of small eccentricity and inclination satellites. Celestial Mechanics 38, 101–109, 1986.

Wytrzyszczak, I., Breiter, S., Borczyk, W. Regular and chaotic motion of high altitude satellites. Advances in Space Research 40, 134–142, 2007.

Zarrouati, O. Trajectoires spatiales. Toulouse Cépaduès Editions CNES, 1987.